Spring 5-15-2015

New Dion-Jacobson and Ruddlesden- Popper Layered Perovskites prepared by Topochemical Methods

Dariush Montasserasadi
mmontass@uno.edu

New Dion-Jacobson and Ruddlesden-Popper Layered Perovskites Prepared by Topochemical Methods

A Dissertation

Submitted to the Graduate Faculty of the
University of New Orleans
in partial fulfillment of the
requirements for the degree of

Doctor of Philosophy
in
Chemistry

by

Dariush Montasserasadi

B.S., Khajeh Nasir-al-din Toosi University, 2002

M.S., University of Tehran, 2006

M.S., University of New Orleans, 2012

May, 2015

This thesis is dedicated to

My mother, Mercedeh Karimkhani

My father, Reza Montasserasadi

My brothers, Reza and Kourosh

Thanks for all happiness, measureless love, support, patience, worries and kindness. I am thankful for having you all in my life.

Acknowledgments

I deeply appreciate to my supervisor Prof John. B. Wiley since 2009, I joined UNO not only because of his excellent guidance but also his support and patience which makes the research easier and enjoyable for me. John, I am proud of being one of your graduate students. I do thank my committee members, Prof. Matthew Tarr, Prof. Branko Jursic and Prof. Leonard Spinu for their helps and supports. I also should thank my previous committee members, Prof. Edwin D. Stevens, Prof. Pierre Ferdinand P. Poudeu and Prof. Gabriel Caruntu. I would like to thank Prof. Mark Trudell for his great helping as a graduate program coordinator. You never forget the people who helped you in your research: Dr. Sanjaya Ranmohotti, Dr. Jonglak Choi, Dr. Jose Vargas and also a good friend Dr. Debasish Mohanti. I had a wonderful opportunity to work with intelligent and hard-working undergraduates as an advisor to help not only in my research process but also it was a great experience for me to lead them in their research. I would like to thank all of them, Mark Granier (2013-2015), Benjamin Wilkins (2013), Cinnamon Mitchell (2013), Andrew Helman (2013), Lauren Franklin (2012), Stephen Guertin (2011) and Théo Brillatz (2010). I am very thankful of previous Wiley group members, Dr. Girija S Chaubey, Dr. Elisha Josepha, Dr. Jin Hee Lim, Dr. Yuan Yao, Dr. Jianxia Zhang, Dr. Jagnyaseni Tripathy (Piku), Dr. Shiva Adireddy, and the current group members, Taha Rostamzadeh, Léa Gustin, Sara Akbarian, Mayra Franco, Treva Brown, Clare Wheeler and Sarah Gauthier. Dr. Arthur Maksymov, Satish Rai, Shankar Khanal, Ali Radmanesh and Daniel Adams, I appreciate for your time in my research. Part of the results conducted at Oak Ridge National Lab's Spallation Neutron Source which was sponsored by the Scientific User Facilities Division, Office of Basic Energy Sciences, U.S. Department of Energy which is gratefully acknowledged. At the end, I am really appreciated for the support comes from the National Science Foundation DMR-1005856 to let me to do research.

Table of Contents

List of Figures

List of Tables

Abbreviations

T_f	Goldschmidt Tolerance Factor
O_f	Octahedral Factor
DJ	Dion-Jacobson
RP	Ruddlesden-Popper
AV	Aurivillius
XRPD	X-Ray Powder Diffraction
NPD	Neutron Powder Diffraction
BVS	Bond Valence Sum
TEM	Transmission Electron Microscopy
SEM	Scanning Electron Microscopy
TGA	Thermogravimetric Analysis
DSC	Differential Scanning Calorimetry
DTA	Differential Thermal Analysis
EDS	Energy Dispersive Spectroscopy
SQUID	Superconducting Quantum Interference Device
PPMS	Physical Properties Measurement System
PM	Paramagnetic
FM	Ferromagnetic
AFM	Antiferromagnetic

Abstract

Layered perovskites can be classified in three major groups: Dion-Jacobson $AA'_{n-1}B_nO_{3n+1}$, Ruddlesden-Popper $A_2A'_{n-1}B_nO_{3n+1}$, and Aurivillius phase $(Bi_2O_2)A'_{n-1}B_nO_{3n+1}$. (A: Alkali metal, Alkali-earth metal; A′: Lanthanides and Bi; B: Ti, Nb, Ta; n: thickness of slabs). For more than two decades researchers have shown much interest in this series because of their magnetic and electrical properties. Tuning synthesis parameters such as temperature, time, and host structure can be used to direct such properties. Low temperature synthetic methods (topochemical methods) allow the preparation of compounds not accessible by traditional high temperature reactions. This dissertation mainly considers the topochemical methods of ion exchange and reductive and oxidative intercalation to build new low temperature or metastable layered perovskites. The two-dimensional Dion-Jacobson $ALaNb_2O_7$ layered perovskites were intercalated reductively to produce $A_2LaNb_2O_7$ and then oxidized with water or hydro-chalcogenides (H_2Ch, Ch: S, Se) to produce the novel alkali metal hydroxide, $(A_2OH)LaNb_2O_7$, and alkali metal hydro-chalcogenides, $(A_2ChH)LaNb_2O_7$, respectively. The synthesis and characterization of these compounds are presented in Chapters 2 and 3. In another set of studies, high temperature ceramic methods lead to the new host $APrNb_2O_7$. When this reaction is followed by ion exchange, $(CuCl)PrNb_2O_7$ can be prepared. The structural refinement, magnetic properties, and thermal stability of new phases have been studied in Chapter 4. The utility of praseodymium niobates for the formation of other metal oxyhalides was also developed; the series $(MX)PrNb_2O_7$ (M: Mn, Fe, Co, Cu and X: F, Cl) were prepared by the ion exchange of $LiPrNb_2O_7$ and the obtained phases characterized (Chapter 5). Further, to expand the library of materials and because of interesting properties of lanthanides (Ln: La, Pr, Nd, Sm), lanthanide tantalates have been explored for the preparation of oxyhalides and

resulted in the compounds (CuCl)$LnTa_2O_7$ (Ln: Pr, Nd) (Chapter 6). Manipulation of Dion-Jacobson layered perovskites are not limited to lanthanides, other hosts with interesting properties have been examined (e.g. $ABiNb_2O_7$) (A: alkali metal, CuCl) and their crystal structures characterized along with thermal stability and magnetic response.

Keywords: Layered perovskites; Topochemical methods; Ion exchange; Intercalation.

Chapter 1

Introduction

1.1. Perovskites

Perovskite "$CaTiO_3$" (Figure1a) was discovered by Gustav Rose in 1839 in the Ural mountains of Russia and received this name in tribute to Russian mineralogist Count Lev Aleksevich Perovski (1792-1856).[1] Perovskites with ABX_3 chemical formula which A-site can be filled either by large alkali (A^+), alkali earth metal (A^{2+}) cation or transition metal (A^{3+}) with 12 coordination number, B-site can be occupied by transition metal (B^{3+}, B^{4+}, B^{5+}) cation with 6 coordination number, and X-site which are anions such as oxygen, carbon, nitrogen or halogen,[1] have a wide range of properties such as insulating, semiconducting, ionic conducting, superconductivity, ferroelectricity, solid oxide fuel cells, etc. For the ideal cubic perovskite ABO_3, A is located in the body centered position (Figure 1.1) and BO_6 octahedral are corner sharing. The nature of B, such as size and charge, can cause displacement in the position of B and create distortions or tilting which may result in different bond lengths with new properties. Table 1.1 shows how the A and B cations can affect the properties, which are related to distortion of BO_6 octahedra.

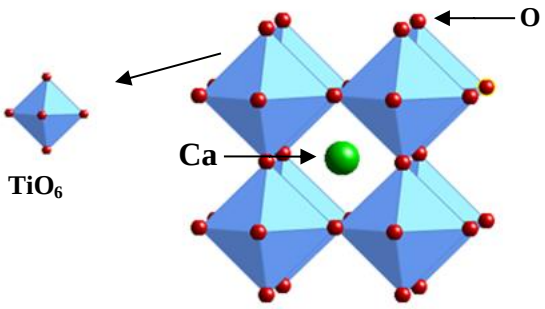

Figure 1.1. The Crystal structure of $CaTiO_3$

Table 1.1. Properties of perovskites

Perovskite	Property	Ref
$BaTiO_3$	Dielectric /Ferroelectric	2
$BaCeO_3$	Proton conductivity	3
$LaFeO_3$	Catalytic	4
$Ba(Pb,Bi)O_3$	Superconductivity	5
$GdFeO_3$	Ferromagnetism	6

The nature of A and B can affect the stability of perovskites. Goldschmidt's tolerance factor (T_f) is value which is used for this purpose and is shown by equation 1:

$$T_f = \frac{rA+rO}{\sqrt{2}(rB+rO)} \qquad \text{(eqn 1)}$$

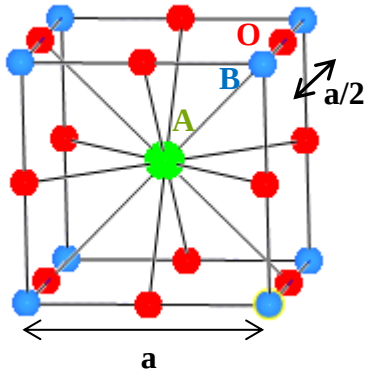

Figure 1.2. The crystal structure of ideal cubic perovskite ABO_3 with unit cell of a.

For ABO_3 perovskite, rA, rB and rO are the radius of the A, B and oxygen, respectively. (rA+ rO = $a/\sqrt{2}$, rB+rO=a/2) If the T_f value reaches 1, the perovskite structure is perfect cubic without any distortion (Figure 1.3 a) and if it is smaller or larger than 1, depending on A and/or B ionic radii, BO_6 octahedra become tilted.[7] Figure 1.3 presents the ideal cubic perovskite and distorted orthorhombic. Octahedral factor O_f (O_f = rB/rO) is also an important factor as tolerance factor for formation of perovskites. It is thought that for the formation of cubic perovskites, the octahedral

factor is in the range of $0.414 \leq O_f \leq 0.732$, which is necessary but not sufficient.[8] Table 1.2 has shown tolerance factor and octahedral factor for some perovskites.

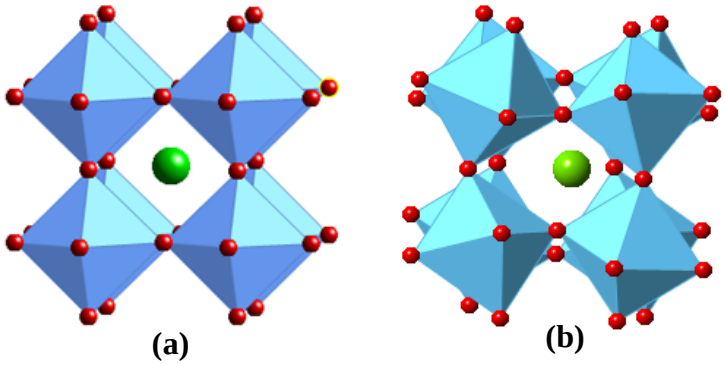

Figure1.3. The Crystal structure of (a) ideal cubic and (b) distorted perovskite.

Table 1.2. Goldschmidt tolerance factor and octahedral factor for perovskites[8]

Perovskite	**T_f**	**O_f**
$BaTiO_3$	1.071	0.448
$BaCeO_3$	0.943	0.644
$LaFeO_3$	0.961	0.478
$CaTiO_3$	0.973	0.448
$CaMnO_3$	1.012	0.393

Layered Perovskites

Layered perovskites consist of 2D slabs of the ABO_3 type structure, which are separated by interlayer species. Layered perovskites are classified in Dion-Jacobson (DJ) $A'A_{n-1}B_nO_{3n+1}$, Ruddlesden-Popper (RP) $A_2'A_{n-1}B_nO_{3n+1}$ and Aurivillius $(Bi_2O_2)A_{n-1}B_nO_{3n+1}$ (AV) (A′: proton, alkali metal, alkali earth metal, ammonium, ammines, transition metal, transition metal halide A: lanthanides, bismuth and B: Ti, Nb and Ta and n: thickness of perovskite slabs). Figure 1-4 presents the crystal structure of $RbLaNb_2O_7$ (DJ) and $Rb_2LaNb_2O_7$ (RP) and Aurivillius (AV) phase $(Bi_2O_2)An_{-1}B_nO_{3n+1}$.[9] The difference between Dion-Jacobson and Ruddlesden-Popper is the latter has more interlayer charge density. In $ALaNb_2O_7$ series, larger alkali metals (A: Rb, Cs) have larger coordination numbers (CN=8) with 100% occupancy in A-site but for smaller

cations (A: Li, Na), tetrahedral geometry is observed with coordination number 4 and 50 % occupancy. When A: K, an intermediate state with trigonal prismatic geometry is observed with 50 % occupancy.[10,11] Incorporation of ions with different sizes and charges in A, A´ and B sites, especially A´ site position where the ions are readily exchangeable, can lead to a variety of new layered perovskites with unique properties. Layered niobates for example can show good photocatalytic activity ($ALaNb_2O_7$, A: K, Rb, Cs),[10] ionic conductivity ($ALaNb_2O_7$, A: K, Na, Li),[11] superconductivity ($KCa_2Nb_3O_{10}$)[12] and ferroelectricity $(Bi_2O_2)Bi_2Ti_3O_{10}$[13] and that's why there has been a lot of interest in varying the interlayer cation site to build novel layered perovskites.

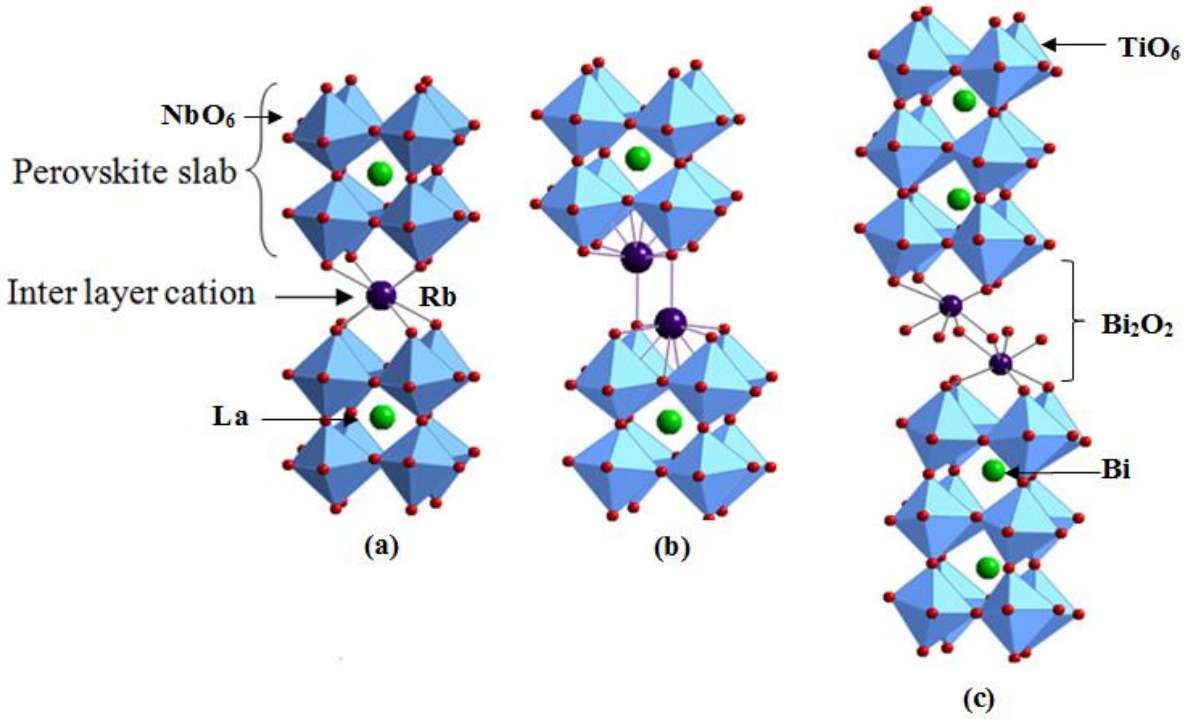

Figure1.4. The crystal structure of (a) $RbLaNb_2O_7$, (b) $Rb_2LaNb_2O_7$ and (c) $(Bi_2O_2)Bi_2Ti_3O_{10}$.

1.2. Synthetic Methods for Layered Perovskites

1.2.1 Solid State (Ceramic, High Temperature, Heat and Beat, Shake and Bake, Traditional, Conventional, Direct Reaction Method)

This method is the most common and probably the oldest one used for synthesizing inorganic materials, especially oxides at very high temperatures (1400 °C). In this method, powdered oxide reactants in stoichiometric ratios with excess amounts of volatile carbonates, hydroxides, sulfates and nitrates (20-50% excess to compensate the volatilization) are ground for periods of 10-15 min by agate mortar and pestle, pelletized, and then calcinated in a furnace at elevated temperatures. (Figure 1.5) After firing, the final powder is often washed with distillated water and dried for a day. Grinding is an important factor because it increases surface area and contact between the reactants and also brings fresh surfaces of reactants into contact.[11] Crucibles and boats used as reaction vessels must be able to withstand high temperatures and be sufficiently inert to the reactants. In the research presented in this dissertation, alumina (Al_2O_3), with maximum operating temperature of 2000 °C, is used. Pelletizing the powders using a hydraulic or hand press increases the contact between crystallites and also minimizes contact with the crucible. Choice of heating temperature can follow Tammann's rule, which suggests a temperature of about 2/3 of lowest melting point of reactants.[14] Heat and beat methods more often favor thermodynamically stable phases; metastable kinetic products are more typically synthesized under diffusion limited conditions.[14]

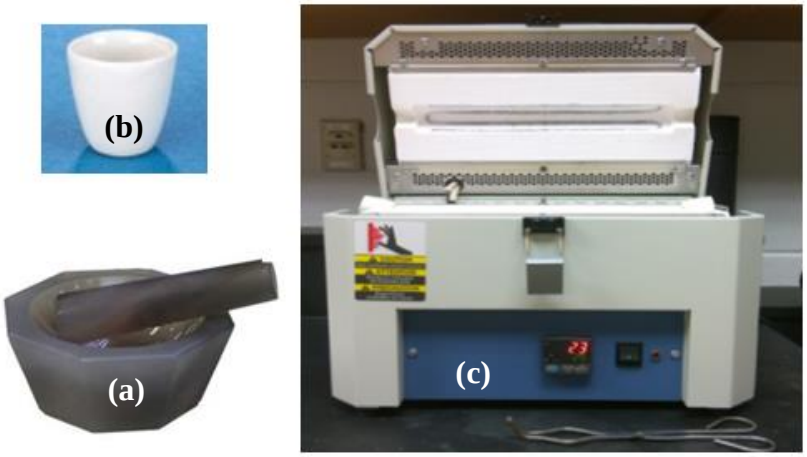

Figure 1.5. (a) Agate mortar and pestle, (b) alumina crucible, and (c) tube furnace.

1.2.1-2 Molten Salt Synthesis (Molten-Salt Fluxes, Flux–Assisted Synthetic Approach)

The flux-assisted method is a type of high temperature technique where a salt with a low melting point is added to the reactants and heated above the melting point of the salt. The molten salt acts as the reactive media (solvent) and can help to control particle size and morphology. The type of flux and the amount of flux (flux to reactant ratio), temperature of reaction and reaction time are parameters which should be considered when reacting ceramic powders. The high-temperature ceramic route is often unable to control the homogeneous distribution of particle shapes and sizes. ACl, A_2SO_4, ANO_3 (A: alkali metal) and in many cases eutectic mixtures of salts (e.g., NaCl+KCl) are examples of molten salts. Table 1.3 presents some of common molten salts with their melting points. The advantage of using molten salt is to increase the degree of homogeneity, to increase the rate of reaction, to shorten synthetic time (in some cases from weeks down to hours or minutes) and reaction temperature, and to control particle size (nm-μm) and shape. The flux can be typically be removed by washing with distillated water.[15]

Table 1.3. Melting points of molten salts and eutectic compositions[16]

Molten Salt	m_p (°C)
NaCl	801
KCl	770
0.5NaCl+ 0.5KCl	650
0.635 Li_2SO_4+ 0.365 Na_2SO_4	594
Na_2SO_4+ K_2SO_4	823

1.2.2 Topochemical Methods (Soft Chemistry, Chimie Douce, wet chemistry, Topotactic Method)

Layered perovskites prepared through the high temperature route are usually not metastable; metastable compounds are more commonly synthesized under moderate conditions (typically ≤ 500 °C). The idea of topochemistry and topochemical reactions was introduced by Kohlschütter in 1919[17] where he pointed out solid state reactions in which the structural elements of starting solid are preserved in the product. The more general term, *chimie douce* meaning soft chemistry, was introduced by French scientist Jacques Livage[18] in 1977 and includes many methods of topochemistry. In the case of reactions described herein, the overall structures of the layered perovskites are maintained (topotactic) but the composition changes sometimes result in the observation of interesting and unusual properties. The choice of effective precursors is vital for this approach in order to prepare the desired product. In this dissertation, ion exchange, layer construction, and intercalation are used. Figure 1.6 has shown examples of products from ion exchange, ion exchange followed by reductive intercalation, and reductive intercalation followed by oxidative intercalation reaction.

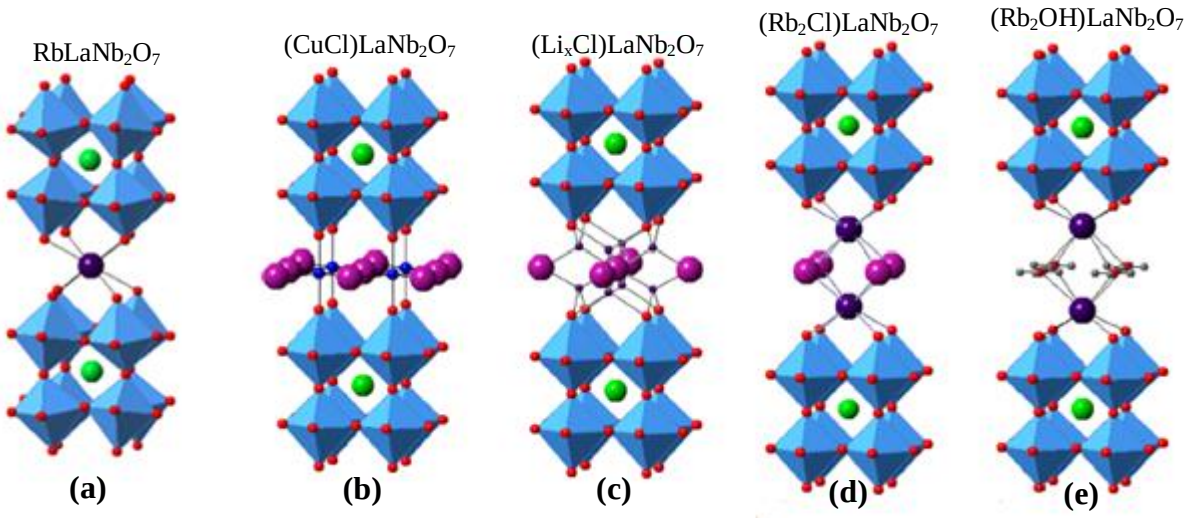

Figure 1.6. Representation of topochemical methods: (a) prepared from solid state,[19](b) ion exchange with $CuCl_2$,[20] (c) ion exchange with $CuCl_2$ then reductive intercalation of Li,[20] (d-e) reductive intercalation followed by oxidative intercalation.[21,22]

1.2.2.1 Ion Exchange of Layered Perovskites

Layered perovskites, mostly (DJ) $A'A_{n-1}B_nO_{3n+1}$ and (RP) $A_2'A_{n-1}B_nO_{3n+1}$, readily undergo replacement of interlayer cations (A′) with monovalent cations (H^+, NH_4^+, Ag^+), aliovalent cations (Rb^+ with Ca^{2+}), and the co-exchange of cations and anions (Rb^+ with $CuCl^+$). The double layered perovskite, $RbLaNb_2O_7$, can be exchanged by smaller alkali metals,[23]protons, and transition metals.[24] A successful ion exchange reaction depends on the geometry of layered perovskites, such as interlayer spacing and distortion/tilting of BO_6 octahedral, type of exchangeable species, and reaction temperature. The ion exchange on layered perovskites with different slabs MO_6 (M: Nb, Ta, Ti) even with the same size (rNb^{5+}=rTa^{5+} =0.74 Å CN=6) [25] can result in different products; this may be related to the distortion or tilting of MO_6 units. Figure 1.6b is an example of co-exchange reaction for $(CuCl)LaNb_2O_7$ prepared from $RbLaNb_2O_7$ and $CuCl_2$.

1.2.2.2 Intercalation (Reductive, Oxidative or Neutral) and De-intercalation

Insertion of cations A^+ (A: alkali metal), anions (oxide, halide) or in some cases neutral species to layered compounds define as reductive, oxidative or neutral intercalation, respectively. De-intercalation is the removal of ions from the structure. Intercalation and de-intercalation can create new properties; the insulator anatase, TiO_2, becomes the superconductor Li_xTiO_2 (T_c=13 K) after reductive intercalation with lithium.[15] Successful intercalation depends on factors such as time, temperature, size and coordination of components.

1.2.2.3 Multistep Topochemical Approach

The combination of two or more topochemical methods is referred to as a multistep reaction. Ion exchange of $ALaNb_2O_7$ with $CuCl_2$ followed by reductive intercalation with n-butyl lithium resulted in $(Li_xCl)LaNb_2O_7$ (sequentially, Figures 1.6a - c). For $(Rb_2Cl)LaNb_2O_7$, $(Rb_2SH)LaNb_2O_7$ and $(Rb_2OH)LaNb_2O_7$[21, 26, 22] also have been prepared through reductive intercalation of $RbLaNb_2O_7$ with Rb° then oxidative intercalation by chlorine, hydrogen sulfide, and water, respectively. $(Rb_2Cl)LaNb_2O_7$ and $(Rb_2OH)LaNb_2O_7$ are shown in Figure 1.6d and 1.6e, respectively.

1.3 Crystal Structure

Solids can be amorphous or crystalline. In amorphous solids, atoms, ions or molecules are randomly orientated and like glass, there is no systematic atomic arrangement or long-range order in their structure. Crystallites, such as seen in single crystals or polycrystalline powder samples, have a highly ordered species in the 3D (Figure 1.7). Polycrystalline materials, like

layered perovskites, contain aggregates of tiny single crystals or grains. The structure of such materials is described by the unit cell, the smallest unit of the crystal structure which has the symmetry of the whole structure. The unit cell parameters are given as a set of lengths (a, b, c) and angles (α, β, γ), which are shown in Figure 1.8. There are 7 crystal systems with 14 Bravais lattices as shown in Table 1.4.

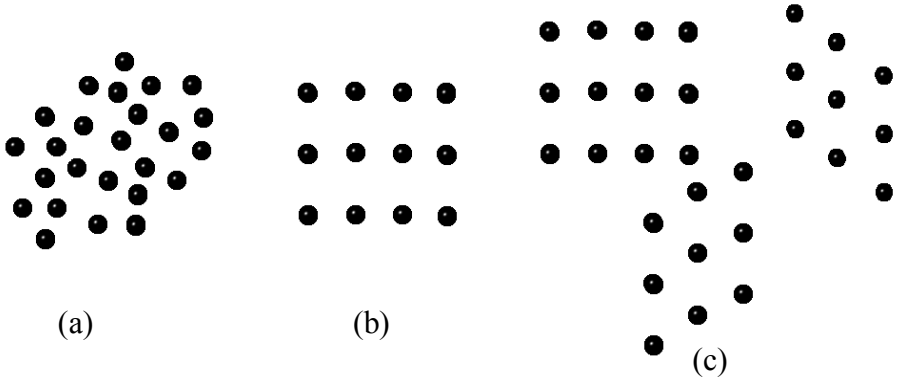

Figure 1.7. (a) Amorphous, (b) single crystal and (c) polycrystalline.

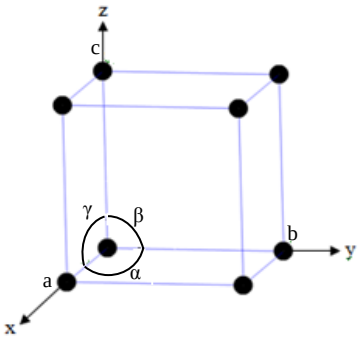

Figure 1.8. Unit cell parameters. (Lengths a, b, c and angles α, β, γ.)

In crystal lattices, according to the positions, atoms are placed in planes define by three integers *h*, *k* and *l* (*hkl*) called the Miller indices. Figure 1.9 shows the cubic crystal system with 100, 010, and 001 Miller indices. The relation between crystal system and Miller indices is shown in Table 1.4. It is important to index powder diffraction data so as to extract unit cell parameters from the scans. This can lead to useful information about crystal structure. The

program used to determine unit cell parameters in this research is ChekCell.[27] In Table 1.4, symbol *P* (primitive) is used for unit cell if there are equivalent points at each corner of unit cell, symbol *I* (body centered) if there is an additional position in the middle of the unit cell, symbol *F* (face centered) if there are additional positions in the middle of each face.

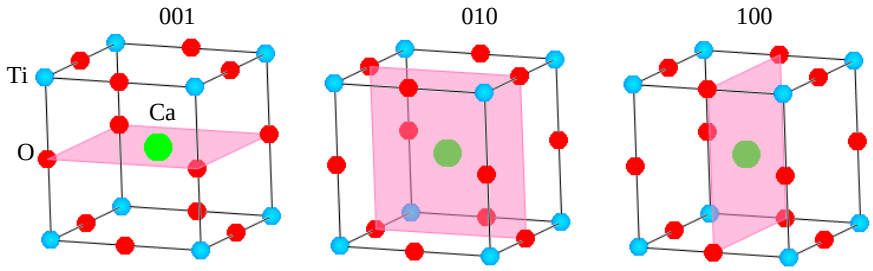

Figure 1.9. Miller indices for cubic $CaTiO_3$.

1.4. Characterization of Layered Perovskites

Spectroscopy techniques can reveal information about the chemical composition and the crystal structure of various materials. Some of the common methods used in this research are: Diffraction techniques (X-ray powder diffraction, neutron powder diffraction, and electron diffraction), ultraviolet-visible spectroscopy, infrared and Raman spectroscopy, magnetic measurements (direct current, alternating current). Macroscopic properties are characterized by techniques such as thermal analysis (gravimetric and differential scanning calorimetry), dielectric analysis and ferroelectric analysis. Microscopic techniques have been used to probe the surface and morphology of the structure are transmission electron microscope and scanning electron microscope.

Table 1.4.Crystal systems with unit cell and interlayer spacing.

Crystal System/ Dimension/Angles	Lattices System	Interplanar spacing	Structure
Cubic (a=b=c, α=β=γ=90°)	P, I, F	$\frac{1}{d^2}=\frac{h^2+k^2+l^2}{a^2}$	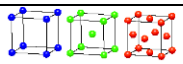
Tetragonal (a=b≠c , α=β=γ=90°)	P, I	$\frac{1}{d^2}=\frac{h^2+k^2}{a^2}+\frac{l^2}{c^2}$	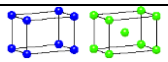
Orthorhombic (a≠b≠c ,α=β=γ=90°)	P, C, I, F	$\frac{1}{d^2}=\frac{h^2}{a^2}+\frac{k^2}{b^2}+\frac{l^2}{c^2}$	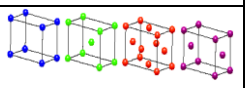
Hexagonal (a=b≠c, α=β=90°, γ=120°)	P	$\frac{1}{d^2}=\left(\frac{4}{3}\right)\left[\frac{h^2+k^2+hk}{a^2}\right]+\frac{l^2}{c^2}$	
Trigonal-Rhombohedral (a=b=c, α=β=γ<120°, ≠90°)	P, R	$\frac{1}{d^2}=\frac{(h^2+k^2+l^2)Sin^2\alpha+2(hk+kl+hlCos^2\alpha-Cos\alpha}{a^2\ (1-3Cos^2\alpha+2Cos^3\alpha)}$	
Triclinic (a≠b≠c ,α≠β≠γ≠90°)	P	$\frac{1}{d^2}=\frac{1}{V^2}[h^2b^2c^2sin\alpha^2+k^2a^2c^2sin\beta^2+l^2a^2b^2sin\gamma^2+2hkabc^2(cos\alpha cos\beta-cos\gamma)+2kla^2bc(cos\beta cos\gamma-cos\alpha)+2hlab^2c(cos\alpha cos\gamma-cos\beta)]$	
Monoclinic (a≠b≠c ,α=γ=90° , β≠180°)	P, C	$\frac{1}{d^2}=\left[\frac{1}{sin\beta^2}\frac{h^2}{a^2}\right]+\left[\frac{1}{sin\beta^2}\frac{k^2}{b^2}\right]+\frac{l^2}{c^2}-\left(\frac{2hlcos\beta}{ac}\right)$	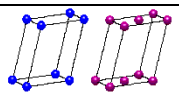

X-Ray Powder Diffraction (XRPD)

XRPD technique is one of the most powerful tools in the analysis of polycrystalline solid phases. It directly probes the crystallographic data, changes of the structure, existence of impurity or starting materials, etc. It also gives useful information and answers questions such as: (1) is your phase amorphous or crystalline? (2) How many crystalline phases exist? (3) What is the crystallite size and does strain exist? (4) What are unit cell parameters and interlayer d-spacing? Looking at Figure 1.10 some of these questions can be answered like; there are two crystalline

phases which are shown by black and red color species. Similar peak widths of black and red in Figure 1.10 prove there have the same sizes of crystals.

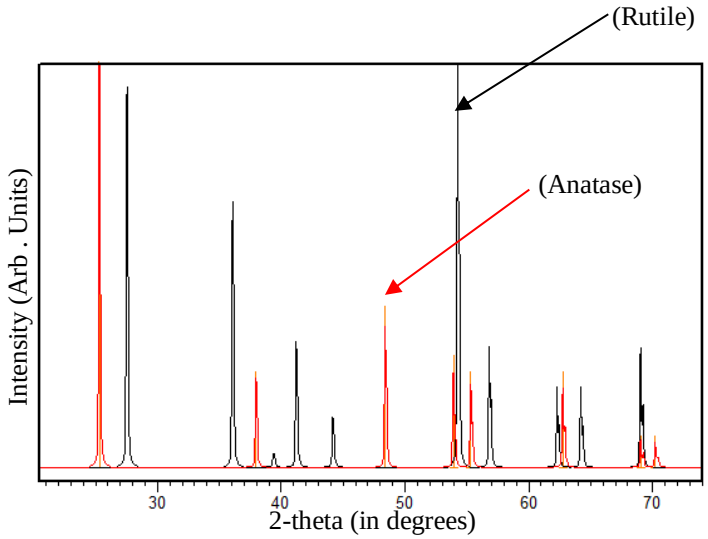

Figure 1.10. XRD Mixture of two crystalline phases of TiO_2 (red and dark).

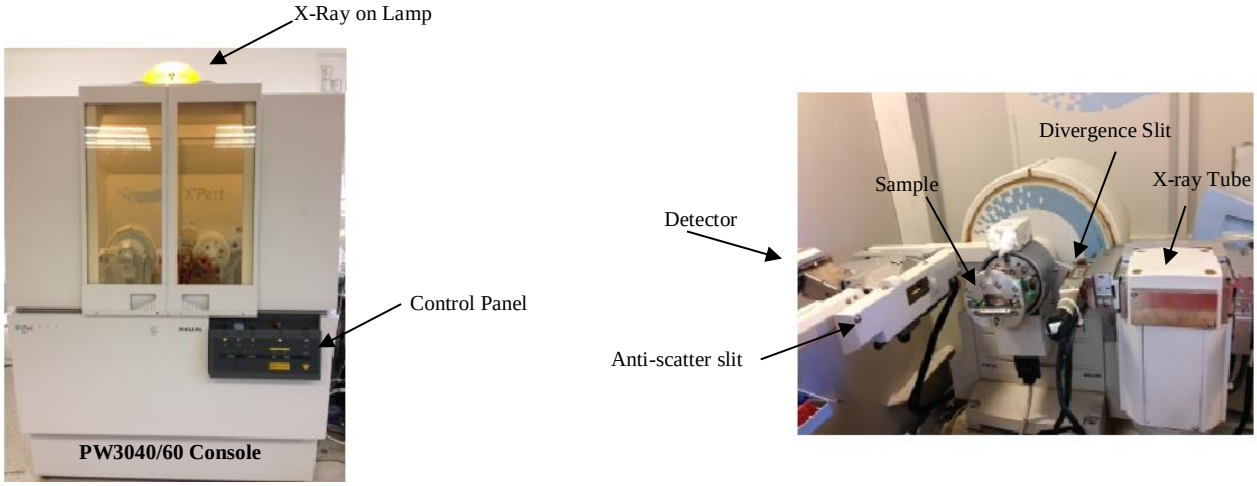

Figure 1.11. Philips X'Pert Pro X-ray Diffractometer PW3040/60X

In the X-ray experiment itself, a monochromatic X-ray beam (Cu-Kα; λ = 1.5418 Å) is emitted from the X-ray tube and then passes through filters and a divergence slit before hitting the sample (Figure 1.11). The electrons of the sample interact with X-ray beam resulted in scattering; when the scattered X-rays constructively interfere, reflections will appear.

Constructive interference only occurs when two parallel X-ray waves from a coherent source scatter from two adjacent planes. Their path difference ($2d_{hkl}\sin\theta$) must be an integer number of wavelengths ($n\lambda$). Two waves add to make a new wave with larger amplitude.

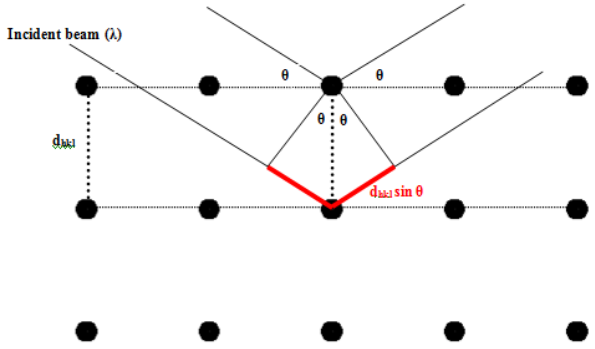

Figure 1.12. Bragg's Law

Bragg's Law, highlighted in Figure 1.12, shows when the scattering waves are constructive it follows the equation, $n\lambda = 2d_{hkl}\sin\theta$ where n is integer number, λ is wavelength of X-ray, d_{hkl} interlayer spacing that depends on crystal system as shown in Table 1.4 and 2θ is the measured angle. It is important to know how different atoms scatter X-rays; this is called the atomic scattering factor and depends on the electron density on the atom. All of the atoms scatter X-rays where the atomic scattering factor (f) equation is $f_0 = c + \sum_{i=1}^{4} a_i \exp(-\frac{b_i \sin^2\theta}{\lambda^2})$. All of the coefficients (c, a_i, b_i) for this equation are given by Cromer and Waber.[28] Temperature factors are expressed as either U_{iso} or U_{ij} where the thermal correction to the structure factor is either: $T = \exp(\frac{-8\pi^2 U_{iso}\sin^2\theta}{\lambda^2})$ for isotropic thermal motion or $T = \exp(-2\pi^2 (U_{11} h^2 a^2 + \cdots + 2U_{12} hkab + \cdots)$ for anisotropic thermal vibration. Atoms that don't vibrate the same amount in all directions can be represented by an anisotropic ellipsoidal model that includes six variables $(U_{11}, U_{22}, U_{33}, U_{12}, U_{13}, U_{23})$. Thermal displacement can reduce the intensity of

diffrcation peaks but does not affect the shape of the peaks. That's why finding positions of light atoms (H, C, and O) because of smaller scattering factor is harder. There are other factors which affect scattering factor such as static disorder, absorption, how tightly an atom is bound in the structure, wrong scaling of measurements, and incorrect atomic scattering functions.

The structure factor in the unit cell, which is the interference reflections of atoms, is calculated by the given equation:

$$F_{(hkl)_\alpha} = \sum_{j=1}^{atom} f_j \exp[2\pi i(hx + ky + lz)]$$

The value of this function is 1 for even multiples of 2π and is -1 for odd multiples of 2π. Based on scattering structure one can conclude some reflections are more intense or why reflections with hkl are missing (Table 1.5). Structure factors are independent of the shape and size of the unit cell.

Table 1.5. Extinction rules for different Bravais lattices in cubic.

Lattice Type	Condition for reflection to be present
P	All planes, reflections are possible
I	h + k + l = 2n (even)
A B C F	k + l = 2n h + l = 2n h + k = 2n h, k, l all odd or all even
R	-h + k + l = 3n

Intensity of a diffraction peak with reflection of hkl in phase α is calculated by the given equation:

$$I_{(hkl)\alpha} = \frac{I_0 \lambda^3}{64\pi r}\left(\frac{e^2}{m_e c^2}\right)^2 \frac{M_{(hkl)}}{V_a^2}\left|F_{(hkl)\alpha}\right|^2 \left(\frac{1+\cos^2(2\theta)\cos^2(2\theta_m)}{\sin^2\theta\cos\theta}\right)\frac{\nu_\alpha}{\mu_S}$$

Parameters are defined in Table 1.6.

Table 1.6. Elements for Intensity of diffraction peak

I_0 : incident beam intensity λ : X − Ray wavelength r: distance from specimen to detector $\left(\frac{e^2}{m_e c^2}\right)^2$: square ofclassical electron radius $M_{(hkl)}$: multiplicity of reflection hkl of phase α	V_a : volume of the unit cell of phase α $F_{(hkl)\alpha}$: structure factor for reflection hkl of phase α θ: Lorentz − polarization correction $2\theta_m$: diffraction angle of the monochromator ν_α : volume fraction of phase α μ_S: linear absorption coefficient of specimen

Neutron Powder Diffraction (NPD)

Another powerful diffraction tool to investigate the crystal structure of inorganic compounds is powder neutron diffraction. The applicable wavelength for NPD is 1.33-1.55 Å. For NPD instead of atomic scattering factor, bound coherent (Coh b) and incoherent (Inc b) scattering length and cross section will be used. Unlike XRPD, where scattering is directly proportional to atomic number, neutrons don't interact with the electron shell but with the nucleus of atoms, more specifically with its spin. The scattering length of elements is not affected by atomic number. This is very applicable in the case of different isotopes of the same elements like for ^{1}H (proton) Coh b= -3.742 fm (1fm=1*10^{-15} m) while for ^{2}H (deuterium) is 6.674 fm which shows NPD can be useful for accurate determination of hydrogen position, also detection of light atoms in the presence of heavy ones and distinguishes atoms adjacent in periodic table like Co (Coh b= 2.49) compare to Ni (Coh b= 14.4) which XRPD is not able to confirm it.[29]

Rietveld Refinement

The Rietveld method was developed by Hugo M. Rietveld[30] to extract information from PXRD and PND patterns and to solve unknown crystal structure, calculation of atomic position (Wyckoff positions), occupancies, thermal/disorder parameters, lattice parameters, symmetry, bond lengths and chemical compositions, determining the percentage of different phases in the sample, and determining the crystallite sizes in sample. There are always limits for refinement, such as structural complexity, which can be found by unit cell indexing and space group symmetry. Also there is a need for good data quality of XRD and NPD with resolved peaks. There are two famous sets of software which are the most applicable for refinements, General Structure Analysis System (GSAS) and Fullprof, but all of the refinements in this dissertation are extracted from GSAS refinement along with EXPGUI, which is a graphical user interface to GSAS. All of the parameters that should be refined are given in this equation:[31]

$$y_{ci} = \mathrm{s}\sum_{K} \mathrm{L}_K \left|F_{(k)}\right|^2 \phi(2\theta_i - 2\theta_k)\mathrm{P}_K \mathrm{A} + y_{bi}$$

All of the parameters are defined in Table 1.7.

Table 1.7. Parameters for Refinement

y_{ci} : calculated intensity S: scale factor L_k: contains the Lorentz, Polarization and Multiplicity factors $F_{(k)}$: *the structure factor for the Kth bragg reflection*	ϕ : the reflection profile function P_K : the preferred orientationfunction A: absorption factor y_{bi}: background intensity at the i th step

Elemental Analysis

(A) Energy Dispersive X-ray Spectroscopy (EDS-EDX-XEDS), Energy Dispersive X-ray Analysis (EXDA), Energy Dispersive X-ray Microanalysis (EDXMDA)

Energy dispersive X-ray spectroscopy (EDS) is an electron microscope based technique used for the elemental analysis of compounds. Figure 1.13 shows a scanning electron microscope

equipped with EDS. After inelastic interaction of electron beam with sample's electrons, secondary electrons (SE) will be created, which leaves thousands atoms of the sample with holes in the electron shells. These holes are in inner shells for atoms with unstable state therefore electrons from outer shells will drop into the inner shells to stabilize the atoms but because the outer shells are at a higher energy state, the atom must lose some energy in the form of X-rays. Two types of X-ray are produced: Characteristic and continuum (Bremsstrahlung) X-rays where the former reveal themselves as peaks imposed upon a background of the latter, a continuum X-rays. (Figure 1.14) The X-ray emitted from the sample atoms is characteristic in energy and wavelength not only for the element of the parent atom but also relates to which shells lost electrons and which shells replaced them.

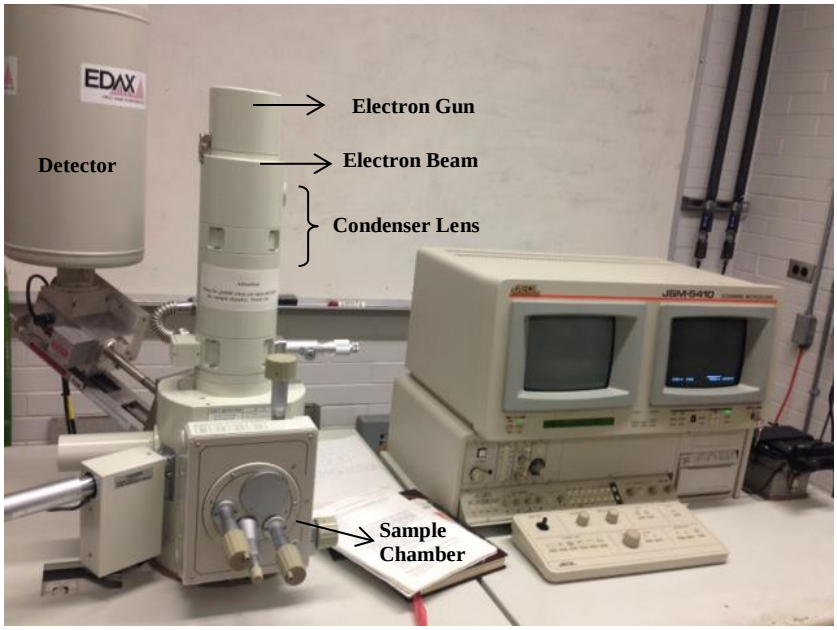

Figure 1.13. Scanning Electron Microscope (JEOL SEM JSM-5410LV)

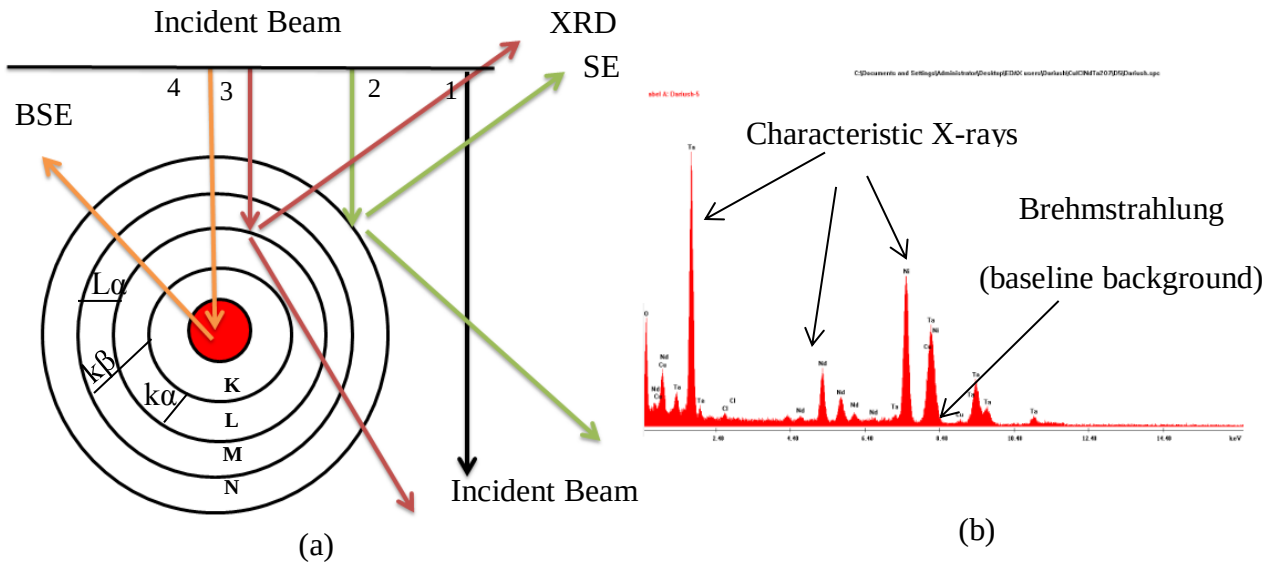

Figure 1.14. (a) Representation of interactions between electron beam and nucleus (Red sphere) .SE: Secondary Electron-BSE: Back Scatter Electron (b) EDS spectrum.

Elements with lower atomic number have fewer filled shells with fewer X-ray peaks and conversely, the elements with higher atomic number have more EDS peaks. Each element has its characteristic X-ray peaks to allow a sample's elemental composition to be identified by a nondestructive technique.[32]

(B) TEM (Transmission Electron Microscope)

In transmission electron microscope, a stream of electrons is formed (by the electron source) and accelerated toward the specimen using a positive electrical potential, this stream is confined and focused using apertures and magnetic lenses into a thin, focused, monochromatic beam then using a magnetic lens the beam is focused onto the sample and interact with the sample and affect the electron beam. These interactions and effects are detected and transformed into an image and result in the information such as morphology (size, shape and arrangement), composition (elemental analysis) and crystallographic information (defects). Transmission

electron microscopy is a valuable and versatile technique for the characterization of materials. It exploits the very small wavelengths of high-energy electrons to probe solids at the atomic scale. In addition, information about local structure (defects), structure (selected area electron diffraction SAED) to identify crystal system and lattice parameters and chemical composition (EDS) may be collected almost simultaneously. Figure 1.15 shows a TEM.

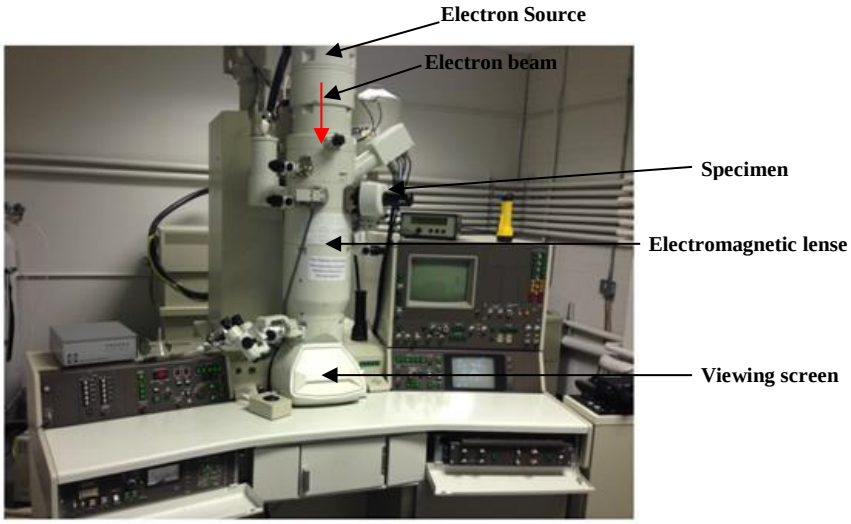

Figure 1.15. Transmission electron microscope.(JEOL JEM-2010 TEM)

Ferroelectric Measurements

Ferroelectric is a term used for non-conducting materials that may have a net electrostatic polarisation (P) induced by an external electric field (E). Materials are polarized along a unique crystallographic direction, in that certain atoms are displaced along this axis, leading to a dipole moment along it. Depending on the crystal system, there may be possibility for the compound to be paraelectric or ferroelectric. Perovskite $BiTiO_3$ is paraelectric above 130 °C where titanium atoms are octahedrally coordinated by oxygen atoms with centrosymmetric position for titanium (no net polarization) but at lower temperature barium moves to an off-center position, lowering

the cubic symmetry to tetragonal in a ferroelectric response. In a crystal, dipole moments of a unit cell lay along one region, a domain, which is a homogenous region of a ferroelectric where all of the dipole moments have the same orientation (Figure 1.16). In a single crystal, there will be many domains, with individual polarizations but with no overall polarization. If we apply a horizontal electric field of sufficient strength, the small ions will be able to overcome the barrier, dipoles will switch direction. If the field is not able to switch domain alignments, then the material will behave as a normal dielectric ($P \propto E$). As E is increased, domains flip and rapidly increase P. When all domains are switched, we reach saturation. The value of polarization at zero field is termed the remnant polarisation (P_r). The value of P extrapolated back from the saturation limit is the spontaneous polarisation (P_s). Reversal of the field will eventually remove all polarization and the field required is the coercive field (H_c). Further increasing the reverse field will completely reverse the polarization, and a hysteresis loop is formed (Figure 1.17).[33]

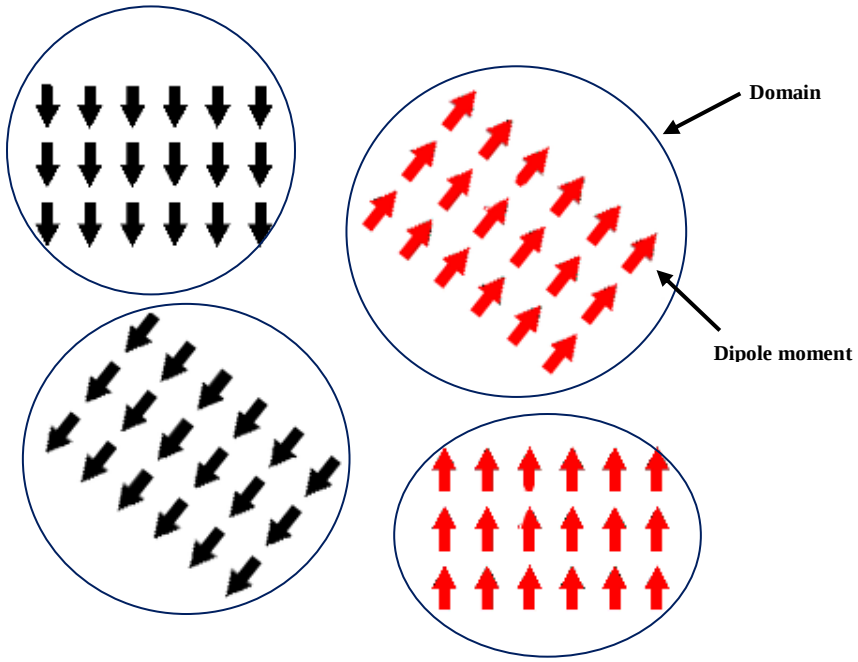

Figure 1.16. The orientation of dipole moments in individual domains.

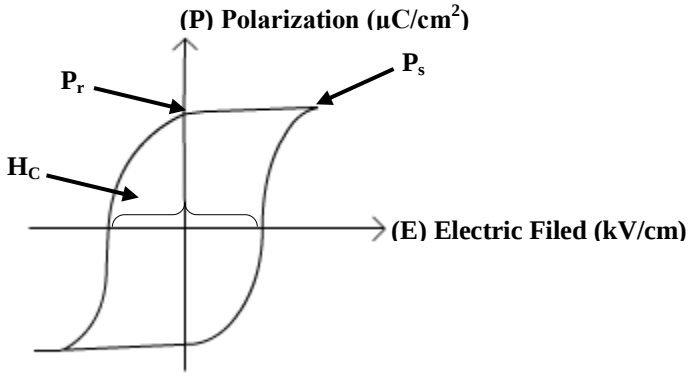

Figure 1.17. The hysteresis loop for ferroelectric material.

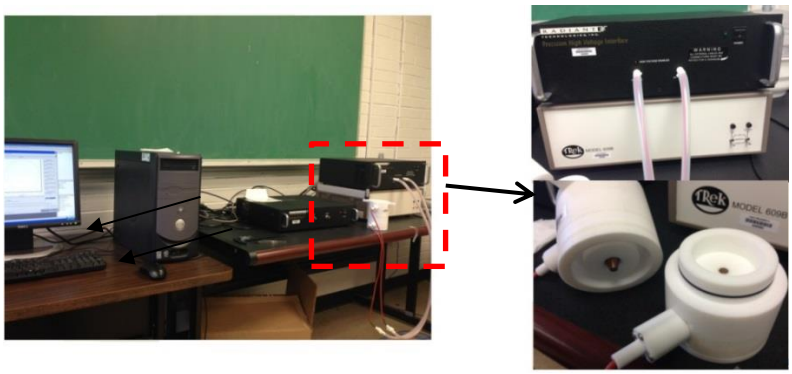

Figure 1.18. The ferroelectric tester has been used in this research.

Infrared, Raman, and UV-Vis Spectroscopy

The principle of spectroscopic techniques such as IR (Infrared), Raman, and UV-Vis (Ultraviolet–visible**)** is based on the interaction of electromagnetic radiation with the material, resulted in absorption or emission of energy in different ranges of frequency that is categorized in UV, visible and IR regions. Figure 1.19 shows a UV-Vis-NIR spectrometer. UV-vis spectroscopy studies the transitions and excitation of electrons in the energy levels of a molecule from the ground state to an excited state such as d-d, n-π, and π-π transitions, metal to ligand (MLCT) and ligand to metal (LMCT) charge transfer, and valence band to conduction band

transitions (band gap in semiconductor). In terms of vibrational spectroscopies, Raman relies on inelastic scattering of light by a material due to bond polarization, while IR spectroscopy is dependent on vibrational transitions.[34]

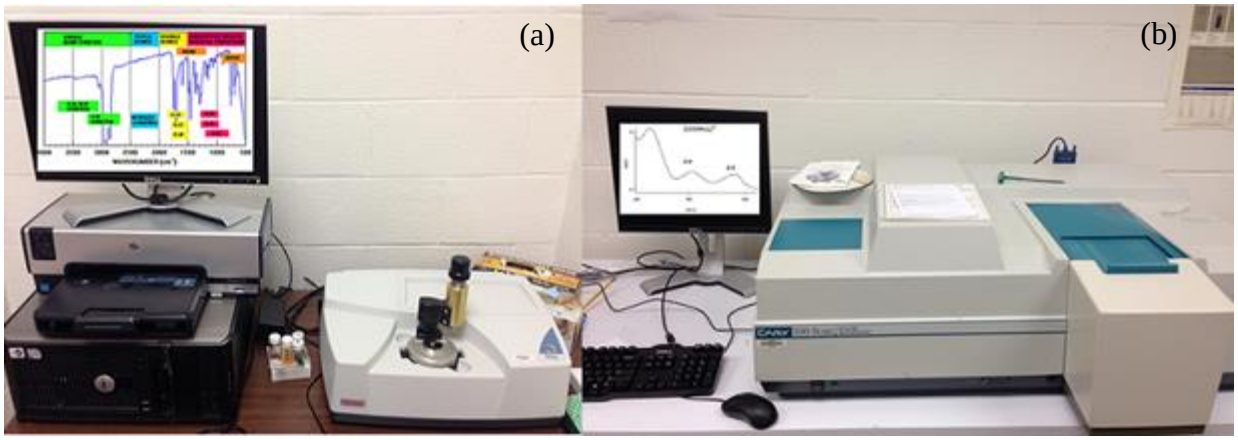

Figure 1.19. (a) IR spectroscopy and (b) UV-Vis-NIR.

TGA-DSC-DTA

Thermal analysis techniques, such as TGA (thermogravimetric analysis), DSC (differential scanning calorimetry) and DTA (differential thermal analysis), provide information about thermal stability, moisture content, volatile organic solvents and decomposition temperatures of a compound. TGA measures the weight loss or gain as a function of temperature with high accuracy (typically to at least 10 μg) to see the sample changes mass (waters of hydration, decompositions, or oxidation of powders). TGA is sometimes performed simultaneously with DTA/DSC. DSC measures the difference in heat flow between a sample and inert reference as a function of temperature and time. This helps to determine if an event is endothermic, such as melting, glass transition, evaporation, or exothermic, such as crystallization, oxidation, and specific heat capacity. DTA records the difference in temperature between a substance and a reference material as a function of time or temperature and like DSC we can obtain very

important quantities like melting point. Figure 1.20 shows TA instrument SDT-Q600 which provides simultaneous measurement of weight change (TGA) and true differential heat flow (DSC) on the same sample from ambient to 1500 °C.

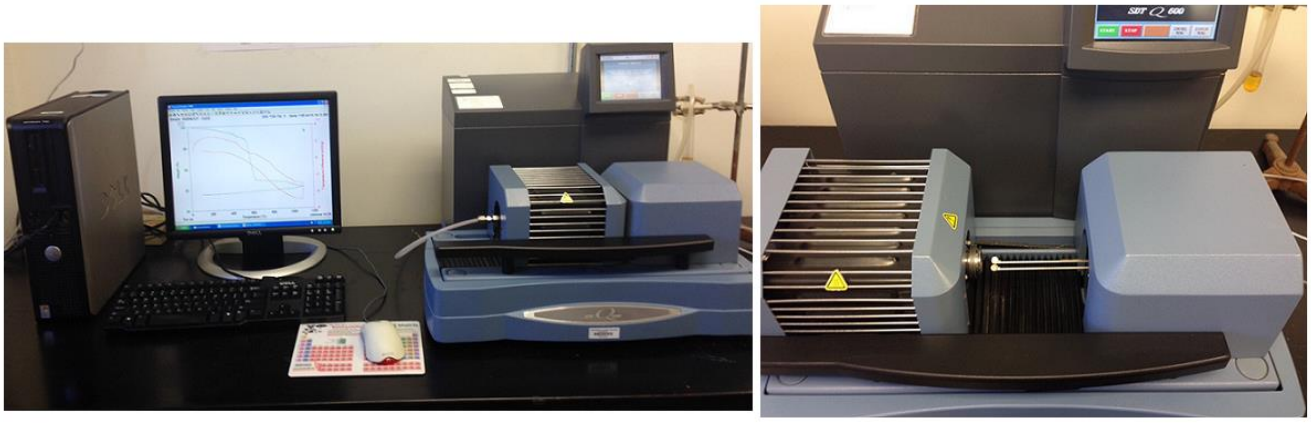

Figure 1.20. TA instrument SDT-Q600 thermogravimetric analyzer with differential scanning calorimeter (TGA-DSC)

Magnetic Measurements

Every material exhibits some kind of magnetic response which can be paramagnetic (PM), diamagnetic (DM), ferromagnetic (FM) and antiferromagnetic (AFM). Each of these has a different magnetization as a function of applied magnetic field M (H) and as a function temperature M(T). Magnetic measurement methods are reciprocating sample option (RSO), DC and AC. In RSO and DC measurements, the external dc magnetic field is applied to the sample and is dependent on types on interactions (only spin, only orbital and spin-orbit). The magnetization M (H) and magnetic susceptibility χ (T), with field cooling (FC) and zero field cooling (ZFC), are measured in the temperature range of 2-400 K and field range of ±7 Tesla. These measurements are usually carried out with a superconducting quantum interference device (SQUID) magnetometer (Quantum Design, MPMS-XL7 in Figure 1.21a).[35] The only difference

between RSO and DC is in RSO mode, a servomotor is used to oscillate the sample while in DC mode the sample is moved through the coil. In AC measurements, a small AC driven magnetic field, H_{AC} (0.005-15 Oe), is superimposed on the DC field (dM/dH), causing a time-dependent moment in the sample (sin (ωt)). The field of the time-dependent moment induces a current allowing measurement without sample motion. The induced AC moment is M_{AC} = (dM/dH) * H_{AC} sin (ωt) where H_{AC} is the amplitude of the driving field, ω is the driving frequency (10-10000 Hz) and χ=d M/ d H is the slope of the M(H) curve. The magnetic susceptibility in AC (χ) is composed of two components, real part or in phase susceptibility (χ′) and imaginary part or out of phase susceptibility (χ″) in form of χ= χ′+iχ″ where both χ′ and χ″ are extremely sensitive to (d M/ d H) but not to the absolute value therefore small magnetic shifts can be detected even when the absolute moment is large. At low frequency, AC measurements are similar to DC and the real component (χ′) is just the slope of the magnetization curve M (H) and imaginary part χ″ is missing in the DC method (M_{AC}=M_{DC}) but at higher frequencies the moment of the sample does not follow along the DC magnetization curve due to the dynamic effects on the sample and that's why the AC susceptibility is often known as the dynamic susceptibility. AC measurements are carried out with a Physical Property Measurement System (PPMS, Quantum Design, ACMS-II). This instrument is also able to measure heat capacity (C_p(T)) (Figure 1.21 b).[36]

Figure 1.21. (a) MPMS SQUID XL7 and (b) PPMS

Table 1.8. The summary of magnetic behaviors for diamagnetic (DM), paramagnetic (PM), ferromagnetic (FM) and antiferromagnetic (AFM) for RSO (DC) and AC magnetic measurements.

Measurement	DM	PM	FM	AFM
χ (T) χ^{-1} (T) M(H)	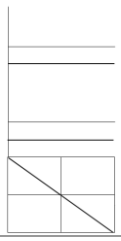	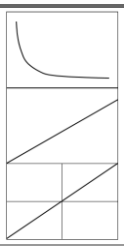	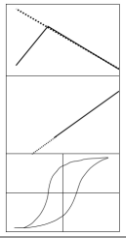	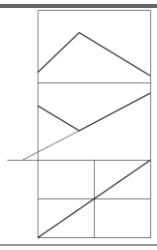
χ (T) (ZFC,FC) split Transition Temperature M(H) Hysteresis loop Magnetization saturation	no no no no	no no no no	yes yes $\theta_c > 0$ θ_c : Curie temperature yes yes	no yes : $\theta_N < 0$ θ_N : Neel temperature no no
χ'(T) Transition Frequency dependence χ'' (T) Transition Frequency dependence	no no no no	no no no no	yes yes yes non zero yes	yes no no : zero no
Field dependence	no	no	yes	no

1.5 References

[1] (a) Kim, H, S.; Hyuk Im, S.; Park, N. G. *J. Phys. Chem. C.* **2014**, *118*, 5615–5625. (b) Loi, M. A.; Hummelen, J. C. *Nat. Mater*. **2013**, *12*, 1087– 1089.

[2] Dimos, D.; Mueller C. H. *Annu. Rev. Mater. Sci*. **1998**, *28*, 397-419.

[3] Iwahara, H.; Uchida, H.; Ono, K.; Ogaki, K. *J. Electrochem. Soc*. **1988**, *135(2)*, 529-533.

[4] Spinicci, R.; Tofanari, A.; Delmastro, A.; Mazza, D.; Ronchetti S. *Mater. Chem. Phys*. **2002**, *76(1)*, 20-25.

[5] Ihringer, J.; Maichle, J.K.; Prandl, W.; Hewat, A.W.; Wroblewski, Th. *Z. Phys B Con Matter*. **1991**, *82(2)*, 171-176.

[6] Jonker, G. H. *Physica*. **1956**, *22(6-12)*, 707-722.

[7] Goldschmidt, V. M. *Die Naturwissenschaften*. **1926**, *21*, 477–484.

[8] Kumar, A.; Verma, A. S.; Bhardwaj, S. R. *TOAPJ*. **2008**, *1*, 11-19.

[9] Montasserasadi, D.; Granier, M.; Spinu, L.; Chandra Rai, S.; Zhou, W.; Wiley, J. B. *J. Chem. Soc. Dalton Trans*, (**2015**) Accepted.

[10] Domen, K.; Kondo, J. N.; Hara, M and Takata, T. *Bull. Chem. Soc. Jpn*. **2000**, *73(6),* 1307-1331.

[11] Sato, M.; Abo, J.; Jin, T.; Ohta, M. *J. Alloys Compd*. **1993**, *192(1-2),* 81-83.

[12] Fukuoka, H.; Isami, T.; Yamanaka, S. *Chem. Lett*. **1997**, *26 (8)*, 703-704.

[13] (a) Subbarao, E. C. *Phys. Rev*. **1961**, *122,* 804-807. (b) Van Uitert, L. G.; Egerton, L. *J. Appl. Phys*. **1961**, *32,* 959.

[14] Merkle, R.; Maier, J. *Z. Anorg. Allg. Chem*. **2005**, *631(6-7)*, 1163-1166.

[15] West, A. R. *Solid State Chemistry and its Applications*. *Preparative Methods,* Second edition; Eds.; John Wiley & Sons Ltd: United Kingdom, 1984.

[16] (a) Arney, D.; Maggard, P. A. *Acs. Catal*. **2012**, *2*, 1711-1717. (b) Porob, D. G.; Maggard, P. A. *Chem. Mater*. **2007**, *19*, 970-972. (c) Sikalidis, C. Advances in Ceramics - Synthesis and Characterization, Processing and Specific Applications. In *Molten Salt Synthesis of Ceramic Powders;* Kimura , T., Eds.; InTech: Rijeka, Croatia, 2011; pp 75-100.

[17] Kohlschutter, V. Z. *Anorg. Allg. Chem.* **1919**, *105(1)*, 1-25.

[18] Levage, Jacques. *New J. Chem*. **2001**, *25,* 1.

[19] Armstrong, A. R.; Anderson, P. A. *Inorg. Chem*. **1994**, *33(19),* 4366−4369.

[20] Viciu, L.; Caruntu, G.; Royant, N.; Koenig, J.; Zhou, W. L.; Kodenkandath, T. A.; Wiley, J. B. *Inorg. Chem*. **2002***, 41(13),* 3385−3388.

[21] Choi, J.; Zhang, X.; Wiley, J. B. *Inorg. Chem*. **2009**, *48(11)*, 4811-4816.

[22] Montasserasadi, D.; Mohanty, D.; Huq, A.; Heroux, L.; Andrew Payzant, E.; Wiley, J. B. *Inorg. Chem*. **2014**, *53(3),* 1773−1778.

[23] Gopalakrishnan, J.; Bhat, V. *Mater. Res. Bull*. **1987**, *22(3)*, 413-417.

[24] Viciu, L.; Kodenkandath, T. A.; Wiley, J. B. *J. Solid State Chem*. **2007**, 180(2), 583-588.

[25] Shannon, R. D. *Acta Crystallogr., Sect. A: Cryst. Phys., Diffr., Theor. Gen. Cryst*. **1976**, *32(5)*, 751-767.

[26] Ranmohotti, K. G. S.; Montasserasadi, D.; Choi, J.; Yao, Y.; Mohanty, D.; Josepha, E.; Adireddy, S.; Caruntu, G.; Wiley, J. B. *Mater. Res. Bull*. **2012**, *47(6),* 1289−1294.

[27] Laugier, J and Bochu, B. LMGP-Suite, ENSP/Laboratoire des Matériaux et du Génie Physique, BP 46. 38042, Saint Martin d'Hères, France, **2002**.

[28] Cromer, D. T and Waber, J. T. International Tables for X-ray Crystallography; Kynoch Press: Birmingham, UK, **1974**.Vol. 4, Table 2.2 A.

[29] Sears, V. F. *Neutron News*. **1992**, *3(3),* 26-37.

[30] (a) Rietveld, H. M. *Acta Cryst*. **1967**, *22(1)*, 151-152. (b) Rietveld, H. M. *J. Appl. Cryst*. **1969**, *2(2),* 65-71.

[31] Young, R. A. *The Rietveld Method*. Eds.; International Union of Crystallography (IUCr) Oxford Science Publications: Oxford, 1993, pp 4.

[32] http://www.seallabs.com/how-sem-works.html

[33] http://www.doitpoms.ac.uk/tlplib/ferroelectrics/polarisation.php

[34] (a) Cotton, Albert. *Chemical Applications of Group Theory*. Eds.; John Wiley & Sons Ltd: New York, 1990. (b) Drago, Russell. *Physical Methods for Chemists*; Eds.; Surfside Scientific Publishers: Gainesville, Fl, 1992.

[35] Quantum Design, MPMS MultiVu Application User's Manual, Chapter 3, Sample measurement, pp 28.

[36] (a) Martien, D. Introduction to: AC susceptibility, Quantum Design. Pages 1-4. (b) Quantum Design, MPMS AC Option User's Manual.

Chapter 2

Introduction

2.1 Novel Metastable Layered Perovskites $(A_2Ch\text{-}H)LaNb_2O_7$ (Ch: O)

Ion-exchangeable layered perovskites, which consist of perovskite slabs separated by interlayer cations, include the two major groups Dion−Jacobson (DJ) $A[A'_{n-1}B_nO_{3n+1}]$ and Ruddlesden−Popper (RP) $A_2[A'_{n-1}B_nO_{3n+1}]$,[1] where typically A: alkali metal, A′: rare earth or alkaline-earth, B: transition metal, and n: number of perovskite layers. Incorporation of ions with different sizes and charges in A, A′, and B sites can lead to a variety of compounds with unique behaviors. In, for example, the double-layered series $ALaNb_2O_7$ (A: alkali metal), Domen et al. has shown them to exhibit photocatalytic activity.[2] Sato et al. have also reported on ionic conductivity for $ALaNb_2O_7$ (A: Li, Na, K).[3] The triple-layered compound $KCa_2Nb_3O_{10}$ was found by Fukuoka and co-workers to exhibit superconductivity on doping with lithium.[4] A further feature of ion-exchangeable layered perovskites is their ability to readily undergo topochemical reactions under relatively low temperatures (<500 °C). This chemistry can be used for the preparation of low temperature and metastable phases,[1] producing compounds typically not accessible by standard high temperature ceramic techniques. Reaction methods are varied and include ion exchange, intercalation, de-intercalation, grafting, etc. One focus in this topochemistry has been the effort by some researchers to form metal-nonmetal layers within the perovskite hosts. This has resulted in the construction of both transition metal and alkali-metal halide arrays. The co-exchange of cation and anion species for example can be used to build transition metal halide layers (e.g. Cu−Cl in $(CuCl)LaNb_2O_7$).[5] A three-step method involving ion exchange followed by reductive intercalation and oxidative de-intercalation can also lead to

the formation of lithium chloride layers, $(Li_2Cl)LaNb_2O_7$.[6] Alkali-metal halide layers are accessible and are formed by a two-step intercalation method; the reductive intercalation of $ALaNb_2O_7$ with rubidium or cesium can lead to $A_2LaNb_2O_7$, then oxidative intercalation of chloride ions from reaction with chlorine gas produces the alkali-metal halide A−Cl array $(A_2Cl)LaNb_2O_7$ (A: Rb, Cs).[7] Beyond metal halides, more recent efforts have resulted in the incorporation of other main-group anionic species; alkali-metal chalcogen layers can be formed with a similar two-step intercalation method where gaseous H_2Ch (Ch: S or Se) is used in the oxidative intercalation step to produce interlayer arrays containing the corresponding chalcogen-hydride species.[8] As a logical expansion of these strategies, our group has sought to develop methods that allow for the incorporation of oxygen into the various metal−nonmetal frameworks. Such strategies could lead to new structurally interesting compounds with significant cooperative properties. Herein we report on an effective strategy for the incorporation of oxygen in the form of hydroxide ion. The approach utilizes a two-step reductive-oxidative method and results in the formation of new alkali-metal hydroxide arrays within double- and triple-layered niobate perovskites.

2.2 Experimental

Synthesis

$ALaNb_2O_7$ (A: Alkali metal) and $RbCa_2Nb_3O_{10}$

$ALaNb_2O_7$ (A: Li, Na, K, Rb, Cs) and $RbCa_2Nb_3O_{10}$. Dion−Jacobson layered perovskites $ALaNb_2O_7$ and $RbCa_2Nb_3O_{10}$were prepared by a simple solid state reaction.[2,9,10] La_2O_3 (Alfa Aesar, 99.99%) was preheated at 1000 °C for a day in order to remove any impurities as carbonates or hydroxides. Then, appropriate stoichiometric mixtures of La_2O_3, Nb_2O_5 (Alfa Aesar, 99.9985%), and $CaCO_3$ (Alfa Aesar, 99.99%) with a 25% excess of A_2CO_3 (A: K, Rb, Cs;

K_2CO_3 Alfa Aesar 99.997%, Rb_2CO_3 Alfa Aesar 99%, Cs_2CO_3 Alfa Aesar 99.994%) were ground together and heated at 850 °C for 12 h and 1050 °C for 24 h with one intermediate grinding. The excess amount of A_2CO_3 was added to compensate for the volatilization of alkali-metal oxide components. The product was washed with distilled water and then dried at 110 °C for one day. $LiLaNb_2O_7$ and $NaLaNb_2O_7$ were prepared via ion exchange reactions by reacting $ALaNb_2O_7$ (A: Rb or Cs) with molten salts of $LiNO_3$ (Alfa Aesar, 99.0% anhydrous) and $NaNO_3$ (Alfa Aesar, 99.999%) in a 1:10 molar ratio ($ALaNb_2O_7/ANO_3$) at 300 and 310 °C, respectively, for 4 days. All reactions produce white to off-white polycrystalline products.

$A_2LaNb_2O_7$ (A: Li, Na, K, Rb, Cs) and $Rb_2Ca_2Nb_3O_{10}$

$A_2LaNb_2O_7$ (A: Na, K, Rb, Cs) and $Rb_2Ca_2Nb_3O_{10}$ were all prepared by a reductive intercalation strategy similar to that reported by Armstrong and Anderson.[11] Pressed pellets of $ALaNb_2O_7$ and $RbCa_2Nb_3O_{10}$, formed by a simple hand press (7 mm dia.), were placed inside a 13 mm Pyrex tube. A 10% molar excess of alkali-metal was weighed and placed inside a smaller Pyrex vial (9 mm). The vial was placed in the Pyrex tube, and the tube assembly was sealed under vacuum ($<10^{-4}$ Torr). The sealed tube was then heated at 310 °C (Na), 290 °C (K), 250 °C (Rb), or 290 °C (Cs) for 4 days.[7] To be sure that the sample was completely exposed to the alkali-metal vapor, the tube was rotated periodically. The sample was then heated in a temperature gradient to remove excess of alkali metal for an additional 3 days by keeping one end of the tube outside of the furnace. The final products, $A_2LaNb_2O_7$ and $Rb_2Ca_2Nb_3O_{10}$, have a dark blue-black color. $Li_2LaNb_2O_7$ was prepared from $LiLaNb_2O_7$ by reaction with an excess of n-BuLi (Aldrich, 2.5 M in hexane) in 1:10 molar ratio.[7] The reaction was carried out under inert atmosphere (Ar) with stirring for 4 days at room temperature. The product was washed several times with dry hexane

to remove the excess lithium reagent. Note that $A_2LaNb_2O_7$ and $Rb_2Ca_2Nb_3O_{10}$ are air sensitive and were all stored and manipulated within an argon-filled dry box. All compounds readily de-intercalate in air to form the starting materials ($ALaNb_2O_7$ and $RbCa_2Nb_3O_{10}$). $A_2LaNb_2O_7$ and $Rb_2Ca_2Nb_3O_{10}$ react immediately on exposure to moisture, changing from a dark blue-black color to white, typically within seconds. Caution! Elemental alkali-metal reagents can explosively react with water and should therefore be handled and disposed with extreme care.

$(A_2OH)LaNb_2O_7$ (A: K, Rb, Cs) and $(Rb_2OH)Ca_2Nb_3O_{10}$

Double- and triple-layer rubidium-hydroxide perovskites were synthesized by oxidative intercalation with stoichiometric amounts of water vapor. Pressed pellets (ca. 0.5 g) of $A_2LaNb_2O_7$ and $Rb_2Ca_2Nb_3O_{10}$ were placed in a sealed evacuated tube with $CaC_2O_4{\cdot}H_2O$ (Sigma-Aldrich) at 200 °C for 2 days (Figure 2.1a); setup is similar to that used in reductive intercalation. Water was generated from the decomposition of $CaC_2O_4{\cdot}H_2O$. The water content of calcium oxalate was confirmed by thermogravimetric analysis prior to use (Figure 2.1b). Both the lithium and sodium compounds showed no obvious reaction under these conditions, while the cesium compound almost always decomposed to the parent, $CsLaNb_2O_7$. Final products, $(A_2OH)LaNb_2O_7$ (A: K, Rb) and $(Rb_2OH)Ca_2Nb_3O_{10}$, are white in color. Products decompose to the parent compounds on exposure to air and were therefore stored and manipulated within an argon-filled dry box. The compounds appear slightly less reactive then the reduced intermediates, decomposing over several minutes.

$(Rb_2OD)LaNb_2O_7$

Deuterated samples $(Rb_2OD)LaNb_2O_7$, were made by a method similar to that used for $(Rb_2OH)LaNb_2O_7$. Initially $CaC_2O_4{\cdot}H_2O$ was dehydrated by heating at 200 °C for 2 days. The

sample was then reacted with deuterium oxide vapor (Sigma-Aldrich 100%, 99.96 atom % D) for 2 days at 65 °C. The resulting $CaC_2O_4 \cdot D_2O$ was sealed in a Pyrex tube with a stoichiometric amount of $Rb_2LaNb_2O_7$ and heated for 2 days at 200 °C.

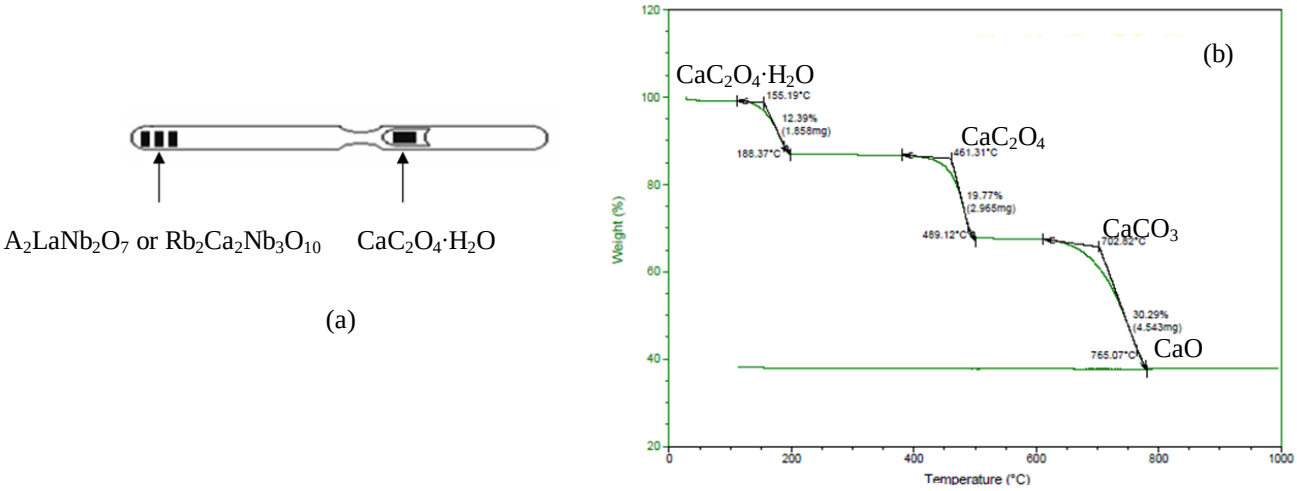

Figure 2.1. (a) Sealed Pyrex tube for carrying out oxidative intercalation of $A_2LaNb_2O_7$ and $Rb_2Ca_2Nb_3O_{10}$ with water where on heating, $CaC_2O_4 \cdot H_2O$ decomposes to release a stoichiometric amount of water. (b) TGA result for $CaC_2O_4 \cdot H_2O$ with three decomposition steps.

Characterization

X-ray powder diffraction (XRPD) data were collected on a Philips X'Pert system equipped with Cu Kα radiation (λ = 1.5418 Å) and a curved graphite monochromator (diffracted beam side). Typical scans were collected in continuous mode with a scan rate of 0.02°/s. All air-sensitive samples were prepared inside an argon filled glove box; samples were mounted on an acrylic sample holder with silicon grease and sealed under polypropylene film. The peak positions and lattice parameters were refined by a least-squares method with the ChekCell program.[12] Crystal structures were refined by the Rietveld method with the GSAS software package.[13, 14] In the case of the double layered perovskites, $(Rb_2Cl)LaNb_2O_7$ was used as a model[7] for refinement and for

triple layered compounds, the model was derived from $RbCa_2Nb_3O_{10}$.[10] Infrared spectral analysis was carried out on a Perkin-Elmer System 2000 FT-IR. KBr salt plates were used for all hygroscopic samples where Para-film and silicon grease were used to seal the air sensitive samples within pairs of plates.

Neutron diffraction data were collected on the POWGEN beam line at the Spallation Neutron Source (SNS) at Oak Ridge National Laboratory (ORNL).[15] Samples, sealed and transported in evacuated Pyrex tubes, were opened at ORNL in a glove box containing helium and sealed in 6 mm diameter vanadium cans. The cans were loaded in a 24 sample changer, and room-temperature neutron diffraction data was collected using a frame of neutrons with a center wavelength of 1.5996 Å.

Elemental analysis was initially examined by energy dispersive spectroscopy (EDS) on a JEOL JSM 5410 scanning electron microscope equipped with an EDAX-DX Prime micro-analytical system. Molar ratios were found to be approximately 2.5(2):1:1.83(9) Rb: La: Nb for $(Rb_2OH)LaNb_2O_7$ and 4.9(7):2.0(2):3.0(4) Rb:Ca:Nb for $(Rb_2OH)Ca_2Nb_3O_{10}$. The rubidium contents as determined by EDS for the series of compounds were unusually high; this is attributed to the air exposure and decomposition that occurs when samples are loaded in the SEM.[8] to complement EDS, a gravimetric approach was used for the water uptake by simply weighing samples before and after the oxidative intercalation step. In each case, 5 trials were used. For the compounds $(K_2OH)LaNb_2O_7$, $(Rb_2OH)LaNb_2O_7$, and $(Rb_2OH)Ca_2Nb_3O_{10}$ the average percent weight increase (theoretical shown parenthetically) was found to be 3.50 ± 0.47 (3.3), 2.98 ± 0.79 (2.8), and 3.10 ±0.58 (2.5), respectively. The relatively large statistical errors in this analysis are primarily attributed to the small sample sizes.

2.3 Results

Synthesis. Two-step topochemical reactions have been effectively used to make new alkali-metal hydroxide layered niobates. Initially alkali metal is intercalated into $ALaNb_2O_7$ to give the Ruddlesden−Popper related compound, $A_2LaNb_2O_7$ (eqn. 1).

$$ALaNb_2O_7 + A^0\,(g) \rightarrow A_2LaNb_2O_7 \text{ (eqn. 1)}$$

Water vapor, generated by the decomposition of calcium oxalate monohydrate at 200 °C (eqn. 2), is then used in the oxidative intercalation reaction of the $A_2LaNb_2O_7$ phase (eqn. 3) to form the hydroxide.

$$CaC_2O_4{\cdot}H_2O\,(s) \xrightarrow{\Delta} CaC_2O_4\,(s) + H_2O_{\,(g)} \qquad \text{(eqn. 2)}$$

$$A_2LaNb_2O_7 + H_2O_{\,(g)} \rightarrow (A_2OH)LaNb_2O_7 + \tfrac{1}{2}\,H_{2\,(g)} \qquad \text{(eqn. 3)}$$

This synthetic approach works well for reactions with the double- and triple-layered compounds, $A_2LaNb_2O_7$ (A: K, Rb) and $Rb_2Ca_2Nb_3O_{10}$. In the case of cesium, this reaction was successful only once (Appendix III Figure C.3)

Structure. X-ray powder diffraction data for $(Rb_2OH)LaNb_2O_7$ is shown in Figure 2.2 relative to that of $RbLaNb_2O_7$ and $Rb_2LaNb_2O_7$. A clear expansion in the layer spacing can be seen with the shift of the 001 reflection to lower angles.$(Rb_2OH)LaNb_2O_7$ can be indexed on a tetragonal cell showing an increase in the c-parameter of almost 3 Å relative to the parent compound (Table 2.1). Similar behavior is seen as well in both $(A_2OH)LaNb_2O_7$ (A: K, Cs) and $(Rb_2OH)Ca_2Nb_3O_{10}$ (Table 2.1, Figures 2.3, 2.4).

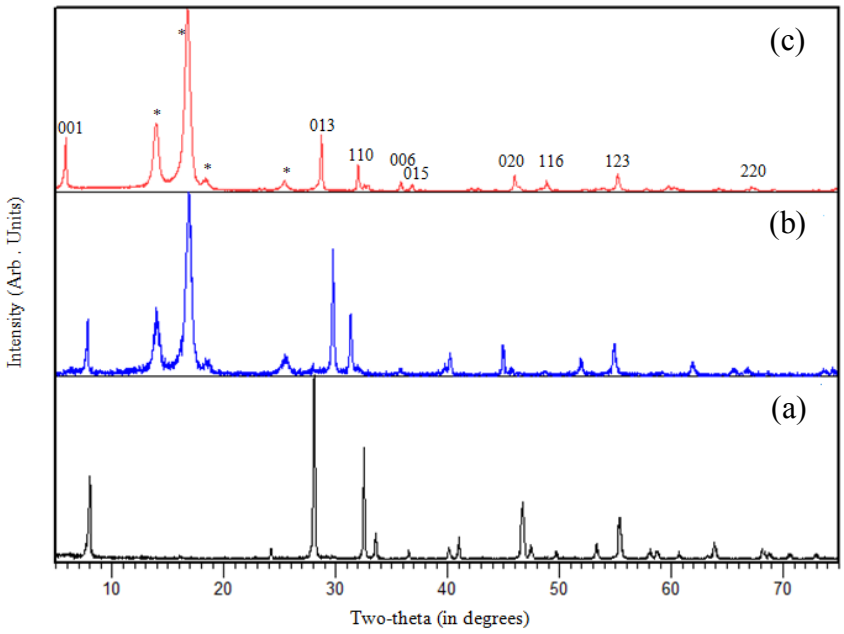

Figure 2.2. XRPD for (a) $RbLaNb_2O_7$, (b) $Rb_2LaNb_2O_7$, (c) $(Rb_2OH)LaNb_2O_7$. Asterisk (*) indicates polypropylene film peaks. Indices for major reflections of $(Rb_2OH)LaNb_2O_7$ are included.

Table 2.1. Unit-cell parameters for double and triple layered perovskite series including parents, intermediates and hydroxide products.

Compound	a (Å)	b (Å)	c (Å)	Cell Volume (Å^3)	Layer (L) Spacing (Å)	ΔL relative to parent (Å)	Ref
$KLaNb_2O_7$ [a]	3.9060(1)	21.6030(7)	3.8879(1)	328.06	10.80	---	3
$K_2LaNb_2O_7$ [a]	3.996(2)	21.49(1)	4.04(3)	346.899	10.74	-0.06	7
$(K_2OH)LaNb_2O_7$ [b]	3.9183(5)	---	14.314(4)	219.77(1)	14.31	3.51	this work
$RbLaNb_2O_7$ [a]	5.4941(1)	21.9901(1)	5.4925(4)	663.58	11.00	---	11
$Rb_2LaNb_2O_7$ [a]	22.3096(1)	5.6975(1)	5.6937(1)	723.70	11.15	0.15	11
$(Rb_2OH)LaNb_2O_7$ [b]	3.9303(1)	---	14.9624(9)	231.13(2)	14.96	3.96	this work
$(Rb_2OH)LaNb_2O_7$ [b,c]	3.9132(1)	---	14.757(1)	225.97(1)	14.76	3.76	this work
$(Rb_2OD)LaNb_2O_7$ [b,c]	3.9348(1)	---	14.7950(7)	229.07(2)	14.80	3.80	this work
$(Rb_2H)LaNb_2O_7$ [b]	3.897(2)	---	14.270(2)	216.7(2)	14.27	3.27	this work
$CsLaNb_2O_7$	3.9065(8)		11.170(2)	170.46	11.17		7
$Cs_2LaNb_2O_7$	23.334(5)	5.871(6)	5.619(5)	769.769	11.67	0.5	7
$RbCa_2Nb_3O_{10}$ [b]	3.8587(6)	---	14.9108(3)	222.01(1)	14.91	---	10
$Rb_2Ca_2Nb_3O_{10}$ [b]	3.904(1)	---	15.2535(1)	232.03(4)	15.25	0.34	this work
$(Rb_2OH)Ca_2Nb_3O_{10}$ [b]	3.8755(7)	---	18.856(5)	283.2(2)	18.86	3.95	this work

[a] orthorhombic cell; [b] tetragonal cell, [c] neutron data.

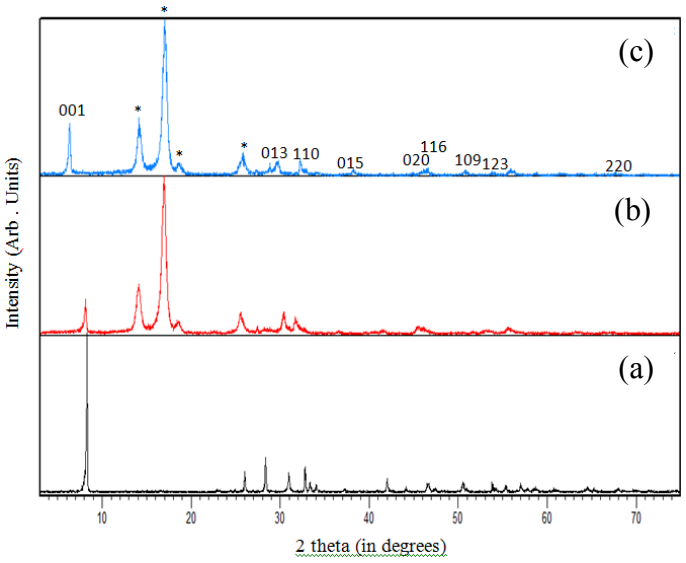

Figure 2.3. X-ray powder diffraction patterns of for (a) $KLaNb_2O_7$, (b) $K_2LaNb_2O_7$, and (c) $(K_2OH)LaNb_2O_7$. Asterisk (*) indicates polypropylene film peaks.

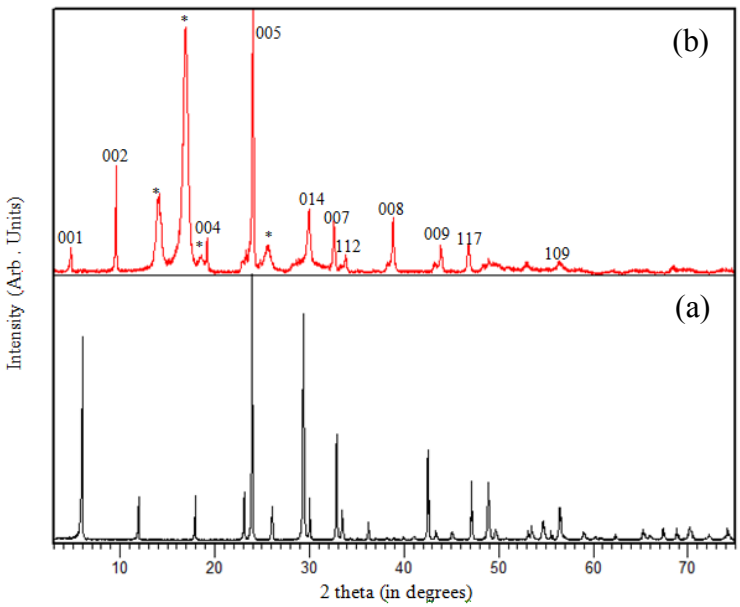

Figure 2.4. XRPD for (a) $RbCa_2Nb_3O_{10}$ and (b) $(Rb_2OH)Ca_2Nb_3O_{10}$. Asterisk (*) indicates polypropylene film peaks. Selected indices are highlighted for $(Rb_2OH)Ca_2Nb_3O_{10}$.

Rietveld Refinement on X-ray diffraction data started from a model similar to that used for $(Rb_2Cl)LaNb_2O_7$ with P4/mmm space group[7] (Figure 2.5, Table 2.2). Neutron diffraction studies on $(Rb_2OD)LaNb_2O_7$ then allowed the inclusion of deuterium atoms in the model immediately adjacent to the interlayer oxygen (O4). The thermal parameter for O4 was found to be slightly large so other models were explored where this atom was located on a more general position. Various sites including (x, x, 1/2), (x, y, 1/2), and (x, y, z) were investigated but all resulted in a significant increase in the tolerance factors relative to the 1d (1/2, 1/2, 1/2) site. In the case of deuterium, several sites were also investigated [(x, y, z), (1/2, 1/2, z), and (1/2, y, 1/2)]; the best fit was with deuterium disordered over the 4o site (x, 1/2, 1/2). The occupancy factors for La, Nb, and O1−O3 were all close to 1 and therefore fixed to 1 in the final refinements. Rb, O4, and D were found to be 1.057(2), 0.987(1), and 0.242(2), respectively. Observed, calculated, and difference plots for the refinement of $(Rb_2OD)LaNb_2O_7$ are shown in

Figure 2.6. Crystallographic data and selected bond distances are presented in Tables 2.3 and 2.4, respectively.

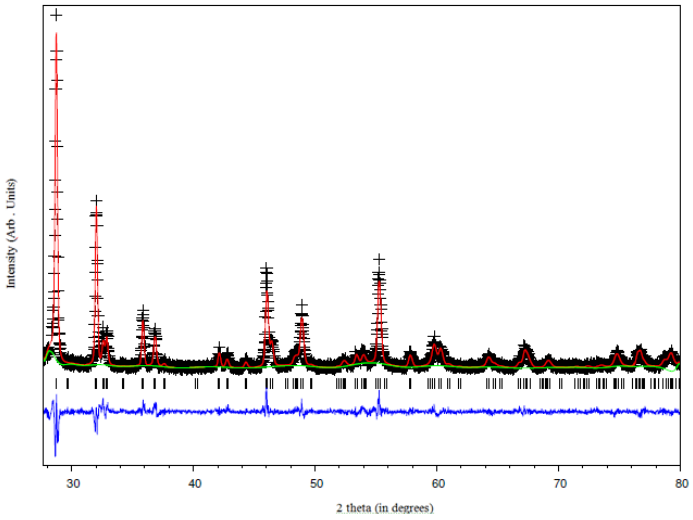

Figure 2.5. Observed and calculated data for the Rietveld refinement of $(Rb_2OH)LaNb_2O_7$ X-ray diffraction data. Observed data are indicated by crosses, calculated pattern by a red solid line, the bottom blue curve is the difference plot and the green is the background.

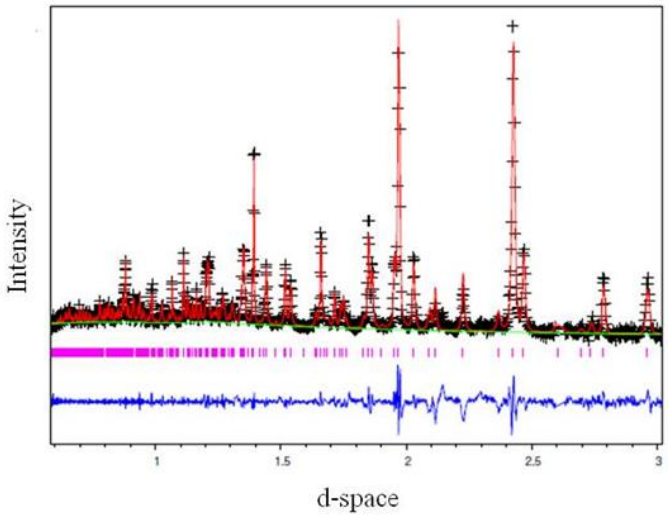

Figure 2.6. Rietveld refinement of $(Rb_2OD)LaNb_2O_7$ neutron diffraction data. Observed data are indicated by crosses, calculated pattern by a solid line (red), and the bottom curve (blue) is the difference plot. Reflection at ~2.2 Å is attributed to the vanadium sample holder. The green line is background.

Table 2.2.Crystallographic Data for $(Rb_2OH)LaNb_2O_7$ from X-ray data.

Atom	Site	x	y	z	$U_{iso}(Å^2)$	g
Rb	2g	0	0	0.3313(5)	0.02(1)	1
O_4	1d	0.5	0.5	0.5	0.02(2)	1
La	1a	0	0	0	0.0001(5)	1
Nb	2h	0.5	0.5	0.1465(4)	0.001(2)	1
O_1	2h	0.5	0.5	0.278(2)	0.001(2)	1
O_2	1c	0.5	0.5	0	0.003(5)	1
O_3	4i	0	0.5	0.129(2)	0.001(4)	1

*P*4/*mmm*; Z=1, a = 3.9303(1) Å, c =14.9624(9) Å, Volume = 231.13(2) $Å^3$ R_p= 15.0%, R_{wp}= 19.4%, χ^2= 1.68, and g = occupation factor

Table 2.3. Neutron Diffraction Data for $(Rb_2OD)LaNb_2O_7$.

Atom	Site	x	y	z	U_{iso} ($Å^2$)	g
Rb	2g	0	0	0.3521(7)	0.019(2)	1.057(2)
La	1a	0	0	0	0.006(1)	1
Nb	2h	0.5	0.5	0.1490(6)	0.006(1)	1
O1	2h	0.5	0.5	0.2674(7)	0.041(3)	1
O2	1c	0.5	0.5	0	0.032(4)	1
O3	4i	0	0.5	0.1286(4)	0.018(1)	1
O4	1d	0.5	0.5	0.5	0.046(1)	0.987(1)
D	4o	0.24(1)	0.5	0.5	0.019(3)	0.242(2)

*P*4/*mmm*, Z = 1, a = 3.9348(1) Å, c =14.7950(7) Å, Volume = 229.07(2) $Å^3$, R_p = 3.12%, R_{wp} = 2.83%, χ^2 = 4.298, and g = occupation factor

Table 2.4. Selected bond lengths for $(Rb_2OD)LaNb_2O_7$

Bond Type	Length (Å)
Rb-O_1 x4	2.9954(1)
Rb-O_3 x4	3.8006(2)
Rb-O_4 x4	3.5873(1)
Nb-O_1 x1	1.8212(1)
Nb-O_2 x1	2.2025(1)
Nb-O_3 x4	1.9934(1)
La-O_2 x4	2.7812(1)
La-O_3 x8	2.7222(1)
D-O_4 x4	0.9837(1)

Vibrational Spectroscopy. Infrared spectroscopy verified the presence of OH^- and OD^- in the $(Rb_2OH)LaNb_2O_7$ and $(Rb_2OD)LaNb_2O_7$ compounds, respectively (Figure 2.7). The O−H stretch was observed at 3600 cm^{-1}. This is consistent with the literature where O−H stretches are in the range 3500−3600 cm^{-1}.[16] As expected, the O−D stretch, due to the greater mass of deuterium, was shifted to lower energies (2605 cm^{-1}). The ~1000 cm^{-1} shift in frequency is consistent with values seen for various alkali-metal hydroxides.[16] Though the deuterium sample was sealed in salt plates during analysis, after 24 h the spectrum shows evidence for water uptake with the appearance of the OH − stretch (Figure 2.7d).

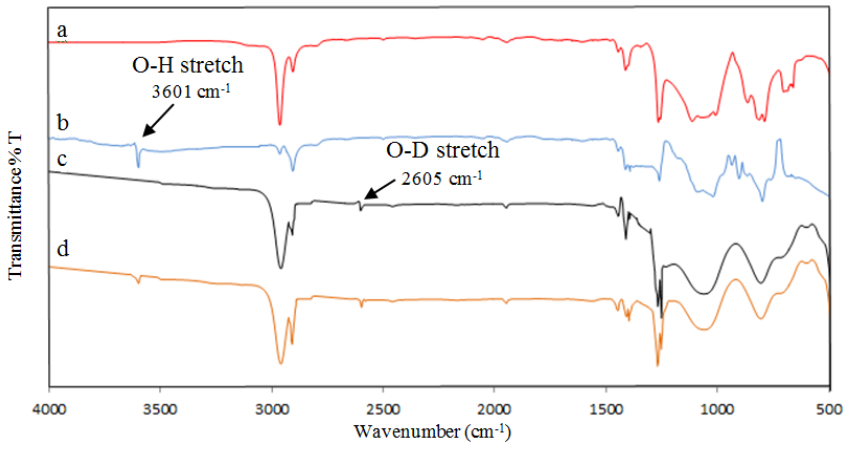

Figure 2.7. Infrared spectra of (a) $RbLaNb_2O_7$, (b) $(Rb_2OH)LaNb_2O_7$,(c) $(Rb_2OD)LaNb_2O_7$, and (d) $(Rb_2OD)LaNb_2O_7$ after 24 h in sealed salt plates.

2.4 Discussion

A two-step topochemical reaction strategy has been used to insert hydroxide ions into Dion−Jacobson-type layered perovskite hosts. Starting with a reductive intercalation procedure similar to that reported by Armstrong and Anderson[11] we were able to prepare the $Rb_2LaNb_2O_7$ intermediate. Treatment with stoichiometric amounts of water then led to $(Rb_2OX)LaNb_2O_7$ (X: H, D). IR data showed clear evidence for both hydroxide and deuteroxide species in the products, respectively, and weight uptake and structure refinement data support the approximate composition of 2:1 for Rb:OH. This approach was successfully applied to both double- and triple-layered perovskites and is effective with potassium and rubidium compounds, but not lithium, sodium, or cesium. Similar topochemistry has been demonstrated for the insertion of chalcogen hydride species[8] but unlike for the hydroxide which was successful only once, in the sulfur hydride system, the cesium analogue is accessible.[17] Though several factors could contribute to this difference in cesium reactivity, the less favorable size ratio in Cs:O (1.88/1.28) versus Cs:S (1.88/1.70) likely is a factor. (Size ratios are presented as relative crystallographic radii (Å) for coordination number (CN) = 8, except for sulfur CN = 6.)[18] The structure of $(Rb_2OH)LaNb_2O_7$ (Figure 2.8) is similar to that of $(Rb_2Cl)LaNb_2O_7$.[7] Rubidium ions sit in cubic sites surrounded by 4 oxygens from the perovskite slab and the 4 hydroxide ions. The hydroxide oxygens are also cubically coordinated with respect to the rubidiums. In terms of the orientation of the O−H groups in $(Rb_2OH)LaNb_2O_7$, the hydrogens are disordered over a 4-fold site (x, 1/2, 1/2) within the x−y plane (Figure 2.9). The position is such that the hydrogen maximizes its distance from the set of four electrostatically repulsive rubidiums. The O−H bond distances are ~0.98 Å, in good agreement with literature values reported for hydroxides.[19, 20] The hydrogens are oriented toward adjacent oxygens with distances to the next nearest (nn) oxygen being

relatively large (D−Onn = 2.94 Å). This CsCl-like structural arrangement in $(Rb_2OH)LaNb_2O_7$ is interesting considering that the alkali-metal hydroxide, RbOD, is known to exist with lower coordination environments for the oxygens; below room temperature RbOD has a thallium-iodide-related structure (coordination number, CN = 5+2) and near room temperature, a rock-salt-related structure (CN = 6).[19, 20] In $(Rb_2OH)LaNb_2O_7$, clearly the interlayer structure of this topochemically prepared compound is greatly influenced by the set of adjacent perovskite blocks. The interlayer environment leads to the stabilization of a higher coordination numbers (CN = 8) for both the alkali-metal and hydroxide ions. Also, in terms of hydrogen bonding, lower temperature RbOD (CN = 5 + 2) has a zigzag O−D···O motif (D−Onn = 2.40 Å) while at higher temperatures, where CN = 6, this interaction dissipates (D−Onn = 2.68 Å) allowing the OD groups to librate freely.[20] In comparison for $(Rb_2OH)LaNb_2O_7$, the D−Onn are 2.94 Å so that hydrogen bonding is not expected to be significant. Figure 2.10 highlights the intermediate orientation of the deuteriums/hydrogens relative to the surrounding set of rubidiums.

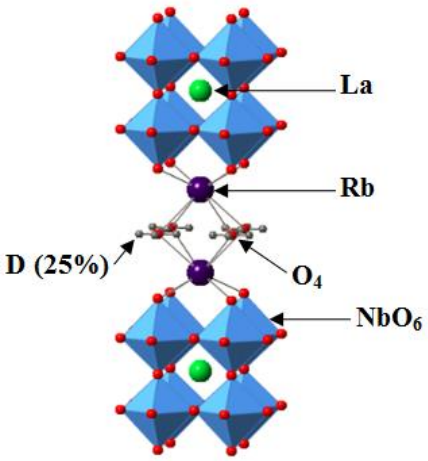

Figure 2.8. Crystal structure of $(Rb_2OD)LaNb_2O_7$ from neutron data. (Key: La: medium green spheres; oxygen: small red; NbO_6 octahedra: light blue; Rb: large dark purple; D: small gray.)

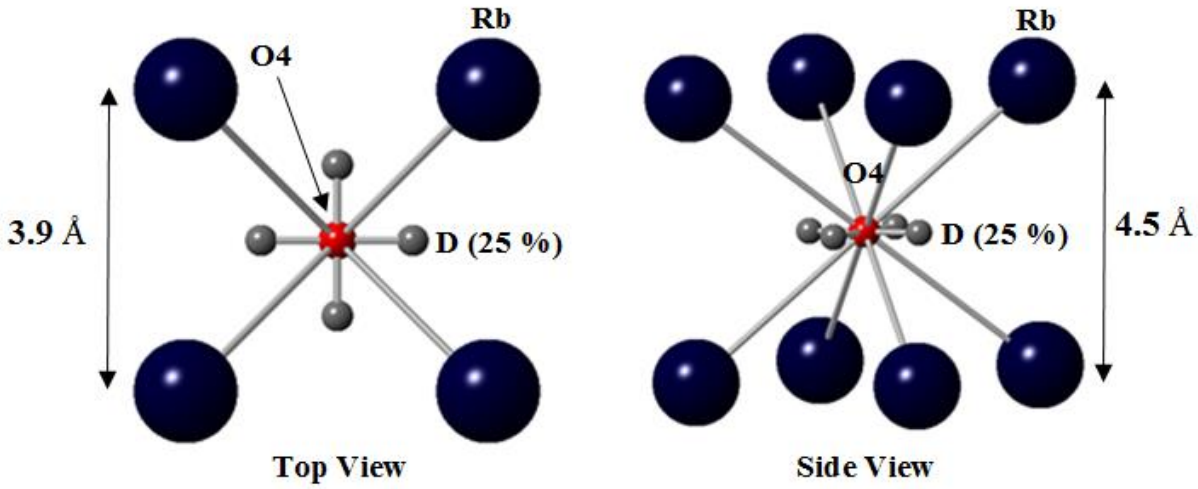

Figure 2.9. Local deuterium environment is shown. Top view (left) and side view (right) showing coordination of deuterium (grey), oxygen (red) and rubidium (dark blue).

The compounds $(K_2OH)LaNb_2O_7$ and $(Rb_2OH)LaNb_2O_7$ are isostructural (Figures 2.2 and 2.3). The slightly smaller layer expansion seen for the potassium compound (Table 2.1) is consistent with the smaller size of K (1.65 Å) relative to Rb (1.75 Å).[18] For the double-layered hydroxide $(Rb_2OH)LaNb_2O_7$ versus the triple-layered hydroxide $(Rb_2OH)Ca_2Nb_3O_{10}$, similar layer expansions are seen around 3.9 Å. It is noteworthy that the slight variation in layer expansion is seen in the X-ray data versus neutron: the X-ray c-parameter is about 0.2 Å larger than the neutron. We believe this to be an effect of a slight exposure of the X-ray sample to moisture during data collection; while the polymer film is effective in minimizing air exposure, it is not perfect, so the slight increase in c is associated with the additional uptake of water by $(Rb_2OH)LaNb_2O_7$. The handling of the neutron samples was such that they received no air exposure. Extended air exposure of samples of over 1−2 h leads to decomposition of product back to the parent compound. There are several other known layered perovskites that contain

hydroxide units. Pelloquin and co-workers have synthesized a series of transition metal double- and triple-layered perovskites that can reversibly take up hydroxide and water.[21] The compounds $Sr_3NdFe_3O_{7.5}(OH)_2$ and $Sr_3NdFe_3O_{7.5}(OH)_2 \cdot H_2O$, for example, have been prepared by treating the anhydrous parent $Sr_3NdFe_3O_{8.5}$ with water at different temperatures. While the hydroxide units are located within the interlayer of the perovskite, the exact positions of the hydrogens were not determined. Other hydroxide-like units are seen in various perovskite solid acids. These compounds, often made by simple proton exchange of alkali metal cations within layered perovskites, also have hydroxide units. Examples here include $HLaNb_2O_7$, $HCa_2Nb_3O_{10}$, $H_2La_2Ti_3O_{10}$, and $HLaTiO_4$. In one detailed structure determination on deuterated samples of $HLaTiO_4$, Nishimoto and co-workers found the hydrogens were attached to apical oxygens within the interlayer and disordered over an 8-fold site.[22] The O−D bonds average about 0.971 Å and are oriented toward adjacent apical oxygens with D−Onn bond distances of about 2.054 Å. Similarly, Yip and Cussen studied the solid solution of $H_{1-x}LixTiO_4$ and observed comparable behavior.[23]

The two-step approach for the formation of alkali-metal hydroxide layers further expands the library of topochemical reactions available for the construction of metal−nonmetal layers within receptive layered perovskite hosts. Figure 2.10 highlights some of the compounds accessible so far through topochemical manipulation of $RbLaNb_2O_7$. Various combinations of ion exchange and/or intercalation can allow for the formation of either transition-metal or alkali-metal halides. Methods for inserting hydroxide anions represent the first among this series for inserting oxide species. This is significant in that many oxides of perovskites can show technologically important cooperative phenomena.[24] Should one be able to further expand this

approach to direct the co-insertion of transition metals and oxides species, these topochemical strategies become especially pertinent.[25]

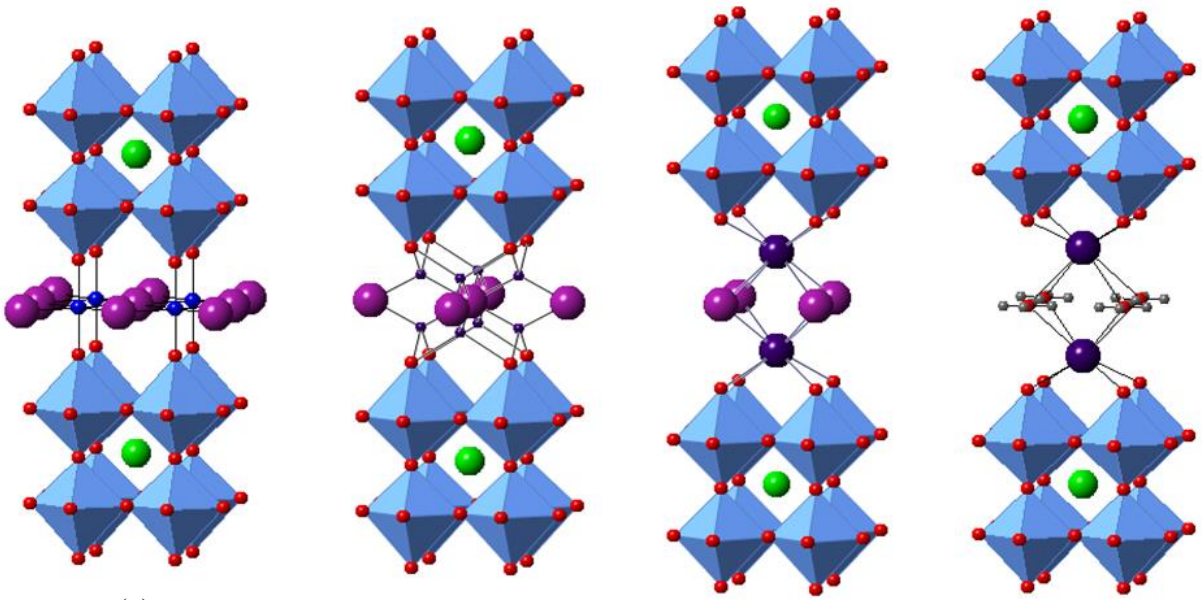

Figure 2.10. Various structures accessible Topochemically within layered perovskite hosts. (a) $(MCl)LaNb_2O_7$ (M: transition metal), (b) $(Li_2Cl)LaNb_2O_7$, (c) $(Rb_2Cl)LaNb_2O_7$, and (d) $(Rb_2OH)LaNb_2O_7$. (Key: M: small blue spheres; Cl: large violet; La: medium green; oxygen: small red; NbO_6 octahedra: light blue; Li: small dark purple; Rb: large dark purple; H/D: gray.)

2.5 References

[1] Ranmohotti, K. G. S.; Josepha, E.; Choi, J.; Zhang, J.; Wiley, J. B. *Adv. Mater*. **2011**, *23(4)*, 442-460.

[2] Domen, K.; Kondo, J. N.; Hara, M.; Takata, T. *Bull. Chem. Soc. Jpn*. **2000**, *73(6)*, 1307−1331.

[3] Sato, M.; Abo, J.; Jin, T.; Ohta, M. *J. Alloys Compd*. **1993**, *192(1-2)*, 81-83.

[4] Fukuoka, H.; Isami, T.; Yamanaka, S. *Chem. Lett*. **1997**, *26(8)*, 703−704.

[5] Viciu, L.; Caruntu, G.; Royant, N.; Koenig, J.; Zhou, W. L.; Kodenkandath, T. A.; Wiley, J. B. *Inorg. Chem*. **2002**, *41(13)*, 3385−3388.

[6] Viciu, L.; Kodenkandath, T. A.; Wiley, J. B. *J. Solid State Chem*. **2007**, *180(2)*, 583−588.

[7] Choi, J.; Zhang, X.; Wiley, J. B. *Inorg. Chem*. **2009**, *48(11)*, 4811−4816.

[8] Ranmohotti, K. G. S.; Montasserasadi, D.; Choi, J.; Yao, Y.; Mohanty, D.; Josepha, E.; Adireddy, S.; Caruntu, G.; Wiley, J. B. *Mater. Res. Bull*. **2012**, *47(6)*, 1289−1294.

[9] Kumada, N.; Kinomura, N.; Sleight, A. W. *Acta Crystallogr., Sect. C: Cryst. Struct. Commun.* **1996**, *52(5)*, 1063−1065.

[10] Liang, Z. H.; Tang, K. B.; Chen, Q. W.; Zheng, H. G. *Acta Crystallogr., Sect. E: Struct. Rep. Online.* **2009**, *65(6)*, i44.

[11] Armstrong, A. R.; Anderson, P. A. *Inorg. Chem*. **1994**, *33(19)*, 4366−4369.

[12] Laugier, J and Bochu, B. LMGP-Suite, ENSP/Laboratoire des Matériaux et du Génie Physique, BP 46. 38042, Saint Martin d'Hères, France, 2002.

[13] Larson, A. C.; Von Dreele, R. B., General Structure Analysis System (GSAS) program. Rep. No. LA-UR-86748, Los Alamos National Laboratory, Los Alamos, CA, 1994.

[14] Toby, B. H. *J. Appl. Cryst*., **2001**, *34(2)*, 210−213.

[15] Huq, A.; Hodges, J. P.; Gourdon, O.; Heroux, L. *Z. Kristallogr. Proc*. **2011**, *1*, 127−135.

[16] Gennick, I.; Harmon, K. M. *Inorg. Chem*. **1975**, *14(9)*, 2214−2219.

[17] Montasserasadi, M. D.; Wiley, J. B. Work in progress.

[18] Shannon, R. D. *Acta Crystallogr., Sect. A: Cryst. Phys., Diffr., Theor. Gen. Cryst*. **1976**, *32(5)*, 751-767.

[19] Jacobs, H.; Kockelkorn, J.; Tacke, Th. *Z. Anorg. Allg. Chem*. **1985**, *531*, 119−124.

[20] Jacobs, H.; Mach, B.; Lutz, H.-D.; Henning, J. *Z. Anorg. Allg.Chem*. **1987**, *544*, 28−54.

[21] Pelloquin, D.; Hadermann, J.; Giot, M.; Caignaert, V.; Michel, C.; Hervieu, M.; Raveau, B. *Chem. Mater*. **2004**, *16 (9),* 1715−1724.

[22] Nishimoto, S.; Matsuda, M.; Harjo, S.; Hoshikawa, A.; Kamiyama, T.; Ishigaki, T.; Miyake, M. *J. Eur. Ceram. Soc*. **2006**, *26 (4−5),* 725−729.

[23] Yip, T. W. S.; Cussen, E. J. *Inorg. Chem*. **2013**, *52(12),* 6985−6993.

[24] Rao, C. N. R.; Raveau, B. *Transition Metal Oxides-Structure, Properties and Synthesis of Ceramic Oxides;* 2nd ed.; Eds.; Wiley-VCH: New York, 1998.

[25] Montasserasadi, D.; Mohanty, D,; Huq, A.; Heroux, L.; Payzant, E. A..; Wiley, J. B. J. *Inorg. Chem*. **2014**, *53(3),* 1773-1778.

Chapter 3

Novel Metastable Layered Perovskites $(A_2Ch\text{-}H)LaNb_2O_7$ (Ch: S, Se)

3.1 Introduction

Topochemical techniques, such as those based on intercalation and ion exchange, are effective tools in the directed synthesis of materials in a wide range of chemical systems. Several examples are known where such Topochemical reaction strategies have been applied to perovskite and perovskite-related compounds. Understanding the nature of these reaction strategies helps one to investigate rational syntheses targeting new compounds with potentially important magnetic and electronic properties.[1] The Dion-Jacobson (DJ), $A[A'_{n-1}B_nO_{3n+1}]$, and Ruddlesden-Popper (RP),$A_2[A'_{n-1}B_nO_{3n+1}]$, series of layered perovskites (A: alkali metal, A′: rare earth or alkaline-earth, B: transition metal, n: number of perovskite layers) have received special attention due to their ability to readily undergo Topochemical manipulation.[1,2] The DJ series are especially flexible with respect to topochemistry compounds like $ALaNb_2O_7$ show an ability to undergo both intercalation[3–6] and ion exchange.[7, 8] With respect to intercalation, on exposure of $RbLaNb_2O_7$ to rubidium vapor, Armstrong and Anderson have shown that the alkali metal can be inserted to make a RP-related phase[9] and for ion exchange, reactions involving both monovalent and multivalent cations have been reported.[10] Co-exchange of cation–anion pairs is also possible where transition metal–halide layers can be constructed within Dion-Jacobson hosts to make the $(MX)LaNb_2O_7$ series (e.g., MX: CuCl) by reaction with metal halides.[11–15] Further manipulation of DJ phases has included multistep reaction strategies. Combinations of ion-exchange and reductive intercalation, for example, have produced alkali–metal–halide layers within a Dion-Jacobson host, $(A_2Cl)LaNb_2O_7$ (A: Li, Na).[16, 17] More recently, a two-step reaction

involving sequential reductive and oxidative intercalation produced $(A_2Cl)LaNb_2O_7$(A: Rb, Cs).[18] In the study reported herein, we have investigated a similar two-step synthetic strategy for the intercalation of chalcogenides into layered perovskites. Following reductive intercalation with an alkali metal, room-temperature oxidative intercalation with gaseous H_2Ch (Ch: S, Se) can be used to insert chalcogenide species into receptive perovskite hosts.

3.2 Experimental

Synthesis

$RbLaNb_2O_7$ was prepared by conventional solid-state reaction between Rb_2CO_3 (Alfa Aesar, 99.8%), La_2O_3 (Alfa Aesar, 99.99%) and Nb_2O_5 (Alfa Aesar, 99.9985%), using a method similar to that described previously;[19] stoichiometric amounts of La_2O_3 and Nb_2O_5 along with a 25% molar excess for Rb_2CO_3 were heated at 850 °C for 12 h and then ground again, followed by heating at 1050 °C for an additional 24 h. The product was washed with distilled water and dried at 120 °C overnight. Note that prior to usage, La_2O_3 was heated for 4 h at 1000 °C in air to decompose any impurities in the form of hydroxides or carbonates. $Rb_2LaNb_2O_7$ was prepared by reacting $RbLaNb_2O_7$ with rubidium metal vapor by a method similar to that of Armstrong and Anderson.[9] $RbLaNb_2O_7$ powder was pressed into pellets (7 mm o.d.) with a hand press (Aldrich), placed in a Pyrex tube (13 mm o.d.) and dried with a heat gun under dynamic vacuum. The evacuated tube was then placed in an argon filled dry box where a 10% molar excess of rubidium metal (Alfa-Aesar, 99.75%), weighed out in a small Pyrex vial (6 mm dia.), was positioned at the opposite end of the Pyrex tube relative to the dry pellets. The sample was sealed under vacuum ($<10^{-4}$ torr) and heated in a tube furnace at 250 °C for 4 days; tubes were rotated periodically to allow for better exposure of unreacted $RbLaNb_2O_7$ during the intercalation process. Excess metal was removed by placing the tube in a temperature gradient (250 → 25 °C) for 7 days. The alkali-

metal and reductive intercalation products are air sensitive; therefore they were all handled in an argon-filled dry box. **Caution:** Rubidium metal can react violently with water and should be handled and disposed of with great care. The reaction between $Rb_2LaNb_2O_7$ and gaseous H_2S was carried out in a closed system. The closed system was needed to protect the extremely air sensitive $Rb_2LaNb_2O_7$ and to contain the toxic H_2S gas. Inside an argon-filled dry box, ca. 0.06 g of $Rb_2LaNb_2O_7$ and about 0.05 g of Na_2S was separately loaded into 20 mL scintillation vials fitted with TFE/silicone septa caps. The two vials were then linked with two syringe needles through the septa caps. The assembly was removed from the dry box and placed in a well ventilated fume hood. A few milliliters of 6 M hydrochloric acid were injected into the vial containing Na_2S; gaseous H_2S was immediately produced to react with $Rb_2LaNb_2O_7$ at room temperature. The vial containing $Rb_2LaNb_2O_7$ was periodically agitated to expose fresh sample to the H_2S gas. Over a 30-min period, the blue-black color of the $Rb_2LaNb_2O_7$ changed to light gray. Prior to separating the vials, the syringe needles were crimped shut and split in half with wire cutters. The vial containing the reaction product was immediately evacuated in the dry box antechamber where the vacuum pump exhaust was vented to a fume hood; this allowed removal of any unreacted H_2S gas. The other vial containing unreacted Na_2S(s) and acid was neutralized in a bleach solution inside the fume hood. Reaction between $Rb_2LaNb_2O_7$ and H_2Se gas was also carried out. This reaction was performed inside an argon-filled dry box where $Rb_2LaNb_2O_7$ and Na_2Se were separately loaded into 20 mL scintillation vials fitted with TFE/silicone septa caps. In a setup similar to that used with the sulfide, the two vials were linked with syringe needles through the septa caps and ~ 3 ml of 9 M sulfuric acid were injected into the vial containing Na_2Se. After an hour exposure to H_2Se gas, the blue-black solid turned dark gray. Following separation of the two vials, as described above, the vial containing the product was immediately

evacuated by connecting the vial via another syringe needle to a vacuum line for several hours to remove any unreacted H_2Se gas. The vial containing the Na_2Se/H_2SO_4 mixture was transferred to a fume hood and neutralized with bleach solution. The intercalation reaction involving sulfur was faster than that with selenium.

Caution: H_2S and H_2Se are highly toxic gases that should be handled with extreme caution. In order to minimize the exposure, it is recommended that one wear a full face respirator with the appropriate filters during every step of the experiment that involves the toxic gases or their precursors. Additionally, the final products are air sensitive, decomposing to give off H_2S and H_2Se gas. These products should also be handled with extreme caution.

Characterization

Elemental analysis on pressed pellets of the sulfide intercalation product was attempted via energy dispersive spectroscopy (EDS) on a JEOL (model JSM-5410) scanning electron microscope (SEM) equipped with an EDAX (DX-PRIME) micro analytical system. Compounds usually showed decomposition and in some instances, the smell of hydrogen sulfide could be detected. While the starting material, $RbLaNb_2O_7$, typically showed a Rb:La:Nb ratio of approximately 1:1:2, analyses on the sulfur compound with minimal air exposure showed approximate Rb:S:La:Nb ratios of 2.5(2):0.75(4):1:1.84(9). In this and other sets of analyses, the rubidium content was high – in some cases, twice that expected; this is attributed to an increase in surface rubidium due to de-intercalation of Rb–S species on decomposition in air. Any excess sulfur on the surface could be lost as H_2S. Due to the limitations of the EDS data for analysis of this material, a gravimetric approach was then utilized to monitor the sulfur uptake by simply weighing samples before and after intercalation. In 6 separate experiments, the average weight

uptake was found to be approximately 5%; a relatively large statistical error (5.15±0.97%) was attributed primarily to the small sample sizes utilized in this analysis. X-ray powder diffraction (XRPD) data were recorded on a Philips X'Pert system equipped with a curved graphite monochromator and Cu Kα radiation (λ = 1.5418 Å). The air sensitive samples (see above caution) were prepared in an argon-filled dry box; after applying a thin coat of silicon grease on a plastic sample holder, samples were placed on the holder and sealed under polypropylene film. Standard X-ray data were collected in a continuous scan mode while the data used in Rietveld refinement were acquired in step-scanning mode with a 0.02° step size and 10 s count time. The cell parameters were indexed with the ChekCell program.[20] Structural refinement of the sulfide was done by the Rietveld method using the GSAS [21] package and the EXPGUI interface.[22] High-resolution transmission electron microscopy (HRTEM) and selected area electron diffraction (SAED) were performed on a JEOL 2010 transmission electron microscope (TEM) operated at 200 kV. For TEM sample preparation, a small amount of powder was dispersed in acetone and sonicated for 15 min. A few drops from this solution were applied onto Cu TEM grids with Quantifoil amorphous carbon support films. For comparison, electron diffraction patterns were simulated from Rietveld refinement output data with the software, Desktop Microscopist.[23] Room temperature Raman spectra were collected between 40 and 3500 cm^{-1} on a Thermo Scientific DXR Raman microscope, using a 532 nm laser excitation line; prior to analysis, samples were sealed in thin glass capillaries under argon due to the sensitivity of the compound to air.

3.3 Results

A two-step Topochemical reaction procedure utilizing chalcogen hydrides has been developed. After reductive intercalation of the $RbLaNb_2O_7$ parent with rubidium metal, the $Rb_2LaNb_2O_7$ Intermediate was oxidatively intercalated with sulfur via gaseous H_2S – the product is designated Rb–S. While the reductive intercalation occurs above 200 °C, the oxidative intercalation reaction takes place at room temperature. Figure 3.1a shows the X-ray powder diffraction pattern for $Rb_2LaNb_2O_7$ versus the sulfur intercalated product. (Figure 3.1b) The pattern of the sulfur compound is very similar to that of the rubidium chloride compound, $(Rb_2Cl)LaNb_2O_7$.[18] Table 3.1 compares the unit cell parameters, volumes, and layer spacing for the parent, its intercalated products, and $(Rb_2Cl)LaNb_2O_7$. Figure 3.1c shows that the simulated powder pattern based on the $(Rb_2Cl)LaNb_2O_7$ model is in reasonable agreement with the observed data.

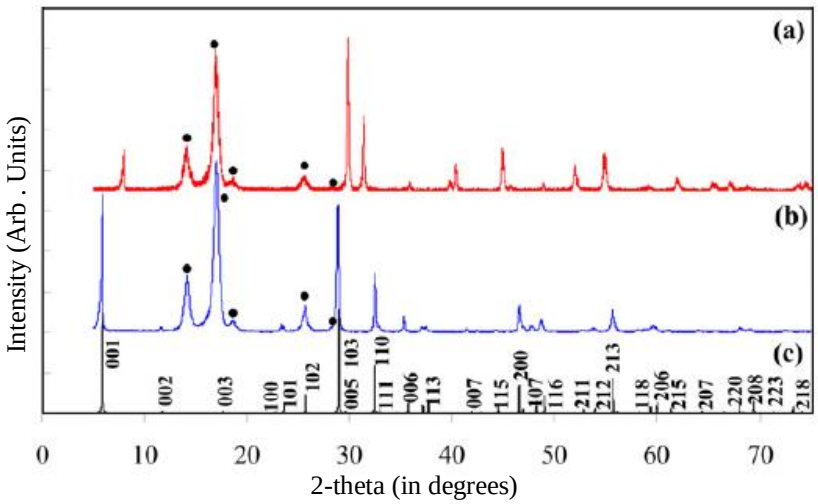

Figure 3.1. XRPD for (a) $Rb_2LaNb_2O_7$, (b) the sulfur intercalation product, and (c) the simulated pattern of the intercalation product. Miller indices are indicated for selected reflections. The peaks from the polypropylene cover film are marked (•).

Table 3.1. Crystallographic data for reactants and products.

Compound	Space group	Unit cell (Å)	Cell vol. (Å^3)	Layer spacing (Å)	Lit.cell (Å)[a]
$RbLaNb_2O_7$[b]	Imma	a=5.501(3) b=22.000(4) c=5.489(3)	664.39	11.00	a=5.4925(4) b=21.9901(6) c=5.489(3)
$Rb_2LaNb_2O_7$[b]	Cmcm	a=22.329(5) b=5.698(1) c=5.695(3)	724.59	11.16	a=22.30955(9) b=5.69748(10) c=5.69365(10)
$(Rb_2S)LaNb_2O_7$[c]	P4/mmm	a=3.8998(2) c=15.255(1)	232.02	15.26	This work
$(Rb_2Se)LaNb_2O_7$[b]	P4/mmm	a=3.904(9) c=15.46(3)	235.57	14.91	This work
$(Rb_2Cl)LaNb_2O_7$[d]	P4/mmm		225.32	15.46	a=3.887(1) c=14.913(1)

(a) Literature values from Ref [9]. (b) Lattice parameters refined with ChekCell. (c) Lattice parameters from Rietveld refinement. (d) From Ref [18].

Rietveld analysis was conducted on X-ray powder diffraction data of the sulfur compound with the space group P4/mmm (no. 123). The $(Rb_2Cl)LaNb_2O_7$ structural model [18] was used with sulfur sitting on the corresponding chlorine site. Throughout the refinement, the thermal parameter for niobium was unstable, so it was fixed at 0.005. Attempts to independently refine the occupation factor (g) of S were initially unsuccessful in that it was highly correlated to its own thermal parameter. Occupation factor refinements for Rb and S were then carried out with both the Nb and S thermal parameters fixed; this resulted in occupancies of 1.06(2) and 0.76(3) for Rb and S, respectively. The crystallographic data and the positional parameters for the final refinement are listed in Table 3.2.

Table 3.2. Crystallographic data for the sulfide intercalation product Rb–S.

Atom	Site	x	y	z	g	U_{iso} (Å^2)
Rb	2g	0	0	0.3488(3)	1.06(2)	0.041(2)
S	1d	0.5	0.5	0.5	0.76(3)	0.014
La	1a	0	0	0	1	0.002(1)
Nb	2h	0.5	0.5	0.1480(2)	1	0.005
O_1	2h	0.5	0.5	0.267(2)	1	0.03(1)
O_2	1c	0.5	0.5	0	1	0.03(1)
O_3	4i	0	0.5	0127(1)	1	0.016(5)

P4/mmm, Z = 1, a = 3.8998(2) A˚, c = 15.255(1) A˚, volume = 232.02(4) A˚^{3}. Rp = 12.63%, Rwp = 16.20% χ^2 = 2.07, g = occupation factor.

The observed, calculated and difference plots are shown in Figure 3.2 and the crystal structure based on the refinement illustrated in Figure 3.3. The structure is consistent with the topotactic nature of these reactions where the perovskite layers remain intact as a rubidium–sulfide network is constructed within the interlayer. In the network, sulfurs reside in cubic sites surrounded by 8 rubidium cations. Selected bond distances are given in Table 3.3. HRTEM images obtained on individual crystallites of the sulfide compound provide further information on the structure.

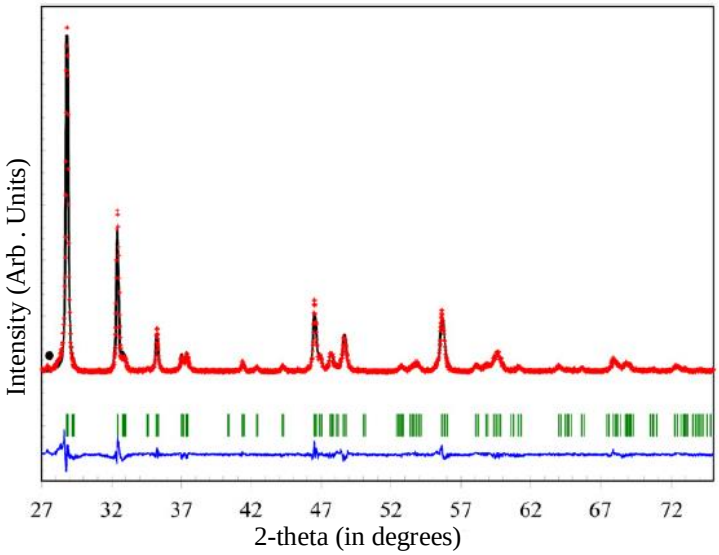

Figure 3.2. Results of rietveld refinement for the structure of the sulfide compound. The measured (crosses), calculated (solid line), and the difference (bottom) profiles are shown. Bragg positions are indicated by tic marks. A very small peak from the polypropylene cover film between 28° and 29° 2θ is marked (•).

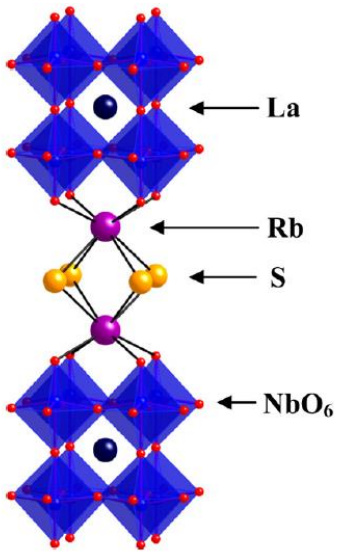

Figure 3.3. Structure of the sulfide product derived from the Rietveld refinement of X-ray powder diffraction data.

Table 3.3. Selected bond distances for Rb–S.

Bond Type	Length (Å)
Rb-S	3.594(3) × 4
Rb-O_1	3.02(1) × 4
La-O_2	2.7576(1) × 4
La-O_3	2.75(1) × 8
Nb-O_1	1.82(2) × 1
Nb-O_2	2.258(4) × 1
Nb-O_3	1.975(3) × 4

Figure 3.4a shows the HRTEM image of the edge of a sulfide crystallite. The regularity of the lattice planes in this image indicates good crystallinity. The spaces between adjacent planes are 0.75 and 0.26 nm, corresponding to (002) and (110) planes of the tetragonal cell, respectively (Figure 3.4b). Selected area electron diffraction data were also obtained on the sulfide product along the [001] zone axis. SAED data, together with the simulated pattern for the sulfide, are shown in Figure 3.4c and d. The simulated pattern was based on the model determined through Rietveld refinement. Good agreement between the observed and calculated patterns can be seen, further supporting tetragonal symmetry and the structure obtained from Rietveld refinement. Several factors suggest that the sulfide species in the interlayer is not simply S^{2-}. The weight uptake was monitored during the sulfide reaction and was found to be ~5.2% (5.15 ± 0.97). The theoretical weight change based on a S^{2-} content of 0.5 (i.e., $(Rb_2S_{0.5})LaNb_2O_7$ is 2.6%, approximately half of what was observed.

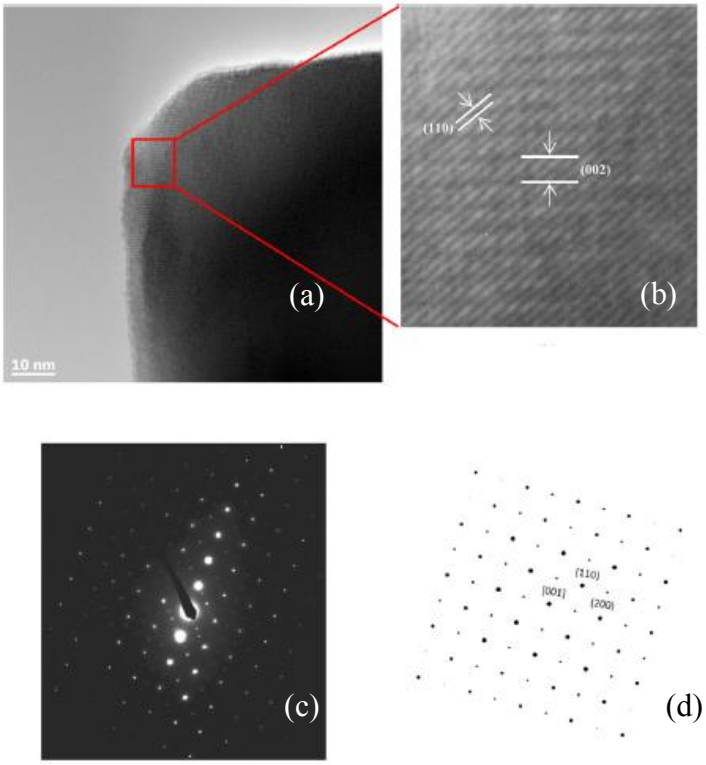

Figure 3.4. TEM images of the sulfide intercalation product. (a) HRTEM image of Rb–S. (b) Blowup image shows lattice fringes corresponding to (110) and (002) planes. (c) Observed and (d) calculated SAED patterns for the sulfide.

The sulfur composition obtained in the Rietveld refinement, ca.~ 0.8 (Table 3.2), is also greater than 0.5. The high sulfur content indicated by these observations could be explained by the presence of HS^- or polyatomic sulfur species. Raman spectroscopy (Figure 3.5) was carried out on both the $RbLaNb_2O_7$ and the sulfide product. The S–H stretch is known to occur in the range 2500–2600 cm^{-1} [24] and that for S–S 490–510 cm^{-1}.[25] The Raman spectrum for Rb–S show a broad band, consistent with the presence of HS^-, centered around 2500 cm^{-1}. The S-S region, while containing bands from the perovskite, shows no clear evidence of polyatomic sulfur in the product (Figure 3.5b). After successful intercalation of sulfur using H_2S, reactions with H_2Se were also investigated. Figure 3.6a shows the powder XRD pattern of the product (Rb–Se) and

Table 3.1 summarizes refined unit cell parameters. A model similar to that of the sulfide was used to simulate the powder pattern for the selenium intercalated product (Figure 3.6b). Although the crystallinity of this phase is not as good as that of the Rb–S, there is reasonable agreement between the simulation based on the $(Rb_2Cl)LaNb_2O_7$ model, indicating that Rb–Se also likely adopts a similar structure. It is important to note that, unlike with the sulfide product; varying amounts of $RbLaNb_2O_7$ could be seen in the final products. This byproduct likely forms from rubidium de-intercalation of $Rb_2LaNb_2O_7$ on exposure to H_2Se (g); similar behavior was seen in the synthesis of $(Rb_2Cl)LaNb_2O_7$ [18] when reacting $Rb_2LaNb_2O_7$ with Cl_2(g).

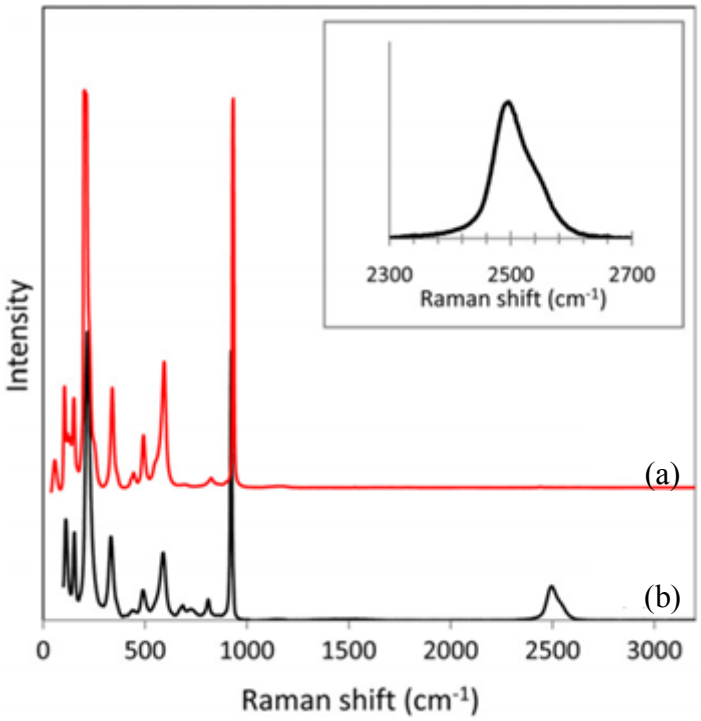

Figure 3.5. Raman spectra in the region 40–3500 cm^{-1} of (a) $RbLaNb_2O_7$ and (b) Rb–S. The S–H stretching band occurs in the range, 2500–2600 cm^{-1}; inset shows an enlargement of this region.

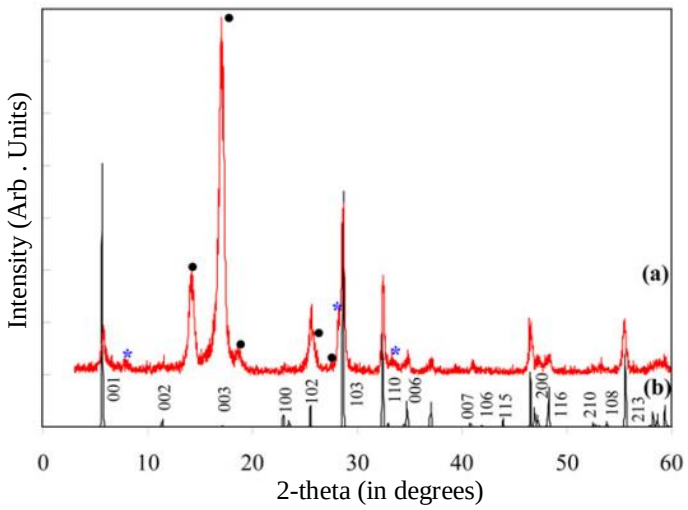

Figure 3.6. X-ray powder diffraction patterns for (a) the selenium intercalation product and (b) the simulated pattern of the intercalation product. The peaks from the polypropylene cover film are marked (•). The $RbLaNb_2O_7$ impurity phase is indicated by asterisks (*).

3.4 Discussion

A two-step reaction strategy has been used to build alkali-metal sulfide layers in a perovskite host. Initially, by the method of Armstrong and Anderson,[9] reductive intercalation into $RbLaNb_2O_7$ with Rb metal was used to make $Rb_2LaNb_2O_7$, then sulfur was oxidatively intercalated by reaction with H_2S gas at room temperature. Weight uptake, refined site occupancy (g(S) ~0.8), along with Raman scattering data, indicate that the sulfur exists primarily as HS^- in the interlayer. Based on the composition obtained from weight uptake, and assuming complete oxidation of $Rb_2LaNb_2O_7$, a formula for the Rb–S product can be approximated as $(Rb_2S_{(1-x)/2}(SH)_x)LaNb_2O_7$ where x = 1.0(2). This formulation accounts for the possibility that some of the interlayer sulfur exists as S^{2-}. Should there not be any sulfide ion present, then the likely composition is close to $(Rb_2Y)LaNb_2O_7$, where $Y = HS^-$. Figure 3.3 shows the structure of Rb–S. Like in $(Rb_2Cl)LaNb_2O_7$, the local of the interlayer cations, rubidium and sulfur, is

formally 8. Selected bond distances are given in Table 3.3 The rubidium–sulfur bond distance, 3.594(3) Å, obtained from the refinement is greater than 3.45 Å , the sum of the Shannon crystal radii [26] for an eight coordinate Rb^{+} (1.75 Å) and six-coordinate S^{2-} (1.70 Å), but does fall in the upper range for some known sulfides; Rb–S bond distances are typically between 3.3 and 3.6 Å. [27–30] Like the sulfide compound, the selenide (Rb–Se) can be prepared by reaction of chalcogen hydride gas with $Rb_2LaNb_2O_7$. Though there was a loss of crystallinity and some evidence for de-intercalation of rubidium, as indicated by the $RbLaNb_2O_7$ in the final product, this reaction is still quite effective. The topochemical reaction strategies presented here will allow the preparation of a series of new perovskite-related oxychalogenides. Many such oxychalcogenides are already known including those that exhibit interesting magnetic and electronic properties.[31–42] The series $Sr_2MnO_2Cu_{2m-\delta}S_{m+1}$ (m: 1, 2, and 3), for example, contains copper-sulfide layers of varying thicknesses (m) and is found to exhibit metamagnetic behavior.[32] Some iron oxychalcogenides exhibit unusual magnetic lattices due to distorted octahedral coordination for Fe^{2+} ion in FeO_2Ch_4. $A_2F_2Fe_2OCh_2$ (A: Sr, Ba; Ch: S, Se) compounds, for instance, display a frustrated antiferromagnetic checkerboard lattice.[42]

Other alkali-metal containing oxysulfides have been prepared topochemically; $Y_2Ti_2O_5S_2$ for example has been reductively intercalated with Li, Na and K.[34–37] The interlayer coordination geometry for K in $KY_2Ti_2O_5S_2$ is similar to that seen for Rb in Rb–S (Figure 3.3) and the titanium mixed valency results in metallic-like behavior.[37] One important aspect in the design of successful Topochemical reactions is the selection of intercalation sources. The intercalation of sulfur into $Rb_2LaNb_2O_7$ by reaction with S_8 is relatively difficult, requiring elevated temperatures.[43] This could arise from the fact that sulfur exists as a polyatomic, so that generating monoatomic chalcogenide anions may not readily occur. The use of H_2S is effective

in that this agent delivers a single sulfur that can be used directly from gas sources or generated via metathesis reactions. The precursors, Na_2S and Na_2Se, were chosen as chalcogen sources since they are commercially available and can react easily to produce H_2S and H_2Se, under mild conditions. It is also noteworthy that the intercalation reaction with H_2S was faster than with H_2Se, while this could depend on many factors, the relative size of the intercalating anions (radii, CN = 6: 1.70 Å for S^{2-} and 1.84 Å for Se^{2-}) [26] is likely important.

In summary, we report a simple two-step method to intercalate chalcogenides into the double layered perovskite, $RbLaNb_2O_7$, through reaction with gaseous H_2Ch (Ch: S, Se). To the best of our knowledge chalcogenides have not been intercalated into any perovskite host previously. Given the success of this multistep approach at room temperature, one can expect that similar strategies could prove useful for intercalation reactions with many other main group hydrides, such as those volatile hydrides of tellurium or members of groups 13, 14, or 15.[44]

3.5 References

[1] Ranmohotti, K. G. S.; Josepha, E.; Choi, J.; Zhang, J.; Wiley, J. B. *Adv. Mater*. **2011**, *23(4)*, 442−460.

[2] Schaak, R. E.; Mallouk, T. E. *Chem. Mater*. **2002**, *14(4)*, 1455-1471.

[3] Gómez-Romero, P.; Palacín, M. R.; Casañ, N.; Fuertes, A. *Solid State Ionics*. **1993**, *63-65*, 424–428.

[4] Palacín, M. R.; Lira, M.; García, J. L.; Caldés, M. T.; Casañ-Pastor, N.; Fuertes, A.; Gómez-Romero, P. *Mater. Res. Bull*. **1996**, *31(2)*, 217-225.

[5] Sato, M.; Jin, T.; Ueda, H. *Chem. Lett*. **1994**, *23 (1)*, 161-164.

[6] Bohnke, C,; Bohnke, O.; Fourquet, J. L. *J. Electrochem. Soc*. **1997**, *144(4)*, 1151-1158.

[7] Sato, M.; Abo, J.; Jin, T.; Ohta, M. *J. Alloys Compd*. **1993**, *192(1-2)*, 81-83.

[8] Viciu, L.; Liziard, N.; Golub, V.; Kodenkandath, T. A.; Wiley, J. B. *Mater. Res. Bull*. **2004**, *39(14-15)*, 2147-2154.

[9] Armstrong, A. R.; Anderson, P. A. *Inorg. Chem*. **1994**, *33(19)*, 4366−4369.

[10] Cushing, B. L.; Wiley, J. B. *Mater. Res. Bull*. **1999**, *34(2)*, 271-278.

[11] Kodenkandath, T. A, Lalena, J. N.; Zhou, W. L.; Carpenter, E. E.; Sangregorio, C.; Falster, A. U.; Simmons Jr, W. B.; O'Connor, C. J.; Wiley, J. B. *J. Am. Chem. Soc*. **1999**, *121(46)*, 10743-10746.

[12] Kodenkandath, T. A.; Kumbhar, A. S.; Zhou, W. L.; Wiley, J. B. *Inorg. Chem*. **2001**, *40(4)*, 710-714.

[13] Viciu, L.; Caruntu, G.; Royant, N.; Koenig, J.; Zhou, W. L.; Kodenkandath, T. A.; Wiley, J. B. *Inorg. Chem*. **2002**, *41(13)*, 3385−3388.

[14] Viciu, L.; Koenig, J.; Spinu, L.; Zhou, W. L.; Wiley, J. B. *Chem. Mater*. **2003**, *15(7)*, 1480-1485.

[15] Viciu, L.; Golub, V. O.; Wiley, J. B. *J. Solid State Chem*. **2003**, *175(1)*, 88-93.

[16] Viciu, L.; Kodenkandath, T. A.; Wiley, J. B. *J. Solid State Chem*. **2007**, *180(2)*, 583-588.

[17] Viciu, L.; Zhang, X.; Kodenkandath, T. A.; Golub, V.; Wiley, J. B. *Mater. Res. Soc. Symp. Proc*. **2006**, *988*, 0988-QQ08-04.

[18] Choi, J.; Zhang, X.; Wiley, J. B. *Inorg. Chem*. **2009**, *48(11)*, 4811−4816.

[19] Gopalakrishnan, J.; Bhat, V.; Raveau, B. *Mater. Res. Bull*. **1987**, *22(3)*, 413-417.

[20] Laugier, J and Bochu, B. LMGP-Suite, ENSP/Laboratoire des Matériaux et du Génie Physique, BP 46. 38042, Saint Martin d'Hères, France, 2002.

[21] Larson, A. C.; Von Dreele, R. B. , General Structure Analysis System (GSAS); Report LAUR 86-748, Los Alamos National Laboratory, Los Alamos, NM, 2000.

[22] Toby, B. H. *J. Appl. Cryst*. **2001**, *34(2)*, 210−213.

[23] Software is available from Virtual Laboratories, Telephone 1-505-828-1640.

[24] (a) Li, H.; Thomas Jr, G. J. *J. Am. Chem. Soc*. **1991**, *113(2)*, 456-462; (b) Vandeberg, J. T.; Anderson, D. G.; Duffer, J. K.; Julian, J. M.; Scott, R.W.; Sutliff, T. M.; Vaickus, M. J. *An Infrared Spectroscopy Atlas for the Coatings Industry*; Eds.; Federation of Societies for Coatings Technology: Philadelphia, 1980.

[25] Bastian Jr, E. J.; Martin, R. B. *J. Phys. Chem*. **1973**, *77(9)*, 1129-1133.

[26] Shannon, R. D, *Acta Crystallogr., Sect. A: Cryst. Phys., Diffr., Theor. Gen. Cryst*. **1976**, *32(5)*, 751-767.

[27] Bronger, W.; Kyas, A.; Müller, P. *J. Solid State Chem*. **1987**, *70(2)*, 262-270.

[28] May, K. *Z. Kristallogr*. **1936**, *94(1)*, 412–413.

[29] Kolb, A.; Gollackner, M.; Klepp, K. O. *Z. Kristallogr. New Cryst. Struct*. **2004**, *219(1-4)*, 393-394.

[30] Yao, J.; Deng, B.; Ellis, D. E.; Ibers, J. A. *Inorg. Chem*. **2002**, *41(26)*, 7094-7099.

[31] Zhu, W. J.; Hor, P. H. *J. Solid State Chem*. **1997**, *130(2)*, 319-321.

[32] Gál, Z. A.; Rutt, O. J.; Smura, C. F.; Overton, T. P.; Barrier, N.; Clarke, S. J.; Hadermann, J. *J. Am. Chem. Soc*. **2006,** *128(26)*, 8530-8540.

[33] Clarke, S. J.; Adamson, P.; Herkelrath, S .J .C.; Rutt, O. J. Parker, D. R.; Pitcher, M. J.; Smura, C. F. *Inorg. Chem*. **2008**, *47(19)*, 8473-8486.

[34] Denis, S.G.; Clarke, S. J. *Chem. Commun*. **2001**, *22*, 2356-2357**.**

[35] Hyett, G.; Rutt, O. J.; Gál, Z. A.; Denis, S. G.; Hayward, M. A.; Clarke, S. J. *J. Am. Chem. Soc*. **2004**, *126(7)*, 1980-1991.

[36] Clarke, S. J.; Denis, S. G.; Rutt, O. J.; Hill, T. L.; Hayward, M. A.; Hyett, G.; Gál, Z. A. *Chem. Mater*. **2003**, *15(26)*, 5065-5072.

[37] Rutt, O. J.; Hill, T. L.; Gál, Z. A., Hayward, M. A.; Clarke, S. J. *Inorg. Chem*. **2003**, *42(24)*, 7906-7911.

[38] Charkin, D. O.; Sadakov, A. V.; Omel'yanovskii, O. E.; Kazakov, S. M. *Mater. Res. Bull*. **2010**, *45(12)*, 2012-2016.

[39] Ueda, K.; Hosono, H.; Hamada, N. *J. Phys. Condens. Matter*. **2004**, *16(28)*, 5179-5186.

[40] Hiramatsu, H.; Yanagi, H.; Kamiya, T.; Ueda, K.; Hirano, M.; Hosono, H. *Chem. Matter*. **2008**, *20(1)*, 326-334.

[41] Hiramatsu, H.; Ueda, K.; Ohta, H.; Orita, M.; Hirano, M.; Hosono, H. *Appl. Phys. Lett*. **2002**, *81(4)*,598-600.

[42] Kabbour, H.; Janod, E.; Corraze, B.; Danot, M.; Lee, C.; Whangbo, M. H.; Cario, L. *J. Am.Chem. Soc.* **2008**, *130(6)*, 8261-8270.

[43] Choi, J.; Ranmohotti, K. G. S.; Montassersadi, D.; Wiley, J. B. in preparation.

[44] Ranmohotti, K.G. S.; Montasserasadi, D.; Choi, J.; Yao, Y.; Mohanty, D.; Josepha, E. A.; Adireddy, S.; Caruntu, G.; Wiley, J. B. *Mater. Res. Bull*. **2012**, *47(6)*, 1289–1294.

Chapter 4

Synthesis and Characterization of the Rare-Earth Dion–Jacobson Layered Perovskites, $APrNb_2O_7$ (A: Rb, Cs and CuCl)

4.1. Introduction

Layered perovskite classes, such as Dion–Jacobson (DJ) $A[A'_{n-1}\text{-}B_nO_{3n+1}]$, Ruddlesden–Popper (RP) $A_2[A'_{n-1}B_nO_{3n+1}]$, and Aurivillius (AV) $(Bi_2O_2)[A'_{n-1}B_nO_{3n+1}]$, where A: alkali metal, A′: alkaline earth metal, bismuth, lanthanides, and B: Ti, Nb, Ta, all contain interlayer cationic species (A^+, $Bi_2O_2^{2+}$) between perovskite anion slabs $[A'_{n-1}B_nO_{3n+1}]^{-1}$ (Figure 4.1).[1,2] Compounds in these series have been investigated because of their interesting electrical, magnetic, and catalytic properties. For example, $ALaNb_2O_7$ (A: K, Rb, Cs) exhibit good photocatalytic activity,[3] $ALaNb_2O_7$ (A: Li, Na, K) ionic conductivity,[4] and doped $KCa_2Nb_3O_{10}$, superconductivity.[5] Double-layered Dion–Jacobson perovskites containing other lanthanide cations have also been investigated.[2,6–8] The initial studies on $ANdNb_2O_7$ were reported by Dion et al. in 1986.[8] Machida et al., motivated by their photocatalytic activity, were the first to study rare-earth layered tantalum-containing perovskites $RbLnTa_2O_7$ (Ln: La, Pr, Nd, Sm).[6] While this study reported on the praseodymium tantalate $RbPrTa_2O_7$, the corresponding niobate has not yet been reported. Herein we present the synthesis and characterization of $APrNb_2O_7$ (A: Rb, Cs) and its derivative $(CuCl)PrNb_2O_7$.

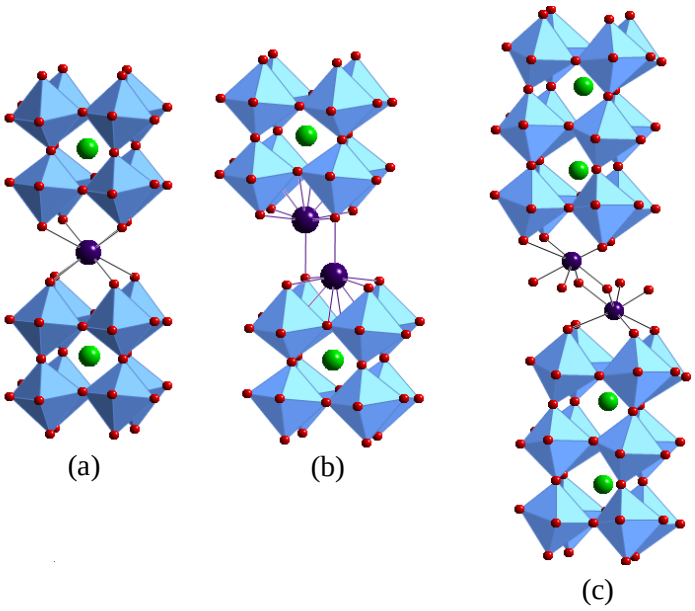

Figure 4.1. The layered perovskite structures (a) Dion–Jacobson $RbLaNb_2O_7$, (b) Ruddlesden–Popper $Rb_2LaNb_2O_7$ and (c) Aurivillius $(Bi_2O_2)Bi_2Ti_3O_{10}$.

4.2. Experimental

Synthesis

$APrNb_2O_7$ (A: Rb, Cs). The parent materials, $APrNb_2O_7$, were prepared by a high temperature solid state reaction similar to that reported for $RbPrTa_2O_7$.[6] First, Pr_6O_{11} (Alfa Aesar, 99.99%) and Pr_2O_3 (Alfa Aesar, 99.9%) were heated at 1000 °C for a day in order to remove any impurities as carbonates or water. Stoichiometric mixtures of Pr_6O_{11} and Nb_2O_5 (Alfa Aesar, 99.9985%), Rb_2CO_3 (Alfa Aesar, 99.8%) and Cs_2CO_3 (Alfa Aesar 99.994%) with 25% excess of A_2CO_3 (A: Rb, Cs) were ground together, placed in an alumina crucible and initially heated in air at 850 °C; $RbPrNb_2O_7$ was then heated at 1100 °C 2 days and $CsPrNb_2O_7$ at 1100 °C for 1 day. The excess of A_2CO_3 was added to compensate the loss of alkali–metal oxides due to its volatilization. The resulting green products were washed with distilled water to remove the

excess of alkali metal carbonate and then dried overnight at 110 °C. $RbPrNb_2O_7$ can also be prepared by reacting (a) Pr_2O_3 with the molar ratio of Rb_2CO_3:Pr_2O_3:Nb_2O_5 1: 1: 2 in O_2 atmosphere at 1000 °C for ~6.5 h (Appendix V Figure D.1) or (b) molten salt of RbCl with the Rb_2CO_3: Pr_6O_{11}:Nb_2O_5: RbCl in the molar ratio of 3: 1: 6: 30 at 1050 °C for 2 h. The final products were washed with warm water and dried at 110 °C for one day.

(CuCl)$PrNb_2O_7$. *A*$PrNb_2O_7$ was ground with a two-fold molar excess of anhydrous $CuCl_2$ (Alfa Aesar 99.995%) in the argon filled glove box, the mixture was pelletized with a hand press, and the pellet was sealed in a Pyrex tube under vacuum. Samples were heated at 325 °C for 7 days for $RbPrNb_2O_7$ and 340 °C for 7 days for $CsPrNb_2O_7$ (Appendix V Figure D.2). The light green powders were washed with distilled water to remove excess $CuCl_2$ and the alkali–metal byproduct and then dried overnight at 110 °C. (CuCl)$PrNb_2O_7$ also can be prepared by ion exchange reaction from $LiPrNb_2O_7$ with 2-fold molar excess of $CuCl_2$ at 300 °C 4 days. (Appendix V)

Characterization X-ray Powder diffraction (XRD) data were collected on a Philips X'Pert system equipped with Cu Kα radiation (λ = 1.5418 Å) and a curved graphite monochromator. Typical scans were collected in continuous mode with a scan rate of 0.02°/s. The peak positions and lattice parameters were refined by a least-squares method with ChekCell.[9] Powder structures were refined by the Rietveld method with the GSAS software package.[10, 11] The thermal behavior of the products was studied by TGA/DSC using a TA Instruments Q600 TGA-DSC system over the temperature range 25-1000 °C with a ramp of 10 °C/min in flowing Ar atmosphere. UV optical absorption measurements were carried out on a Varian Cary 500 UV-VIS NIR spectrophotometer. Measurements were taken from 800 to 200 nm at a scan rate of 600 nm min^{-1}

with a spectral bandwidth of 2 nm. Samples were deposited on 25 × 75 mm microscopic slides from suspensions of ethanol. Transmission electron microscopy (TEM) and selected area electron diffraction (SAED) were performed on a JEM 2010 operated at 200 kV. TEM samples were prepared by crushing them in ethanol, then ethanol suspensions were drop-cast on Ni-TEM grids (Ted Pella). Elemental analysis was carried out by energy dispersive spectroscopy (EDS) on TEM. DC magnetic measurements were performed on a superconducting quantum interference device (SQUID) magnetometer (Quantum Design, MPMS-7) in the temperature range 2–300 K in different magnetic fields up to 6 T, both under zero-field cooled field cooled (ZFC) and field-cooled (FC) conditions. AC susceptibility measurements were carried out on a Quantum Design physical properties measurements system (PPMS) ac/dc magnetometer option with an ac drive field of 10 Oe and oscillating at 0.1, 1.0, 5.0 and 10.0 kHz.

4.3. Results

Synthesis

$APrNb_2O_7$ (A: Rb, Cs) have been prepared by direct reaction:

$$3\ A_2CO_3 + Pr_6O_{11} + 6\ Nb_2O_5 \rightarrow 6\ APrNb_2O_7 + 3\ CO_2 + O_2\ (g) \quad (1)$$

$APrNb_2O_7$ can also be synthesized from Pr_2O_3 (Pr^{3+}), but only under pure oxygen–Pr_2O_3 in air is not an effective reactant. A flux method with Pr_6O_{11} and a large molar excess of RbCl is also useful where this approach rapidly results in quality products within 2 h. $APrNb_2O_7$ (A: Rb, Cs) are both open to topochemical manipulation such that $(CuCl)PrNb_2O_7$ is readily prepared by ion exchange with anhydrous $CuCl_2$:

$$APrNb_2O_7 + CuCl_2 \rightarrow (CuCl)PrNb_2O_7 + ACl\ (aq) \quad (2)$$

Structure analysis

X-ray powder diffraction patterns for the $APrNb_2O_7$ (A: Rb, Cs and CuCl) series are presented in Figure 4.2. The unit cell parameters are shown in Table 4.1. The slight reduction in the cell volume of $APrNb_2O_7$ relative to $ALaNb_2O_7$ is seen in the series and relates to the reduction in ionic radii in going from La^{3+} (1.16 Å) to Pr^{3+} (1.13 Å).[12] Rietveld Refinement was carried out on the series

$APrNb_2O_7$ (A: Rb, Cs and CuCl). The structure of $RbLaNb_2O_7$[2] with the Imma space group was chosen as a model for $RbPrNb_2O_7$. Observed, calculated, and difference plots for the refinement of $RbPrNb_2O_7$ are shown in Figure 4.3 Refinement was also carried out with the P4/mmm space group but this did not give a good fit. The crystallographic data for $RbPrNb_2O_7$ are presented in Table 4.2 and the bond lengths for $RbLaNb_2O_7$ and $RbPrNb_2O_7$ are presented in Table 4.3. The structure of $RbPrNb_2O_7$, isostructural with $RbLaNb_2O_7$, is shown in Figure 4.4. Results from bond valence sum (BVS) calculations (Table 4.4) are consistent with expected values for Rb^+, Pr^{3+} and Nb^{5+}. For $CsPrNb_2O_7$, the crystal structure, the bond distances and BVS calculations are presented in the Appendix V.

Table 4.1. Unit cell parameters for *A*$LnNb_2O_7$ (A: Rb, Cs, CuCl; Ln: La, Pr)

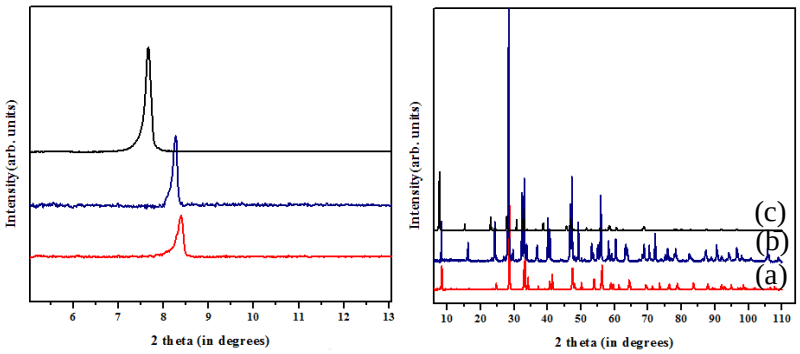

Figure 4.2. XRPD of (a) $RbPrNb_2O_7$, (b) $CsPrNb_2O_7$, and (c) $(CuCl)PrNb_2O_7$. Left figure shows shift in 2 theta as a function of layer expansion.

Table 4.1. Unit cell parameters for *A*LnNb$_2$O$_7$ (A: Rb, Cs, CuCl; Ln: La, Pr)

Compound	Space group	Unit Cell (Å)	Cell Vol. (Å^3)	Layer Spacing(Å)	Ref
RbLaNb$_2$O$_7$	*Imma*	a = 5.4941(4) b=21.9901(6) c = 5.4925(4)	663.58	11.00	2
CsLaNb$_2$O$_7$	*P4/mmm*	a = 3.908(1) c = 11.160(4)	170.44	11.16	7
(CuCl)LaNb$_2$O$_7$	*Pbam*	a = 7.76290(8) b=7.76197(7) c= 11.73390(6)	707.03	11.73	13a
RbPrNb$_2$O$_7$	*Imma*	a = 5.4534(7) b=22.012(1) c = 5.4549(7)	654.84(7)	11.00	This work
CsPrNb$_2$O$_7$	*P4/mmm*	a = 3.8668(2) c = 11.163(1)	166.92(2)	11.16	This work
(CuCl)PrNb$_2$O$_7$	*Pbam*	a = 7.7328(6) b=7.7113(4) c= 11.6706(3)	695.92(4)	11.67	This work

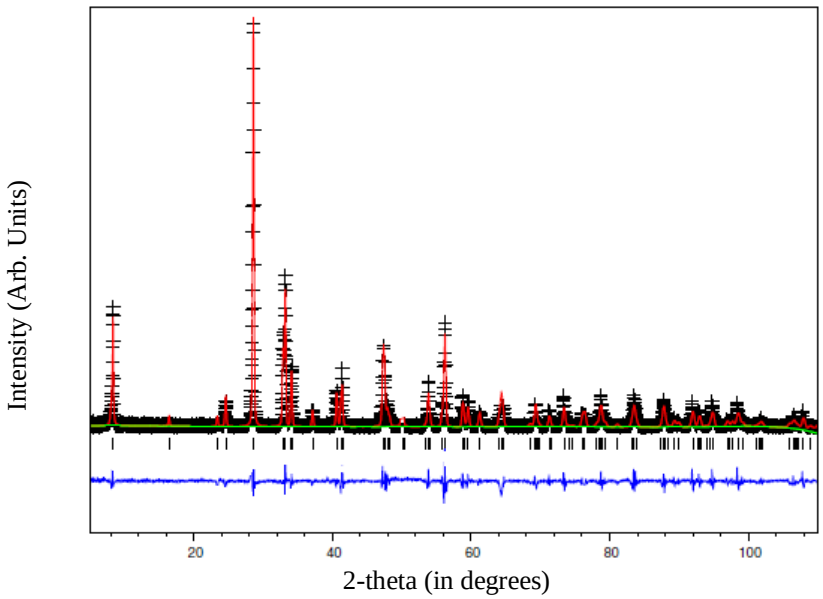

Figure 4.3. Observed and calculated data for the Rietveld refinement of RbPrNb$_2$O$_7$. Observed data are indicated by crosses, calculated pattern by a (red) solid line, and the bottom (blue) curve is the difference plot. Reflection positions are presented by vertical hash marks.

Table 4.2. Crystallographic data for $RbPrNb_2O_7$

Atom	Site	x	y	z	g	U_{iso} (Å^2)
Rb	4a	0	0	0	1.09(1)	0.024(1)
Pr	4e	0.5	0.25	0.503(1)	1.04(1)	0.004(1)
Nb	8h	0	0.3525(1)	0.505(1)	1.05(1)	0.005(1)
O1	4e	0	0.25	0.557(1)	1	0.02(1)
O2	8h	0	0.4363(3)	0.500(1)	1	0.016(6)
O3	8g	0.25	0.3380(3)	0.25	1	0.006(3)
O4	8g	0.75	0.3286(4)	0.75	1	0.03(1)

Imma, g = occupancy; Z= 4; R_p=14.2%, R_{wp} = 13.2%, and χ^2 = 1.727; a = 5.4534(7), b = 22.012(1), c = 5.4549(7) Å, V = 654.84(7) Å^3

Table 4.3. Selected bond lengths extracted from the refined structure of $RbPrNb_2O_7$

$RbLaNb_2O_7$ [2]		**$RbPrNb_2O_7$**	
Bond Type	**Length (A°)**	**Bond Type**	**Length (A°)**
Rb-O2	3.351(6) × 2 2.898(6) × 2 3.133(6) × 4	Rb-O2	3.066(6) × 2 3.064(6) × 2 3.063(3) × 4
La-O1	2.758(8) × 2 3.082(8) × 1 2.411(8) × 1	Pr-O1	2.740(3) × 2 3.050(4) × 1 2.402(4) × 1
La-O3	2.807(7) × 4	Pr-O3	2.754(3) × 4
La-O4	2.607(6) × 4	Pr-O4	2.582(3) × 4
Nb-O1	2.277(8) × 1	Nb-O1	2.272(4) × 1
Nb-O2	1.744(7) × 1	Nb-O2	1.845(8) × 1
Nb-O3	1.949(4) × 2	Nb-O3	1.969(6) × 2
Nb-O4	2.024(4) × 2	Nb-O4	1.978(6) × 2

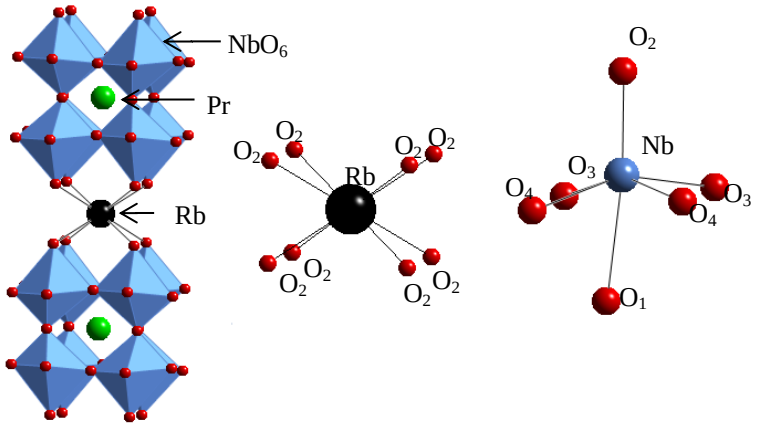

Figure 4.4. The crystal structure of $RbPrNb_2O_7$ based on refinement. The (blue) octahedral represent NbO_6, the medium-sized (green) spheres represents praseodymium, and the large dark sphere is rubidium.

Table 4.4. BVS results for $RbLaNb_2O_7$ and $RbPrNb_2O_7$

$RbLaNb_2O_7$ [2]		$RbPrNb_2O_7$	
Rb	0.8461	Rb	0.9176
La	2.9734	Pr	2.9292
Nb	5.1678	Nb	5.0177

Figure 4.5 shows the Rietveld refinement plot of $(CuCl)PrNb_2O_7$. The space group Pbam was used as has been reported for $(CuCl)LaNb_2O_7$.[13a] Atomic positions of the refined structures are presented in Table 4.5. Figure 4.6 shows the crystal structure of $(CuCl)PrNb_2O_7$; the copper is octahedrally coordinated, $CuCl_4O_2$, with the Cl's in the equatorial positions and the oxygens from the perovskite blocks in the apical positions. The $CuCl_4O_2$ octahedral units then edge share with each other and share corners with the NbO_6 octahedra. Selected bond distances for $(CuCl)PrNb_2O_7$ are given in Table 4.6 and the BVS for $(CuCl)PrNb_2O_7$ compared to $(CuCl)LaNb_2O_7$ [13a] in Table 4.7.

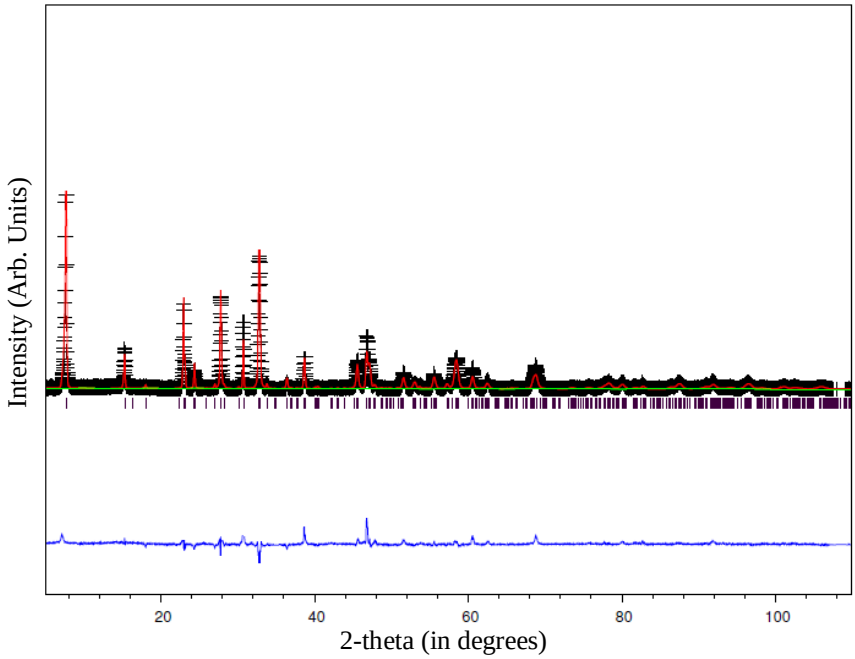

Figure 4.5. Observed and calculated data for the Rietveld refinement of (CuCl)$PrNb_2O_7$. Observed data are indicated by crosses, calculated pattern by a (red) solid line, and the bottom (blue) curve is the difference plot. Reflection positions are presented by vertical hash marks.

Table 4.5. Crystallographic data for (CuCl)$PrNb_2O_7$

Atom	**Site**	**x**	**y**	**z**	**g**	**U_{iso} (Å^2)**
Cu	4h	0.7327(1)	0.5241(4)	0.5	0.96(1)	0.0036(6)
Cl	4h	0.5560(6)	0.2279(6)	0.5	1.13(2)	0.020(6)
Pr	4g	0.0011(3)	0.2581(4)	0	0.981(6)	0.0052(4)
Nb	8i	0.7477(2)	0.4987(1)	0.8111(2)	1.04(4)	0.0001(2)
O1	4f	0	0.5	0.8365(4)	1	0.0029(2)
O2	8i	0.2829(2)	0.7634(7)	0.8341(2)	1	0.0021(1)
O3	8i	0.2321(8)	0.0404(6)	0.6446(8)	1	0.0087(4)
O4	4g	0.7451(2)	0.5536(6)	0	1	0.0058(9)
O5	4e	0	0	0.8789(9)	1	0.0030(5)

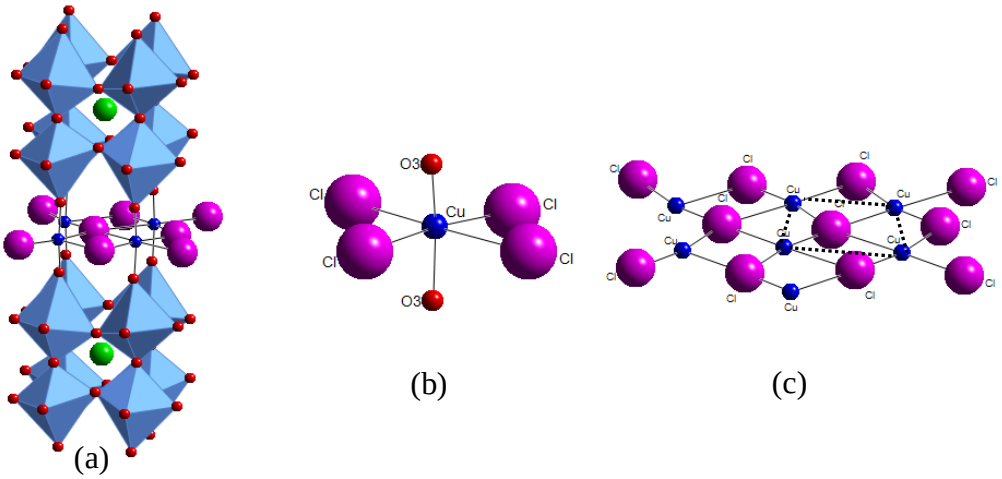

(a) (b) (c)

Figure 4.6. (a) Crystal structure of (CuCl)$PrNb_2O_7$ based on refinement. The (blue) octahedra represent NbO_6, the medium sized (green) sphere represents niobium, the large (pink) sphere chlorine, the small dark (blue) copper and the small light (red) sphere oxygen. (b) $CuCl_4O_2$ octahedral unit and (c) extended Cu–Cl layer.

Table 4.6. Selected bond lengths for (CuCl)$PrNb_2O_7$

(CuCl)$LaNb_2O_7$ [13a]		(CuCl)$PrNb_2O_7$	
Bond Type	Length (Å)	Bond Type	Length (Å)
Cu-O3	1.847 × 2	Cu-O3	1.76043(5) × 2
Cu-Cl	3.214 × 1 3.035 × 1 2.426 × 1 2.410 × 1	Cu-Cl	3.1673(1) × 1 2.9394(1) × 1 2.6613(1) × 1 2.2668(1) × 1
La-O1	2.838 × 2	Pr-O1	2.66796(9) × 2
La-O2	2.667 × 2 2.620 × 2	Pr-O2	2.5570(1) × 2 2.9329(1) × 2
La-O4	2.534 × 1 2.816 × 1 2.678 × 1 2.957 × 1	Pr-O4	2.4406(1) × 1 3.0187(1) × 1 2.4723(1) × 1 3.0562(1) × 1
La-O5	2.591 × 2	Pr-O5	2.4407(1) × 2
Nb-O1	1.957 × 1	Nb-O1	1.9732(1) × 1
Nb-O2	2.013 × 1 1.974 × 1	Nb-O2	2.0532(1) × 1 1.8733(1) × 1
Nb-O3	1.782 × 1	Nb-O3	1.9696(6) × 1
Nb-O4	2.258 × 1	Nb-O4	2.2448(7) × 1
Nb-O5	2.016 × 1	Nb-O5	2.0730(1) × 1

Table 4.7. BVS for $(CuCl)PrNb_2O_7$ and $(CuCl)LaNb_2O_7$ [13a]

$(CuCl)LaNb_2O_7$		$(CuCl)PrNb_2O_7$	
Cu	2.02	Cu	2.06
La	3.02	Pr	3.26
Nb	5.12	Nb	4.96

Transmission electron microscopy and compositional analysis

Figure 4.7 presents a TEM image of a $(CuCl)LaNb_2O_7$ crystallite with a plate-shaped morphology. SAED shows the four-fold symmetry (pseudo-tetragonal) with lattice parameters of a = b ≈ 7.72 Å (Figure 4.7) which are in reasonable agreement with the refinement data a = 7.7328(6), b = 7.7113(4) Å. Elemental analysis with EDS shows no evidence for alkali metal residue (Appendix V) and molar ratio was found to be approximately 0.9(8) : 1 : 2.3(1) Rb : Pr : Nb for $RbPrNb_2O_7$, 0.9(1) : 1 : 2.1(3) Cs : Pr : Nb for $CsPrNb_2O_7$, and 0.8(7) : 0.8(1) : 1 : 2.3(2) Cu : Cl : Pr : Nb for $(CuCl)PrNb_2O_7$. SAED of $APrNb_2O_7$ (A: Rb, Cs) along with elemental analysis are given in (Appendix V) with the unit cell parameters of a = b ≈ 3.93 Å for $CsPrNb_2O_7$ and a ≈ c ≈ 5.42 Å for $RbPrNb_2O_7$ are comparable with refinement results of a = 3.8668(2), and a = 5.4534(7), c = 5.4549(7) Å, respectively.

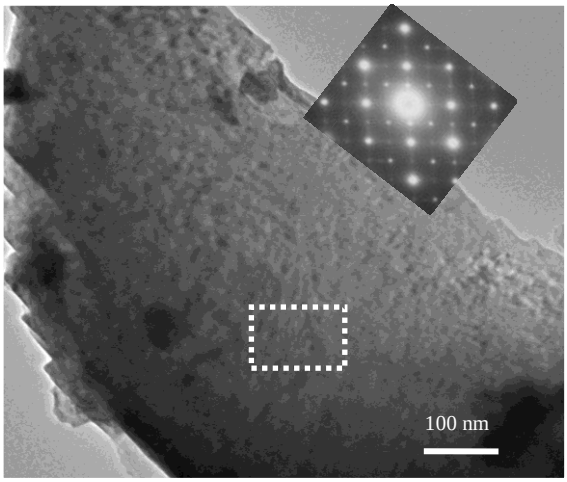

Figure 4.7. TEM and inset SAED along [001] of (CuCl)$PrNb_2O_7$ from dashed rectangle.

Magnetic measurements

Variable temperature magnetic susceptibility data (FC/ZFC) were collected on $RbPrNb_2O_7$, $CsPrNb_2O_7$, and (CuCl)$PrNb_2O_7$. Magnetic measurements of $RbPrNb_2O_7$ follows Curie–Weiss behavior with θ_{CW} = −47.3 (2) K and an effective magnetic moment μ_{eff} = 3.34(1) μ_B (Figure 4.8). $CsPrNb_2O_7$ exhibits similar behavior (Appendix V Figure D.7) with θ_{CW} = −59.5(9) K and an effective magnetic moment of μeff = 3.60(2)μ_B. Figure 4.9a shows the magnetic susceptibility versus temperature for (CuCl)$PrNb_2O_7$. Curie–Weiss behavior is observed from 20–300 K (θcw = −60.7 (4) K) with an effective magnetic moment of μeff = 4.020(8) μ_B; reciprocal susceptibility χ^{-1} versus temperature is shown in Figure 4.9b. At lower temperatures, an antiferromagnetic-like transition is seen at around 19.43(1) K with a small Curie-tail below 2 K. M–H curve at 2 K and 300 K are presented in (Appendix V) with ~15 Oe coercivity at 2 K. AC susceptibility at different frequencies (Figure 4.10) shows a similar DC transition at 20 K in for real component χ′(T), which is frequency independent. The lack signal in imaginary component χ″ (T) is consistent with antiferromagnetic ordering.

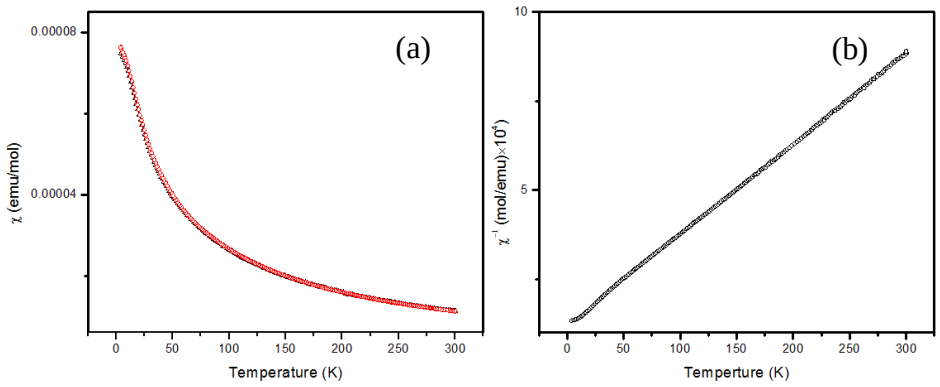

Figure 4.8. (a) Temperature dependence of magnetic susceptibility of $RbPrNb_2O_7$ at a constant field of 100 Oe (red open circle shows FC and black filled triangle shows ZFC) and (b) plot of inverse susceptibility.

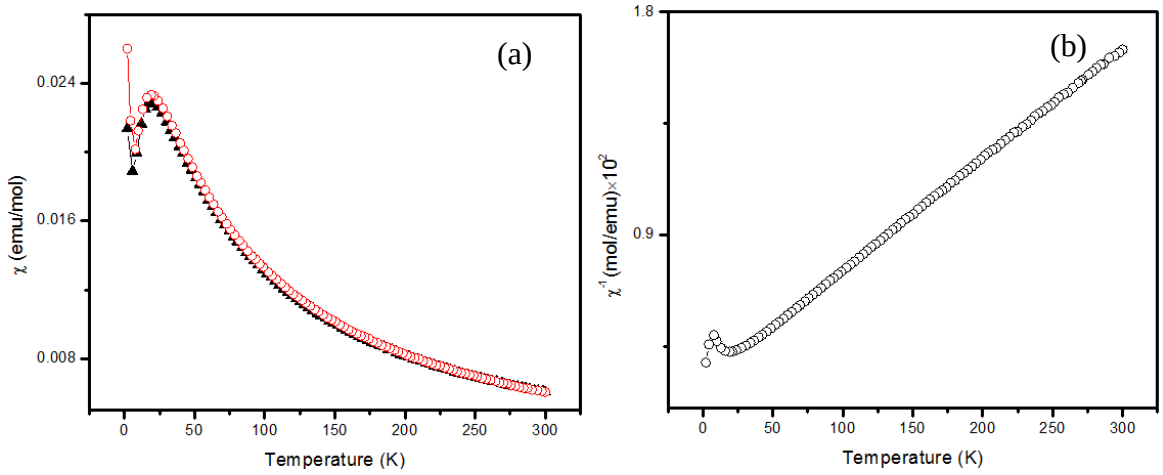

Figure 4.9. (a) Temperature dependence of magnetic susceptibility of $(CuCl)PrNb_2O_7$ at 100 Oe (red open circle shows FC and black close triangle shows ZFC). (b) Reverse susceptibility Measurements were carried out on FC at a constant field of 100 Oe.

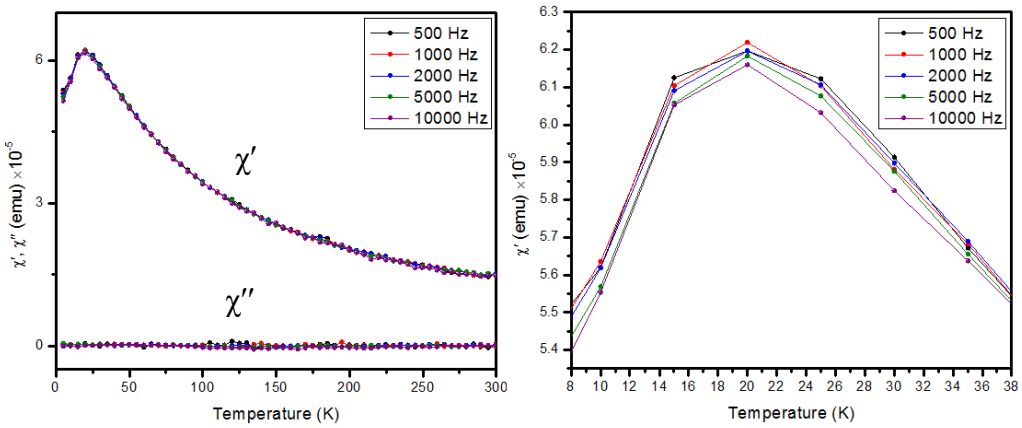

Figure 4.10. AC susceptibility at 10 Oe with 0.1, 0.5, 1.0, 2.0, 5.0 and 10.0 kHz frequencies.

Spectroscopic measurements

The visible spectroscopic data for $APrNb_2O_7$ (A: Rb, Cs) versus pure Pr_2O_3 are presented in Figure 4.11. The spectra shows absorption peaks correspond to Pr_2O_3 to confirm Pr^{3+} in the final structure. $(CuCl)PrNb_2O_7$, (Appendix V Figure D.10) shows none of the spectroscopic detail associated with the Pr^{3+} transitions, exhibiting only very broad features.

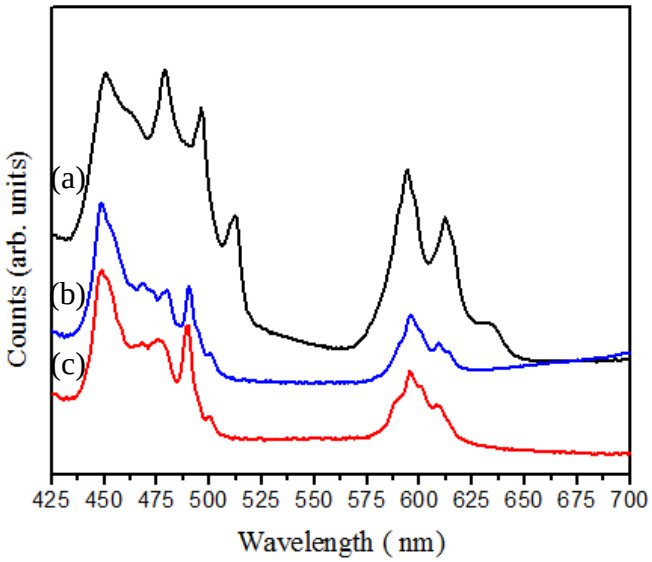

Figure 4.11. Visible spectra of the (a) Pr_2O_3 (b) $CsPrNb_2O_7$ and (c) $RbPrNb_2O_7$.

Thermal analysis

The stability of $APrNb_2O_7$ (A: Rb, Cs) in argon as a function of temperature shows these compounds are stable up to 1100 °C. In the case of $(CuCl)PrNb_2O_7$ (Figure 4.12), it decomposes with two endothermic steps (690 °C, 930 °C) with the total weight loss of 12.81%. The major decomposition product was found to be $PrNbO_4$. (Appendix V)

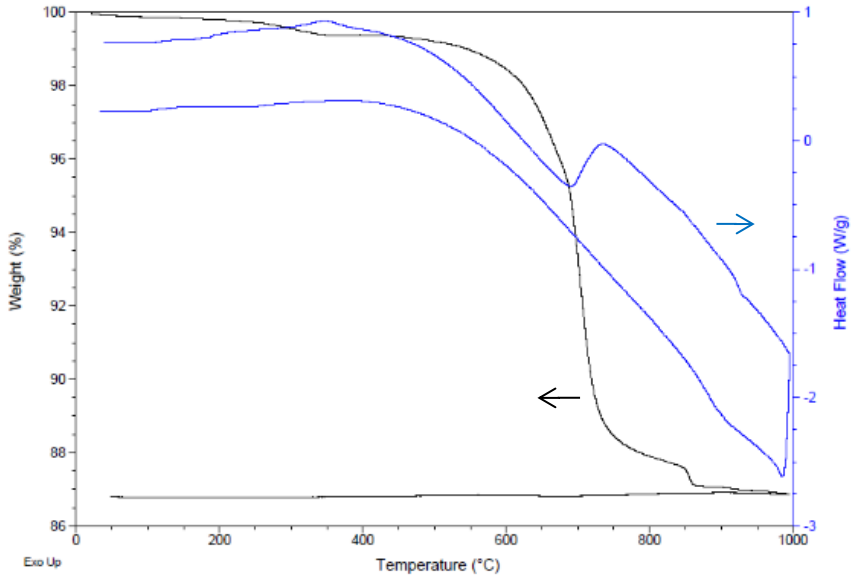

Figure 4.12. Thermal analysis results for $(CuCl)PrNb_2O_7$. The dark black line is TGA and the light blue line is DSC.

4.4. Discussion

Synthesis

There are 7 sub oxide phases reported for PrOx (x = 1.5–2) such as the θ phase Pr_2O_3 (x = 1.5), the β phase Pr_6O_{11} (x = 1.833), and the α phase PrO_2 (x = 2), all of which interconvert by means of heating/cooling under controlled oxygen pressure.[14] The PrO_2 is unstable phase and

decomposes to other sub oxide under the reaction conditions used in this study to prepare $APrNb_2O_7$ (A: Rb, Cs). Pr_6O_{11} readily leads to the target compounds for reactions carried out in air. Conversely, Pr_2O_3 is not reactive in air, but under flowing oxygen readily reacts to produce the layered perovskites. Since Pr_6O_{11} likely forms under these conditions, the presence of this phase seems to readily favor the formation of $APrNb_2O_7$ (A: Rb, Cs). This may be one of the reasons previous researchers have not reported these phases. The synthesis of $(CuCl)PrNb_2O_7$ was also studied. Reactions starting from $LiPrNb_2O_7$ were faster and occurred at lower temperatures (4 days, 300 °C), while those with $RbPrNb_2O_7$ (7 days, 325 °C) and $CsPrNb_2O_7$ (7 days, 340 °C) required higher temperatures and longer reaction times. This likely relates to the relative mobility of the various alkali–metal cations, the smaller cations being more mobile: Li > Rb > Cs.

Structure

In Figure 4.6b, copper ion in $(CuCl)PrNb_2O_7$ has octahedral coordination with two apical oxygens from the perovskite layers and four equatorial chlorine ions. Figure 4.2 and Table 4.1 show exchanging of Rb/Cs with larger copper chloride species leads to expansion of the layers (0.5–0.7 Å) which is the same as seen in $(CuCl)LaNb_2O_7$. Yoshimura et al. used refined synchrotron data for $(CuCl)LaNb_2O_7$ in P4/mmm[15] but later Tsirlin and coworkers found evidence for an α-phase $(CuCl)LaNb_2O_7$ at room temperature where Cu and Cl are both disordered (x, y, 1/2) with superlattice structure refined in Pbam space group (2a,2b,c).[13a] It would appear that $(CuCl)PrNb_2O_7$ exhibits similar structural features. The tilting of NbO_6 in $APrNb_2O_7$ (A: Rb and CuCl) may cause transition from nonpolar to polar at lower temperature than room temperature such described for the series $ALnNb_2O_7$ (A: Rb, Cs; Ln: La, Nd).[16a,16b]

Magnetic behavior

In Figure 4.8 and (Appendix V) the inverse susceptibility (χ^{-1}) of $APrNb_2O_7$ (A: Rb, Cs) versus temperature confirm paramagnetic (Curie–Weiss) behavior in these compounds. In terms of magnetic moments, they exhibit the values μ_{eff} (Rb) = 3.34(1)μ_B and μeff (Cs) = 3.60(2)μ_B. These are in reasonable agreement with the value calculated for Pr^{3+} ion (Pr^{3+}: $4f^2$ S = 1, L = 5, J = 4, g = 0.8). Also, literature moments for Pr^{3+} containing compounds are typically 3.57μ_B.[17] Further, values are also in a good agreement with the structurally-related tantalum phase, $RbPrTa_2O_7$, with the effective magnetic moment of μ_{eff} = 3.58μ_B.[18] The susceptibility behavior of $(CuCl)PrNb_2O_7$ (μ_{eff} = 4.020(8)μ_B) resembles that of $(CuCl)PrTa_2O_7$ [18] with magnetic moment of μ_{eff} = 3.87(1)μ_B. The moments in these compounds understandably increase relative to the parents (e.g., $RbPrNb_2O_7$ μ_{eff} = 3.34(1)μ_B) due to the addition Cu^{2+} ions. The moments, however, are in a very good agreement with what is expected for that simply calculated for non-interacting magnetic ions of Cu^{2+}(1.7μ_B) and Pr^{3+}(3.57μ_B) μ_{Total} = 3.95μ_B based on $\sqrt{\mu Cu^2 + \mu Pr^2}$. In $CuPrO_2$, the effective magnetic moment (μeff = 3.75(6)μ_B) is slightly larger than the moment of Pr^{3+} ion due to the presence of Cu^{2+} ions.[19] The negative and strong value of Curie–Weiss constant of θ_{cw} = −60.7(4) K for $(CuCl)PrNb_2O_7$ indicates that the magnetic interaction observed at low temperatures tends towards antiferromagnetism (AFM) (Figure 4.9). 2D frustrated square lattice of $(CuCl)LaNb_2O_7$ (S = 1/2)[13a] shows a broad peak at 16.5 K which is similar to $(CuCl)PrNb_2O_7$ that shifted to higher temperature 19.43(1) K, indicating a slightly higher ordering temperature. There is also a Curie tail at 2 K for $(CuCl)PrNb_2O_7$ which for $(CuCl)LaNb_2O_7$ that transition below 4 K is due to impurities or defects of in the CuCl layer.[20] Structure of $(CuCl)PrNb_2O_7$ is made of magnetic $(CuCl)^+$ planes separated by magnetic perovskite slabs of Pr^{3+}, which are more complicated than $(CuCl)LaNb_2O_7$ with no magnetic

perovskite slabs. The real part (χ') of AC susceptibility (Figure 4.10b) shows that the 20 K transition is frequency independent and corresponds to that observed in DC measurements. The Imaginary part (χ'') does not show any transition (Figure 4.10a). This with the lack of hysteresis in M–H DC susceptibility are all consistent with (CuCl)$PrNb_2O_7$ with AFM-like behavior. Further, magnetic data can be fit by Rushbrook and Wood's equation for the 2-D Heisenberg model: [21]

$$\chi = \frac{S(S+1)Ng^2\mu_B}{3kT}\sum_{n=0}^{6}\left((-1)^n\ \left(\frac{b_n}{\theta^n}\right)\right)$$

Where N = Avogadro's number (6.023×10^{23}), k = Boltzmann constant (1.38×10^{-16} erg K^{-1}), μ_B = Bohr magneton (9.274×10^{-21} erg Oe^{-1}), θ = kT/J, J = exchange constant and the b_n coefficients for S = 3/2 system, which were calculated to be $b_0 = 1$, $b_1 = -10$, $b_2 = 30$, $b_3 = -42.6666$, $b_4 = 262.916666$, $b_5 = -1043.85$ and $b_6 = 790.1125$. Figure 4.23 represents the fit of the ZFC susceptibility with the 2D Heisenberg model for S = 3/2. J/k = −3.44(2) K and g = 2.150 (3) were extracted from the fitting. No difference in ZFC and FC was observed, so only ZFC data are presented here. The calculated values for J/k extracted from $\frac{kT(\chi_{\max})}{|J|S(S+1)}$= 2.10(1) and $\frac{\chi_{\max}|J|}{Ng^2{\mu_B}^2} =$ 0.0539 [22] for S = 3/2 with S(S + 1) = 15/4 and T(χ_{max}) = 20 K, are −3.51 K and −3.55 K, respectively. The model and the experimental results are in very good agreement to the estimated exchange constant (−3.44(2) K) and are also close to what has been reported before for (MnCl)$LaNb_2O_7$ with S = 5/2 (J/k = −3.77 K, g = 1.9)[13b] but smaller than (FeCl)$LaNb_2O_7$ with S = 2 (J/k =−7.78 K, g = 2.24).[23] The 2D Heisenberg model can be used on anisotropic models like in our system, where the distorted CuCl layer (Figure 4.6c) deviates from the ideal square planar.

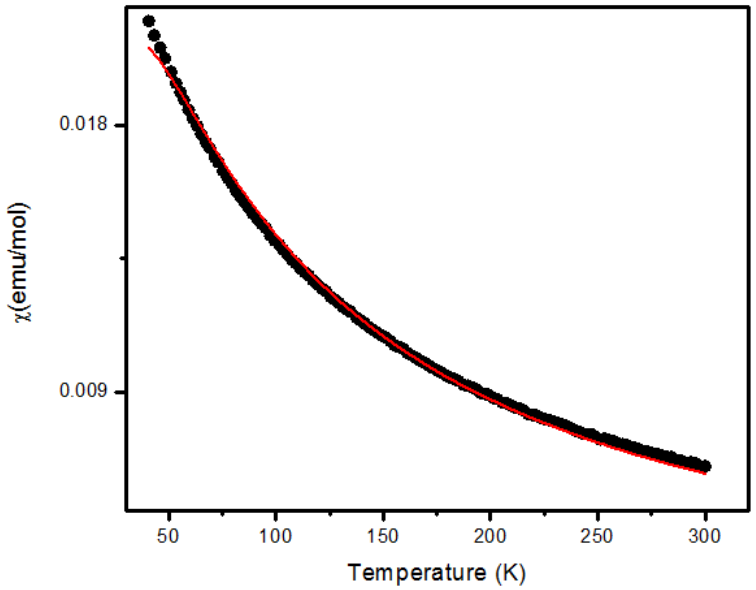

Figure 4.13. Fitting of 2D AFM Heisenberg system with S = 3/2 to DC susceptibility data. The solid red line is the model and the black is DC susceptibility at 100 Oe in 30–300 K.

Thermal behavior

TGA/DTA results show no event for the $APrNb_2O_7$ (A: Rb, Cs). In the case of $(CuCl)PrNb_2O_7$ (Figure 4.12), the decomposition is similar to $(CuCl)PrTa_2O_7$ [18] with two steps (690 °C, 930 °C) and a total weight loss of 12.81%. This is thought to be related the evolution of Cl_2 (13.8%). Decomposition products included $PrNbO_4$ and possibly $CuNbO_3$, which were found to form around 690 °C (Appendix V). Thermal analysis of $(CuCl)PrTa_2O_7$[18] showed similar behavior with the decomposition product of $PrTaO_4$ at 875 °C. There is no evidence in $(CuCl)PrTa_2O_7$ for the formation of an intermediate phase of $Cu_{0.5}PrNb_2O_7$ in spite of formation of $Cu_{0.5}LaNb_2O_7$ from $(CuCl)LaNb_2O_7$.[24]

4.5 References

[1] Aurivillius, B. *Ark. Kemi*. **1949**, *1,* 499.

[2] Armstrong, A. R.; Anderson, P. A. *Inorg. Chem*. **1994**, *33(19),* 4366−4369.

[3] Domen, K.; Kondo, J. N.; Hara, M.; Takata, T. *Bull. Chem. Soc. Jpn*. **2000**, *73(6),* 1307−1331.

[4] Sato, M.; Abo, J.; Jin, T.; Ohta, M. *J. Alloys Compd*. **1993**, *192(1-2)*, 81-83.

[5] Fukuoka, H.; Isami, T.; Yamanaka, S. *Chem. Lett*. **1997**, *26(8),* 703−704.

[6] Machida, M.; Yabunaka, J.; Kijima, T. *Chem. Mater*. **2000**, *12(3),* 812-817.

[7] Kumada, N.; Kinomura, N.; Sleight, A. W. *Acta Crystallogr*., Sect. C: Cryst. Struct. Commun. **1996**, *52(5),* 1063−1065.

[8] (a) Dion, M.; Ganne, M.; Tournoux, M. *Rev. Chim. Miner*. **1986**, *23*, 61-69; (b) Snedden, A.; Knight.; K. S.; P. Lightfoot, P. *J. Solid State Chem*. **2003**, *173(2),* 309-313.

[9] Laugier, J and Bochu, B. LMGP-Suite, ENSP/Laboratoire des Matériaux et du Génie Physique, BP 46. 38042, Saint Martin d'Hères, France, 2002.

[10] Larson, A. C and Von Dreele, R. B. , General Structure Analysis System (GSAS) program. Rep. No. LA-UR-86748, Los Alamos National Laboratory, Los Alamos, CA, 1994.

[11] Toby, B. H. *J. Appl. Cryst*. **2001**, *34(2),* 210−213.

[12] Shannon, R. D. *Acta Crystallogr., Sect. A: Cryst. Phys., Diffr., Theor. Gen. Cryst*. **1976**, *32(5),* 751-767.

[13] *(a)* Tsirlin, A. A.; Abakumov, A. M.; Tendeloo, G. V.; Rosner, H. *Phys. Rev. B: Condens. Matter*, **2010**, *82,* 054107; *(b)* Viciu, L.; Golub, V. O.; Wiley, J. B. *J. Solid State Chem*. **2003**, *175(1),* 88-93.

[14] (a) Thangadurai, V.; Huggins, R. A.; Weppner, W. *J. Solid State Electrochem*. **2001**, *5(7-8),* 531-537*;* (b) Burnham, D. A.; Eyring, L. *J. Phys. Chem*. **1968**, *72(13),* 4415-4424.

[15] Oba, N.; Kageyama, H.; Saito, T.; Azuma, M.; Paulus, W.; Kitano, T.; Ajiro, Y.; Yoshimura, K. *J. Magn. Magn. Mater*. **2007**, *310(2),* 1337-1339.

[16] (a) Sim, H.; Kim, B. G. *Phys. Rev. B*: *Condens. Matter*. **2014**, *89,* 144114; (b) Benedek, N. A. *Inorg. Chem*. **2014**, *53(7),* 3769-3777.

[17] (a) O'Connor, C. *J. Prog. Inorg. Chem*. **1982**, *29,* 203-283; (b) Kittel, C. *Introduction to Solid State Physics*; 6th ed., Chapter 14; Eds.; John Wiley & Sons, Ltd: New York, 1978; pp 405.

[18] Montasserasadi, D.; Granier, M.; Spinu, L.; Chandra Rai, S.; Zhou, W.; Wiley, J. B., *J. Chem. Soc, Dalton Trans*. (**2015**) Accepted.

[19] Miyasaka, N.; Doi, Y.; Hinatsu, Y. *J. Solid State Chem*. **2009**, *182(8)*, 2104-2110.

[20] Kageyama, H.; Kitano, T.; Oba, N.; Nishi, M.; Nagai, S.; Hirota, K.; Viciu, L.; Wiley, J. B.; Yasuda, J.; Baba, Y.; Ajiro, Y.; Yoshimura, K. *J. Phys. Soc. Jpn*. **2005**, *74(6)*, 1702-1705.

[21] Rushbrooke, G. S.; Wood, P. J. *Mol. Phys*. **1963**, *6(4)*, 409-421.

[22] De Jongh, L. J.; Miedema, A. R. *Adv. Phys*. **1974**, *23(1)*, 1-260.

[23] Viciu, L.; Koenig, J.; Spinu, L.; Zhou, W. L.; Wiley, J. B. *Chem. Mater*. **2003**, *15(7)*, 1480-1485.

[24] Hermann, A. T.; Wiley, J. B. *Mater. Res. Bull*. **2009**, *44(5)*, 1046-1050.

Chapter 5

Copper Oxychloride Rare-Earth Tantalate Layered Perovskites

5.1. Introduction

Dion-Jacobson (DJ) $A[A'_{n-1}B_nO_{3n+1}]$ layered perovskites consist of perovskite slabs $[A'_{n-1}B_nO_{3n+1}]$ separated by interlayer cations (A^+). These compounds can be prepared by conventional high temperature reactions or topochemical low temperature methods such as ion exchange and intercalation. Topochemistry can lead to metastable compounds often not accessible by high temperature methods. Such low temperature strategies have been developed for the formation of various metal-nonmetal layers such as CuCl in $(CuCl)LaNb_2O_7$ or $(CuCl)PrNb_2O_7$ by ion exchange.[1,2] Should this reaction be preceded by reductive intercalation with n-butyl lithium, $(Li_xCl)LaNb_2O_7$ is accessible.[3] Similarly, combinations of reductive intercalation and oxidative intercalation can lead to other compounds such as $(Rb_2Cl)LaNb_2O_7$, $(Rb_2OH)LaNb_2O_7$ and $(Rb_2SH)LaNb_2O_7$.[4-6]

Incorporation of ions with different sizes and charges in the A, A′ and B sites of layered perovskites can produce a variety compounds with interesting properties such as photocatalytic activity in $ALnM_2O_7$ (A: alkali metal; Ln: La, Pr, Nd, Sm; M: Nb, Ta)[7, 8] and $RbPb_2Nb_3O_{10}$,[9] ionic conductivity in $ALaNb_2O_7$ (A = alkali metal),[10] superconductivity in $KCa_2Nb_3O_{10}$,[11] lead-free ferroelectrics in $RbBiNb_2O_7$,[12] and proton conduction in $HPb_2Nb_3O_{10}\cdot xH_2O$.[13] $ALnM_2O_7$ (Ln: La, Pr, Nd, Sm; M: Nb, Ta) layered perovskites have been prepared.[2,8] For those compounds with the lanthanides beyond samarium, the smaller size of the cation no longer favors the perovskite structure and other compounds such as pyrochlore can be observed.[14] $(CuCl)PrNb_2O_7$ [2] has been recently reported and is found to exhibit antiferromagnetic behavior; there are no reports on the corresponding praseodymium or neodymium tantalates. In this paper, $ALnTa_2O_7$

(Ln: Nd, Pr) have been used as precursors to build new copper-chloride layered perovskites with interesting magnetic and thermal behavior.

5.2.Experimental

Synthesis

$ALnTa_2O_7$ (A: Rb, Cs and Ln: Pr, Nd). Dion-Jacobson double-layered perovskites $ALnTa_2O_7$ were prepared by high temperature solid state reaction.[8] Nd_2O_3 (Alfa Aesar, 99.99%) and Pr_6O_{11} (Alfa Aesar, 99.99%) were heated at 1000 °C for a day in order to remove any impurities as carbonates or water. Stoichiometric mixtures of Ln_2O_3, Pr_6O_{11}, and Ta_2O_5 (Alfa Aesar, 99.9985%) were combined with a 25% excess of A_2CO_3 (Rb_2CO_3: Alfa Aesar, 99%; Cs_2CO_3: Alfa Aesar, 99.994%). Samples were ground together and heated at 1100 °C for 10 h. The excess amount of A_2CO_3 was added to compensate for the volatilization of alkali-metal oxide components at very high temperatures. The final products were washed with distilled water, then dried at 110 °C for 24 h.

(CuCl)$LnTa_2O_7$. $ALnTa_2O_7$ were mixed with a 2-fold molar excess of anhydrous $CuCl_2$ (Alfa Aesar 99.995 %) in an argon-filled glove box. The mixtures were pelletized with a hand press (Aldrich) and sealed in Pyrex tubes under vacuum. (CuCl)$PrTa_2O_7$ was prepared from $RbPrTa_2O_7$ or $CsPrTa_2O_7$ by heating samples for 7 days at 325 °C and 400 °C, respectively. (CuCl)$NdTa_2O_7$ was prepared from $CsNdTa_2O_7$ by heating the samples at 400 °C for 72 h. All the new phases were washed with DI-water and dried at 110 °C for 24 h.

Characterization

X-ray Powder diffraction (XRD) data were collected on a Philips X'Pert system equipped with Cu Kα radiation (λ = 1.5418 Å) and a curved graphite monochromator. Typical scans were

collected in continuous mode with a scan rate of 0.02 °/s. The peak positions and lattice parameters were refined by a least-squares method with the program ChekCell.[15] Crystal structures were refined by the Rietveld method with the GSAS software package.[16-17] Transmission electron microscopy (TEM) and selected area electron diffraction (SAED) were performed on a JEM 2010 operated at 200 kV. The samples were prepared by crushing them under ethanol, and then ethanol suspensions of the samples were drop-cast on Ni-TEM grids (Ted Pella). Elemental analysis was carried out by energy dispersive spectroscopy (EDS) on TEM equipped with an EDAX-DX Prime microanalytical system. The thermal behavior of the products was studied by TGA/DSC using a TA Instruments Q600 TGA-DSC system over the temperature range 25-1000 °C with a ramp of 10 °C/min in flowing Ar atmosphere. Magnetic susceptibility measurements were performed on a superconducting quantum interference device (SQUID) magnetometer (Quantum Design, MPMS-7) in the temperature range 2-300 K in magnetic fields up to 6T. Magnetic susceptibility measurements were carried out in zero field cooled (ZFC) and field cooled (FC) conditions.

5.3. Results

Synthesis

A new set of copper halide perovskite compounds have been readily prepared topochemically. Ion exchange reactions under mild conditions (325 - 400 °C) with the double-layered perovskites, $ALnTa_2O_7$ (Ln: Pr, Nd), led to $(CuCl)PrTa_2O_7$ and $(CuCl)NdTa_2O_7$, respectively. Reactions starting from parents containing either the rubidium or cesium are effective. EDS data for $(CuCl)PrTa_2O_7$ (0.9(1):0.8(1):1:2.1(3)) (Appendix VII) and $(CuCl)NdTa_2O_7$ (0.9(2):0.9(4):1:2.0(2)) (Appendix VII) are consistent with the composition 1:1:1:2 for Cu:Cl:Ln:Ta.

Diffraction Studies

X-ray powder diffraction patterns for $(CuCl)LnTa_2O_7$ (Ln: Pr, Nd) are presented in Figure 5.1 relative to their respective parents. The two $(CuCl)LnTa_2O_7$ compounds have been indexed on orthorhombic cells and their refined unit cell parameters are given in Table 5.1.

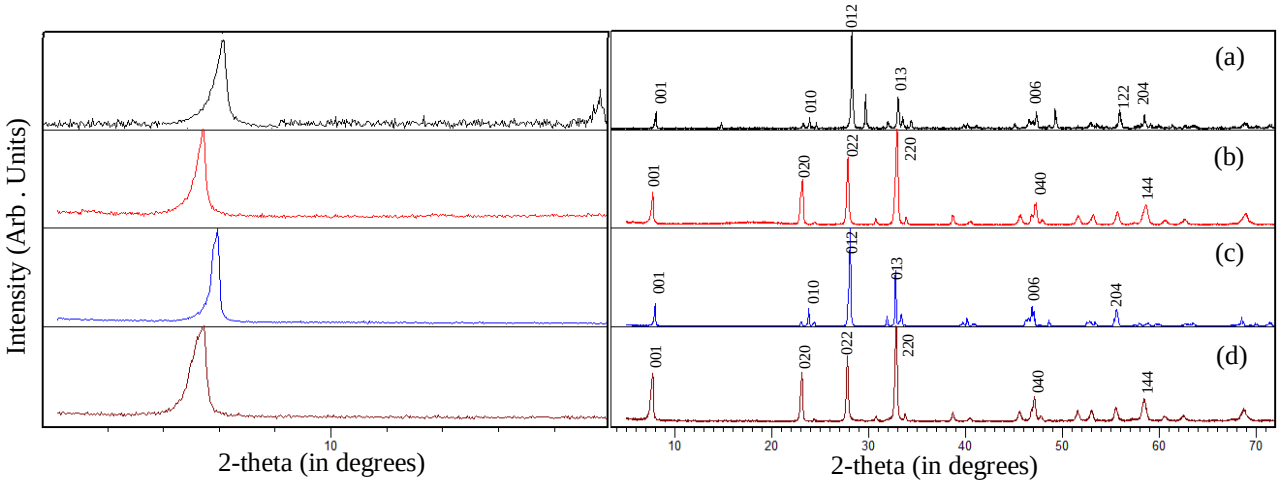

Figure 5.1. X-ray powder diffraction patterns for (a) $CsNdTa_2O_7$, (b) $(CuCl)NdTa_2O_7$, (c) $CsPrTa_2O_7$ and (d) $(CuCl)PrTa_2O_7$.

Table 5.1. Unit cell parameters for $(CuCl)LnTa_2O_7$ (Ln: Pr, Nd).

Compounds	**Space group**	**Unit Cell (Å)**	**Cell Vol. (Å^3)**	**Layer Spacing(Å)**	**Ref**
$RbLaTa_2O_7$	P4/mmm	a = 3.8807(6) c = 11.0852(1)	166.94	11.09	18
$(CuCl)LaTa_2O_7$	Pbam	a = 7.7663(5) b=7.7640(3) c= 11.7374(5)	707.74	11.74	18
$RbPrTa_2O_7$	P4/mmm	a = 3.884 c = 11.115	167.67	11.12	8
$(CuCl)PrTa_2O_7$	Pbam	a = 7.7362(2) b=7.7131(6) c= 11.6746(3)	696.67(3)	11.67	This work
$RbNdTa_2O_7$	P4/mmm	a = 3.846 c = 11.097	164.14	11.10	8
$CsNdTa_2O_7$	P4/mmm	a = 3.8391(2) c = 11.220(1)	165.37(2)	11.22	8
$(CuCl)NdTa_2O_7$	Pbam	a = 7.7094(5) b=7.6953(5) c= 11.6398(1)	690.54(1)	11.64	This work

Rietveld refinement was carried out on (CuCl)$LnTa_2O_7$ (Ln: Pr, Nd). Initially, P4/mmm was used as the starting model but resulted in very large R factors and large displacement parameters, especially for O3 (U_{iso} = 0.6 - 0.8 $Å^2$). The space group *Pbam*, which has been used for similar niobates, [2, 19] was then successfully applied. The Rietveld refinement data, structural model, and crystallographic data for (CuCl)$PrTa_2O_7$ are presented in Figures 5.2 and 5.3 and Table 5.2, respectively. Corresponding data for (CuCl)$NdTa_2O_7$ are presented in Appendix VII. Selected bond distances for both (CuCl)$PrTa_2O_7$ and (CuCl)$NdTa_2O_7$ are presented in Table 5.3 along with calculated bond valence sums (BVS) in Table 5.4.[20]

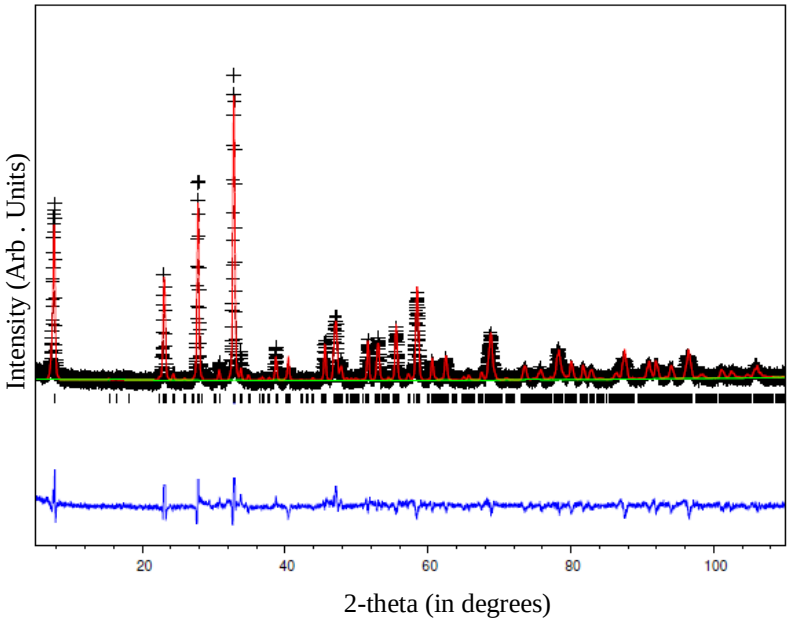

Figure 5.2. Observed and calculated data for the Rietveld refinement of (CuCl)$PrTa_2O_7$. Observed data are indicated by crosses, calculated pattern by a red solid line, and the bottom blue curve is the difference plot. Peak positions are represented by black tick marks.

Table 5.2. Crystallographic Data for $(CuCl)PrTa_2O_7$.

Atom	Site	x	y	z	g	U_{iso} ($Å^2$)
Cu	4h	0.7360(2)	0.5196(1)	0.5	0.93(2)	0.0042(4)
Cl	4h	0.5518(4)	0.2220(6)	0.5	1.09(4)	0.032(1)
Pr	4g	0.0002(3)	0.2592(5)	0	0.96(2)	0.0058(2)
Ta	8i	0.7456(1)	0.5014(3)	0.8454(3)	1.04(4)	0.0009(1)
O_1	4f	0	0.5	0.8483(3)	1	0.0032(1)
O_2	8i	0.2819(4)	0.7634(7)	0.8160(3)	1	0.0018(1)
O_3	8i	0.2290(1)	0.8880(1)	0.6433(2)	1	0.0095(3)
O_4	4g	0.7433(2)	0.5544(1)	0	1	0.0043(5)
O_5	4e	0	0	0.8766(1)	1	0.0032(7)

Pbam; Z=4; a=7.7362(2) Å, b=7.7136(5) Å, c= 11.6746(3) Å, V=696.67(3) $Å^3$; R_p=11.38%, R_{wp}= 14.53%, χ^2 =1.368

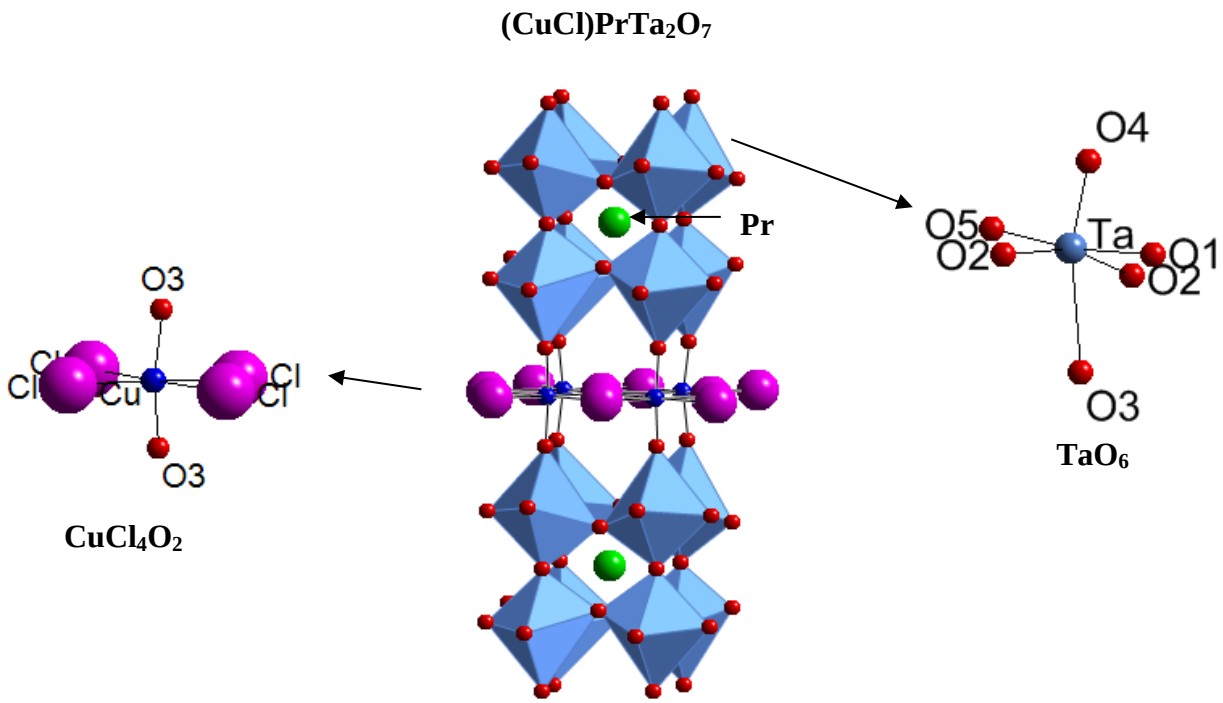

Figure 5.3. Structure of $(CuCl)PrTa_2O_7$.

Table 5.3. Selected Bond Lengths of $(CuCl)PrTa_2O_7$ and $(CuCl)NdTa_2O_7$.

$(CuCl)PrTa_2O_7$		**$(CuCl)NdTa_2O_7$**	
Bond Type	**Length (Å)**	**Bond Type**	**Length (Å)**
Cu-O3	1.8191(2) ×2	Cu-O3	1.8065(3) ×2
Cu-Cl	3.0732(6) ×1 2.9881(3) ×1 2.7023(3) ×1 2.2654(1) ×1	Cu-Cl	3.0114(2) ×1 3.0255(1) ×1 2.7386(3) ×1 2.2346(5) ×1
Pr-O1	2.6481(2) ×2	Nd-O1	2.5683(1) ×2
Pr-O2	2.7313(3) ×2 3.0670(1) ×2	Nd-O2	2.7424(3) ×2 3.0558(2) ×2
Pr-O4	3.0648(6) ×1 3.0223(2) ×1 2.4581(6) ×1 2.4507(3) ×1	Nd-O4	3.0425(1) ×1 3.0178(4) ×1 2.4596(3) ×1 2.4443(2) ×1
Pr-O5	2.4642(1) ×2	Nd-O5	2.4423(2) ×2
Ta-O1	1.9704(3) ×1	Ta-O1	1.9654(3) ×1
Ta-O2	2.0821(2) ×1 1.8682(2) ×1	Ta-O2	2.0596(3) ×2 1.8806(3) ×2
Ta-O3	2.5121(3) ×1	Ta-O3	2.5224(1) ×1
Ta-O4	1.8512(2) ×1	Ta-O4	1.8515(3) ×1
Ta-O5	1.9353(1) ×1	Ta-O5	1.9305(2) ×1

Table 5.4. Bond Valence Sums (BVS) for $(CuCl)LnTa_2O_7$ series.

$(CuCl)PrTa_2O_7$		**$(CuCl)NdTa_2O_7$**	
Cu	2.13	Cu	2.21
Pr	2.92	Nd	2.85
Ta	5.03	Ta	5.06

Electron Diffraction

Selected area electron diffraction (SAED) for $(CuCl)LnTa_2O_7$ (Figure 5.4, Figure G.4) reveal pseudo-tetragonal symmetry with superstructure reflections and lattice parameters of ≈ 8.03 Å (2 a_p × 2 a_p where a_p is the ideal perovskite cell edge ~ 4 Å), in rough agreement with refinement results.

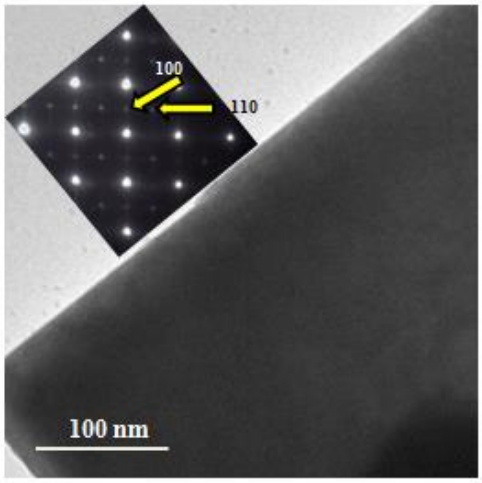

Figure 5.4. (CuCl)$PrTa_2O_7$ TEM with SAED inset (B = [001]).

Magnetism

The magnetic susceptibility of the precursors $RbPrTa_2O_7$ and $CsNdTa_2O_7$ fit well to the Curie-Weiss law showing effective magnetic moments of 3.53(2) and 3.67(2) μ_B for Pr and Nd, respectively (Appendix VII). These are in good agreement with expected values for free Pr^{3+} and Nd^{3+} ions, which are 3.57 and 3.62 μ_B, respectively.[21] (CuCl)$NdTa_2O_7$ also exhibits Curie-Weiss behavior with effective magnetic moment of μ_{eff} = 4.06(1) μ_B and Weiss constant θ_{cw} = -5.5(1) K ((Appendix VII)). While no cusp is observed in the susceptibility versus temperature curve, the Weiss constant does indicate weak antiferromagnetic interaction. In contrast, (CuCl)$PrTa_2O_7$ shows a clear antiferromagnetic transition (Figure 5.5) with a Neel temperature (T_N) of 18.11(5) K. Curie-Weiss like behavior is observed at higher temperatures where μ_{eff} = 3.87(1) μ_B with a Weiss constant of θ_{cw} = -73.8(7) K. The magnetization at 4 and 300 K ((Appendix VII)) linearly increases with applied field (H) indicating mainly an antiferromagnetic ordering of the spins.[22]

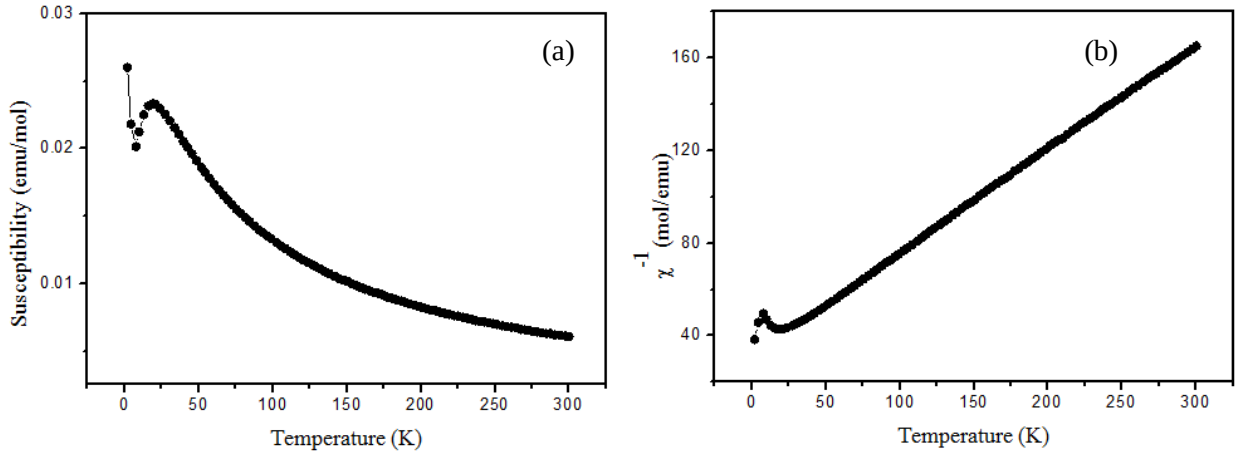

Figure 5.5. Magnetic behavior of (CuCl)$PrTa_2O_7$. (a) Temperature dependence of magnetic susceptibility of at 1000 Oe (b) Inverse susceptibility with Curie-Weiss behavior from 30 - 300 K at 1000 Oe.

Thermal Stability

Thermal analysis results obtained from (CuCl)$LnTa_2O_7$ series show decomposition of the oxy-chlorides in Ar atmosphere. (CuCl)$PrTa_2O_7$ exhibits a weight loss of 10.3 % with evolution of Cl_2 (9.93 %) which starts from 550 °C and is completed at 1000 °C (Figure 5.6). DSC shows an event at 710°C for one step decomposition to $PrTaO_4$ (Figure 5.6). (CuCl)$NdTa_2O_7$ has a weight loss of 11.43% which is related to evolution of Cl_2 (9.8 %) (Figure G.10). DSC shows a similar exothermic event at 730 °C related to decomposition and XRD confirmed that $NdTaO_4$ and $CuTaO_3$ form as byproducts. (Figure G.11)

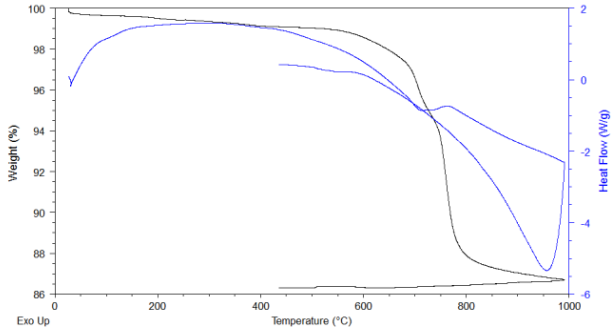

Figure 5.6. TGA-DSC of (CuCl)$PrTa_2O_7$

5.5. Discussion

Figure 5.3 shows the refined structure of (CuCl)$PrTa_2O_7$. Similar to what is seen in (CuCl)$LaNb_2O_7$,[18] copper is found to bridge between the perovskite blocks while forming an extended Cu-Cl array within the interlayer. Unit cell values (Table 5.1) for the (CuCl)$LnTa_2O_7$ series reveal a layer expansion relative to the rubidium parent of Nd (0.54 Å) to Pr (0.55 Å) to La (0.65 Å); this variation is expected based on relative sizes of the lanthanide ions (Nd^{3+} = 1.109 Å Pr^{3+} = 1.126 Å, La^{3+} = 1.16 Å for coordination number of 12) (Figure 5.7).[23] Further, decreasing the ionic size of lanthanides leads to more deviation of ideal Goldschmidt tolerance factor[24] producing more irregular TaO_6 and $CuCl_4O_2$ octahedra. Figure 5.7 highlights the distortions within the Cu-Cl layer by considering just the Cu-Cu network in the La, Pr and Nd compounds. The smaller tolerance factor for Nd relative to Pr and La leads to the greater distortion angle in the Cu-Cu-Cu linkages θ =173.35 ° for Nd versus θ = 173.86 ° for La.

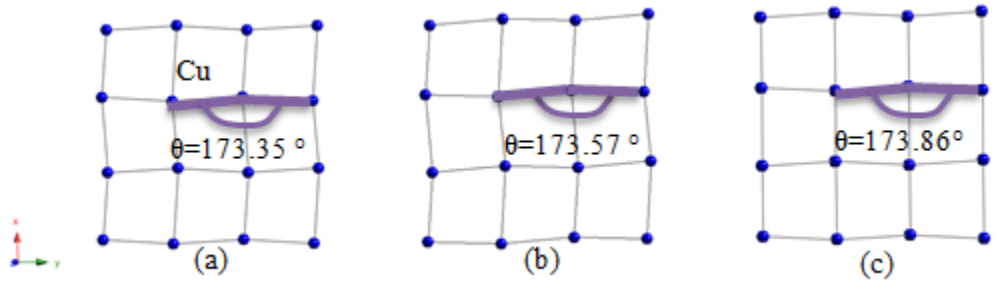

Figure 5.7. 2D Cu-Cu network for (a) $(CuCl)NdTa_2O_7$ (b) $(CuCl)PrTa_2O_7$ and (c) $(CuCl)LaTa_2O_7$ extracted from refinement.

Magnetism

Magnetic measurements on the $(CuCl)PrM_2O_7$ series exhibit strong antiferromagnetic interactions with the Weiss constant of -60.7(4) K and -73.8(7) K for M: Nb and Ta, respectively.[2] Takase et al. show in the oxy-pnictides layers of (LnO)MnAs (Ln: Pr and Nd) that the magnetic susceptibility of (PrO)MnAs[25] follows Curie-Weiss behavior similar to $(CuCl)PrM_2O_7$ (M: Nb, Ta) with antiferromagnetic transition cusp at 32 K,[2] while in the (NdO)MnAs phase, the antiferromagnetic transition shifts to lower temperatures, 23 K.[25] Similar behavior may be occurring in $(CuCl)NdTa_2O_7$ phase, but in this case the antiferromagnetic transition appears at temperatures less than 2K. No magnetic studies have been reported for $(CuCl)NdNb_2O_7$ to see if the same relative behavior is observed in the corresponding niobates.

In the $(CuCl)LnTa_2O_7$ series, momentum contribution of copper to the Nd^{3+}/Pr^{3+} compounds is similar to $(CuCl)PrNb_2O_7$.[2] The total calculated magnetic momentum of 3.99 μ_B and 3.95 μ_B obtained for Nd and Pr, respectively, from $\sqrt{\mu_{Cu}{}^2 + \mu_{Ln}{}^2}$ (Cu^{2+}: $3d^9$ s=1/2 μ_s=1.7; Nd^{3+}: $4f^3$ s=3/2, l=6 and J=9/2 g=8/11 μ_j=3.62 μ_B; Pr^{3+}: $4f^2$ s=1, l=5, J=4, g=0.8 μ_j=3.57 μ_B) are comparable to the observed values 4.06(1) and 3.87(1) for Nd and Pr. In the case of $(CuCl)PrTa_2O_7$, this is close to that observed for $(CuCl)PrNb_2O_7$ (4.020(8)).[2] $(CuCl)PrM_2O_7$ (M:

Nb, Ta) behaves as 2D antiferromagnetic with a large Curie-Weiss constant (θ_{cw}) -60.7(4) K and -73.8(7) K for Nb and Ta compounds, respectively. The magnetic interaction observed for (CuCl)$PrTa_2O_7$ is antiferromagnetic with a transition temperature T_N = 18.11(5) K as compared T_N = 19.8(1) K in (CuCl)$PrNb_2O_7$. 2D frustrated AFMs can be fit to Rushbrook and Wood's equation for the Heisenberg model: [26]

$$\chi = \frac{S(S+1)Ng^2\mu_B}{3kT}\sum_{n=0}^{6}\left((-1)^n\ \left(\frac{b_n}{\theta^n}\right)\right)$$

where N = Avogadro's number, k = Boltzmann constant, μ_B = Bohr magneton, θ = kT/J, J = exchange constant and the b_n coefficients for S=3/2 system were calculated and used from (CuCl)$PrNb_2O_7$ system.[2] Figure 5.8 represents the fit of the ZFC susceptibility to the 2D Heisenberg model. The values J/k = -3.29(2) K and g = 2.156 (1) are extracted from the fitting. Because of no difference in ZFC and FC was observed, only ZFC data are presented here. These are in good agreement with niobate phase (J/k = -3.44(2) K and g = 2.150 (3)).[2] The calculated values for J/k extracted from $\frac{kT(\chi_{\max})}{|J|S(S+1)} = 2.10(1)$ and $\frac{\chi_{\max}|J|}{Ng^2{\mu_B}^2} = 0.0539$ [27] for S = 3/2 with $T_{(\chi max)}$ = 18.11(5) K and χ_{max}= 0.23(3) (Figure 5.6a) are -2.29 K and -4.06 K, respectively. The model and the experimental results are in good agreement with the estimated exchange constant. (CuCl)$NdTa_2O_7$ shows a very small negative Weiss constant (-1.47 K) indicating a weak antiferromagnetic interaction.[28] The magnetic properties of the starting materials match well with expected values (3.62 μ_B for Nd^{3+} and 3.57 μ_B for Pr^{3+}).[21] (Figure G.5). Overall one can highlight that the (CuCl)LnM_2O_7 (Ln: La, Pr and M: Nb, Ta) compounds tend to show antiferromagnetic-like behavior.

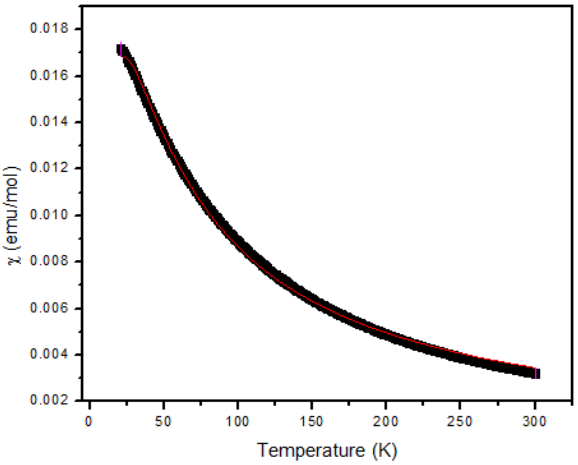

Figure 5.8. Fitting of 2D AFM Heisenberg system with S=3/2 for (CuCl)$PrTa_2O_7$ and DC susceptibility. The solid red line is the model and the black is ZFC DC susceptibility at 1000 Oe in 20-300 K.

Thermal Analysis

Thermal analysis showed that the topochemically prepared copper oxychloride phases readily decompose at elevated temperatures. On decomposition of (CuCl)$LnTa_2O_7$ (Ln: Pr, Nd), $CuTaO_3$ and $LnNbO_4$ form. (Figure G.9 and G.11) In all reactions, there is no evidence for formation of the intermediate phase of $Cu_{0.5}LnTa_2O_7$, which is different than observed for (CuCl)$LaNb_2O_7$.[29] Thermal studies on the niobate series, (CuCl)$LnNb_2O_7$ series (Ln: La, Nd and Pr), shows the decomposition products, $LnNbO_4$, form in the range of 500 - 870 °C.[29, 30] The decomposition of (CuCl)PrM_2O_7 (M: Nb, Ta)[2] and (CuCl)NdM_2O_7 are comparable, all being low temperature phases that decompose between 690 and 730°C.

5.5 References

[1] Viciu, L.; Caruntu, G.; Royant, N.; Koenig, J.; Zhou, W. L.; Kodenkandath, T. A.; Wiley, J. B. *Inorg. Chem*. **2002**, *41(13)*, 3385−3388.

[2] Montasserasadi, D.; Granier, M.; Spinu, L.; Chandra Rai, S.; Zhou, W.; Wiley, J. B., *J. Chem. Soc, Dalton Trans*. (**2015**) Accepted.

[3] Viciu, L.; Kodenkandath, T. A.; Wiley, J. B. *J. Solid State Chem*. **2007**, *180(2)*, 583-588.

[4] Choi, J.; Zhang, X.; Wiley, J. B. *Inorg. Chem*. **2009**, *48(11)*, 4811−4816.

[5] Montasserasadi, D.; Mohanty, D.; Huq, A.; Heroux, L.; Payzant, A.; Wiley, J. B, *Inorg. Chem*. **2014**, *53(3)*, 1773-1778.

[6] Ranmohotti, K. G. S.; Montasserasadi, D.; Choi, J.; Yao, Y.; Mohanty, D.; Josepha, E.; Adireddy, S.; Caruntu, G.; Wiley, J. B. *Mater. Res. Bull*. **2012**, *47(6)*, 1289−1294.

[7] Domen, K.; Kondo, J. N.; Hara, M.; Takata, T. *Bull. Chem. Soc. Jpn*. **2000**, *73(6)*, 1307−1331.

[8] Machida, M.; Yabunaka, J.; Kijima, T. *Chem. Mater*. **2000**, *12(3)*, 812-817.

[9] Yoshimura, J.; Ebina, Y.; Kondo, J,; Domen, K.; Tanaka, A. *J. Phys. Chem*. **1993**, *97*, 1970-1973.

[10] Sato, M.; Abo, J.; Jin, T.; Ohta, M. *J. Alloys Compd*. **1993**, *192(1-2)*, 81-83.

[11] Fukuoka, H.; Isami, T.; Yamanaka, S. *Chem. Lett*. **1997**, *26(8)*, 703−704.

[12] Li, B. W.; Osada, M.; Ozawa, T.C.; Sasaki, T. *Chem. Mater*. **2012**, *24*, 3111-3113.

[13] Subramanian, M.A.; Gopalakrishnan, J.; Sleight, A.W. *Mater. Res. Bull*. **1988**, *23*, 837-842.

[14] Tinga, J.; Kennedya, B. J.; Withers, R. L.; Avdeev, M. *J. Solid State Chem*. **2009**, *182*, 836-840.

[15] Laugier, J and Bochu, B. LMGP-Suite, ENSP/Laboratoire des Matériaux et du Génie Physique, BP 46. 38042, Saint Martin d'Hères, France, 2002.

[16] Larson, A. C and Von Dreele, R. B. , General Structure Analysis System (GSAS) program. Rep. No. LA-UR-86748, Los Alamos National Laboratory, Los Alamos, CA, 1994.

[17] Toby, B. H. *J. Appl. Cryst*. **2001**, *34(2)*, 210−213.

[18] Tsirlin, A. A.; Abakumov, A. M.; C. Ritter, C.; Rosner, H. *Phys. Rev. B: Condens. Matter*. **2012**, *86*, 064440.

[19] Tsirlin, A. A.; Abakumov, A. M.; Tendeloo, G. V.; Rosner, H. *Phys. Rev. B: Condens. Matter*. **2010**, *82*, 054107

[20] Brown, I. D.; Altermatt, D. *Acta Crystallogr., Sect. B: Struct. Sci*. **1985**, *41*, 244- 247.

[21] (a) O'Connor, C. *J. Prog. Inorg. Chem*., **1982**, *29,* 203-283; (b) Kittel, C. *Introduction to Solid State Physics*; 6th ed., Chapter 14; Eds.; John Wiley & Sons, Ltd: New York, 1978; pp 405.

[22] Köferstein, R. *J. Alloys Compd*. **2014**, *590*, 324-330.

[23] Shannon, R. D. *Acta Crystallogr., Sect. A: Cryst. Phys., Diffr., Theor. Gen. Cryst*. **1976**, *32(5)*, 751-767.

[24] Baszczuk, A.; Dabrowski, B.; Avdeev, M . *J. Chem. Soc, Dalton Trans*. (**2015**) Accepted.

[25] Morosawa, Y.; Naito, A.; Watanabe, T.; Takano, T.; Takase, K. *Joint European Magnetic Symposia*. **2014**, *75*, 07004.

[26] Rushbrooke, G. S.; Wood, P. *J. Mol. Phys*. **1963**, *6(4)*, 409-421.

[27] De Jongh, L. J.; Miedema, A. R. *Adv. Phys*. **1974**, *23(1)*, 1-260.

[28] Beaurepaire, E.; Scheurer, F.; Bulou, H.; Kappler, J. P.,*Magnetism: A Synchrotron Radiation Approach*, Lect. Notes Phys, Springer, Berlin Heidelberg, 2006,*697*, page 346.

[29] Hermann, A. T.; Wiley, J. B. *Mater. Res. Bull*. **2009**, *44(5)*, 1046-1050.

[30] Josepha, E. A.; Farooq, S.; Mitchell, C. M. ; Wiley, J. B. *J. Solid State Chem*. **2014**, *216* , 85-90.

Chapter 6

Conclusions

Topochemical methods such as ion exchange, reductive intercalation followed by oxidative intercalation resulted in novel double and triple layered perovskites. These compounds are not accessible by high temperature ceramic methods because they are low temperature potentially metastable phases that decompose at elevated temperatures. The prepared materials in this dissertation show a variety of interesting magnetic properties such as paramagnetism, antiferromagnetism, ferromagnetism and spin glass-like behavior. Electron diffraction technique accompanied with Rietveld refinement confirms the final structures. This chemistry has been applied to the other perovskite hosts with various compositions to obtain additional new materials with interesting magnetic properties. Here the results proved there is essential relation between the synthesis method, temperature, time of reaction, precursors and the nature of the elements utilized in this chemistry.

Appendix I

Oxidative Intercalation of $A_2Ca_2Nb_3O_{10}$

$ACa_2Nb_3O_{10}$ (A: Alkali metal)

$ACa_2Nb_3O_{10}$ (A: K, Rb, Cs) have been synthesized by solid state ceramic method and firing A_2CO_3, $CaCO_3$ and Nb_2O_5 at 850 °C for 1d and 1050 °C for1d with excess amount of A_2CO_3 (25-35 %). $ACa_2Nb_3O_{10}$ (A: Li, Na, K) have been manipulated by ion exchange of $ACa_2Nb_3O_{10}$ (A: Rb, Cs) with $A'NO_3$ (A′: Li, Na) with 10-fold molar excess at 350 °C 4 d for Li and 400 °C 7d for Na and K. Table A.1 shows the unit cell parameters for $ACa_2Nb_3O_{10}$ series. In Figure A.1, layer expansion has been seen through Li to Cs. In the case of Na because of its hygroscopic property, d-spacing is larger than K.

Table A.1. Unit cell parameters for $ACa_2Nb_3O_{10}$ series.

$ACa_2Nb_3O_{10}$	Space group	Unit cell Parameters (Å)	Volume(Å^3)	Ref
$LiCa_2Nb_3O_{10}$	$P4_22_12$	a=7.720(7) c=28.331(3)	1688.48	1
	P-1	a=5.4809(3) b=5.4804(3) c=26.5533(16) α=89.999(4) ° β=90.245(4) ° γ=89.999(5) °	797.59(8)	2
α-$NaCa_2Nb_3O_{10}$	$P4_22_12$	a=7.740(8) c=28.576(10)	1711.9	1
β-$NaCa_2Nb_3O_{10}$	$P4_22_12$	a=7.730(3) c=28.978(8)	1731.5	1
$NaCa_2Nb_3O_{10}\cdot H_2O$	$P4_22_12$	a=7.724(4) c=15.137(8)	903.1	1
$KCa_2Nb_3O_{10}$	Cmcm	a=3.8802(9) b=29.508(6) c=7.714(1)	883.2(2)	3
	P 21/m	a=7.7418(6) b=7.7073(6) c=14.859(1) , β=97.51(1) °		4
	$P4_22_12$	a=7.727(5) c=29.466(11)	1759.3	1
$RbCa_2Nb_3O_{10}$	P4/mmm	a=3.85865(6) c=14.9108(3)	222.01(1)	5
	P-42_1m, $P4_22_12$	a=7.725(2) c=14.909(5)	889.70	1
$CsCa_2Nb_3O_{10}$	Pnam	a=30.185(3) b=7.740(2) c=7.746(2)	1809.7	6
	$P4_22_12$	a=7.737(2) c=30.176(8)	1806.3	1

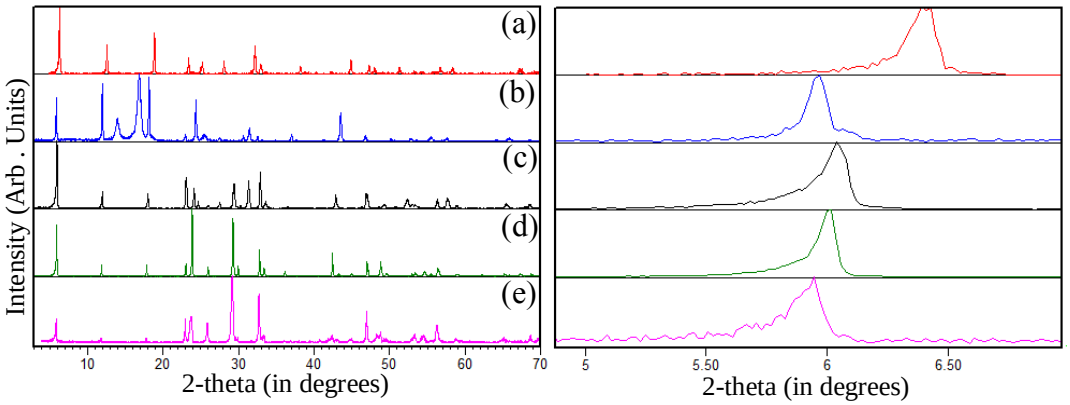

Figure A.1. XRPD patterns of (a) $LiCa_2Nb_3O_{10}$ (b) $NaCa_2Nb_3O_{10}\cdot H_2O$ (c) $KCa_2Nb_3O_{10}$ (d) $RbCa_2Nb_3O_{10}$ (e) $CsCa_2Nb_3O_{10}$.

$A_2Ca_2Nb_3O_{10}$

Reductive intercalation of $ACa_2Nb_3O_{10}$ phases with n-BuLi for Li phase with 10-fold molar excess at room temperature for 3 d and A (A: Na, K, Rb and Cs) at 310 °C, 290 °C, 250 °C and 290 °C for 7 d, respectively, to prepare $A_2Ca_2Nb_3O_{10}$ (Figure A.2). The final air sensitive products ($A_2Ca_2Nb_3O_{10}$) with dark blue color decompose to $ACa_2Nb_3O_{10}$ after expose to air. Table A.2 represents the unit cell parameters for $A_2Ca_2Nb_3O_{10}$ series.

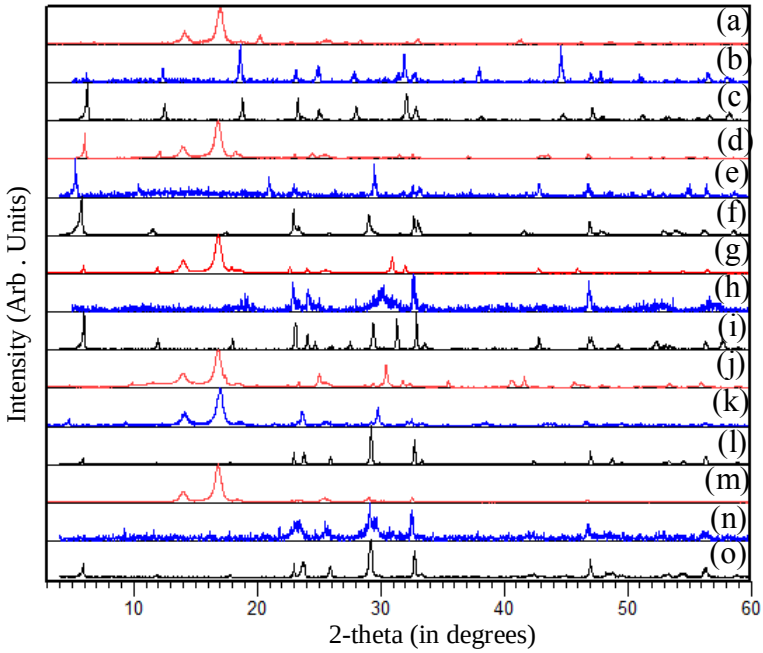

Figure A.2. XRPD patterns of (a),(b) $Li_2Ca_2Nb_3O_{10}$ with and without polymer, (c) $LiCa_2Nb_3O_{10}$, (d),(e) $Na_2Ca_2Nb_3O_{10}$ with and without polymer, (f) $NaCa_2Nb_3O_{10}$ (g) , (h) $K_2Ca_2Nb_3O_{10}$ with and without polymer, (i) $KCa_2Nb_3O_{10}$, (j) $Rb_2Ca_2Nb_3O_{10}$ with polymer, (k) $Rb_2Ca_2Nb_3O_{10}$ with polymer after 1 day, (l) $RbCa_2Nb_3O_{10}$ (m), (n) $Cs_2Ca_2Nb_3O_{10}$ with and without polymer and (o) $CsCa_2Nb_3O_{10}$.

Table A.2. Unit cell parameters for $A_2Ca_2Nb_3O_{10}$ series.

$A_2Ca_2Nb_3O_{10}$	Space group	Unit cell Parameters (Å)	Volume(Å^3)	Ref
$Li_2Ca_2Nb_3O_{10}$	P 222_1	a=13.125(7), b=5.896(4), c=4.825(4)	373.40	This work
$Na_2Ca_2Nb_3O_{10}$	P 222_1	a=14.527(4), b=3.995(1), c=3.8739(7)	224.82	This work
$K_2Ca_2Nb_3O_{10}$	P 222_1	a=14.777 (3), b=4.610(1), c=3.9470(6)	268.90	This work
$Rb_2Ca_2Nb_3O_{10}$	P4/mmm	a=3.904(1), c=15.2535(3)	232.03	This work
$Cs_2Ca_2Nb_3O_{10}$	P4/mmm	a=3.892(4), c=15.650(4)	237.07	This work

$(A_2OH)Ca_2Nb_3O_{10}$

Oxidative intercalation of $A_2Ca_2Nb_3O_{10}$ series by $CaC_2O_4{\cdot}H_2O$ resulted in $(Rb_2OH)Ca_2Nb_3O_{10}$ but not in the case of A:Li, Na, K and Cs which no reaction happened and after exposure to air, decomposed to $ACa_2Nb_3O_{10}$. Figure A.3 represents the unsuccessful oxidative intercalation in the case of K and Cs and decomposition to starting material.

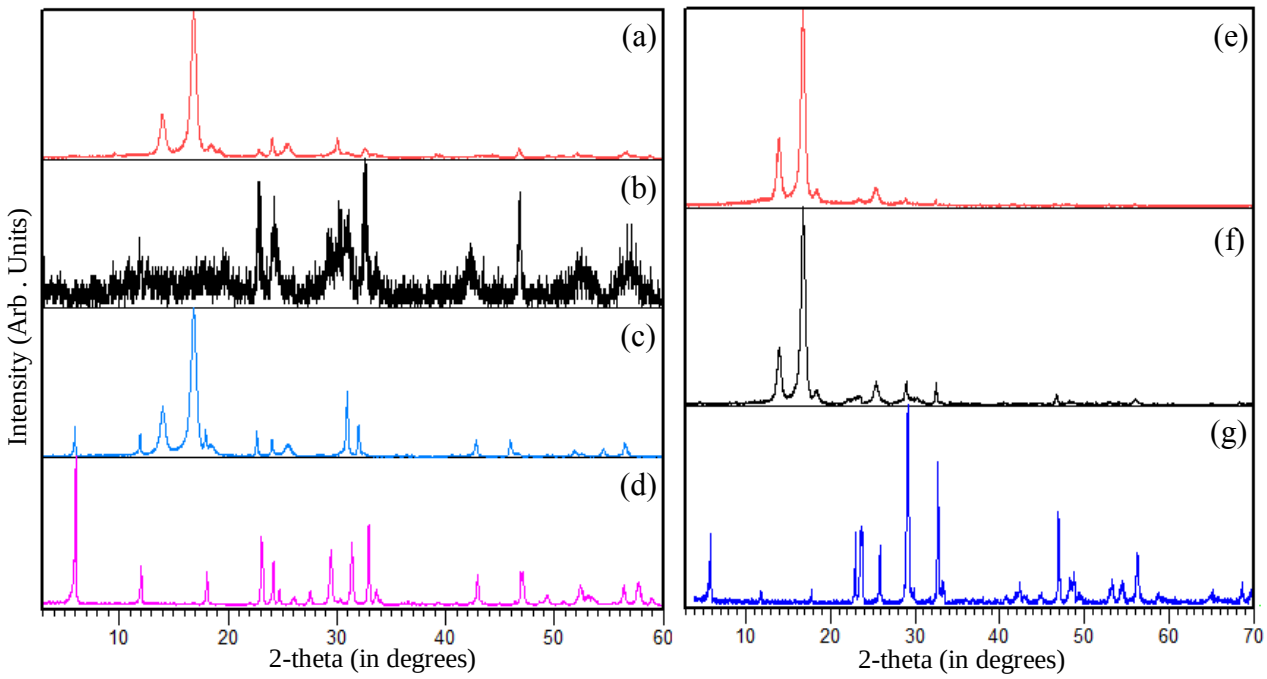

Figure A.3. XRPD pattern of (a), (b) $K_2Ca_2Nb_3O_{10}$+CaOX.H_2O with and without polymer film, (c) $K_2Ca_2Nb_3O_{10}$, (d) $KCa_2Nb_3O_{10}$, (e) $Cs_2Ca_2Nb_3O_{10}$+CaOX.H_2O, (f) $Cs_2Ca_2Nb_3O_{10}$ and (g) $CsCa_2Nb_3O_{10}$.

Morphology of $(Rb_2OH)Ca_2Nb_3O_{10}$ is shown in Figure A.4 which shows plated shape.

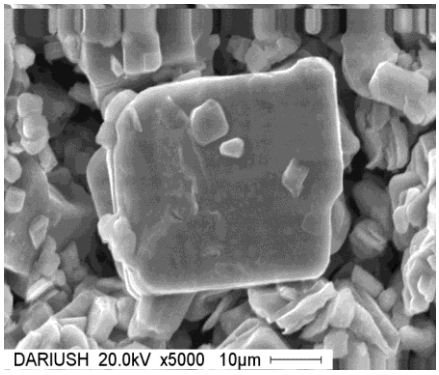

Figure A.4. SEM of $(Rb_2OH)Ca_2Nb_3O_{10}$.

References

[1] Dion, M.; Ganne, M.; Tournoux, M. *Mater. Res. Bull*. **1981**, *16(11)*, 1429-1435.

[2] Ishizawa, N.; Yamashita, R.; Oishi, S.; Hester, J. R.; Kishimoto, S. *Acta Crystallogr., Sect. C: Cryst. Struct. Commun*. **2001**, *57(5)*, 1006−1009.

[3] Fukuoka, H.; Isami, T.;Yamanaka, S. *Solid State Chem*. **2000**, *151(1)*, 40-45.

[4] Tokumitsu, T.; Toda, K.; Aoyagi, T.; Sakuraba, D.; Uematsu, K.; Sato, M. *J.Ceram. Soc. Jpn*. **2006,** *114(9)*, 795-797.

[5] Liang, Z. H.; Tang, K. B.; Chen, Q. W.; Zheng, H. G. *Acta Crystallogr*., Sect. E: Struct. Rep. Online. **2009**, *65(6)*, i44.

[6] Dion, M.; Ganne, M.; Tournoux, M.; Ravez, J. *Rev. Chim. Miner*. **1984**, *21*, 92-103.

Appendix II

Oxidative Intercalation of $Rb_2LaNb_2O_7$ for Topochemical Manipulation of $(Rb_2O_x)LaNb_2O_7$

(a) $Rb_2LaNb_2O_7 + O_2$ (g), $Rb_2LaNb_2O_7 + Ag_2O$ and $Rb_2LaNb_2O_7 + KClO_3$

The reductive intercalation of $Rb_2LaNb_2O_7$ with O_2 (g) (LB, Matheson, UHP 99.98 %,), Ag_2O (Alfa Aesar 99.99%) and $KClO_3$ (Alfa Aesar 99%) for preparation of $(Rb_2O_x)LaNb_2O_7$ have been studied.

$Rb_2LaNb_2O_7 + O_2$

$CaC_2O_4 \cdot H_2O$ has been used as oxidizing agent to synthesize $(Rb_2OH)LaNb_2O_7$, therefore O_2 as another oxidant examined. In the case of O_2, reaction was carried out at room temperature under inert atmosphere inside the glove box (Figure B.1) to avoid exposure to moisture, which decomposes all phases to staring material. The reaction also has been tried at low temperature (-10 °C) inside the refrigerator of the glove box.(first cooling the sample for 2h then flowing O_2 for 3 min).

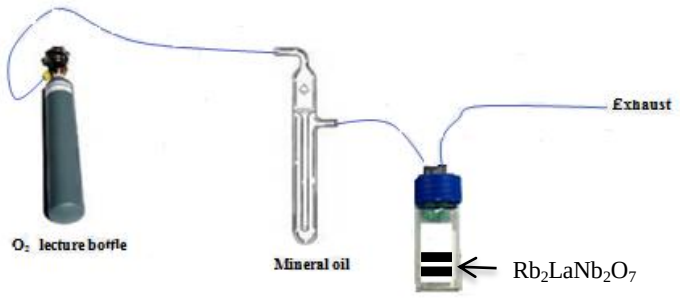

Figure B.1. Set up experiment inside the glove box.

XRPD results in all cases show evidence of $(Rb_2OH)LaNb_2O_7$ for short exposure to air then decomposition to $RbLaNb_2O_7$.

$Rb_2LaNb_2O_7$ + Ag_2O and $KClO_3$

Ag_2O and $KClO_3$ have been selected as an oxidizer because decomposition temperatures are lower than decomposition of $Rb_2LaNb_2O_7$. Ag_2O decompose to from Ag and O_2 around 197-217 °C ($Ag_2O(s) \rightarrow 2Ag(s) + ½ O_2(g)$)[1] and $KClO_3$ decompose to KCl and O_2 ($2KClO_3 \rightarrow 2KCl + 3O_2$ around 360 °C).[2] Figure B.2 represents the tube designed for oxidation intercalation in this research with temperature range of 200-300 °C 2-5 days for Ag_2O and 360-450 °C 1-3 days for $KClO_3$. Results from XRPD show in both cases similar to O_2 (lecture bottle), $(Rb_2OH)LaNb_2O_7$ after more exposure to air converts to $RbLaNb_2O_7$.

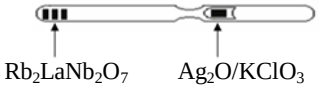

Figure B.2. Pyrex tube designed for oxidative intercalation.

(b) $Rb_2LaNb_2O_7$ +HCl(g)

$(Rb_2Cl)LaNb_2O_7$ has been prepared before by topochemical oxidative intercalation of $Rb_2LaNb_2O_7$ and Cl_2 gas.[3] Flowing of HCl (LB, Matheson, UHP 99 %) through $Rb_2LaNb_2O_7$ needs the set up like Figure B.1. The reaction carried out at very low temperature (-10 °C) and room temperature for 20-30 min. Figure B.3 shows $(Rb_2Cl)LaNb_2O_7$ as desired phase and RbCl as impurity which has been detected by XRPD.

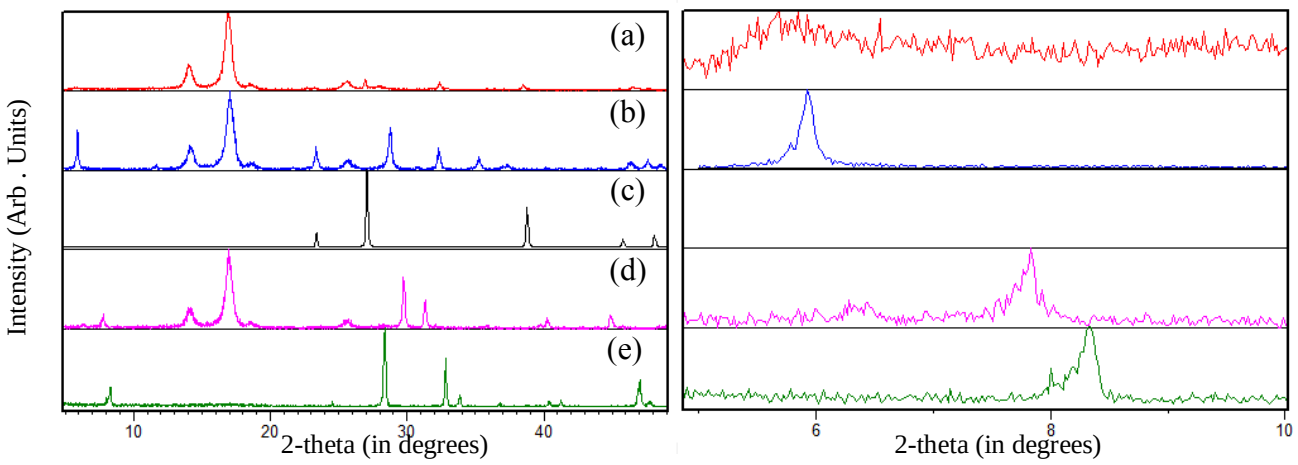

Figure B.3. XRPD pattern of (a) $Rb_2LaNb_2O_7$ + HCl with polymer film (b) $(Rb_2Cl)LaNb_2O_7$ (c) RbCl (d) $Rb_2LaNb_2O_7$ and (e) $RbLaNb_2O_7$.

(c) $Rb_2LaNb_2O_7$ + $LiAlH_4$

$LiAlH_4$ as a strong reducing agent which is also hygroscopic, decompose to H_2 (g) at two steps (a) 150-175 °C and (b) 180-220°C.[4] Figure B.2 shows the set up for this reaction. . XRPD of results from 180-240 °C for 1-2 day(s) in Figure B.4 shows evidence for $(Rb_2H)LaNb_2O_7$ which synthesized at 240 °C for 1 day with smaller unit cell compare to $(Rb_2OH)LaNb_2O_7$ (Figure B.4 d).

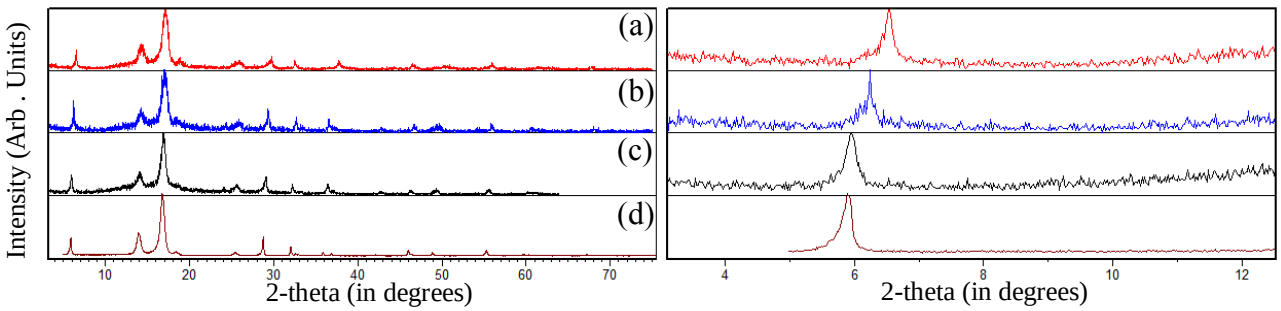

Figure B.4. XRPD pattern of (a) $Rb_2LaNb_2O_7$ + $LiAlH_4$ at 240 °C 1 day, (b) $Rb_2LaNb_2O_7$ + $LiAlH_4$ at 240 °C 1 day after 1 day with polymer film, (c) $Rb_2LaNb_2O_7$ + $LiAlH_4$ 180 °C-2 days after 2 days with polymer film and (d) $(Rb_2OH)LaNb_2O_7$.

The Rietveld refinement on only one sample at 240 °C for 1 d has been done (GSAS) and although the quality of XRPD is not perfect but it shows expansion of unit cell more than $Rb_2LaNb_2O_7$ but less than $(Rb_2OH)LaNb_2O_7$. The crystallographic structure, atomic positions and bond length for $(Rb_2H)LaNb_2O_7$ extracted from refinement for one sample are presented in Figure B.5 and Table B.1 and Table B.2.

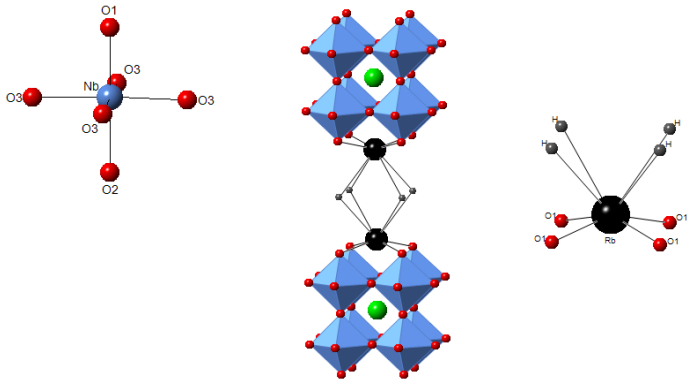

Figure B.5. Crystal structure of $(Rb_2H)LaNb_2O_7$.(Key: La: medium green spheres; oxygen: small red; NbO_6 octahedra: light blue; Cs: large dark purple; H: small gray)

Table B.1. Crystallographic Data for $(Rb_2H)LaNb_2O_7$ from X-ray data.

Atom	Site	x	y	z	$U_{iso}(Å^2)$	g
Rb	2g	0	0	0.306(5)	0.024(4)	1
H	1d	0.5	0.5	0.5	0.09(3)	1
La	1a	0	0	0	0.08(6)	1
Nb	2h	0.5	0.5	0.135(6)	0.01(1)	1
O_1	2h	0.5	0.5	0.26(2)	0.02(2)	1
O_2	1c	0.5	0.5	0	0.01(5)	1
O_3	4i	0	0.5	0.13(2)	0.003(4)	1

*P*4/*mmm*; Z=1,a = 3.897(2) Å, c =14.275(2) Å, Volume = 216.7(2) $Å^3$

R_p = 14.42%, R_{wp} = 15.31%, χ^2= 1.771, and g = occupation factor

Table B.2. Selected bond lengths for $(Rb_2H)LaNb_2O_7$.

Bond Type	**Length (Å)**
Rb-H ×4	3.9063(3)
Rb-O_1 ×4	2.835(8)
Nb-O_1 ×1	1.793(1)
Nb-O_2 ×1	1.934(1)
Nb-O_3 ×4	1.949(8)
La-O_2 ×4	2.7556(1)
La-O_3 ×8	2.716(2)

(d) $Rb_2LaNb_2O_7$ + NH_3 (g)

Anhydrous ammonia gas as a nitro-hydride source has been used for oxidative intercalation of $Rb_2LaNb_2O_7$ with NH_2^-, NH^{2-} or N^{3-} for desire products: $(Rb_2NH_x)LaNb_2O_7$ (x=0, 1, 2). Anhydrous ammonia (LB, Matheson, 99.99%) flew from very low temperature (-10 °C) to 210 °C for 5-20 min, (Figure B.1) but the XRPD results in all cases confirm $(Rb_2OH)LaNb_2O_7$ phase.

References

[1] Shahcheraghi, S. H.; Khayati, G. R. *Trans. Nonferrous Met. Soc. China*. **2014**, *24(9)*, 2991−3000.

[2] Liao, L. Q.; Yan, Q. L.; Zheng, Y.; Song, Z.W.; Li, J. Q.; Liu, P. *Indian J. Eng. Mater. Sci*. **2011**, *18*, 393-398.

[3] Choi, J.; Zhang, X.; Wiley, J. B. *Inorg. Chem*. **2009**, *48(11)*, 4811−4816.

[4] Ares, J. R.; Aguey-Zinsou, K. F.; Porcu, M.; Sykes, J. M.; Dornheim, M.; Klassen, T.; Bormann, R., *Mater. Res. Bull*. **2008**, *43(5)*, 1263−1275.

Appendix III

Oxidative Intercalation of $A_2LaNb_2O_7$ with S_8, Se and Te powder.

S_8, Se (99.999% Alfa Aesar) and Te (99.99% Alfa Aesar) powders as Other source of chalcogenides have been used for oxidative intercalation of $A_2LaNb_2O_7$ (A: K, Rb and Cs) but the results have shown no reaction and $A_2LaNb_2O_7$ is left over and after exposure to air, $(A_2OH)LaNb_2O_7$ and then decompose to $ALaNb_2O_7$. (Figure C.1, C.2, C.3)

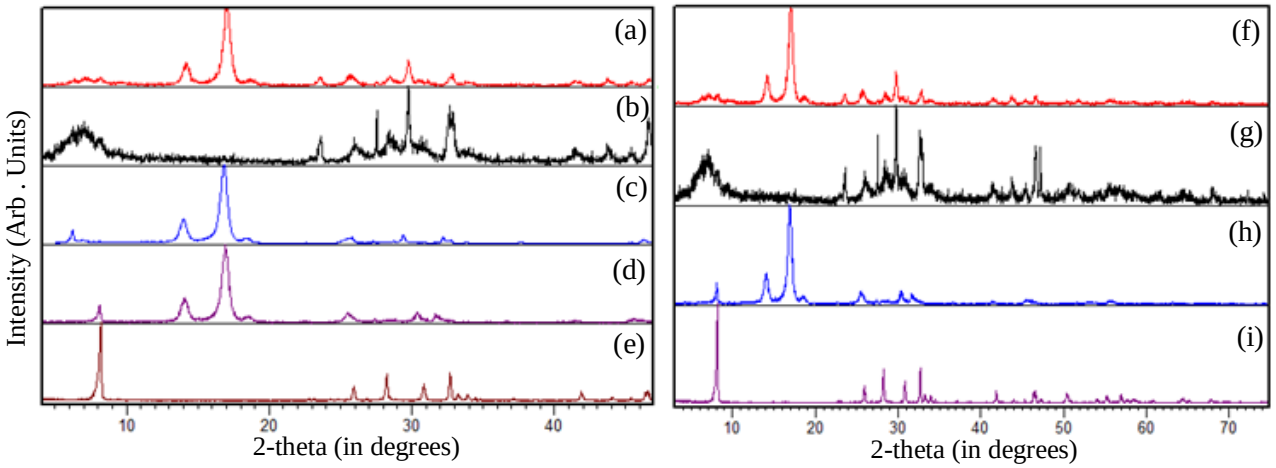

Figure C.1. (a) $K_2LaNb_2O_7$+Se with polymer, (b) after 2h expose to air without polymer, (c) $(K_2OH)LaNb_2O_7$,(d) $K_2LaNb_2O_7$, (e) $KLaNb_2O_7$, (f) $K_2LaNb_2O_7$+Te with polymer, (g) after 2h expose to air without polymer, (h) $K_2LaNb_2O_7$ and (i) $KLaNb_2O_7$.

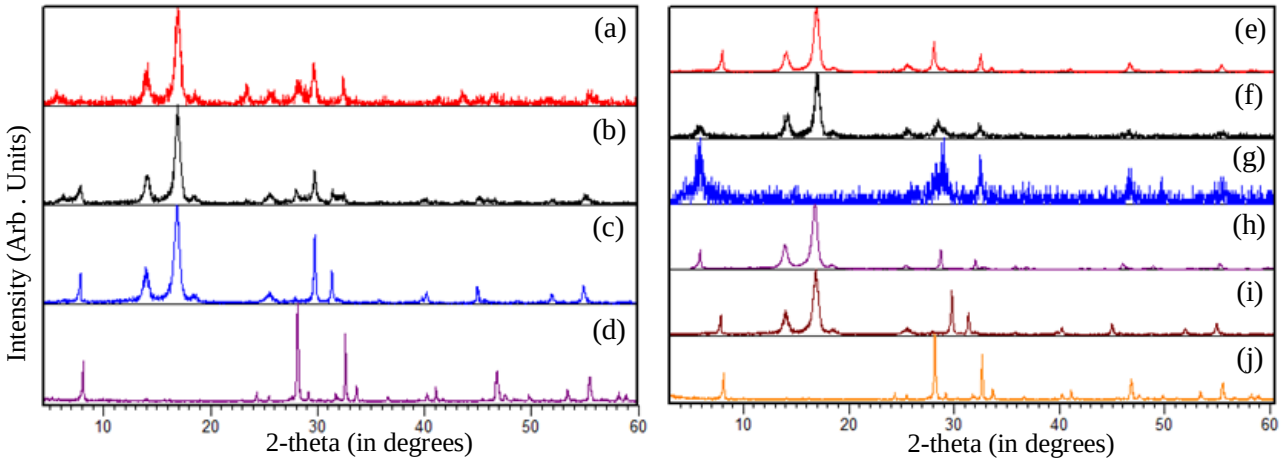

Figure C.2. (a) $Rb_2LaNb_2O_7$+Se at 50 °C 8 days with polymer, (b) after 2h expose to air, (c) $Rb_2LaNb_2O_7$, (d) $RbLaNb_2O_7$, (e) $Rb_2LaNb_2O_7$+Te 80-425 °C 2-7 days with polymer, (f) after 2h expose to air with polymer , (g) without polymer, (h) $(Rb_2OH)LaNb_2O_7$, (i) $Rb_2LaNb_2O_7$ and (j) $RbLaNb_2O_7$.

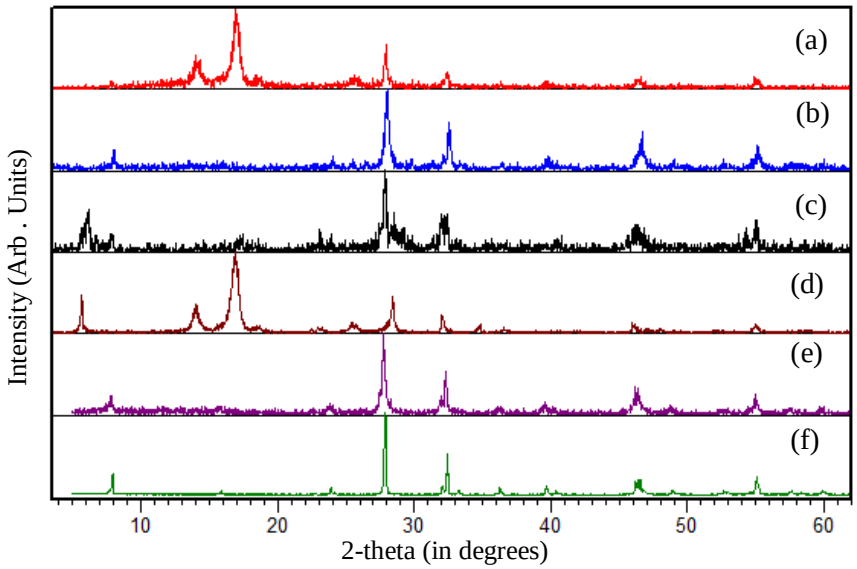

Figure C.3. (a) $Cs_2LaNb_2O_7$+Te 180 °C 1 day with polymer, (b) without polymer, (c) without polymer after 2h, (d) $(Cs_2OH)LaNb_2O_7$, (e) $Cs_2LaNb_2O_7$ and (f) $CsLaNb_2O_7$.

No oxidative intercalation reaction occurs between $A_2Ca_2Nb_3O_{10}$ (A: Na, K) and S_8 and the precursors after exposure to air decompose to $ACa_2Nb_3O_{10}$. (Figure C.4)

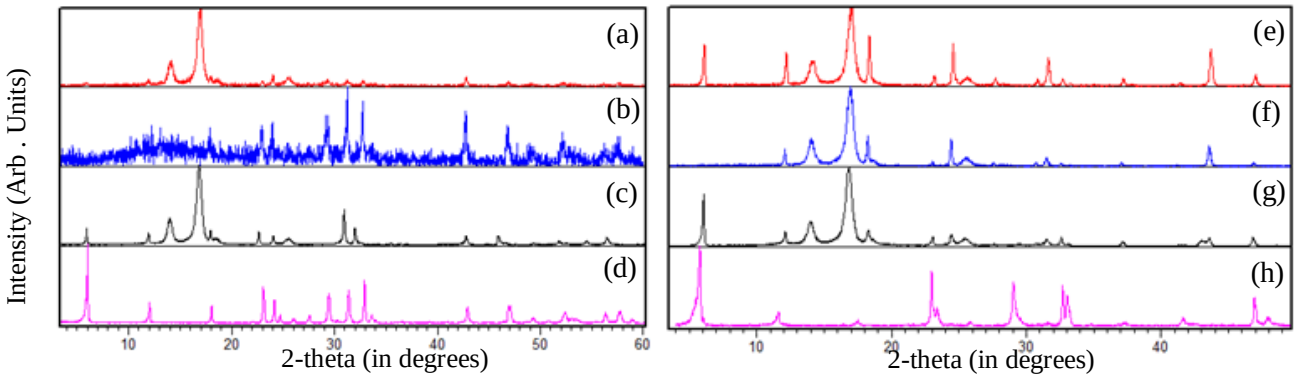

Figure C.4. (a) $K_2Ca_2Nb_3O_{10}+S_8$ with polymer, (b) $K_2Ca_2Nb_3O_{10}+S_8$ without polymer, (c) $K_2Ca_2Nb_3O_{10}$ (d) $KCa_2Nb_3O_{10}$, (e) $Na_2Ca_2Nb_3O_{10}+S_8$ 300 °C 13 days, (f) $Na_2Ca_2Nb_3O_{10}+S_8$ 400 °C 13 days, (g) $Na_2Ca_2Nb_3O_{10}$ and (h) $NaCa_2Nb_3O_{10}$.

Appendix IV

Oxidative Intercalation of $A_2Ca_2Nb_3O_{10}$ (A: Li, Na, K and Cs) with H_2Ch (Ch: Se and Te)

Triple layered perovskites $A_2Ca_2Nb_3O_{10}$ reacted with H_2S produced by injecting HCl to the Na_2S vial (Figure D.1) which results show no reaction and after expose to air $(A_2OH)Ca_2Nb_3O_{10}$ (A: Na) and then $ACa_2Nb_3O_{10}$ (A: Li, K and Cs)) phase. (Figures D.2 and D.3).

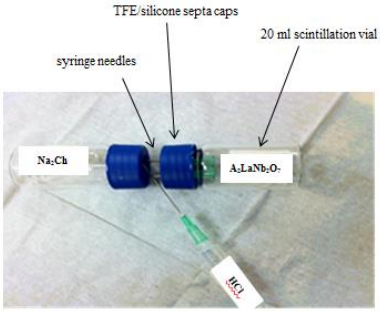

Figure D.1. Set up experiment for chalcogenide oxidative intercalation

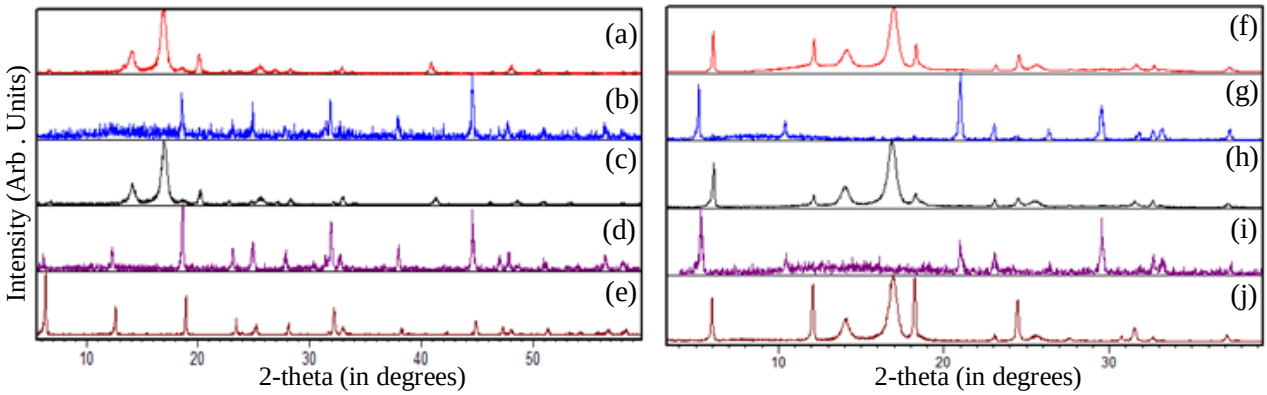

Figure D.2. (a) $Li_2Ca_2Nb_3O_{10}$+H_2S with polymer film, (b) $Li_2Ca_2Nb_3O_{10}$+H_2S without polymer film, (c) $Li_2Ca_2Nb_3O_{10}$ with polymer film, (d) $Li_2Ca_2Nb_3O_{10}$ without polymer film, (e) $LiCa_2Nb_3O_{10}$, (f) $Na_2Ca_2Nb_3O_{10}$+H_2S with polymer film, (g) $Na_2Ca_2Nb_3O_{10}$ + H_2S without polymer film, (h) $Na_2Ca_2Nb_3O_{10}$ with polymer film, (i) $Na_2Ca_2Nb_3O_{10}$ without polymer film and (j) $NaCa_2Nb_3O_{10}$.

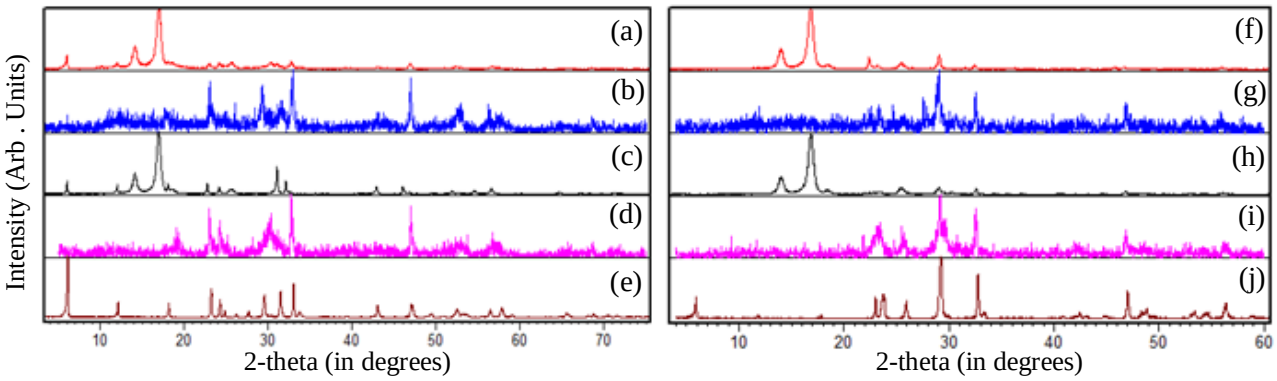

Figure D.3. (a) $K_2Ca_2Nb_3O_{10}$ + H_2S with polymer film, (b) $K_2Ca_2Nb_3O_{10}$ + H_2S without polymer film, (c) $K_2Ca_2Nb_3O_{10}$ with polymer film, (d) $K_2Ca_2Nb_3O_{10}$ without polymer film, (e) $KCa_2Nb_3O_{10}$, (f) $Cs_2Ca_2Nb_3O_{10}$ + H_2S with polymer film, (g) $Cs_2Ca_2Nb_3O_{10}$ + H_2S without polymer film, (h) $Cs_2Ca_2Nb_3O_{10}$ with polymer film, (i) $Cs_2Ca_2Nb_3O_{10}$ without polymer film and (j) $CsCa_2Nb_3O_{10}$.

Appendix V

Characterization of $APrNb_2O_7$ (A: Rb, Cs and CuCl)

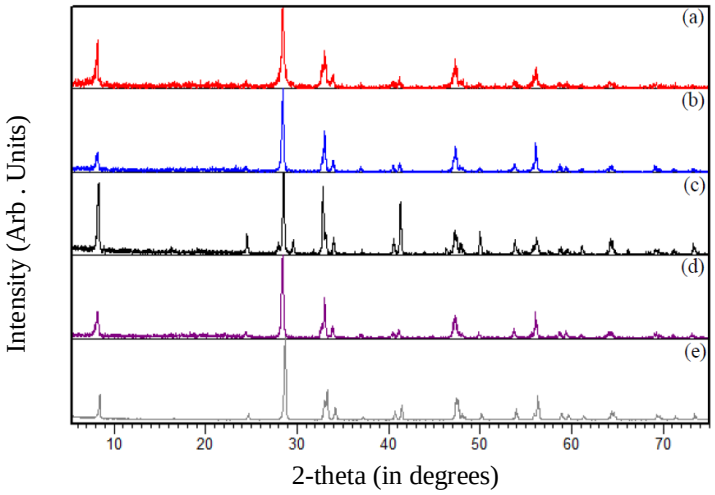

Figure E.1. XRDs of $RbPrNb_2O_7$ prepared from molten salt RbCl and from Pr_2O_3 and O_2. (a-c) ½ Rb_2CO_3 : 1/6 Pr_6O_{11} : Nb_2O_5 : 5 RbCl -temperature 1050 °C 2hrs -temperature 1060 °C 2 hrs -temperature 1200°C 2 hrs, (d) ½ Rb_2CO_3: ½ Pr_2O_3 : Nb_2O_5 + O_2 temperature 1000 °C 6.5hrs and (e) ½ Rb_2CO_3: 1/6 Pr_6O_{11}: Nb_2O_5 temperature 1100 °C 2 days.

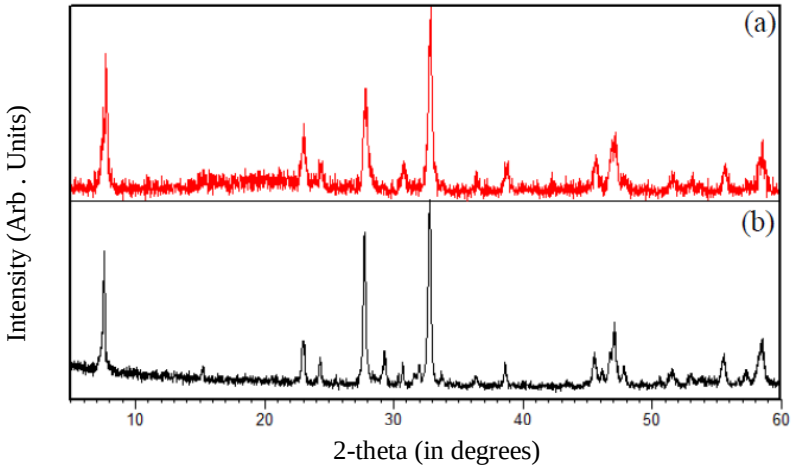

Figure E.2. The XRPD pattern of $(CuCl)PrNb_2O_7$ which has been prepared from (a) $RbPrNb_2O_7$ at 325 °C for 7 days and (b) $CsPrNb_2O_7$ 340 °C for 7 days.

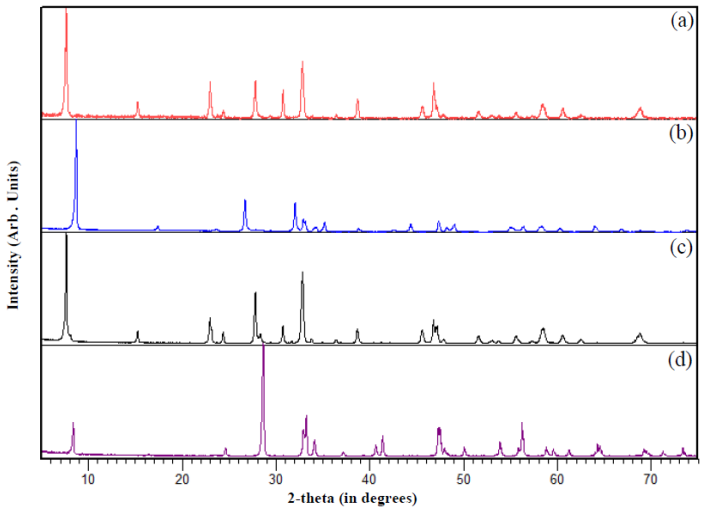

Figure E.3. XRD (CuCl)$PrNb_2O_7$ prepared from $LiPrNb_2O_7$ and $CuCl_2$. (a) (CuCl)$PrNb_2O_7$ ($LiPrNb_2O_7$:$CuCl_2$ 1:2) at 300 °C, 4 days, (b) $LiPrNb_2O_7$, (c) (CuCl)$PrNb_2O_7$ prepared from $RbPrNb_2O_7$ 355 °C 7 days and (d) $RbPrNb_2O_7$.

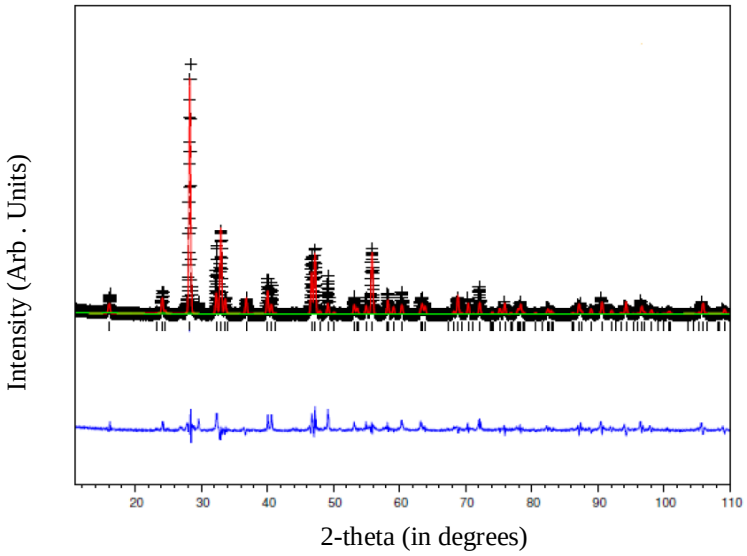

Figure E.4. Observed and calculated data for the Rietveld refinement of $CsPrNb_2O_7$ in *P*4/*mmm* space group. Observed data is indicated by crosses, calculated pattern by a (red) solid line, and the bottom (blue) curve is the difference plot. Peak positions are presented as black tic marks. (Z=1; R_p=13.17% R_{wp}= 12.26%; χ^2 = 1.837.)

Table E.1. Crystallographic Data for $CsPrNb_2O_7$.

Atom	Site	x	y	z	g	U_{iso} (Å^2)
Cs	1b	0	0	0.5	1.09(8)	0.023(1)
Pr	1a	0	0	0	1.01(9)	0.012(1)
Nb	2h	0.5	0.5	0.2014(1)	1.03(9)	0.011(3)
O_1	4i	0	0.5	0.1671	1	0.005(5)
O_2	2h	0.5	0.5	0.3692	1	0.01(2)
O_3	1c	0.5	0.5	0	1	0.08(2)

P4/mmm; Z=1; R_p=13.17% R_{wp}= 12.26% and χ^2 = 1.837, a = 3.8668(2), c = 11.163(1) V = 166.92(2) Å^3

Table E.2. Bond valence sum results for $CsLaNb_2O_7$ and $CsPrNb_2O_7$.

$CsLaNb_2O_7$		**$CsPrNb_2O_7$**	
Cs	0.9876	Cs	1.0529
La	2.8808	Pr	3.0805
Nb	5.2305	Nb	5.2374

Table E.3. Selected Bond Lengths Extracted from the Refined Structure of $CsPrNb_2O_7$ versus $CsLaNb_2O_7$.

$CsLaNb_2O_7$		**$CsPrNb_2O_7$**	
Bond Type	**Length (Å)**	**Bond Type**	**Length (Å)**
Cs-O2 × 8	3.191(4)	Cs-O2 × 8	3.1673(9)
La-O1 × 8	2.672(4)	Pr-O1 × 8	2.6021(1)
La-O3 × 4	2.763(1)	Pr-O3 × 4	2.73427(1)
Nb-O1 × 4	1.999(1)	Nb-O1 × 4	1.9987(6)
Nb-O2 × 1	1.736(7)	Nb-O2 × 1	1.7350(1)
Nb-O3 × 1	2.248(1)	Nb-O3 × 1	2.2481(1)

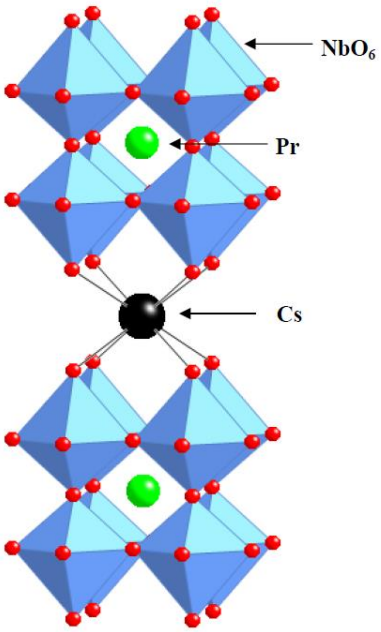

Figure E.5. Crystal structure for $CsPrNb_2O_7$.

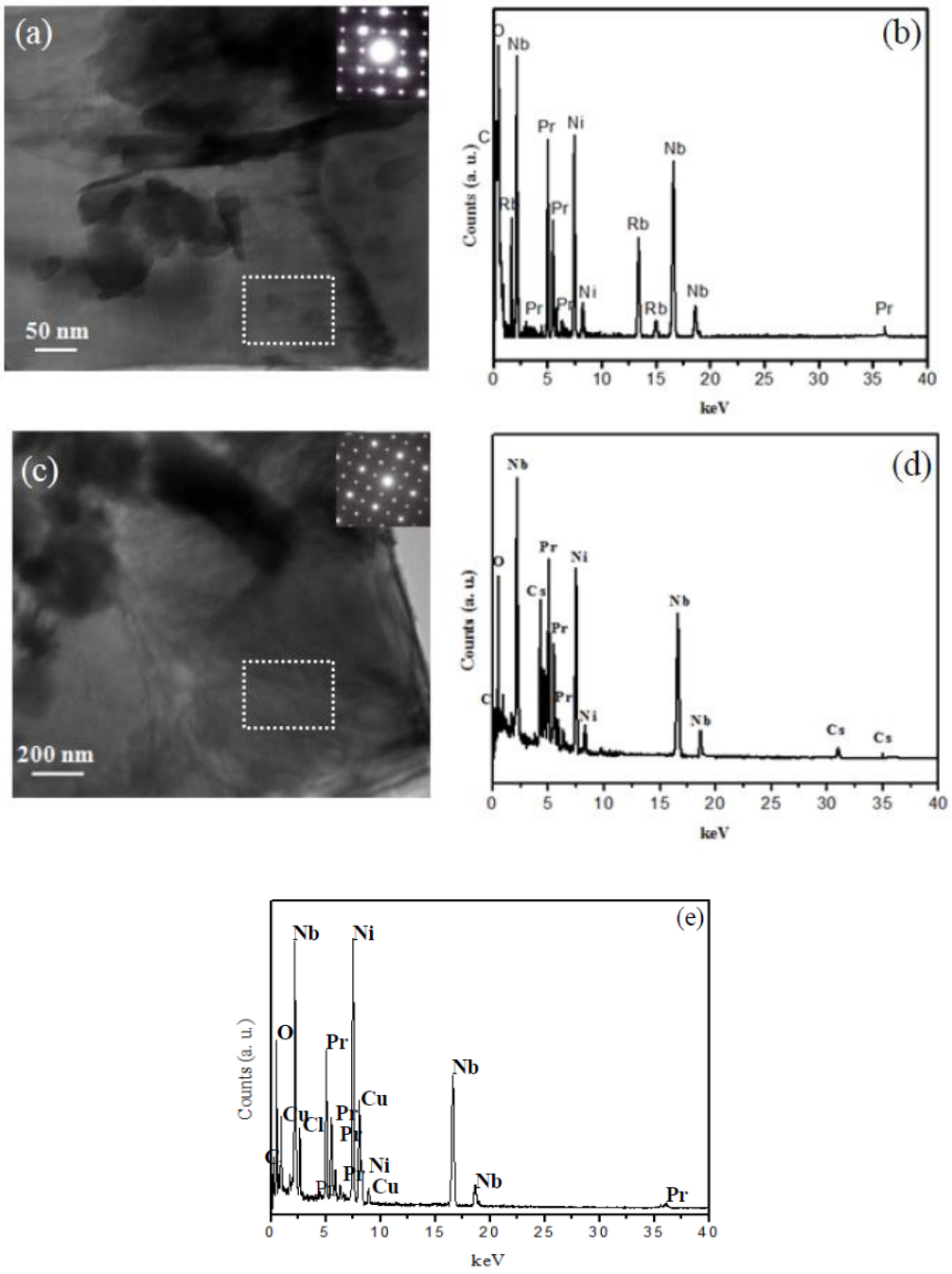

Figure E.6. TEM image, SAED and elemental analysis of (a,b) $CsPrNb_2O_7$, (c,d) $RbPrNb_2O_7$, and (e) elemental analysis of $(CuCl)PrNb_2O_7$.

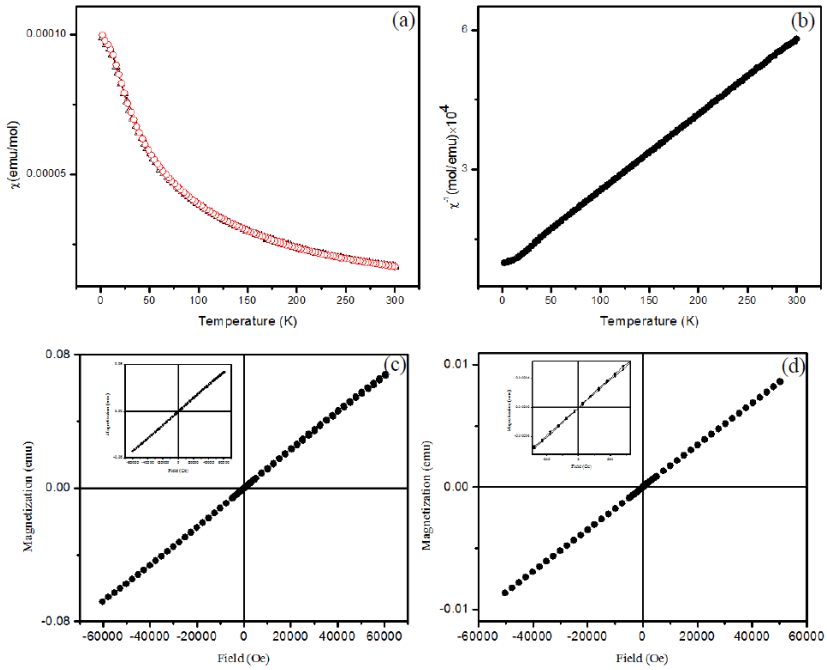

Figure E.7. (a) Temperature dependence of magnetic susceptibility and (b) reverse susceptibility of $CsPrNb_2O_7$. Measurements were carried out on cooling at a constant field of 100 Oe. (red circle shows FC and occluded black triangle shows ZFC). The magnetization vs the magnetic field for $CsPrNb_2O_7$ at (c) 2 K and (d) 300 K.

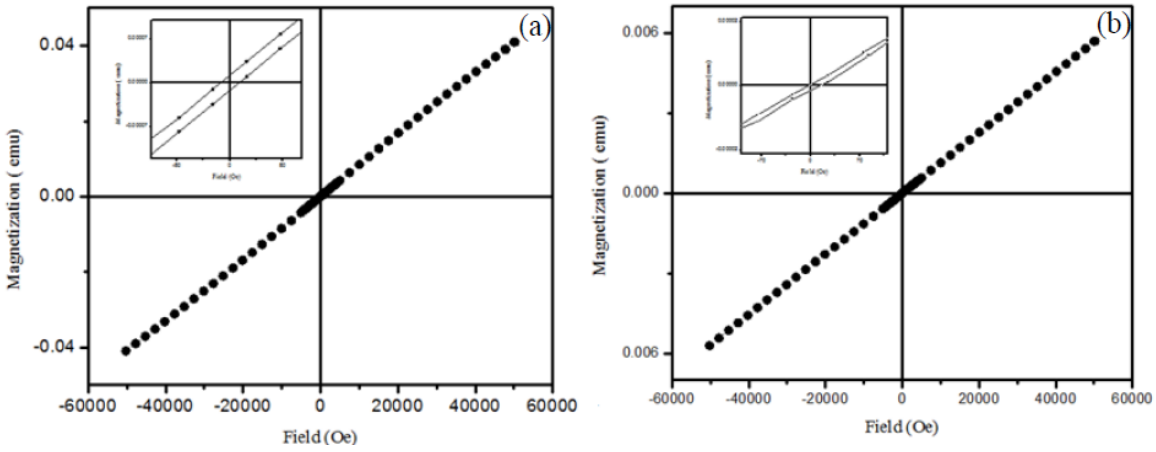

Figure E.8. The magnetization vs the magnetic field for $RbPrNb_2O_7$ at (a) 4K and (b) 300 K.

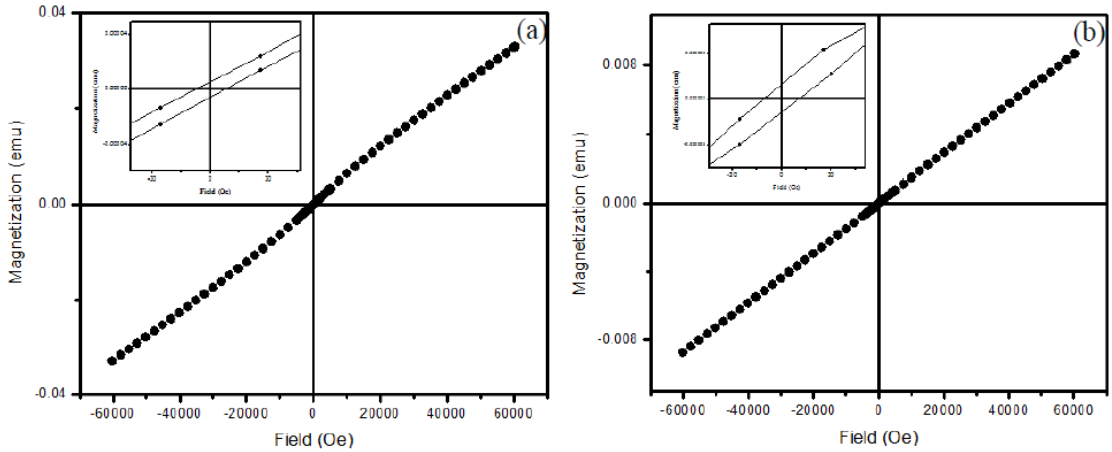

Figure E.9. The magnetization versus magnetic field for (CuCl)$PrNb_2O_7$ at (a) 2 K (inset shows slight hysteresis of 15 Oe) and (b) 300 K (inset, hysteresis of 40 Oe).

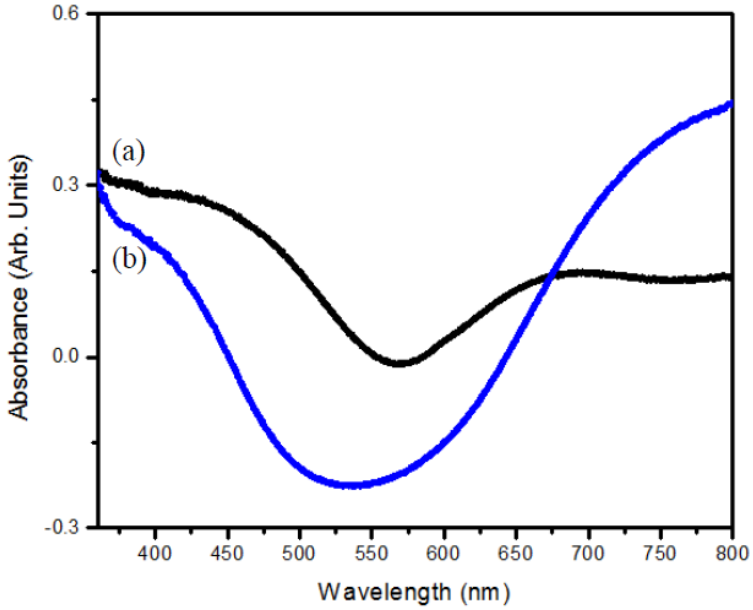

Figure E.10. UV-Vis spectra of the (a) $CuCl_2 \cdot 2H_2O$ and (b) (CuCl)$PrNb_2O_7$.

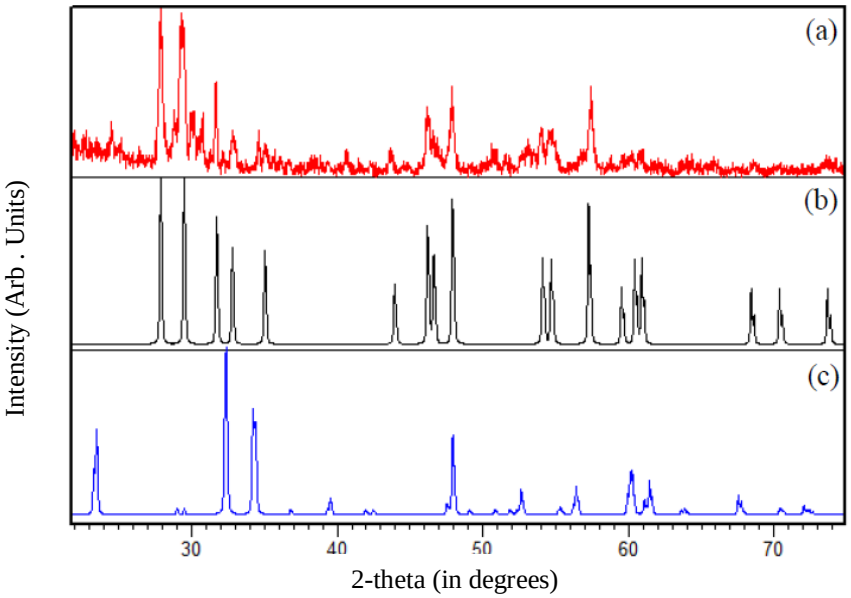

Figure E.11. XRD of (CuCl)$PrNb_2O_7$ after TGA/DTA (a) at 1000 °C, (b) $PrNbO_4$ and (c) $CuNbO_3$.

Appendix VI

Synthesis of $ABiNb_2O_7$ (A: Rb and CuCl) Layered Perovskites

Abstract

$RbBiNb_2O_7$ has been prepared with molten salt method then undergo ion exchange under Topochemical condition, $(CuCl)BiNb_2O_7$ has been manipulated and characterized: P4/mmm a=3.8029(6)Å, c= 11.901(2)Å. Magnetic studies showed the material exhibits ferromagnetism. This phase decompose to $CuBi_xNb_yO_7$ at 1000 °C.

Introduction

Ion exchange at low temperature can lead to construction of layers at interlayer site of layered perovskites such as Dion-Jacobson $A[A'_{n-1}B_nO_{3n+1}]$ Ruddlesden-Popper $A_2[A'_{n-1}B_nO_{3n+1}]$ and Aurivillius $(Bi_2O_2)[A'_{n-1}B_nO_{3n+1}]$.[1] The charge to radii ratio and the nature of A, A′, B and the number of perovskite slabs (n) can affect the final product with a wide range of properties: photocatalytic activity,[2] ionic conductivity,[3] superconductivity,[4] photoluminescence,[5] and ferroelectrics.[6] In this work, $ABiNb_2O_7$ as a ferroelectric precursor has been used to build a new layered perovskite by topochemical ion exchange with interesting magnetic property.

Experimental

$ABiNb_2O_7$ (A: Rb, Cs)

25-30 % Excess amount of A_2CO_3 (Rb_2CO_3 Alfa Aesar 99.8%, Cs_2CO_3 Alfa Aesar 99.994%) and stoichiometric amount of Bi_2O_3 (Alfa Aesar 99.99%) and Nb_2O_5 (Alfa Aesar 99.9985%)

were grinded together and calcinated for 24 h at 1000 °C.[7] $RbBiNb_2O_7$ also will be synthesized by flux method by grinding Rb_2CO_3, Bi_2O_3, Nb_2O_5 and RbCl (Alfa Aesar 99.98%) with 1:1:2:10 molar ratio and firing at 1100 °c for 2 h.

$(CuCl)BiNb_2O_7$

$ABiNb_2O_7$ add to 2-fold molar excess of $CuCl_2$ (Alfa Aesar 99.995 %) in the argon-filled glove box and then the mixture was pelletized by hand press and sealed in a Pyrex tube under vacuum and heated: $CsBiNb_2O_7$ with $CuCl_2$ at 340 °C for 14 days resulted in $(CuCl)BiNb_2O_7$ but the products of $RbBiNb_2O_7$ and $CuCl_2$ would be starting material ($RbBiNb_2O_7$) and BiOCl as a byproduct.[8] $(CuCl)BiNb_2O_7$ also will be synthesized from $RbBiNb_2O_7$ by: (a) using molten salt ($LiNO_3$) to synthesize $LiBiNb_2O_7$ then with $CuCl_2$ at 325 °C for 7 days (b) using molten salt ($CuCl_2$/KCl) with this molar ratio $RbBiNb_2O_7$:$CuCl_2$:KCl 1:85:85 at 400 °C for 7 days.[9] (Figure F.1).

Characterization

X-ray Powder diffraction (XRPD) data were collected on a Philips X'Pert system equipped with Cu Kα radiation (λ = 1.5418 Å) and a curved graphite monochromator. Typical scans were collected in continuous mode with a scan rate of 0.02 °/s. The peak positions and lattice parameters were refined by a least-squares method with program; ChekCell [10] Crystal structures were refined by the Rietveld method with the GSAS software package.[11, 12] Transmission electron microscopy (TEM) and selected area electron diffraction (SAED) was performed on a JEM 2010 operated at 200 kV. The samples were prepared by crushing them in ethanol, and then ethanol suspensions of the samples were drop-cast on Ni-TEM grids (Ted Pella). Elemental analysis was carried out by energy dispersive spectroscopy (EDS) on TEM.

The thermal behavior of the products was studied by TGA/DSC using a TA Instruments Q600 TGA-DSC system over the temperature range 25-1000 °C with a ramp of 10 °C/min in flowing Ar atmosphere. Magnetic Susceptibility measurements were performed on a superconducting quantum interference device (SQUID) magnetometer (Quantum Design, MPMS-7) in the temperature range 2-300 K in different magnetic fields up to 6T. Magnetic susceptibility measurements were carried out in zero field cooled (ZFC) and field cooled (FC) conditions. The P-E loops were recorded by Precision High-Voltage Interface RADIANT (HVI) attached to Precision Premier II Precision Materials Analyzer and Trek model 609B measurements of up to ±10,000 Volts can be made. For $ABiNb_2O_7$ (A: Rb, Cs and CuCl) series, pellets have been made with surface area 1.31 cm^2 and thickness 800 μm for Rb, 0.45 cm^2 and 1800 μm for Cs and 0.4071 cm^2 and 1770 μm for CuCl.

Results

Synthesis

High temperature ceramic method followed by Ion exchange reaction resulted in:

$$A_2CO_3 + Bi_2O_3 + Nb_2O_5 \rightarrow 2ABiNb_2O_7 + CO_2\,(g)$$

$$ABiNb_2O_7 + CuCl_2 \rightarrow (CuCl)BiNb_2O_7 + ACl$$

Diffraction Studies

X-ray powder diffraction patterns for $RbBiNb_2O_7$ is presented in Figure F.1a shows at 1000 °C still is evidence for impurity. $ABiTa_2O_7$ phase is not accessible and confirm $A_{3.2}Bi_{6.4}Ta_{16}O_{51.2}$ is the stable phase. (Figure F.2) $(CuCl)BiNb_2O_7$ has been prepared from (a) $RbBiNb_2O_7$ and molten salt ($CuCl_2$/KCl), (b) $CsBiNb_2O_7$ and ion exchange with $CuCl_2$ and (c) $LiBiNb_2O_7$ which

synthesized by ion exchange with $LiNO_3$ then followed by ion exchange with $CuCl_2$ are shown in Figure F.3.

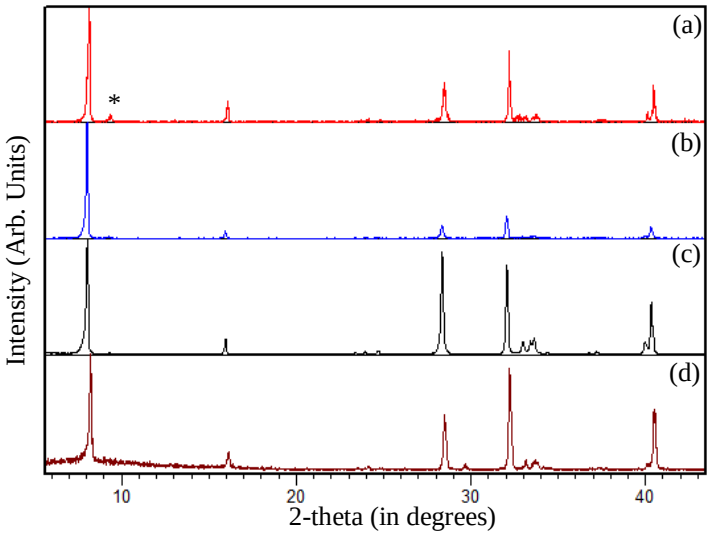

Figure F.1. XRPD of $RbBiNb_2O_7$ synthesized by ceramic method (a) 1000 °C -1d (b) 1000 °C -2d (c) 1100 °C -2d and molten salt (d) Rb_2CO_3:Bi_2O_3:Nb_2O_5:RbCl 0.5:0.5:1:5 molar ratio 1100 °C -2hr. * shows $BiNbO_4$ as impurity.

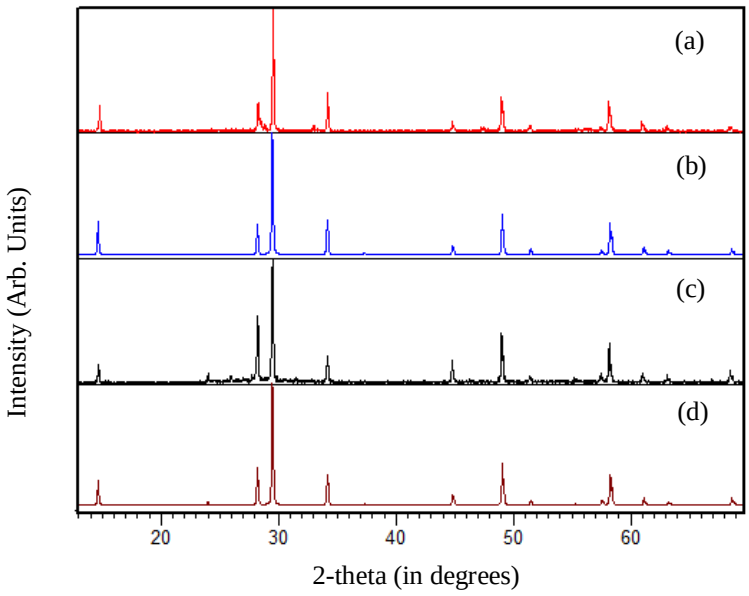

Figure F.2. XRPD reaction of (a) Rb_2CO_3, Bi_2O_3 and Ta_2O_5 1000 °C -1d (b) $Rb_{3.2}Bi_{6.4}Ta_{16}O_{51.2}$ (c) Cs_2CO_3, Bi_2O_3 and Ta_2O_5 1000 °C -1d and (d) $Cs_{3.2}Bi_{6.4}Ta_{16}O_{51.2}$.

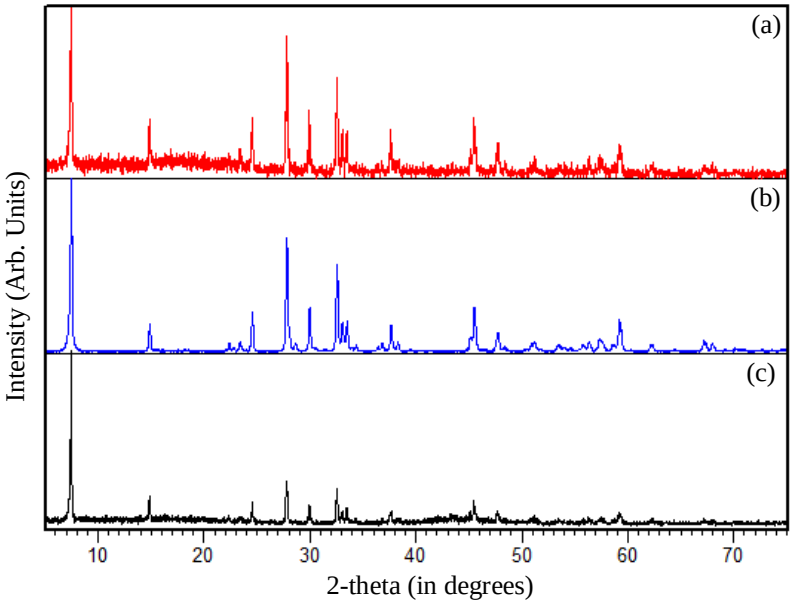

Figure F.3. XRPD of (CuCl)$BiNb_2O_7$ synthesized from (a) $RbBiNb_2O_7$+$CuCl_2$/KCl 400 °C -7d (b) $CsBiNb_2O_7$+$CuCl_2$ 340 °C -14d (c) $LiBiNb_2O_7$+$CuCl_2$ 325 °C -7d.

Thermal Stability

TGA-DSC in Figure F.3 shows the (CuCl)$BiNb_2O_7$ will decompose with a step weight loss of 11.48% to Cl_2 (cal:11.7%) around 515 °C and decomposing completely above 650°C to $CuBi_xNb_yO_7$.(Figures F.4-F.5) XRPD has shown at 370-500 °C there is still evidence for (CuCl)$BiNb_2O_7$ but at 630°C $CuBi_xNb_yO_7$ will be the only compound.

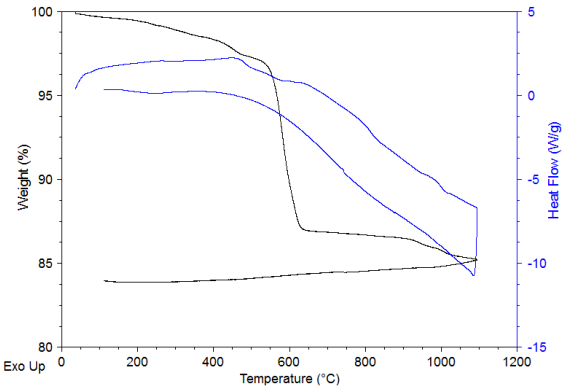

Figure F.4. TGA-DSC of (CuCl)$BiNb_2O_7$ under Ar atmosphere.

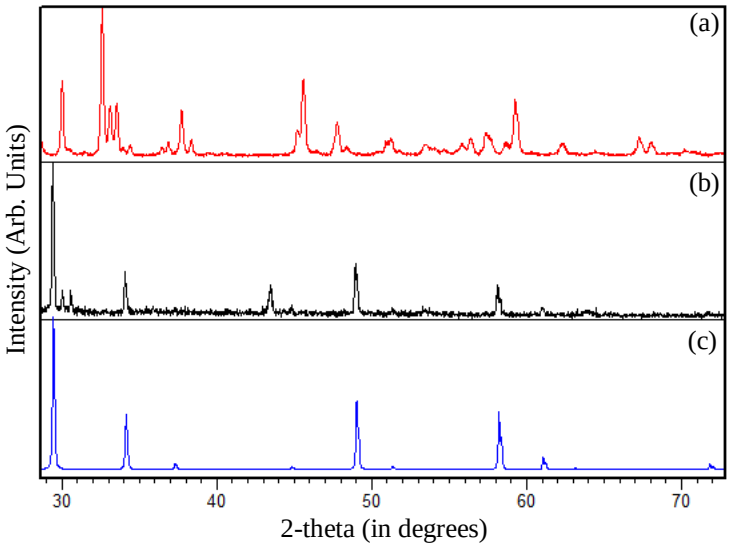

Figure F.5. XRPD of (a) (CuCl)$BiNb_2O_7$, (b) after TGA at 1000 °C and (c) $CuBi_{1.4}Nb_{1.6}O_7$.

Table F.1. Unit cell parameters for $ABiNb_2O_7$ (A: Alkali metal, CuCl).

(CuCl)AM_2O_7	**Space group**	**Unit Cell (Å)**	**Cell Vol. (Å^3)**	**Layer Spacing(Å)**	**Ref**
(CuCl)$BiNb_2O_7$	P4/mmm	a = 3.8029(6) c=11.901(2)	172.12(5)	11.90	This work
$CsBiNb_2O_7$	$P2_1am$	a = 5.49528(7) b= 5.42251(7) c=11.37663(14)	339.00	11.37	13
$RbBiNb_2O_7$	$P2_1am$	a = 11.232(4) b= 5.393(2) c=5.463(1)	330.91	11.23	6
(CuCl)$LaNb_2O_7$	Pbam	a = 7.76290(8) b=7.76197(7) c= 11.73390(6)	707.03	11.73	14
$CsLaNb_2O_7$	P 4/mmm	a = 3.908(1) c = 11.160(4)	170.44	11.16	15
$RbLaNb_2O_7$	Imma	a = 5.4941(4) b=21.9901(6) c = 5.4925(4)	663.58	11.00	16

Rietveld Refinement

The structures of (CuCl)$LnNb_2O_7$ (Ln: La, Pr) with *P*bam and *P*4/mmm [1, 14] was examined as a model for (CuCl)$BiNb_2O_7$ and *P*4/mmm symmetry has been selected. Observed, calculated, and

difference plots for the refinement of $(CuCl)BiNb_2O_7$ is shown in Figure F.6. The crystallographic data for $(CuCl)BiNb_2O_7$ are presented in Table F.2. Bond Lengths and atomic positions are represented in Tables F.2-F.3.

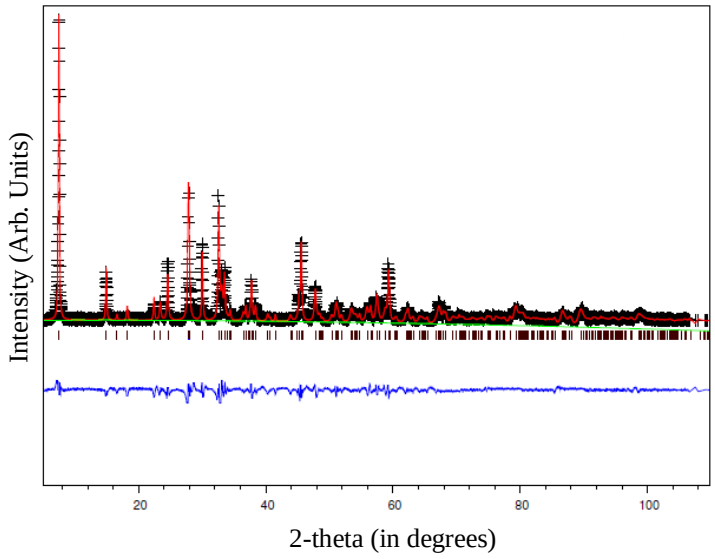

Figure F.6. Observed and calculated data for the Rietveld refinement of $(CuCl)BiNb_2O_7$. Observed data are indicated by crosses, calculated pattern by a red solid line, and the bottom blue curve is the difference plot. Peak positions are presented by black ticks.

Table F.2. Crystallographic Data for (CuCl)$BiNb_2O_7$.

Atom	Site	x	y	z	g	U_{iso} ($Å^2$)
Cu	1d	0.5	0.5	0.5	0.98(8)	0.09(1)
Cl	1b	0	0	0.5	0.97(9)	0.001(3)
Bi	1a	0	0	0	0.96(6)	0.003(5)
Nb	2h	0.5	0.5	0.1887(9)	1.92(7)	0.0023(7)
O_1	4i	0	0.5	0.1578(3)	4	0.0043(7)
O_2	2h	0.5	0.5	0.3170(3)	2	0.0027(2)
O_3	1c	0.5	0.5	0	1	0.0022(2)

P4/mmm; Z=1, a = 3.8545(4) Å, c = 11.924(1) Å Volume = 177.15(3) $Å^3$ Rp=12.8% Rwp= 15.0% and $\chi^2 = 1.75$

TableF.3. Selected Bond Lengths Extracted from the Refined Structure of (CuCl)$BiNb_2O_7$.

Bond Type	**Length (Å)**
Cu-O_2 ×2	2.181(4)
Cu-Cl ×4	2.7269(3)
Nb-O_1 ×4	1.962(8)
Nb-O_2 ×1	2.1823(3)
Nb-O_3 ×1	2.2507(4)
Bi-O_1 ×8	2.6935(3)
Bi-O_3 ×4	2.7261(5)

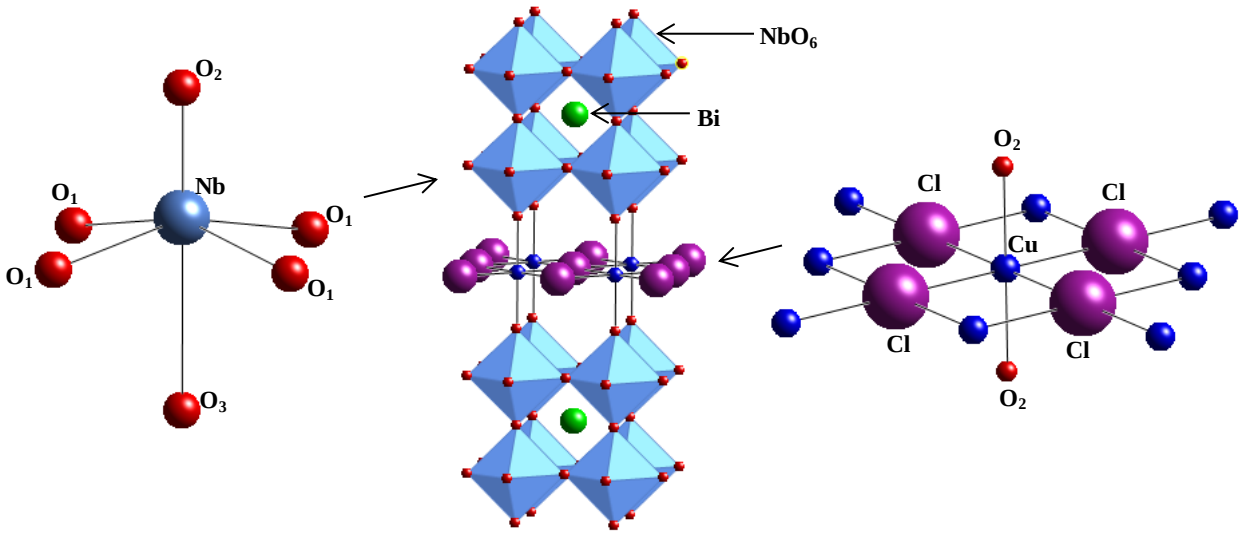

Figure F.7. Crystal structure of (CuCl)$BiNb_2O_7$ based on refinement. The blue octahedral represent NbO_6, the green sphere represents Bismuth, the Pink chlorine, the dark blue copper and the red oxygen.

Electron Microscopy

Selected Area Electron Diffraction (SAED) of (CuCl)$BiNb_2O_7$ shows the fourfold symmetry appears with lattice parameters of a=b ≈4.02 Å (Figure F.8a). The elemental analysis extracted from TEM confirms no evidence for alkali metal residual and molar ratio was found to be approximately 0.95(4):0.98(8):1:2.4(2) Cu:Cl:Bi:Nb.

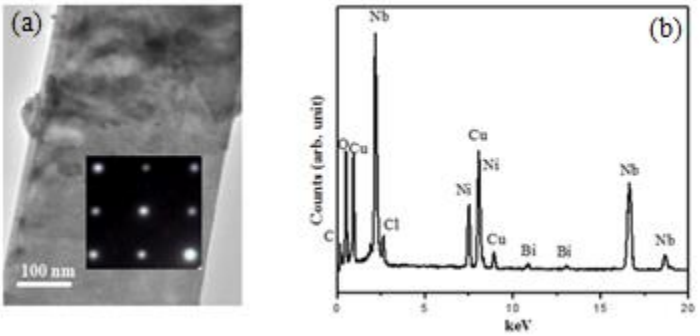

Figure F.8. TEM, SAED and Energy dispersive spectroscopy of (CuCl)$BiNb_2O_7$.(B=[001])

Magnetism

ZFC-FC magnetic measurements on $(CuCl)BiNb_2O_7$ shows bifurcation started from low temperature (Figure F.9a) and hysteresis loop in Figure F.9b at 300 K (200 Oe) and 2K (250 Oe) confirm the hysteresis confirm ferromagnetic behavior at T_c=7.5 K with μ_{eff} = 1.69(5) μ_B Weiss constant θ_{cw} = 311.7(3) K which is close to magnetic momentum of free Cu^{2+} ion. (Figure F.9a). The hysteresis about 180 Oe is seen in Figure F.9b.

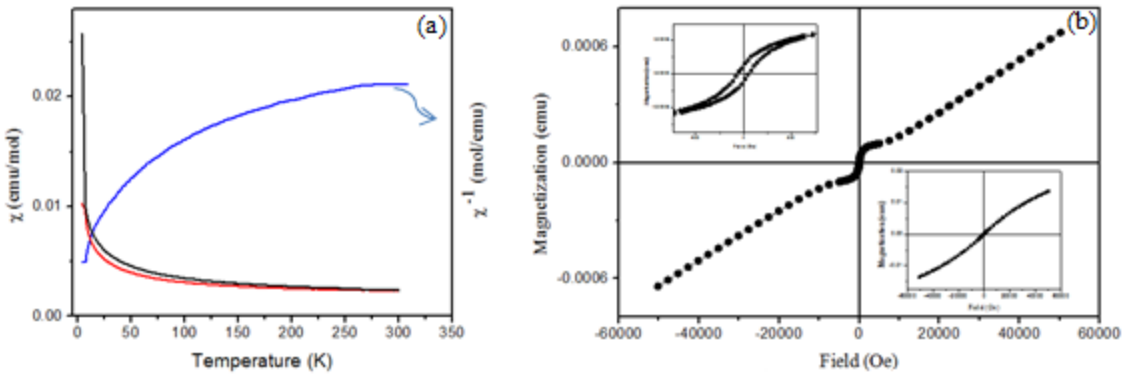

Figure F.9. (a) Temperature dependence of magnetic susceptibility and inverse susceptibility at 100 Oe and (b) Hysteresis loop for $(CuCl)BiNb_2O_7$. (inset on top is hysterisis at 300 K and on bottom is 2K)

Polarization Measurements

Polarization *vs.* electric field (P-E) curves for $ABiNb_2O_7$ (A: Rb, Cs) under various ac electric fields at room temperature are presented in the Figure F.10 and for A: CuCl in Figure F.11.

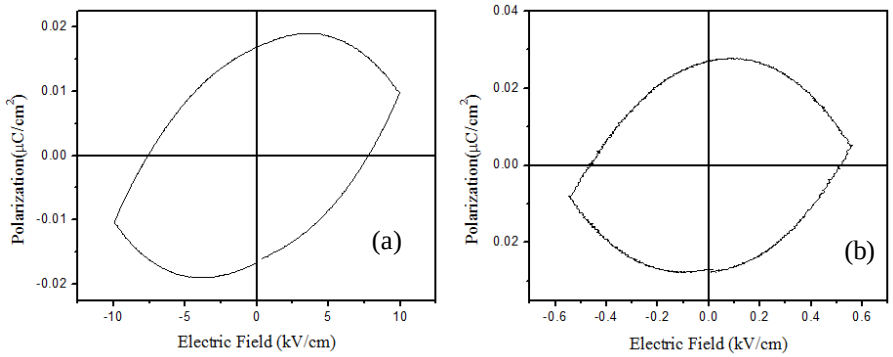

Figure F.10. Room temperature P-E hysteresis loop for (a) $RbBiNb_2O_7$ and (b) $CsBiNb_2O_7$. (Applied voltage 800 V and 100 V for Rb and Cs respectively)

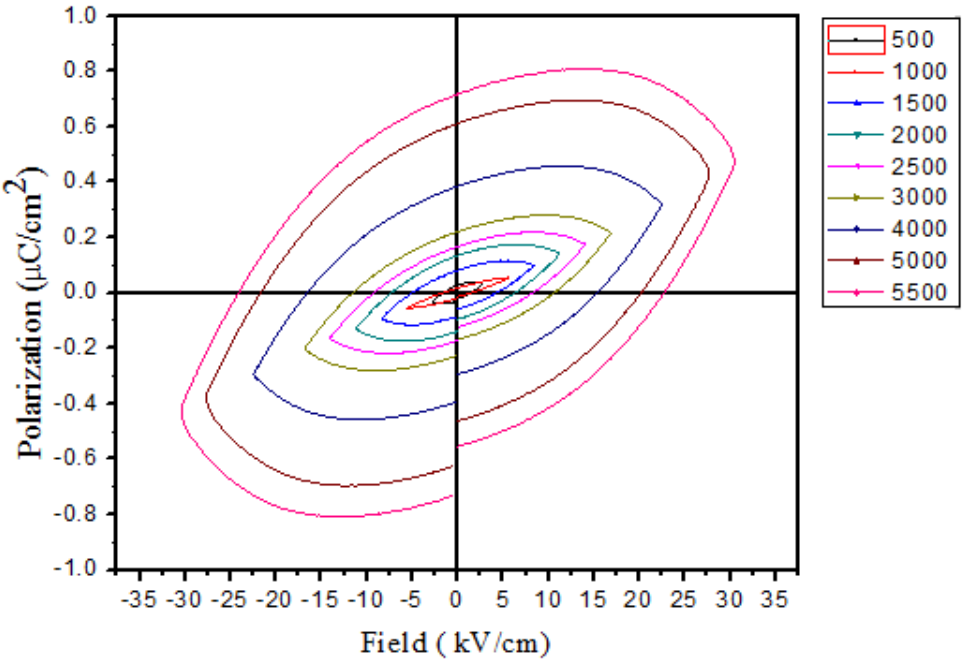

Figure F.11. Room temperature P-E hysteresis loop for $(CuCl)BiNb_2O_7$. (Applied Field 500-5500 V)

Discussion

Synthesis

$ABiNb_2O_7$ (A: Rb, Cs) prepared at 1000 °C for 24 h with a small impurity ($BiNbO_4$) in case of rubidium (Figure F.1) [5, 16] but the results in Figure F.1 shows at 1000 °C for 2 days and also

1100 °C for only 2hrs leads to $ABiNb_2O_7$. The stoichiometric amount of Bi_2O_3 is necessary otherwise $ABi_2Nb_5O_{16}$ is the major phase. [17] Layered perovskite of $ABiTa_2O_7$ (A: Rb, Cs) are not manipulated because the final products resulted in is $A_{3.2}Bi_{6.4}Ta_{16}O_{51.2}$ (Figure F.2) The manipulation of $(CuCl)BiNb_2O_7$ has been done before which shows incomplete ion exchange reaction of $RbBiNb_2O_7$ with $CuCl_2$ even after 3 weeks[8] but the results from Figure F.3 confirmed the desired copper oxychloride phase accessible by Li and Cs phase also adding molten salt (KCl) to Rb phase resulted in pure phase of $(CuCl)BiNb_2O_7$.

Characterization

Diffraction techniques (XRPD, SAED, TEM and elemental analysis)

The X-ray powder diffraction and refinement study of $(CuCl)BiNb_2O_7$ confirmed that final phase analysis with the desired model and the unit cell parameters extracted from TEM are in a very good agreement with the unit cell refinement data and there is no evidence of starting material. $(CuCl)BiNb_2O_7$ with $a=b \approx 4.02$ Å is close to $a=b=3.8029(6)$ Å and 0.95(4):0.98(8):1:2.4(2) Cu:Cl:Bi:Nb with 0.98(8):0.97(9):0.96(6):2.84(7) confirms the refinement and electron diffraction are in good agreement.

Thermal Analysis (TGA-DSC)

Thermal analysis proved that the manipulated copper chloride phase will decompose and release chlorine gas[18] as the temperature elevates $(CuCl)BiNb_2O_7$ decompose to $(CuBi_{1.4}Nb_{1.6}O_7$ (Figure F.4-F.5) is left over after decomposition and there is no evidence for formation of intermediate phase of $Cu_{0.5}PrNb_2O_7$ in opposite confirmation of $(CuCl)LaNb_2O_7$.[19]

Structure Refinement

In the case of copper and chlorine occupancy refinement were done and the final values are in very good agreement with what we expected (0.98(8) for Cu(1) and 0.97(9) for Cl(1)). As we can see the occupancy refinement for 0.95(3) for Cu(1) and 1.01(7) for Cl(1)) confirmed the desired structure. Tetragonal symmetry extracted from Rietveld refinement is in agreement with electron diffraction. Pbam space group, $(CuCl)LnNb_2O_7$ (Ln: La, Pr)[1] has been tried but the refinement parameters, thermal displacements and fitting parameters are large values.

Magnetization

Starting material $CsBiNb_2O_7$ shows diamagnetic behavior at higher magnetic field than 2 Tesla, and ferromagnetic behavior at 0.5 Tesla with about 325 Oe coercivity, which is illustrated in Figure F.12. The electronic configuration of Bi^{3+} ($4f^{14}$,$5d^{10}$, $6s^2$), confirm the diamagnetic spin ordering but ferromagnetic interaction at lower field can be related to presence of lone pair electrons of 6s orbital . The hybridization of Bi 6s/6p and O 2p orbitals play an important role in ferromagnetic interaction.[20] Magnetic measurements for $(CuCl)BiNb_2O_7$ confirm the ferromagnetic behavior (T_c=7.5 K) and effective magnetic moment (μ_{eff}) 1.76(1) μ_B agreed with the expected because of the presence of Cu^{2+} where moments is 1.75-2.10 μ_B.[21] In $(CuCl)BiNb_2O_7$ contribution of Cu^{2+} in Bi^{3+} may create ferromagnetic property.

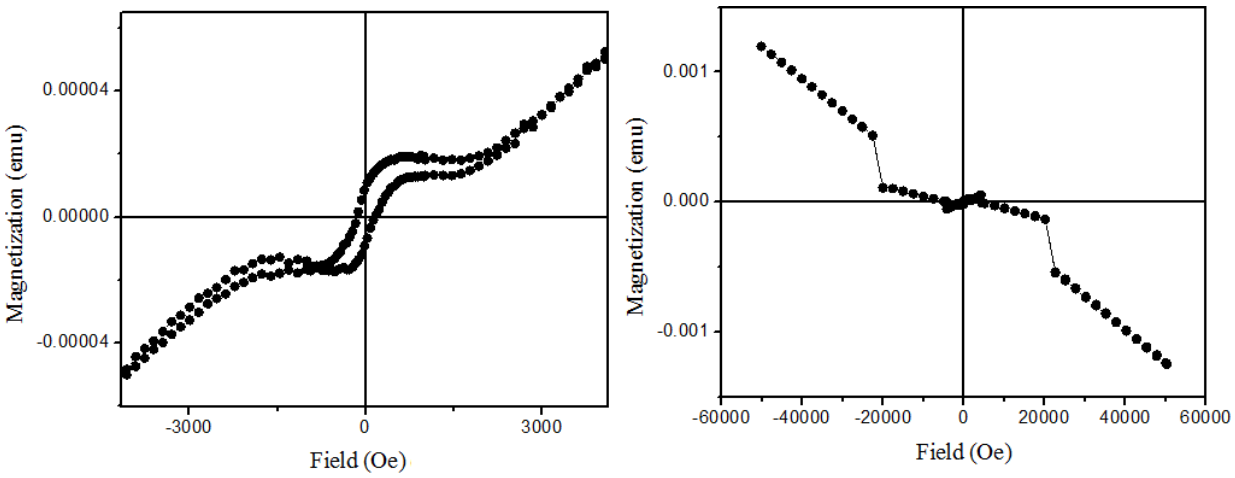

Figure F.12. Magnetic field dependence of magnetization for $CsBiNb_2O_7$.

Polarization Measurements

In the case of $ABiNb_2O_7$ (A: Rb, Cs) with no evidence for $BiNbO_4$ which plays a key role for ferroelectricity, the stating materials without impurity disappear ferroelectric property and the loops looks like ideal resistor response with no saturation for P-E loops even at higher fields.[22] For $(CuCl)BiNb_2O_7$ in Figure F.11, the polarization vs. electric field curve under various ac electric fields at room temperature shows hysteresis looks like exact what have reported for $RbBiNb_2O_7$ ferroelectrics[6] but dominated by the leakage current contribution to the measured polarization and because P-E is not saturated and looks like banana then it's not ferroelectric and is lossy dielectric (Figure F.11) [23] and also results confirm $RbBiNb_2O_7$ without impurity does not show ferroelectricity response.

References

[1] Montasserasadi, D.; Granier, M.; Spinu, L.; Chandra Rai, S.; Zhou, W.; Wiley, J. B., *J. Chem. Soc, Dalton Trans*. (**2015**) Accepted.

[2] Machida, M.; Mitsuyama, T.; Ikeue, K. *Phys. Chem* B. **2005**, *109(16)*, 7801-7806.

[3] Sato, M.; Abo, J.; Jin, T.; Ohta, M. *J. Alloys Compd*. **1993**, *192(1-2)*, 81-83.

[4] Fukuoka, H.; Isami, T.; Yamanaka, S. *Chem. Lett*. **1997**, *26(8)*, 703-704.

[5] Ida, S.; Ogata, C.; Eguchi, M.; Youngblood, W. J.; Mallouk, T.; Matsumoto, Y. *J. Am. Chem. Soc*. **2008**, *130(22)*, 7052-7059.

[6] Li, B. W.; Osada, M.; Ozawa, T.C.; Sasaki, T. *Chem. Mater*. **2012,** *24(16)*, 3111-3113.

[7] Subramanian, M.A.; Gopalakrishnan, J.; Sleight, A.W. *Mater. Res. Bull*. **1988**, *23(6)*, 837-842.

[8] Kodenkandath, T. A.; Kumbhar, A. S.; Zhou, W. Wiley, J. B. *Inorg. Chem*. **2001**, *40(4)*, 710-714.

[9] Hyeon, K. A.;Byeon, H. S. *Chem. Mater*. **1999**, *11(2)*, 352-357.

[10] Laugier, J.; Bochu, B, LMGP-Suite, ENSP/Laboratoire des Matériaux et du Génie Physique, BP 46. 38042, Saint Martin d'Hères, France, 2002.

[11] Larson, A. C and Von Dreele, R. B. , General Structure Analysis System (GSAS) program. Rep. No. LA-UR-86748, Los Alamos National Laboratory, Los Alamos, CA, 1994.

[12] Toby, B.H. *J. Appl. Crystallogr*. **2001**, *34(2)*, 210-213.

[13] Snedden, A.; Knight, K.S.; Lightfoot, P. *J. Solid State Chem* . **2003**, *173(2)*, 309-313.

[14] Tsirlin, A. A.; Abakumov, A. M.; Tendeloo, G. V.; Rosner, H. *Phys. Rev. B: Condens. Matter*. **2010**, 82, 054107.

[15] Kumada, N.; Kinomura, N.; and Sleight, A. W. , Acta Crystallogr., Sect. C: Cryst. Struct. Commun. **1996***,* 52(5), 1063-1065.

[16] Armstrong, A. R.; Anderson, P. A. *Inorg. Chem*. **1994**, *33(19)*, 4366-4369.

[17] Ehlert, M. K.; Greedan, J. E. *J. Solid State Chem*. **1988**, *75(1)*, 188-196.

[18] Montasserasadi, D.; Granier, M.; Helman, A, Chandra Rai, S.; Weilie, Zhou.; Wiley. J. B. (Manuscription)

[19] Hermann, A, T.; Wiley, J. B. *Mater. Res. Bull*. **2009**, *44(5)*, 1046-1050.

[20] Singh,M. P.; Truong, K. D.; Fournier, P.; Rauwel, P.; Rauwel, E.; Carignan, L. P.; Ménard, D.; *Appl. Phys. Lett*. **2008**, *92*, 112505.

[21] O'Connor, C. *J. Prog. Inorg. Chem*. **1982**, *29*, 203-283.

[22] Stewart, M.; Cain, M. G; Hall, D. A. Ferroelectric Hysterisis Measurment & Analysis. National Physical Laboratory & University of Manchester. May 1999.

[23] Scot, J. F. *J. Phys. Condens. Matter*. **2008**, *20*, 021001.

Appendix VII

Copper Oxychloride Rare-Earth Tantalate Layered Perovskites

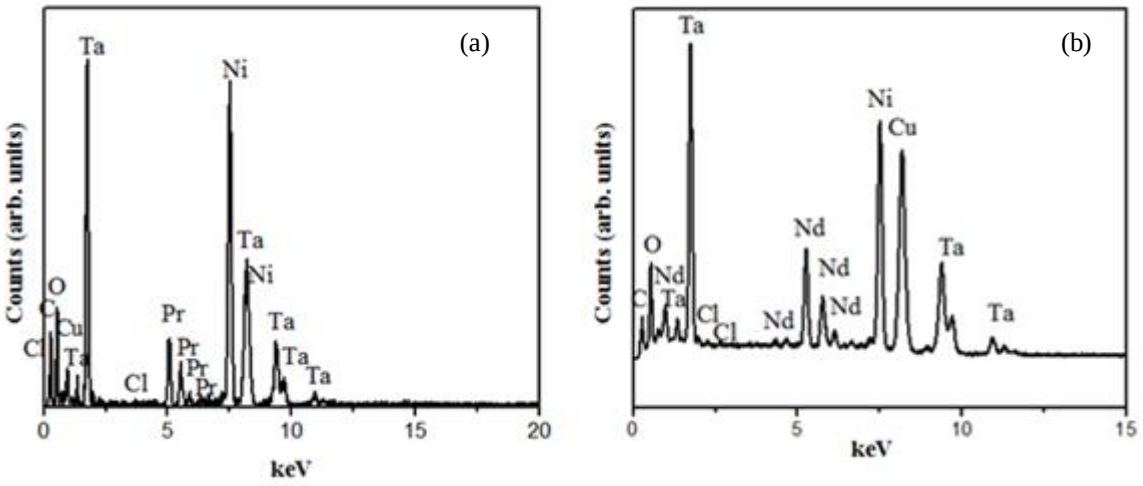

Figure G.1. EDS data for (a) (CuCl)$PrTa_2O_7$ and (b) (CuCl)$NdTa_2O_7$.

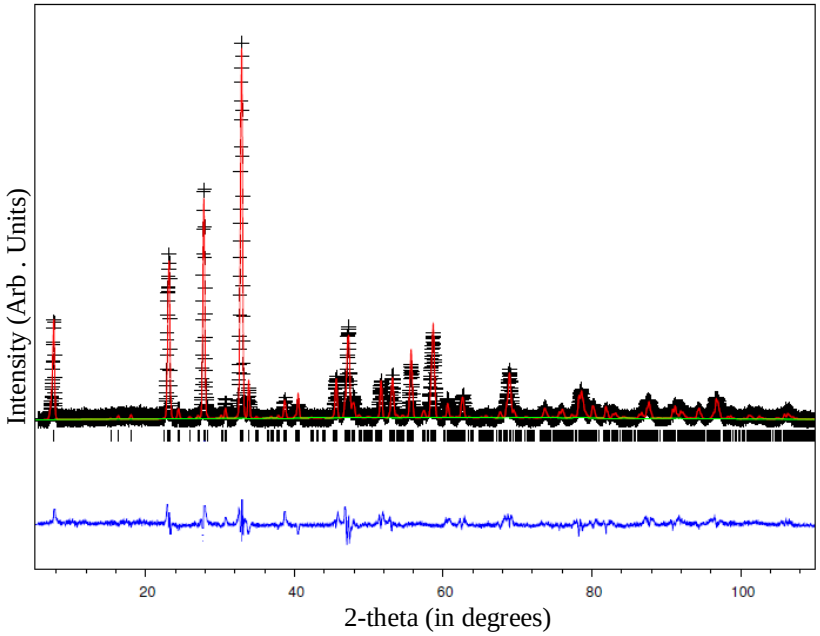

Figure G.2. Observed and calculated data for the Rietveld refinement of $(CuCl)NdTa_2O_7$. Observed data are indicated by crosses, calculated pattern by a red solid line, and the bottom blue curve is the difference plot. Peak positions are represented by black tick marks.

Table G.1. Crystallographic Data for (CuCl)$NdTa_2O_7$.

Atom	Site	x	y	z	g	U_{iso} ($Å^2$)
Cu	4h	0.7310(3)	0.5250(3)	0.5	0.96(3)	0.0057(5)
Cl	4h	0.5518(4)	0.2220(3)	0.5	1.13(1)	0.046(6)
Nd	4g	0	0.2585(2)	0	0.98(8)	0.0052(4)
Ta	8i	0.7477(1)	0.497(1)	0.809(4)	1.00(1)	0.0002(2)
O_1	4f	0	0.5	0.836(1)	1	0.0059(4)
O_2	8i	0.278(9)	0.773(3)	0.836(7)	1	0.0021(1)
O_3	8i	0.245(2)	0.066(9)	0.659(6)	1	0.0082(4)
O_4	4g	0.759(1)	0.558(1)	0	1	0.0048(9)
O_5	4e	0	0	0.865(1)	1	0.0049(3)

Pbam; Z=4; a=7.7316(5) Å, b=7.6956(5) Å, c= 11.6516(1) Å, V=693.26(1) $Å^3$; R_p=12.59%, R_{wp}= 13.68%, χ^2 =1.293

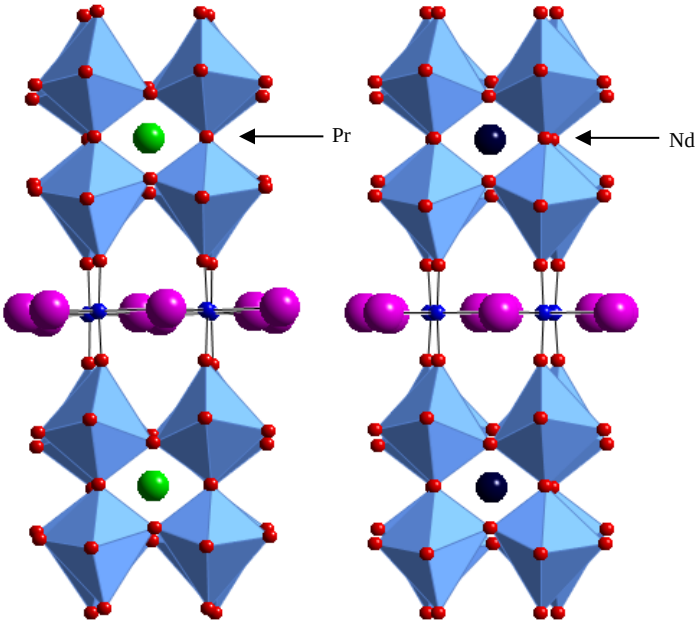

Figure G.3. Crystal structures of $(CuCl)LnTa_2O_7$. (TaO_6: light blue, Pr: green sphere, Nd: dark blue, Cl: the pink ,Cu: the dark blue and O:the red.

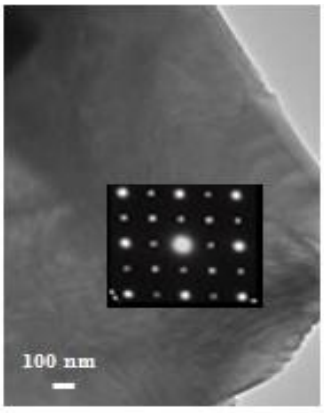

Figure G.4. TEM and inset SAED (B=[001]) $(CuCl)NdTa_2O_7$.

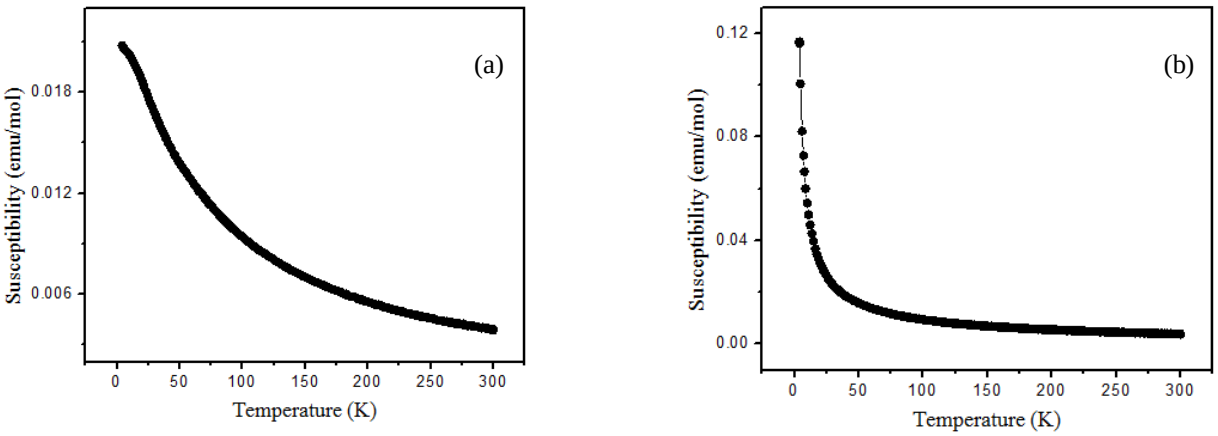

Figure G.5. Temperature dependence of magnetic susceptibility of (a) $RbPrTa_2O_7$ and (b) $CsNdTa_2O_7$.

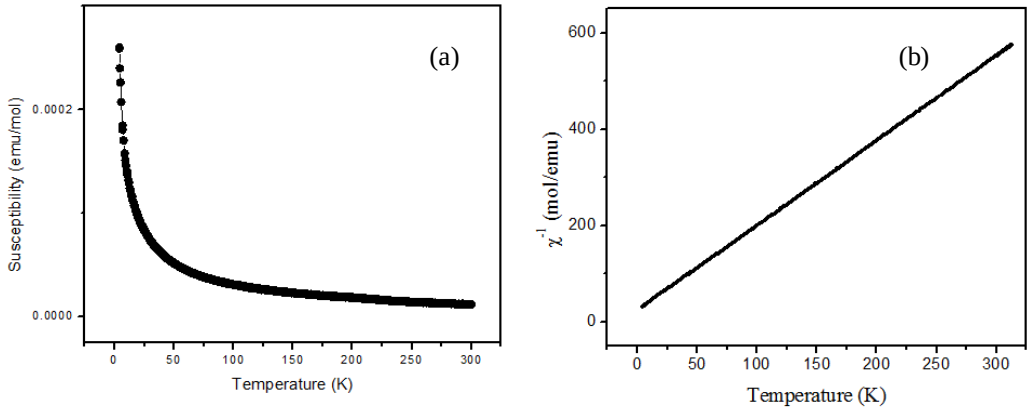

Figure G.6. Magnetic behavior of $(CuCl)NdTa_2O_7$. (a) Temperature dependence of susceptibility (ZFC-FC; H=100 Oe field) and **(**b) temperature dependence of inverse magnetic susceptibility.

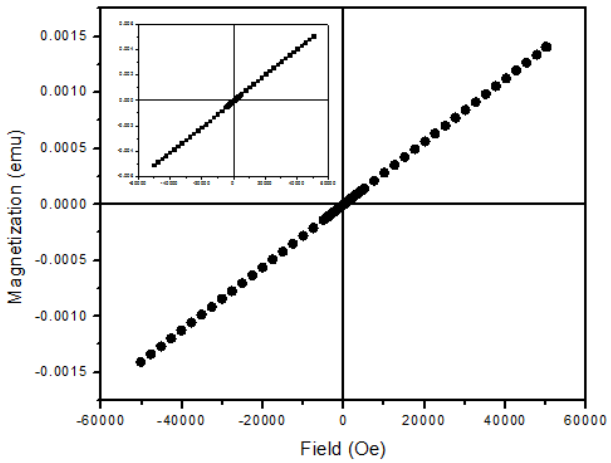

Figure G.7. The magnetization against the magnetic field for (CuCl)$PrTa_2O_7$ at 300 K and (inset) 4 K.

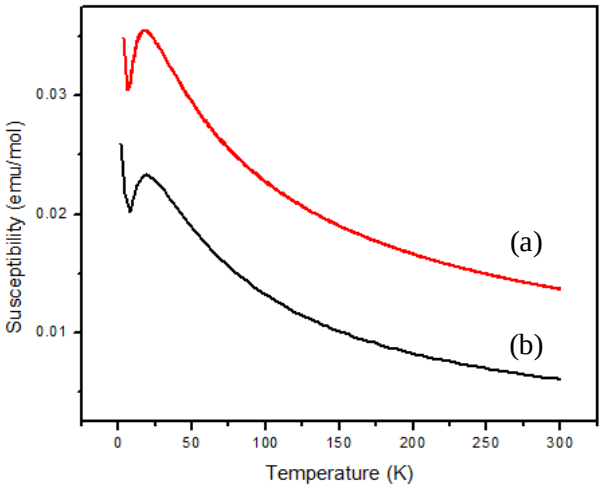

Figure G.8. Temperature dependence of magnetic susceptibility of (a) (CuCl)$PrTa_2O_7$ at 1000 Oe and (b) (CuCl)$PrNb_2O_7$ at 100 Oe.

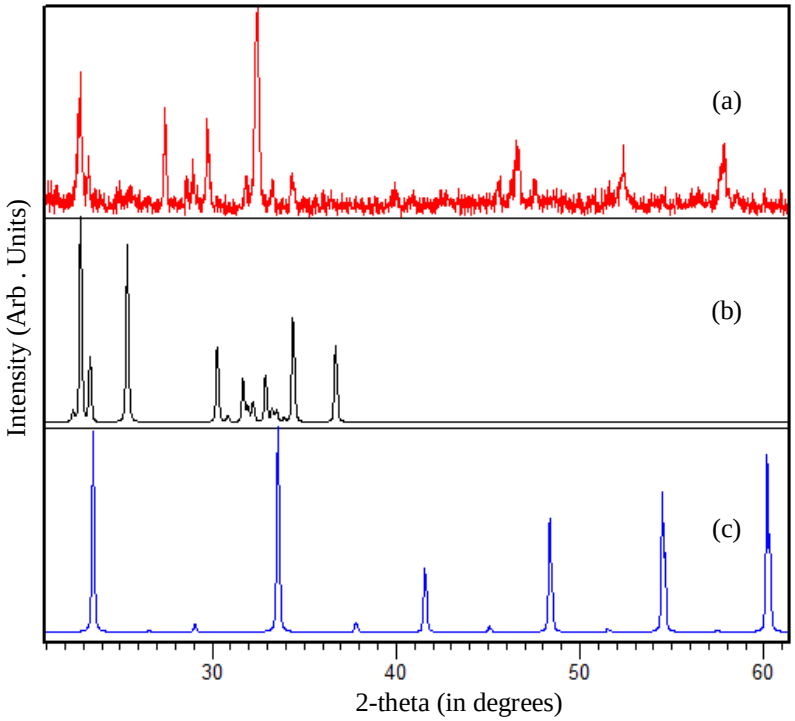

Figure G.9. XRD of (CuCl)$PrTa_2O_7$ after (a) TGA at 1000 °C, (b) $PrTaO_4$, and (c) $CuTaO_3$.

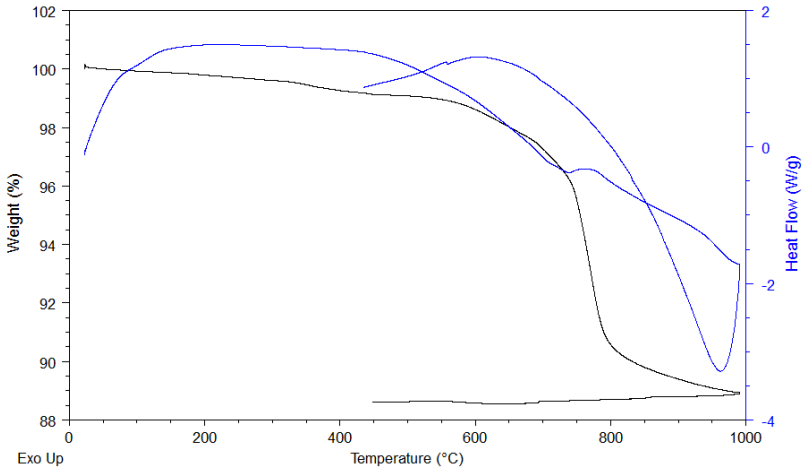

Figure G.10. TGA-DSC results of (CuCl)$NdTa_2O_7$.

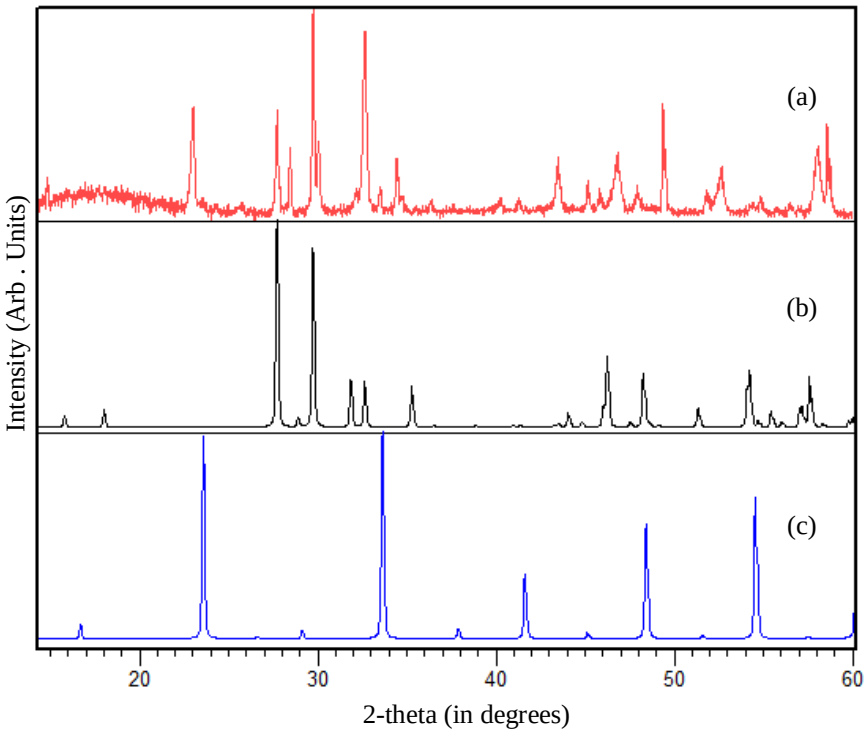

Figure G.11. (a) XRD of (CuCl)$NdTa_2O_7$ after TGA at 1000 °C as compared to (b) $NdTaO_4$ and (c) $CuTaO_3$.

Appendix VIII

Layered Copper Oxy-chloride of Lead Niobate

Abstract

The new Dion-Jacobson triple layered perovskite of $(CuCl)Pb_2Nb_3O_{10}$ have been prepared by exchanging of $CuCl^+$ with alkali metal (A) in $APb_2Nb_3O_{10}$ precursor with $(CuCl)Pb_2Nb_3O_{10}$ a = 3.9202(1) Å c = 16.0045(4) Å unit cell parameters. The purity of final product was confirmed by diffraction techniques. Magnetic property shows $RbPb_2Nb_3O_{10}$ is diamagnetic but $(CuCl)Pb_2Nb_3O_{10}$ has transition from diamagnetic to ferromagnetic at room temperature.

Introduction

Dion-Jacobson (DJ) $A[A'_{n-1}B_nO_{3n+1}]$ Layered perovskites consist of perovskite slabs $[A'_{n-1}B_nO_{3n+1}]$ separated by interlayer cation (A^+) have been prepared by conventional high temperature or Topochemical low temperature methods such as ion exchange and intercalation. Topochemical methods can be used for the preparation of metastable compounds often not accessible by high ceramic methods and the overall structures are maintained. Topochemistry have been developed for the formation of metal-nonmetal layers such as CuCl in $(CuCl)LaNb_2O_7$[1] or $(CuCl)PrNb_2O_7$[2] through ion exchange, ion exchange followed by reductive intercalation in $(Li_xCl)LaNb_2O_7$[3] and the reductive intercalation followed by oxidative intercalation in $(Rb_2Cl)LaNb_2O_7$, $(Rb_2OH)LaNb_2O_7$ and $(Rb_2SH)LaNb_2O_7$.[4-6] Incorporation of ions with different sizes and charges in A, A´ and B sites can lead to a variety of layered perovskites with interesting properties such as photo catalytic activity of $ALnM_2O_7$ (A: alkali

metal, Ln: La, Pr, Nd, Sm and M:Nb, Ta)[7,8] and $RbPb_2Nb_3O_{10}$,[9] ionic conductivity of $ALaNb_2O_7$ (A: alkali metal),[10] $KCa_2Nb_3O_{10}$ with superconductivity,[11] $RbBiNb_2O_7$ as a lead-free ferroelectrics[12] and $HPb_2Nb_3O_{10}\cdot xH_2O$ as proton conductor.[13] $ALnM_2O_7$ (A: alkali metal, Ln: La, Pr, Nd, Sm and M:Nb, Ta) layered perovskites has been prepared but for the lanthanides after Samarium having Dion-Jacobson layered perovskite structure $ALnM_2O_7$ maybe because of smaller size of lanthanide which affect the tolerance factor and geometry of slab and interlayer cation looks less promising and possibility of other structures (Pyrochlore) increase, therefore construction of new layered perovskites with Ln-based includes new magnetic and electronic properties can be interesting. $APb_2Nb_3O_{10}$ has been used as precursors to build new copper-chloride layered perovskites by ion exchange first to expand the library of metastable rare-earth and lead layered perovskites and also study their magnetic and thermal behavior.

Experimental

$APb_2Nb_3O_{10}$

Nb_2O_5 (Alfa Aesar, 99.9985%) and PbO_2 (Alfa Aesar, 97.0%) were heated at 1000 °C for a day in order to remove any impurities as carbonates or water. Then stoichiometric mixtures of PbO_2, Nb_2O_5, Rb_2CO_3 (Alfa Aesar, 99 %) and Cs_2CO_3 (Alfa Aesar 99.994 %) with 25 % excess of A_2CO_3 (A: Rb, Cs) were ground together and heated at 850 °C for 24 h and 1000 °C for 48 h to synthesis of yellow powder $APb_2Nb_3O_{10}$ (A: Rb, Cs). The excess amount of A_2CO_3 was added to all compounds to compensate for the volatilization of alkali-metal oxide components. The product was washed with distilled water then dried at 110 °C for one day.[13]

$(CuCl)Pb_2Nb_3O_{10}$

$APb_2Nb_3O_{10}$ add to 2-fold molar excess of $CuCl_2$ (Alfa Aesar 99.995 %) in the argon-filled glove box and then the mixture was pelletized by hand press and sealed in a Pyrex tube under vacuum and heated. The lead phase, $RbPb_2Nb_3O_{10}$ and $CuCl_2$ at 325 ℃-14 days and 350 ℃ 10 days for $CsPb_2Nb_3O_{10}$ resulted in $(CuCl)Pb_2Nb_3O_{10}$. All the new phases have been washed with DI-water and dried at oven 110 ℃ for a day.

Characterization

X-ray Powder diffraction (XRPD) data were collected on a Philips X'Pert system equipped with Cu Kα radiation (λ = 1.5418 Å) and a curved graphite monochromator. Typical scans were collected in continuous mode with a scan rate of 0.02 °/s. The peak positions and lattice parameters were refined by a least-squares method with program; ChekCell [14] Crystal structures were refined by the Rietveld method with the GSAS software package.[15, 16] Transmission electron microscopy (TEM) and selected area electron diffraction (SAED) was performed on a JEM 2010 operated at 200 kV. The samples were prepared by crushing them in ethanol, and then ethanol suspensions of the samples were drop-cast on Ni-TEM grids (Ted Pella). Elemental analysis was carried out by energy dispersive spectroscopy (EDS) on TEM.

The thermal behavior of the products was studied by TGA/DSC using a TA Instruments Q600 TGA-DSC system over the temperature range 25-1000 °C with a ramp of 10 °C/min in flowing Ar atmosphere. Magnetic Susceptibility measurements were performed on a superconducting quantum interference device (SQUID) magnetometer (Quantum Design, MPMS-7) in the temperature range 2-300 K in different magnetic fields up to 6T. Magnetic susceptibility measurements were carried out in zero field cooled (ZFC) and field cooled (FC) conditions.

Results

Synthesis

High temperature ceramic method has been used to form starting material (equation 1)

$$A_2CO_3 + 4\ PbO_2 + 3Nb_2O_5 \rightarrow 2APb_2Nb_3O_{10} + CO_2\,(g)\ \text{(eqn 1)}$$

Ion exchange reaction of the DJ phase is shown in equation 2.

$$APb_2Nb_3O_{10} + CuCl_2 \rightarrow (CuCl)Pb_2Nb_3O_{10} + ACl\ \ \text{(eqn 2)}$$

Diffraction Studies

XRPD. X-ray powder diffraction patterns for $(CuCl)Pb_2Nb_3O_{10}$ is presented in Figure H.1. $APb_2Nb_3O_{10}$ (A: Rb, Cs, CuCl) series have been indexed and refined which unit cell parameters are shown in Table H.1.

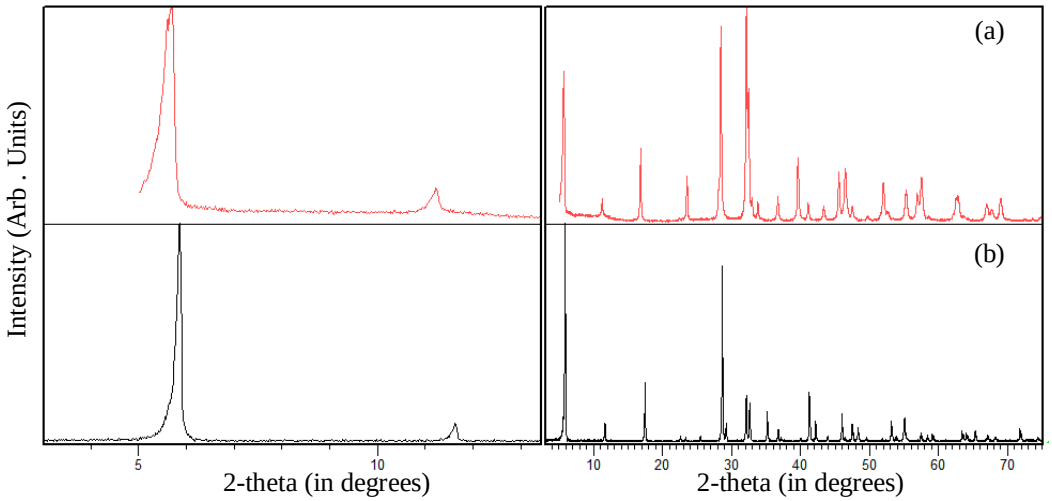

Figure H.1. XRPD for (a) $(CuCl)Pb_2Nb_3O_{10}$ and (b) $CsPb_2Nb_3O_{10}$.

Table H.1. Unit cell parameters for $AA'_2Nb_3O_{10}$ (A: Rb, Cs, CuCl and A′: Ca, Pb)

Compounds	Space group	Unit Cell (Å)	Cell Vol. (Å^3)	Layer Spacing(Å)	Ref
$(CuCl)Ca_2Nb_3O_{10}$	P 4/mmm	a = 3.8496(2) c = 15.6593(2)	232.06	15.66	17
$RbCa_2Nb_3O_{10}$	P 4/mmm	a = 3.85865(6) c = 14.9108(3)	222.01(1)	14.91	18
$(CuCl)Pb_2Nb_3O_{10}$	P 4/mmm	a = 3.9265(5) c = 15.994(2)	246.59(5)	15.99	This work
$CsPb_2Nb_3O_{10}$	P 4/mmm	a = 7.888(6) c = 15.093(5)	939.09	15.09	13
$RbPb_2Nb_3O_{10}$	P 4/mmm	a = 7.863(6) c = 14.979(10)	926.10	*14.98*	13

Structure Refinement

Rietveld refinement was carried out on $(CuCl)Pb_2Nb_3O_{10}$. The Rietveld refinement for $(CuCl)Pb_2Nb_3O_{10}$ is illustrated in Figure H.2. The crystallographic data for $(CuCl)Pb_2Nb_3O_{10}$ is presented in Table H.2 with bond lengths in Table H.3 and crystal structure is in Figure H.3.

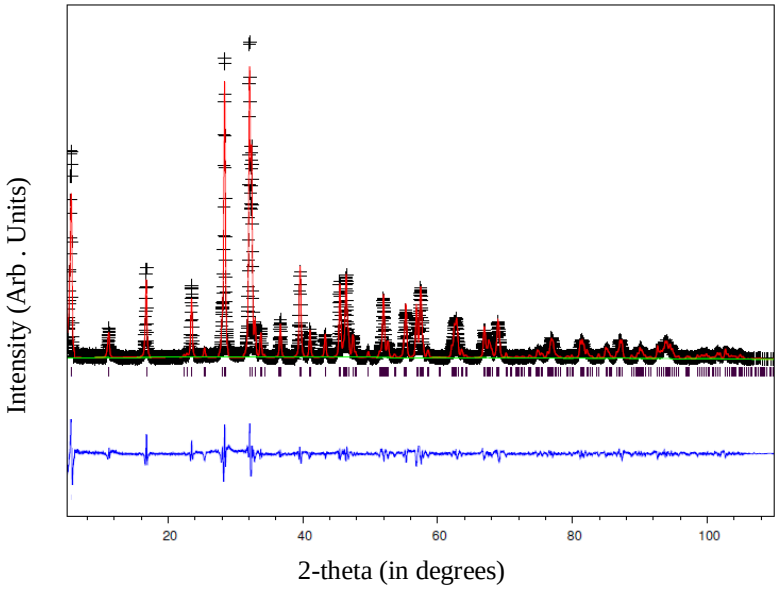

Figure H.2. Observed and calculated data for the Rietveld refinement of $(CuCl)Pb_2Nb_3O_{10}$. Observed data are indicated by crosses, calculated pattern by a red solid line, and the bottom blue curve is the difference plot. Peak positions are presented by black dot color.

Table H.2. Crystallographic Data for $(CuCl)Pb_2Nb_3O_{10}$

Atom	Site	x	y	z	g	U_{iso} ($Å^2$)
Cu	1b	0	0	0.5	0.97(2)	0.025(8)
Cl	1d	0.5	0.5	0.5	1.01(4)	0.083(5)
Pb	2h	0.5	0.5	0.141(2)	1.05(1)	0.0048(2)
Nb1	1a	0	0	0	1.02(1)	0.0021(4)
Nb2	2g	0	0	0.275(1)	1.05(2)	0.0069(3)
O_1	2f	0	0.5	0	1	0.0233(1)
O_2	2g	0	0	0.121(1)	1	0.0149(2)
O_3	4i	0	0.5	0.261(7)	1	0.0153(5)
O_4	2g	0	0	0.388(3)	1	0.0151(5)

P4/mmm z=1 a=3.9265(5) Å, c= 15.994(2) Å Volume =246.59(5) $Å^3$ Rp=15.28% Rwp= 16.45% $\chi^2 = 1.66$

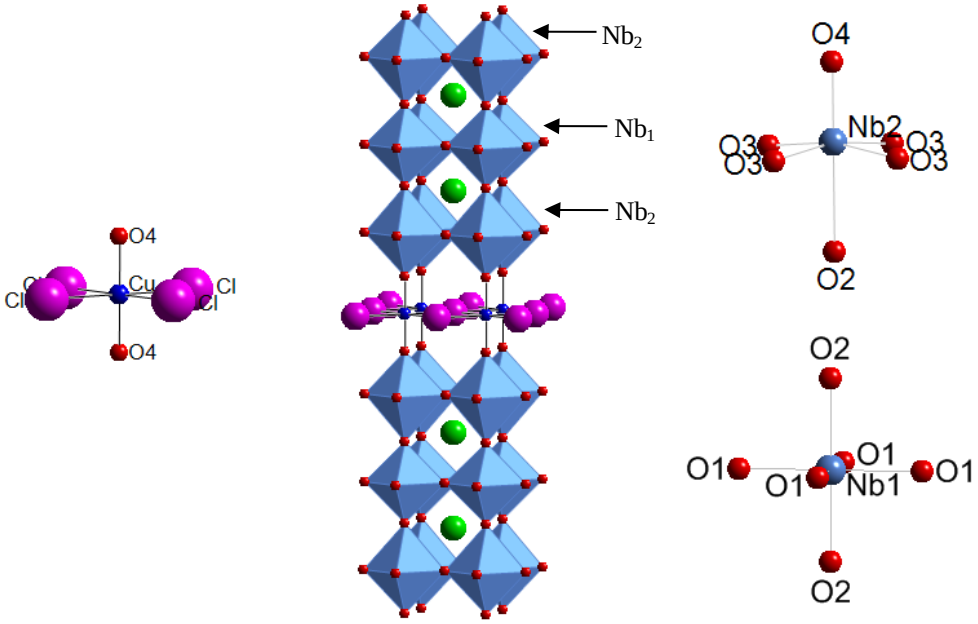

Figure H.3. Crystal structure of $(CuCl)Pb_2Nb_3O_{10}$ based on refinement. The blue octahedral represent NbO_6, the green sphere represents Lead.

Table H.3. Selected Bond Lengths of $(CuCl)Pb_2Nb_3O_{10}$ and $(CuCl)Ca_2Nb_3O_{10}$

$(CuCl)Pb_2Nb_3O_{10}$		$(CuCl)Ca_2Nb_3O_{10}$ [17]	
Bond Type	**Length (Å)**	**Bond Type**	**Length (Å)**
Cu-O_4×2	1.785(2)	Cu-O_4×2	1.993(1)
Cu-Cl×4	2.7766(3)	Cu-Cl×4	2.7221(1)
Pb-O_1×4	2.9882(2)	Ca-O1×4	2.946
Pb-O_2×4	2.7945(5)	Ca-O2×4	2.737
Pb-O_3×4	2.7481(2)	Ca-O3×4	2.477
Nb_1-O_1×4	1.9633(2)	Nb_1-O_1×4	1.9248(1)
Nb_1-O_2×2	1.935(1)	Nb_1-O_2×2	1.94(2)
Nb_2-O_2×1	2.464(1)	Nb_2-O_2×1	2.28(2)
Nb_2-O_3×4	1.976(3)	Nb_2-O_3×4	1.971(3)
Nb_2-O_4×1	1.812(1)	Nb_2-O_4×1	1.616(3)

TableH.4. BVS for $(CuCl)Pb_2Nb_3O_{10}$ *vs* $(CuCl)Ca_2Nb_3O_{10}$

$(CuCl)Pb_2Nb_3O_{10}$		**$(CuCl)Ca_2Nb_3O_{10}$**	
Cu	1.99	Cu	1.42
Pb	2.02	Ca	1.79
Nb1	5.42	Nb1	5.77
Nb2	4.95	Nb2	6.06

Electron Microscopy

The morphology of $(CuCl)Pb_2Nb_3O_{10}$ show plated-shape. Electron diffraction, TEM and elemental analysis of $(CuCl)Pb_2Nb_3O_{10}$ is presented in Figure H.4 which is a=b ≈3.86Å with elemental composition of 0.9(2):0.8(1):2:3.2(3) Cu:Cl:Pb:Nb for $(CuCl)Pb_2Nb_3O_{10}$.

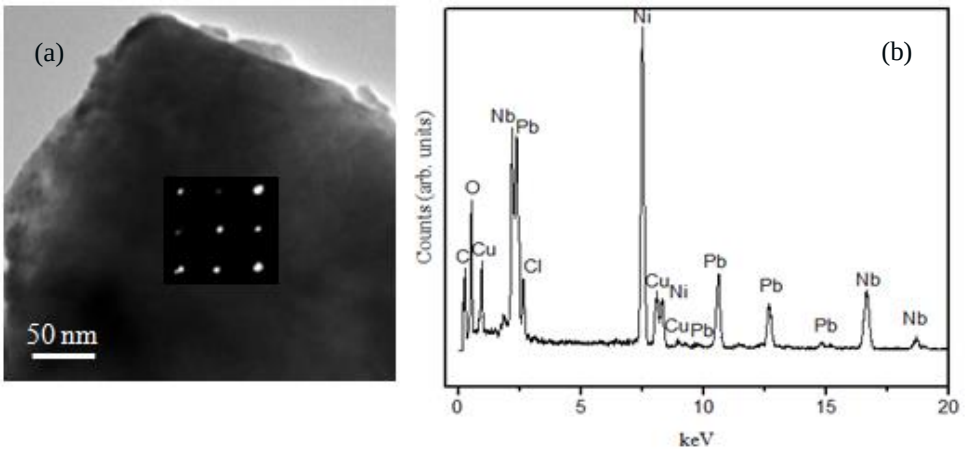

Figure H.4. (a-b) TEM, SAED and Energy dispersive spectroscopy of $(CuCl)Pb_2Nb_3O_{10}$.B=[001]

Magnetism

The magnetic susceptibility and magnetization of starting material is shown in Figure H.5 which shows diamagnetic behavior. Figure H.6 shows hysteresis loops of $(CuCl)Pb_2Nb_3O_{10}$ at 2K and 300 K with no hysteresis. The magnetic susceptibility is presented in Figure H.7. Curie-Weiss behavior with an effective magnetic moment (μ_{eff}) 1.85(2) μ_B is extracted from ZFC at 100 Oe which is close to expected value for free Cu^{2+} ion [19] and curie constant of -3.0(1) K.(weak AFM)

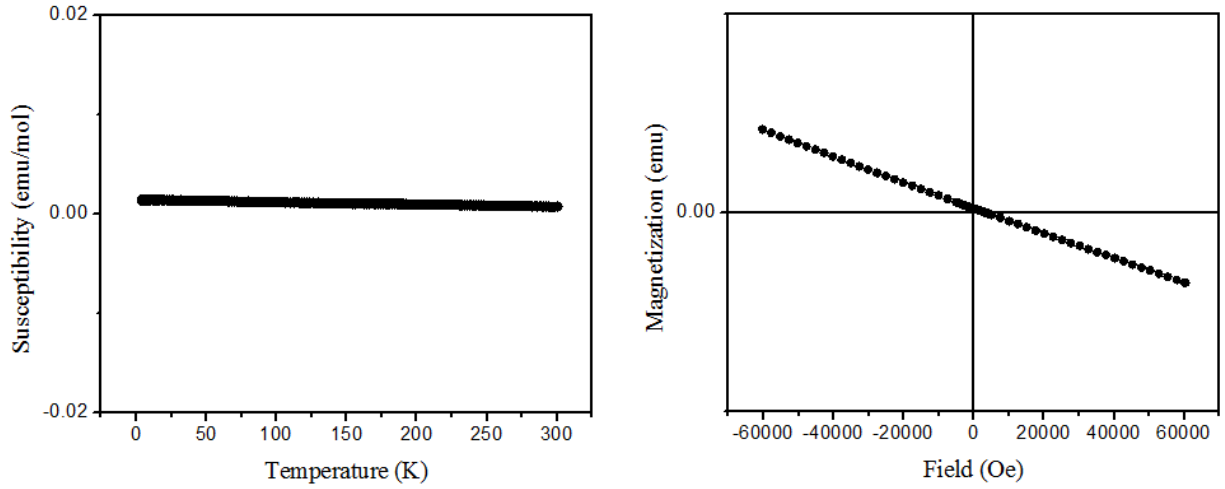

Figure H.5. (a) Temperature dependence of magnetic susceptibility of $RbPb_2Nb_3O_{10}$ (ZFC-FC at 100 Oe field) and (b) Magnetization at 4 K.

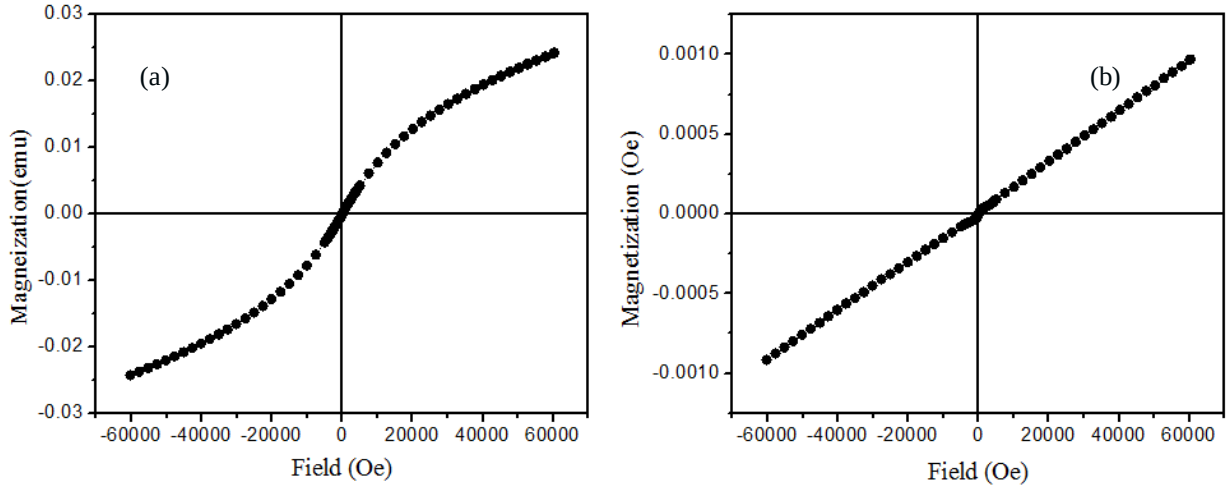

Figure H.6. Magnetization of $(CuCl)Pb_2Nb_3O_{10}$ at (a) 2 K and (b) 300 K.

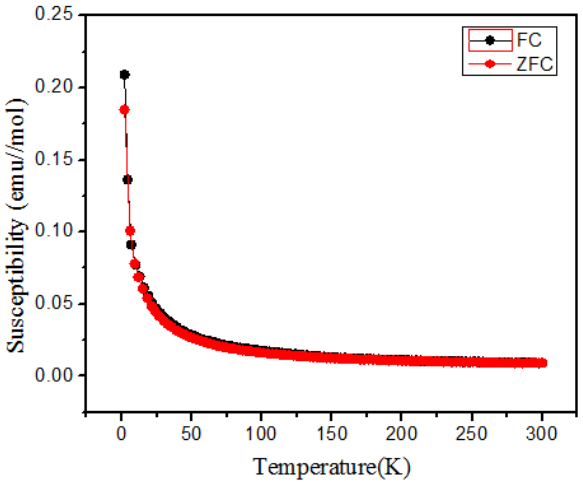

Figure H.7. Temperature dependence of magnetic susceptibility for $(CuCl)Pb_2Nb_3O_{10}$ at 100 Oe.

Thermal Stability

Thermal analysis results show that $(CuCl)Pb_2Nb_3O_{10}$ will decompose. Experiments carried out in inert (flowing Ar). Figure H.8 shows TGA/DSC results for $(CuCl)Pb_2Nb_3O_{10}$ which shows it decomposes under inert atmosphere (Ar) at 1000 °C to $PbNb_2O_6$ and Cu_6PbO_8. (Figure H.9) The weight loss of ~7.22 % is related to evolution of Cl_2. (~7.46 %). XRPD of $APb_2Nb_3O_{10}$ after TGA at 1000 °C represents that these starting material don't decompose.

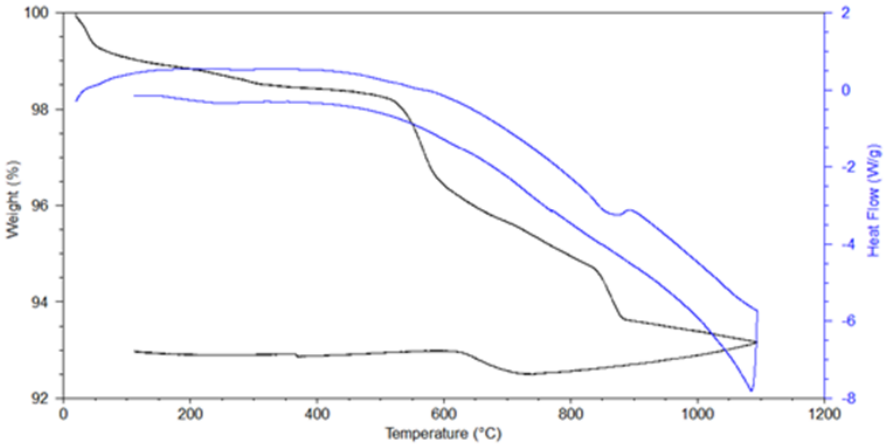

Figure H.8. TGA/DSC results of $(CuCl)PbNb_3O_{10}$.

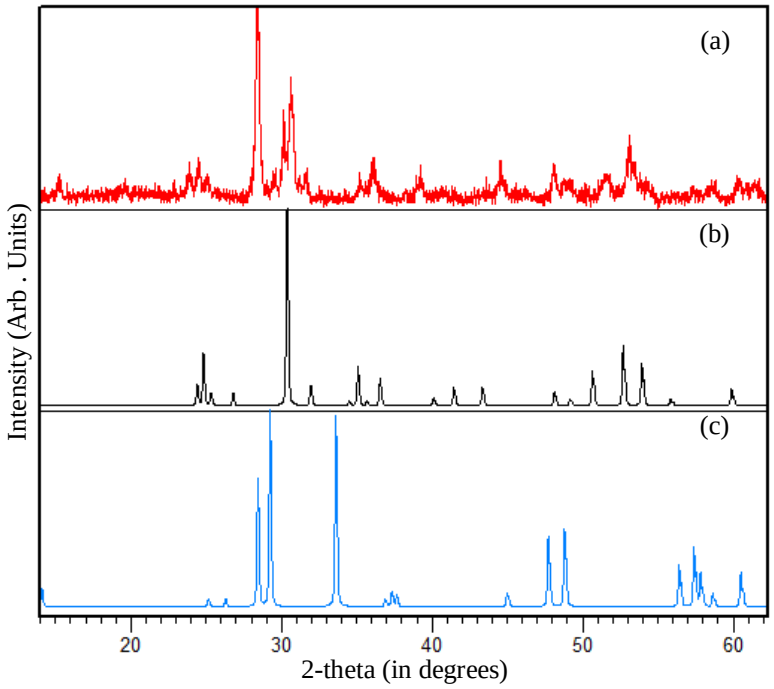

Figure H.9. XRPD of $(CuCl)Pb_2Nb_3O_{10}$ (a) after TGA at 1000 ° C, (b) $CuNb_2O_6$ and (c) $Pb_2Nb_2O_7$.

Discussion

Synthesis

$APb_2Nb_3O_{10}$ (A: Rb, Cs) and $(CuCl)Pb_2Nb_3O_{10}$ prepared by solid state and ion exchange methods, respectively. Layered perovskite of $APb_2Ta_3O_{10}$ are not manipulated because the final products resulted in $Pb_2Ta_2O_7$. (Figure H.10-H.11)

Diffraction Studies (XRPD, SAED, TEM and elemental analysis)

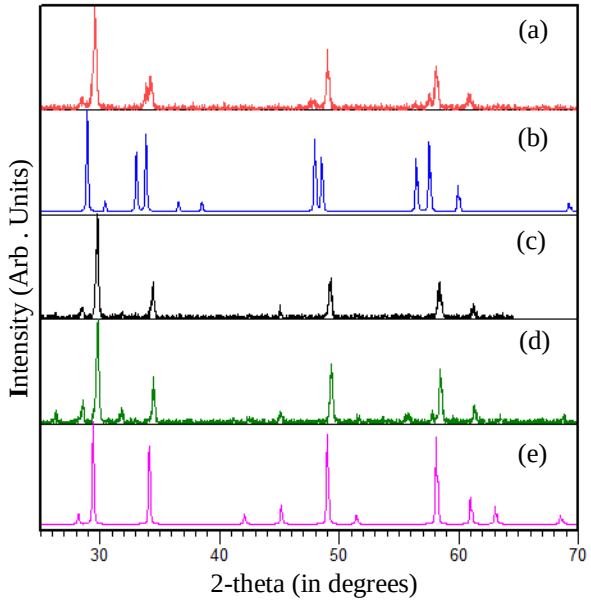

Figure H.10. PXRD of Rb_2CO_3 + PbO_2 + Ta_2O_5 at (a) 850° C 1d, (b) $Pb_3Ta_2O_8$, (c) 1000 ° C 1d, (d) 1000 ° C 2d and (e) $Pb_3Ta_4O_{13}$.

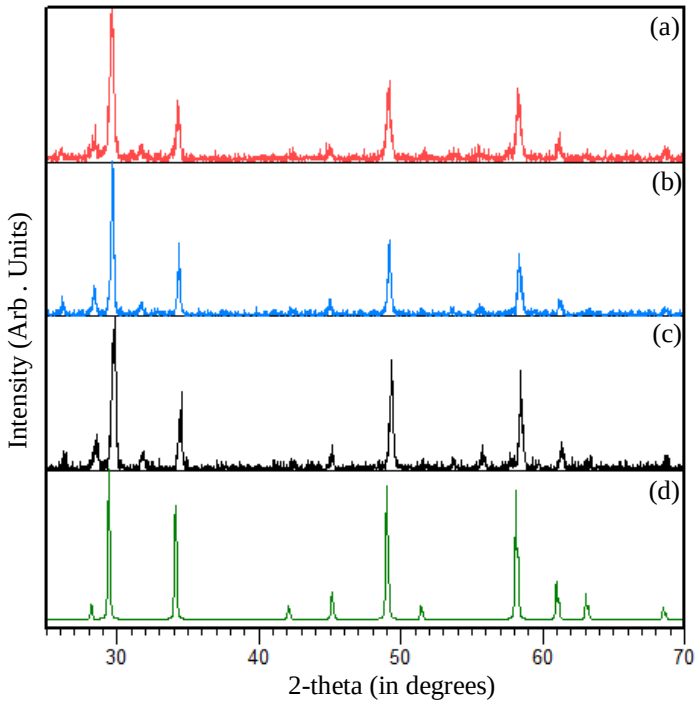

Figure H.11. PXRD of Cs_2CO_3 + PbO_2 + Ta_2O_5 at (a) 850° C 1d, (b) 1000 ° C 1d, (c) 1000 ° C 2d and (d) $Pb_3Ta_4O_{13}$.

XRPD

The unit cell parameters of $(CuCl)Pb_2Nb_3O_{10}$ series extracted from TEM confirm the refinement data (a=b≈3.9 Å for $(CuCl)Pb_2Nb_3O_{10}$). There is no evidence of starting material in final phase and the molar ratio from EDS fits well with refinement and expected ones 0.9(2):0.8(1):2:3.2(3) for Cu:Cl:Pb:Nb.

Magnetization

The magnetic susceptibility of $RbPb_2Nb_3O_{10}$ shows diamagnetic behavior which is expected for Pb^{2+} ($6s^2 5d^{10}$) but for $(CuCl)Pb_2Nb_3O_{10}$ the magnetization at 2 and 300K (Figure H.6) shows no coercivity (Figure H.12). The magnetic susceptibility in Figure H.7 shows no bifurcation of ZFC-FC.

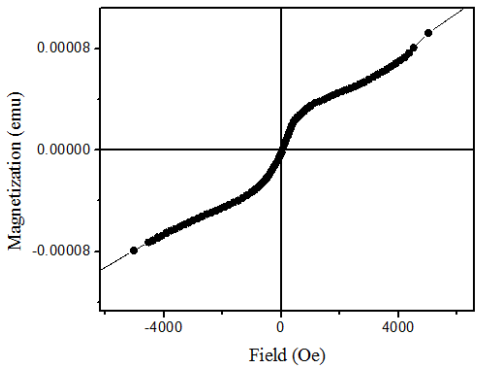

Figure H.12. Magnetization of $(CuCl)Pb_2Nb_3O_{10}$ at 300 K.

Thermal Analysis

Thermal analysis proved that the manipulated copper chloride phases will decompose and release chlorine gas as the temperature elevates. $PbNb_2O_6$ and Cu_6PbO_8 in $(CuCl)Pb_2Nb_3O_{10}$ similar to its iso-structural $(CuCl)Ca_2Nb_3O_{10}$ [17] that decompose to $CaNb_2O_6$ (Figure H.8) and are left over after decomposition and there is no evidence for formation of intermediate phase of $Cu_{0.5}Pb_2Nb_2O_{10}$ which is in opposite confirmation of $(CuCl)LaNb_2O_7$.[20]

References

[1] Viciu, L.; Caruntu, G.; Royant, N.; Koenig, J.; Zhou, W. L.; Kodenkandath, T. A.; Wiley, J. B. *Inorg. Chem*. **2002**, *41(13)*, 3385−3388.

[2] Montasserasadi, D.; Granier, M.; Spinu, L.; Chandra Rai, S.; Zhou, W.; Wiley, J. B., *J. Chem. Soc, Dalton Trans*. (**2015**) Accepted.

[3] Viciu, L.; Kodenkandath, T. A.; Wiley, J. B. *J. Solid State Chem*. **2007**, *180(2)*, 583−588.

[4] Choi, J.; Zhang, X.; Wiley, J. B. *Inorg. Chem*. **2009**, *48(11)*, 4811−4816.

[5] Ranmohotti, K. G. S.; Montasserasadi, D.; Choi, J.; Yao, Y.; Mohanty, D.; Josepha, E.; Adireddy, S.; Caruntu, G.; Wiley, J. B. *Mater. Res. Bull*. **2012**, *47(6)*, 1289−1294.

[6] Montasserasadi, D.; Mohanty, D.; Huq, A.; Heroux, L.; Payzant, E. A..; Wiley, J. B. J. *Inorg. Chem*. **2014**, *53(3)*, 1773-1778.

[7] Domen, K.; Kondo, J. N.; Hara, M.; Takata, T. *Bull. Chem. Soc. Jpn*. **2000**, *73(6)*, 1307−1331.

[8] Machida, M.; Yabunaka, J.; Kijima, T. *Chem. Mater*. **2000**, *12(3)*, 812-817.

[9] J. Yoshimura, Y. Ebina, J. Kondo, K. Domen, A. Tanaka, J. *Phys. Chem*. **1993**, *97*, 1970-1973.

[10] Sato, M.; Abo, J.; Jin, T.; Ohta, M. *J. Alloys Compd*. **1993**, *192(1-2)*, 81-83.

[11] Fukuoka, H.; Isami, T.; Yamanaka, S. *Chem. Lett*. **1997**, *26(8)*, 703−704.

[12] Li, B. W.; Osada, M.; Ozawa, T.C.; Sasaki, T.; *Chem. Mater*. **2012,** *24*, 3111-3113.

[13] Subramanian, M.A.; Gopalakrishnan, J.; Sleight, A.W. *Mater. Res. Bull*. **1988**, *23*, 837-842.

[14] Laugier, J and Bochu, B. LMGP-Suite, ENSP/Laboratoire des Matériaux et du Génie Physique, BP 46. 38042, Saint Martin d'Hères, France, 2002.

[15] Larson, A. C.; Von Dreele, R. B., General Structure Analysis System (GSAS) program. Rep. No. LA-UR-86748, Los Alamos National Laboratory, Los Alamos, CA, 1994.

[16] Toby, B. H. *J. Appl. Cryst*. **2001**, *34(2)*, 210−213.

[17] Kodenkandath, T. A.; Kumbhar, A. S.; Zhou, W. Wiley, J. B. *Inorg. Chem*. **2001**, *40(4)*, 710-714.

[18] Liang, Z. H.; Tang, K. B.; Chen, Q. W and Zheng, H. G., Acta Crystallogr., Sect. E: Struct. Rep. Online. **2009**, *E65*, i44.

[19] (a) O'Connor, C. *J. Prog. Inorg. Chem*. **1982**, *29,* 203-283; (b) Kittel, C. *Introduction to Solid State Physics*; 6th ed., Chapter 14; Eds.; John Wiley & Sons, Ltd: New York, 1978; pp 405.

[20] Hermann, A. T.; Wiley, J. B. *Mater. Res. Bull*. **2009**, *44(5)*, 1046-1050.

Appendix IX

Oxyhalides of $APrNb_2O_7$ Family (A: Li, MnF, MnCl, CoCl, CuF, FeCl)

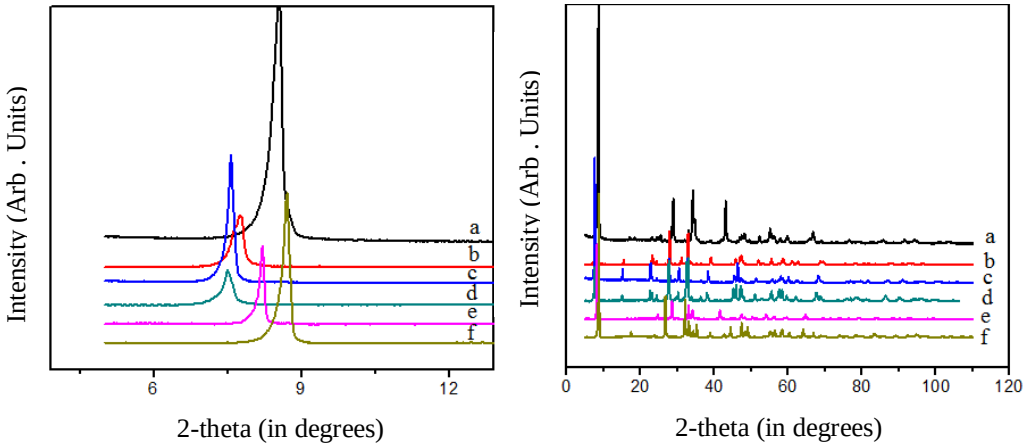

Figure I.1. X-ray powder diffraction patterns for (a) $LiPrNb_2O_7$, (b) $(MnF)PrNb_2O_7$, (c) $(MnCl)PrNb_2O_7$, (d) $(FeCl)PrNb_2O_7$, (e) $(CoCl)PrNb_2O_7$ and (f) $(CuF)PrNb_2O_7$.

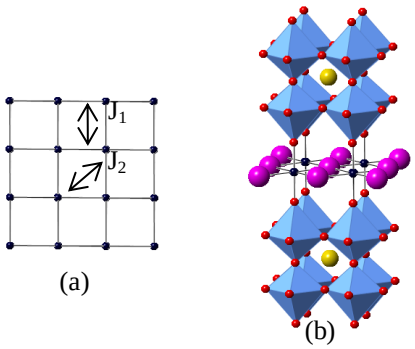

Figure I.2. (a) Frustration in square lattice on J_1-J_2 model (Fe: dark sphere) (b) Crystal structure. (NbO_6: light blue, Pr: yellow sphere, Cl: pink, Fe: dark and O: the red.

Table I.1. Unit cell parameters for $ALnNb_2O_7$ series (A: alkali metal, Ln: La, Pr)

Compound	Space Group	Unit cell (Å)	Volume (Å^3)	Ref
$LiPrNb_2O_7$	I4/mmm	3.8473(1), 20.4781(9)	303.11(2)	This work
$LiLaNb_2O_7$	I4/mmm	3.8837 (1), 20.371(1)	307.26	1
$NaPrNb_2O_7$	I4/mmm	3.897(4),20.9969(2)	318.94	This work
$NaLaNb_2O_7$ *	I4/mmm	3.9022(1), 21.1826(8)	319.33	2
$KPrNb_2O_7$	C222	3.911(9), 21.804(2), 3.816(5)	325.40	This work
$KLaNb_2O_7$	C222	3.9590(8), 21.798(1), 3.851(8)	332.34	3
$RbPrNb_2O_7$	Imma	5.4334(7), 22.012(1), 5.4549(7)	654.84(7)	4
$RbLaNb_2O_7$	Imma	5.4941(4), 21.9901(6), 5.4925(4)	663.58	5
$CsPrNb_2O_7$	P4/mmm	3.8668(2), 11.163(1)	166.92(2)	4
$CsLaNb_2O_7$	P4/mmm	3.908(1), 11.160(4)	170.44	6
$(CuF)PrNb_2O_7$	Pbam	7.7691(3),7.6809(7), 10.5434(4)	629.16(2)	This work
$(CuCl)PrNb_2O_7$	Pbam	7.7328(6),7.7113(4), 11.6706(3)	695.92(4)	4
$(CuCl)LaNb_2O_7$	Pbam	7.76290(8),7.76197(7),11.73390(6)	707.03	7
$(CoCl)PrNb_2O_7$	Pbam	7.7358(2),7.7124(5), 11.6796(7)	696.83(3)	This work
$(CoCl)LaNb_2O_7$	P4/mmm	3.888(1), 11.614(7)	175.6	8
$(FeCl)PrNb_2O_7$	P4/mmm	3.8579(3), 11.7883(9)	175.45(3)	This work
$(FeCl)LaNb_2O_7$	P4/mmm	3.879(1), 11.861(5)	178.46	9
$(MnF)PrNb_2O_7$	P4/mmm	3.8466(3),10.9009(1)	161.29(2)	This work
$(MnCl)PrNb_2O_7$	P4/mmm	3.8648(4),11.8961(1)	177.69(5)	This work
$(MnCl)LaNb_2O_7$	P4/mmm	3.900(2),12.019(7)	182.8	10

*: anhydrate form. a=3.8981(1) c=25.7131(9) Å for hydrated form.

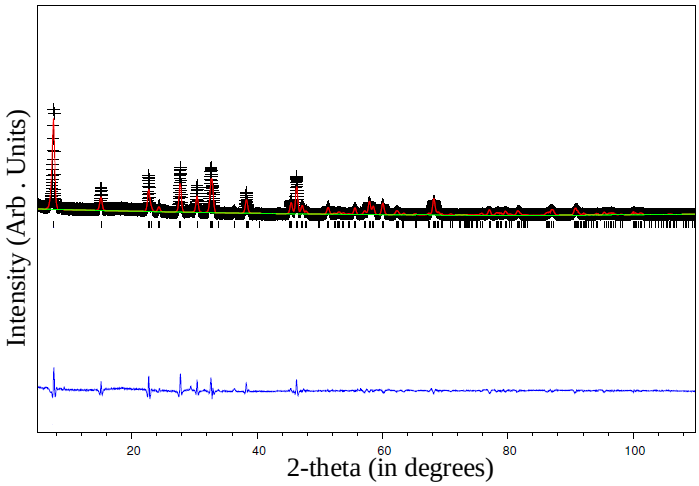

Figure I.3. Rietveld refinement of $(FeCl)PrNb_2O_7$. Observed data are indicated by crosses, calculated pattern by a solid line (red), and the bottom curve (blue) is the difference plot. The green line is background. (R_p=12.64% R_{wp}= 14.42% χ^2 =1.396

Table I.2. Crystallographic Data for (FeCl)$PrNb_2O_7$.

Atom	Site	x	y	z	g	U_{iso} ($Å^2$)
Fe	4o	0.508(1)	0.5	0.5	0.26(2)	0.0018(5)
Cl	1b	0	0	0.5	1.06(5)	0.047(7)
Pr	1a	0	0	0	1.04(1)	0.0007(2)
Nb	2h	0.5	0.5	0.1901(2)	1.03(1)	0.0050(5)
O_1	4i	0	0.5	0.1475(5)	1	0.0108(3)
O_2	2h	0.5	0.5	0.3354(3)	1	0.0126(2)
O_3	1c	0.5	0.5	0	1	0.015(1)

P4/mmm Z=1 a=3.8579(3) Å, c= 11.7883(9) Å V=175.45(3) $Å^3$.

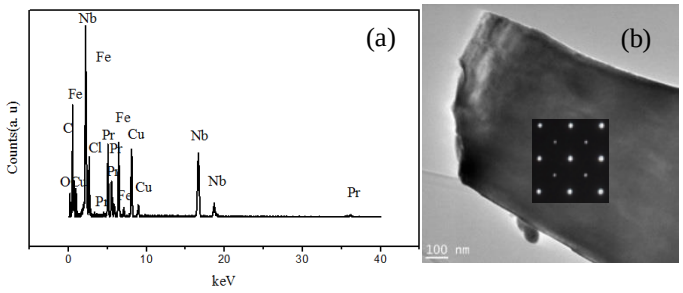

Figure I.4. (a) EDS of (FeCl)$PrNb_2O_7$ and (b)TEM with SAED inset and (B = [001])

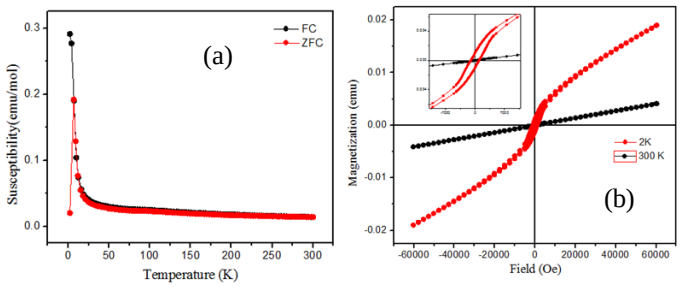

Figure I.5. (a) Temperature dependence of magnetic susceptibility and (b) M (H) for (FeCl)$PrNb_2O_7$ at 2 K and 300 K. The inset shows the hysteresis about 2000 Oe at 2 K.

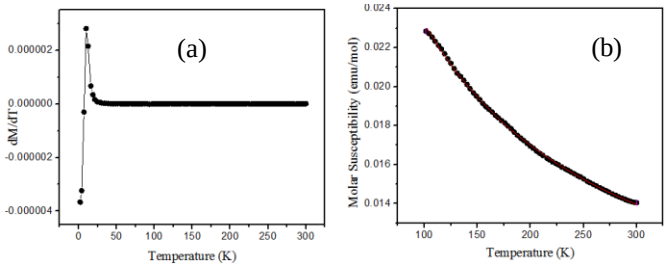

Figure I.6. (a) Temperature derivative *dM/dT* of the ZFC data and (b) temperature dependence susceptibility for (FeCl)$PrNb_2O_7$ at 100 Oe from 100-300 K.

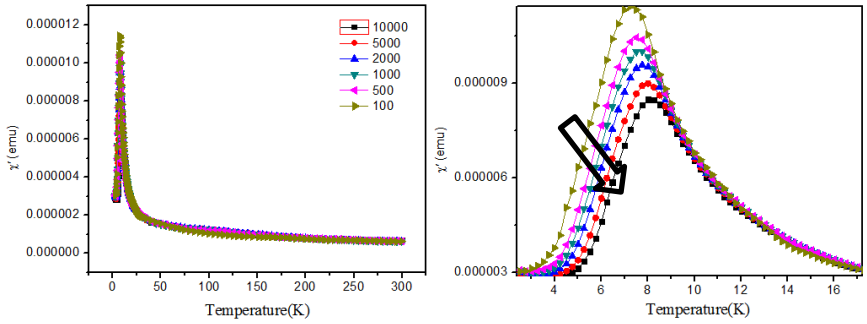

Figure I.7. Real susceptibility of (FeCl)$PrNb_2O_7$ at 10 Oe with 0.1, 0.5, 1.0, 2.0, 5.0 and 10.0 kHz frequencies.(arrow shows movement of cusp at different frequencies)

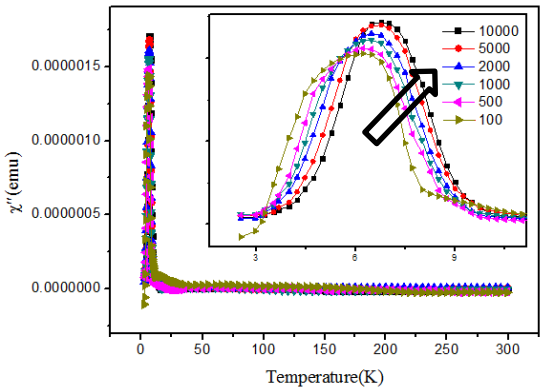

Figure I.8. Imaginary susceptibility for (FeCl)$PrNb_2O_7$ at 10 Oe and 0.1,0.5,1,2,5,10 kHz.

Table I.3. Thermal stability of $APrNb_2O_7$ family under Ar and O_2 atmospheres.

Compound	Decomposition Products under Ar and (O_2)
$LiPrNb_2O_7$	$PrNbO_4$ + $LiNbO_3$
(MnCl)$PrNb_2O_7$	$PrNbO_4$ + $MnNb_2O_6$ ($MnNbO_4$)
(FeCl)$PrNb_2O_7$	$PrNbO_4$ + $FeNb_2O_6$ ($FeNbO_4$)
(CoCl)$PrNb_2O_7$	$PrNbO_4$ + $CoNb_2O_6$ ($CoNbO_4$)
(MnF)$PrNb_2O_7$	$PrNbO_4$ + $MnNb_2O_6$
(CuF)$PrNb_2O_7$	$PrNbO_4$ + $CuNb_2O_6$

Table I.4. Crystallographic Data for $LiPrNb_2O_7$ from X-ray data.

Atom	Site	x	y	z	g	U_{iso}(Å^2)
Li	4d	0	0.5	0.25	0.5	0.080(6)
Pr	2a	0	0	0	1.02(4)	0.0042(7)
Nb	4e	0	0	0.3902(2)	1.1(1)	0.0059(1)
O_1	8g	0	0.5	0.1022(1)	1	0.088(1)
O_2	4e	0	0	0.3151(2)	1	0.0026(2)
O_3	2b	0	0	0.5	1	0.027(17)

*I*4/*mmm*; Z=2, a = 3.8473(1) Å, c =20.4781(9) Å, Volume = 303.11(2) Å^3

Table I.5. Selected bond lengths for $LiPrNb_2O_7$ *vs* $LiLaNb_2O_7$ [1]

$LiLaNb_2O_7$ [1]		**$LiPrNb_2O_7$**	
Bond Type	**Length (Å)**	**Bond Type**	**Length (Å)**
Li-O_2×4	2.234	Li-O_2×4	2.3310(1)
La-O_1×8	2.660	Pr-O_1×8	2.7290(2)
La-O_3×4	2.744	Pr-O_3×4	2.7206(1)
Nb-O_1×4	1.990	Nb-O_1×4	1.9480(6)
Nb-O_2×1	1.720	Nb-O_2×1	1.5582(3)
Nb-O_3×1	2.262	Nb-O_3×1	2.2445(4)

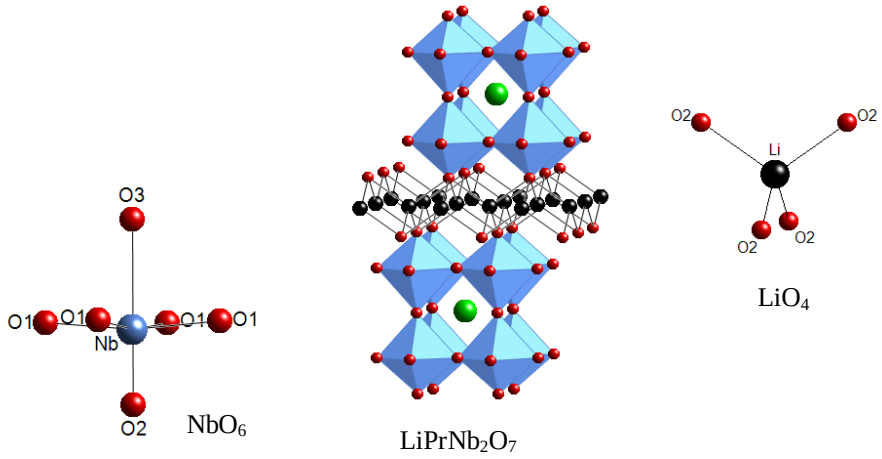

Figure I.9. Crystal structure of $LiPrNb_2O_7$.(Pr: green sphere, NbO_6: light blue octahedra, O: red sphere, Li: dark)

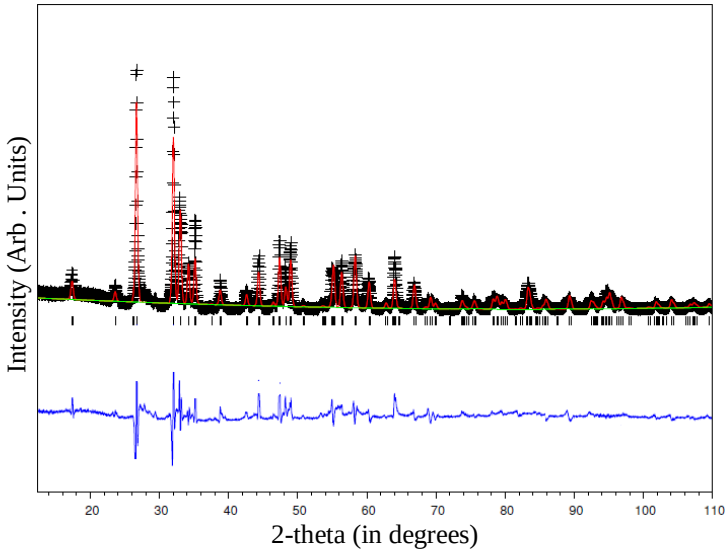

Figure I.10. Rietveld refinement of $LiPrNb_2O_7$. Observed data are indicated by crosses, calculated pattern by a solid line (red), and the bottom curve (blue) is the difference plot. The green line is background.

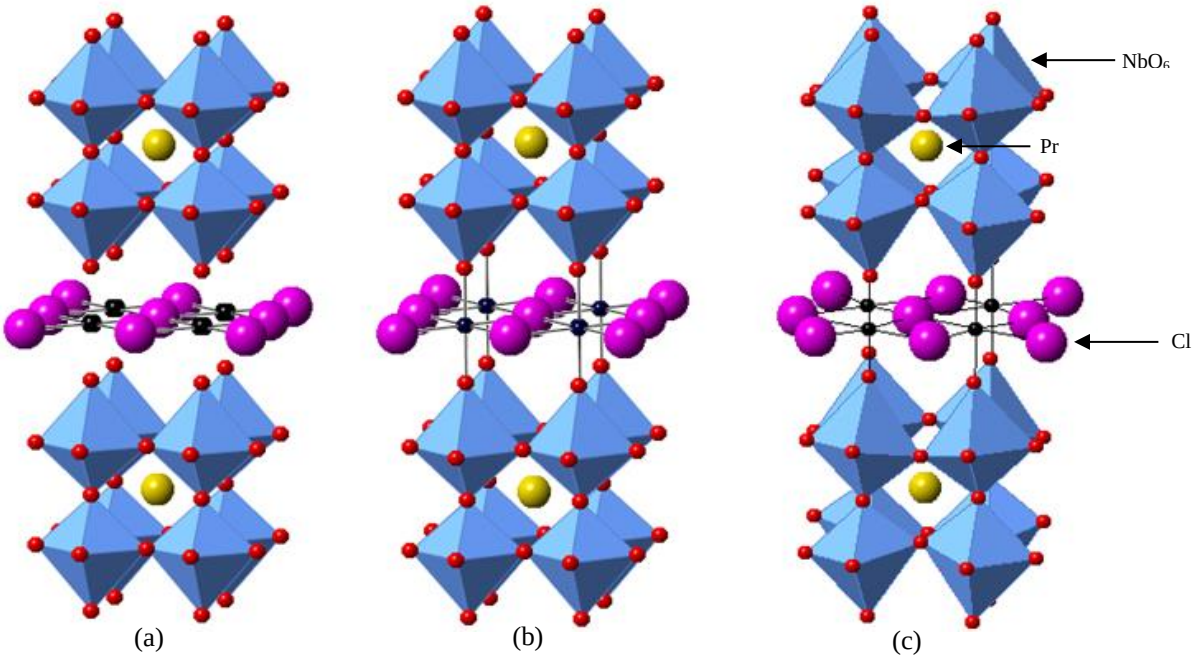

Figure I.11. Crystal structure of (a) $(MnCl)PrNb_2O_7$ (b) $(FeCl)PrNb_2O_7$ and (c) $(CoCl)PrNb_2O_7$

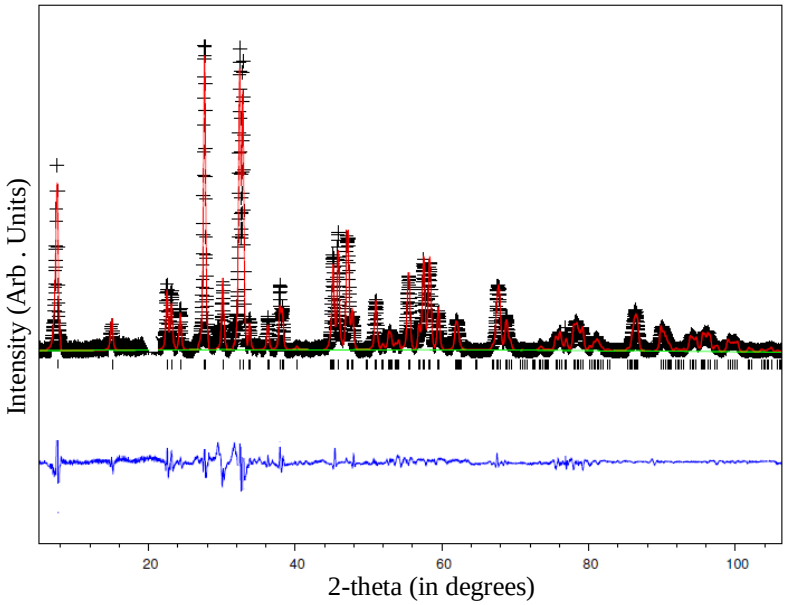

Figure I.12. Rietveld refinement of (MnCl)$PrNb_2O_7$. Observed data are indicated by crosses, calculated pattern by a solid line (red), and the bottom curve (blue) is the difference plot. The green line is background.

Table I.6. Crystallographic Data for (MnCl)$PrNb_2O_7$ from X-ray data.

Atom	Site	x	y	z	g	U_{iso} ($Å^2$)
Mn	4o	0.491(2)	0.5	0.5	0.24(2)	0.0018(5)
Cl	1b	0	0	0.5	1.04(3)	0.047(7)
Pr	1a	0	0	0	0.983(3)	0.0007(2)
Nb	2h	0.5	0.5	0.1881(3)	1.03(1)	0.0050(5)
O_1	4i	0	0.5	0.1489(5)	1	0.0108(3)
O_2	2h	0.5	0.5	0.3365(3)	1	0.0126(2)
O_3	1c	0.5	0.5	0	1	0.015(1)

P4/mmm, Z=1 a=3.8648(4) Å, c= 11.8961(1) Å V=177.69(5)$Å^3$ R_p=14.6% R_{wp}= 16.52% χ^2 =1.65

Table I.7. Selected bond lengths for (MnCl)$PrNb_2O_7$ *vs* (FeCl)$PrNb_2O_7$

(FeCl)$PrNb_2O_7$		**(MnCl)$PrNb_2O_7$**	
Bond Type	**Length (Å)**	**Bond Type**	**Length (Å)**
Fe-O_2	1.936(2)×2	Mn-O_2	1.945(6)×2
Fe-Cl	2.706(6)×2 2.750(3)×2	Mn-Cl	2.709(4)×2 2.757(3)×2
Pr-O_1	2.597(2)×8	Pr-O_1	2.621(4)×8
Pr-O_3	2.728(1)×4	Pr-O_3	2.733(2)×4
Nb-O_1	1.994(3)×4	Nb -O_1	1.988(5)×4
Nb -O_2	1.713(2)×1	Nb -O_2	1.765(2)×1
Nb -O_3	2.246(3)×1	Nb -O_3	2.238(7)×1

Table I.8. Selected Bond Lengths of (FeCl)$PrNb_2O_7$ and (FeCl)$LaNb_2O_7$ [9]

(FeCl)$PrNb_2O_7$		**(FeCl)$LaNb_2O_7$**	
Bond Type	**Length (Å)**	**Bond Type**	**Length (Å)**
Fe-O_2	1.936(2)×2	Fe-O_3	1.972(6)×2
Fe-Cl	2.706(6)×2 2.750(3)×2	Fe-Cl	2.536(4)×2 2.967(5)×2
Pr-O_1	2.597(2)×8	La-O_1	2.669(2)×2
Pr-O_3	2.728(1)×4	La-O_3	2.742(1)×2
Nb-O_1	1.994(3)×4	Nb -O_1	1.986(1)×4
Nb -O_2	1.713(2)×1	Nb -O_2	1.723(6)×1
Nb -O_3	2.246(3)×1	Nb -O_3	2.260(1)×1

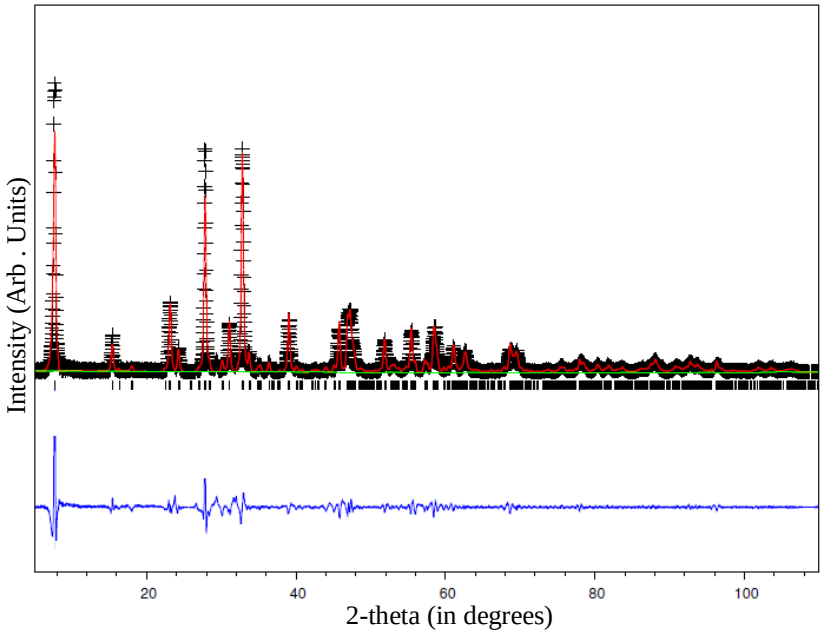

Figure I.13. Rietveld refinement of (CoCl)$PrNb_2O_7$. Observed data are indicated by crosses, calculated pattern by a solid line (red), and the bottom curve (blue) is the difference plot. The green line is background.

Table I.9. Crystallographic Data for (CoCl)$PrNb_2O_7$ from X-ray data.

Atom	Site	x	y	z	g	U_{iso} ($Å^2$)
Co	4h	0.7319(2)	0.5249(1)	0.5	0.93(2)	0.0042(4)
Cl	4h	0.5550(4)	0.2293(6)	0.5	1.09(4)	0.032(1)
Pr	4g	0.0005(3)	0.2589(5)	0	0.96(2)	0.0058(2)
Nb	8i	0.7469(1)	0.4993(3)	0.8099(3)	1.04(4)	0.0009(1)
O_1	4f	0	0.5	0.8350(3)	1	0.0032(1)
O_2	8i	0.2802(4)	0.7650(7)	0.8339(3)	1	0.0018(1)
O_3	8i	0.2315(1)	0.0422(1)	0.6472(2)	1	0.0095(3)
O_4	4g	0.7465(2)	0.5535(1)	0	1	0.0043(5)
O_5	4e	0	0	0.8760(1)	1	0.0032(7)

Pbam, Z=4 a=7.7358(2) Å, b=7.7124(5) Å c= 11.6796(7) Å V=696.83(3)$Å^3$ R_p=12.90% R_{wp}= 13.86% χ^2 =1.267

Table I.10. Crystallographic Data for (CuF)$PrNb_2O_7$ from X-ray data.

Atom	Site	x	y	z	g	U_{iso} (Å^2)
Cu	4h	0.7295(3)	0.5217(2)	0.5	0.93(2)	0.0042(4)
F	4h	0.5304(1)	0.2133(1)	0.5	1.09(4)	0.032(1)
Pr	4g	0.9857(2)	0.2271(3)	0	0.96(2)	0.0058(2)
Nb	8i	0.7408(2)	0.4888(1)	0.7928(3)	1.04(4)	0.0009(1)
O_1	4f	0	0.5	0.1755(1)	1	0.0032(1)
O_2	8i	0.2843(2)	0.6973(1)	0.7388(6)	1	0.0018(1)
O_3	8i	0.2228(6)	0.1570(1)	0.600(2)	1	0.0095(3)
O_4	4g	0.7315(2)	0.6013(2)	0	1	0.0043(5)
O_5	4e	0	0	0.8144(4)	1	0.0032(7)

Pbam Z=4 a=7.7691(3) Å, b=7.6809(7), c= 10.5434(4) Å V=629.16(2)Å^3 R_p=8.67% R_{wp}= 12.03% χ^2 =1.628

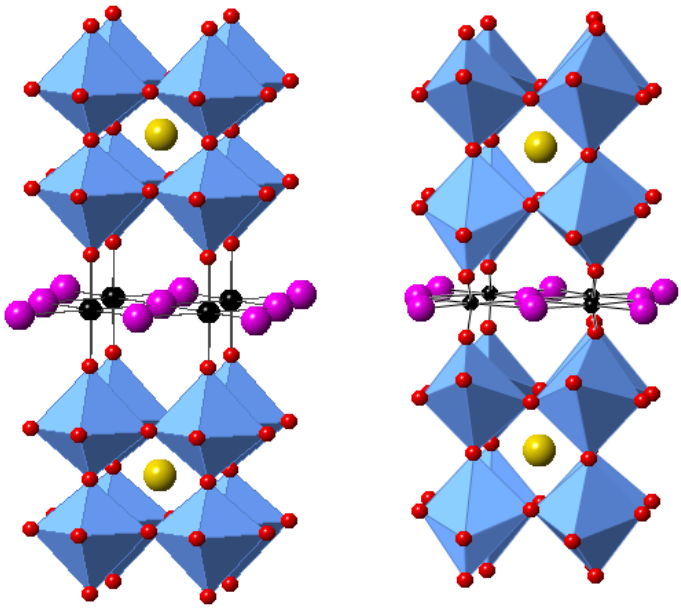

(a) (b)

Figure I.14. Crystal structure of (a) (MnF)$PrNb_2O_7$ and (b) (CuF)$PrNb_2O_7$.

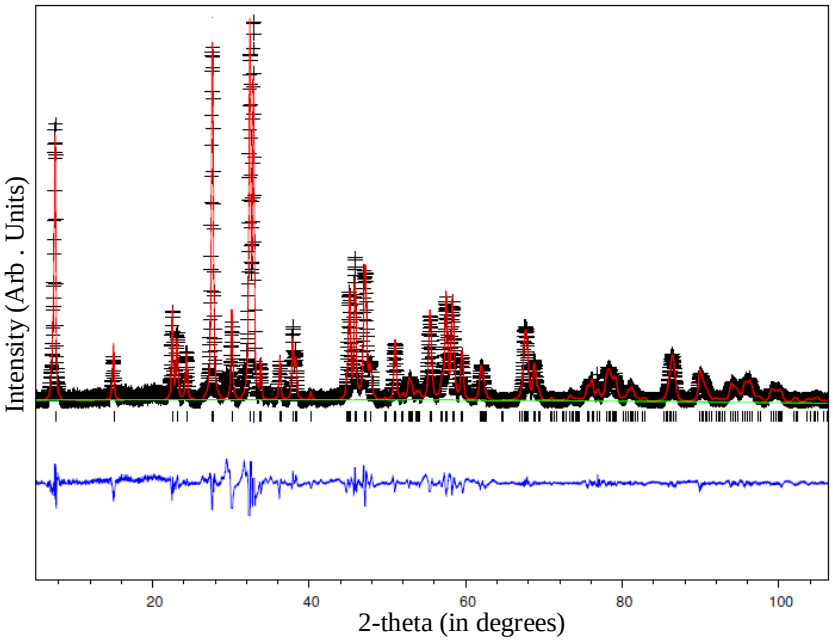

Figure I.15. Rietveld refinement of (MnF)$PrNb_2O_7$. Observed data are indicated by crosses, calculated pattern by a solid line (red), and the bottom curve (blue) is the difference plot. The green line is background

Table I.11. Crystallographic Data for (MnF)$PrNb_2O_7$ from X-ray data.

Atom	Site	x	y	z	g	U_{iso} ($Å^2$)
Mn	1d	0.5	0.5	0.5	0.97(9)	0.0044(3)
F	1b	0	0	0.5	0.95(8)	0.027(7)
Pr	1a	0	0	0	1.09(9)	0.0013(4)
Nb	2h	0.5	0.5	0.1894(2)	1.11(4)	0.0011(5)
O_1	4i	0	0.5	0.1655(5)	1	0.0074(4)
O_2	2h	0.5	0.5	0.3179(2)	1	0.0043(2)
O_3	1c	0.5	0.5	0	1	0.0053(1)

P4/mmm, Z=1 a=3.8466(3) Å, c= 10.9009(1) Å V=161.29(2)$Å^3$ R_p=8.67% R_{wp}= 12.03% χ^2 =1.628

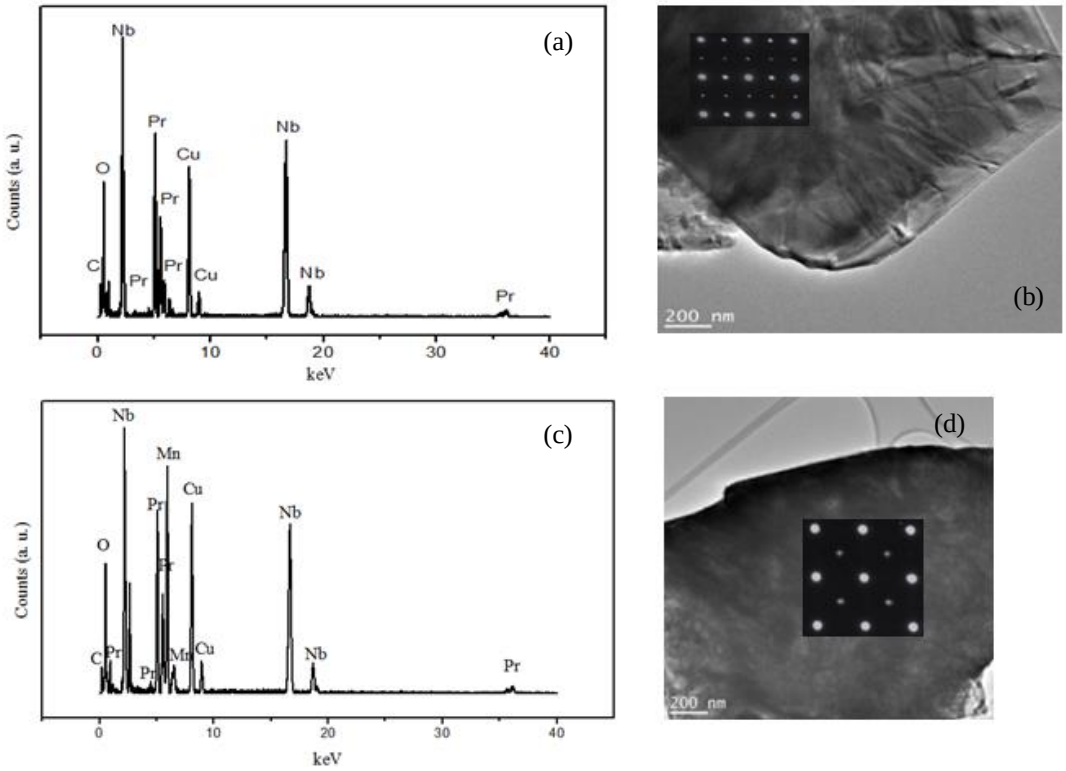

Figure I.16. EDS and SAED of $LiPrNb_2O_7$ (a-b) and $(MnCl)PrNb_2O_7$ (c-d).

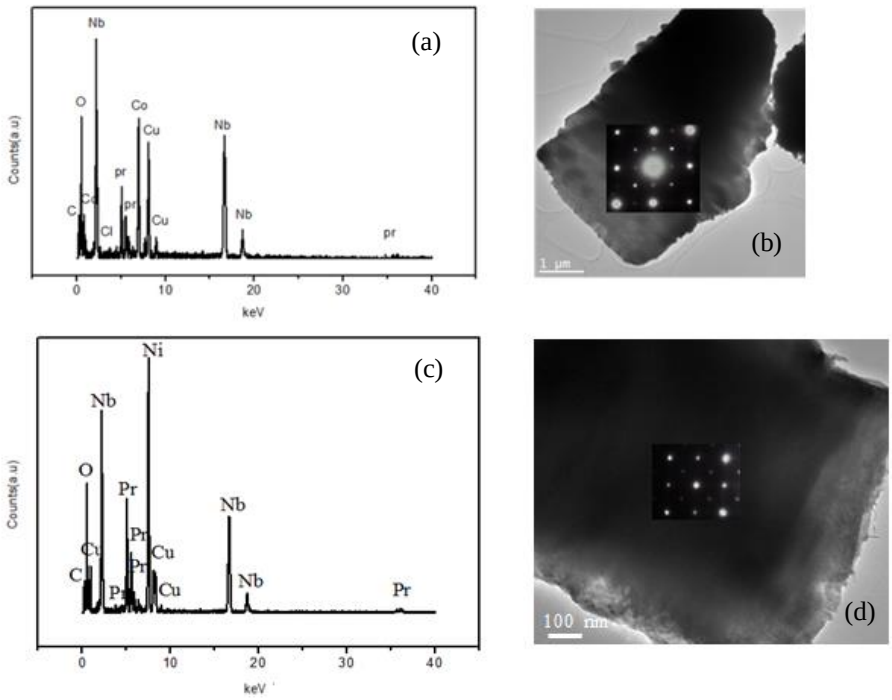

Figure I.17. EDS and SAED of $(CoCl)PrNb_2O_7$ (a-b) and$(CuF)PrNb_2O_7$ (c-d).

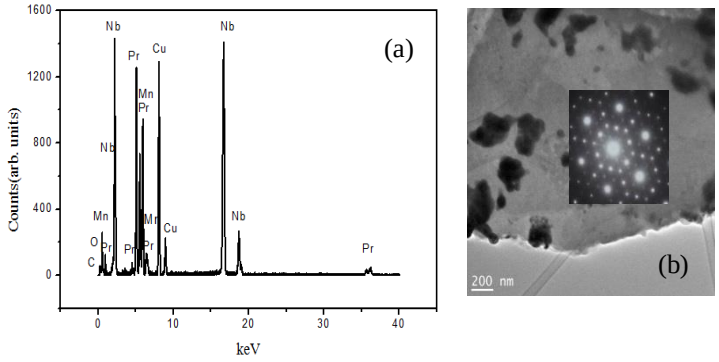

Figure I.18. (a) EDS of (MnF)$PrNb_2O_7$ and (b)SAED.

Table I.12. Elemental Analysis of *A*$PrNb_2O_7$ series.

Compound	Elemental Analysis	refinement
$LiPrNb_2O_7$ (Rb:Pr:Nb)	0.02(4):1:2.09(2)	1.02(4):1.1(1)
(MnF)$PrNb_2O_7$ Mn:F:Pr:Nb	2.0(5):1.1(9):1:1.9(6)	0.92(3):0.91(3):1.09(3):1.09(1)
(MnCl)$PrNb_2O_7$	0.93(3):0.91(5):1:2.02(6)	0.98(8):1.12(3):0.98(8):1.00(1)
(FeCl)$PrNb_2O_7$ Fe:Cl:Pr:Nb	2.5(2):1:1.83(9)	0.96(5):0.98(4):1.09(2):1.05(2)
(CoCl)$PrNb_2O_7$ Co:Cl:Pr:Nb	2.5(2):1:1.83(9)	0.93(4):0.91(5):1.07(4):1.09(2)
(CuF)$PrNb_2O_7$ Cu:F:Pr:Nb	2.5(2):1:1.83(9)	0.97(3):0.91(3)1.09(3):1.09(1)

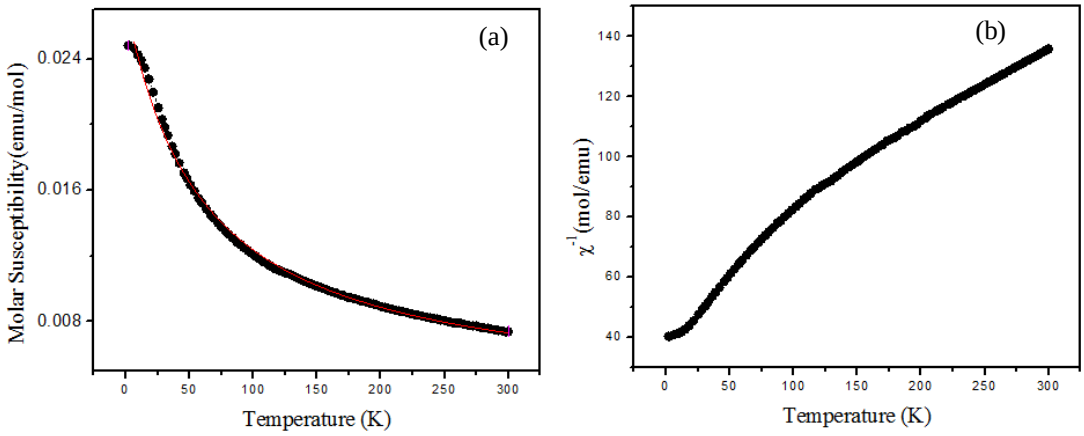

Figure I.19. (a)Temperature dependence susceptibility and (b) inverse susceptibility for $LiPrNb_2O_7$ at 100 Oe.

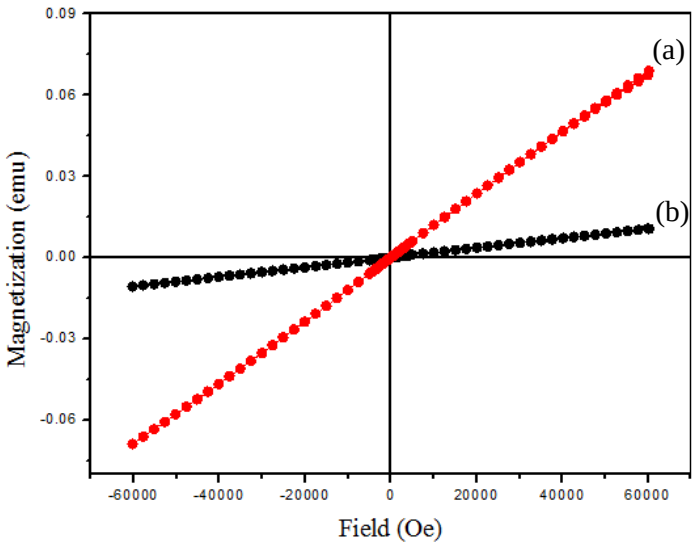

Figure I.20. M(H) for $LiPrNb_2O_7$ at (a) 2 K and (b) 300 K.

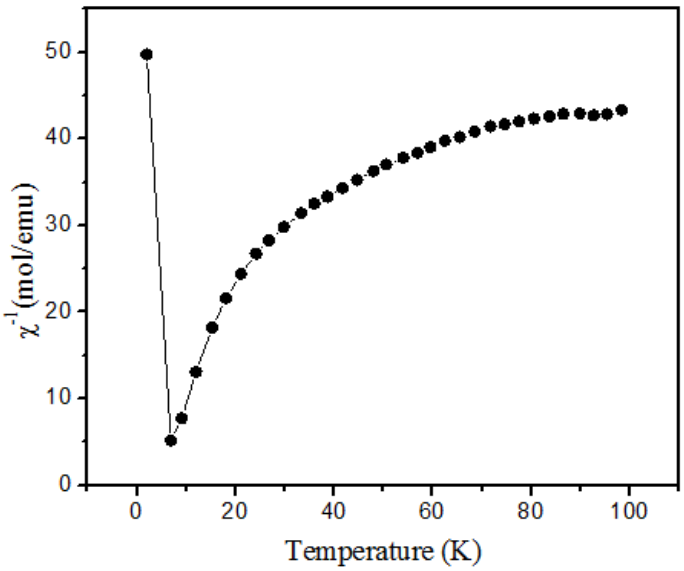

Figure I.21. The inverse susceptibility for $(FeCl)PrNb_2O_7$ at 100 Oe.

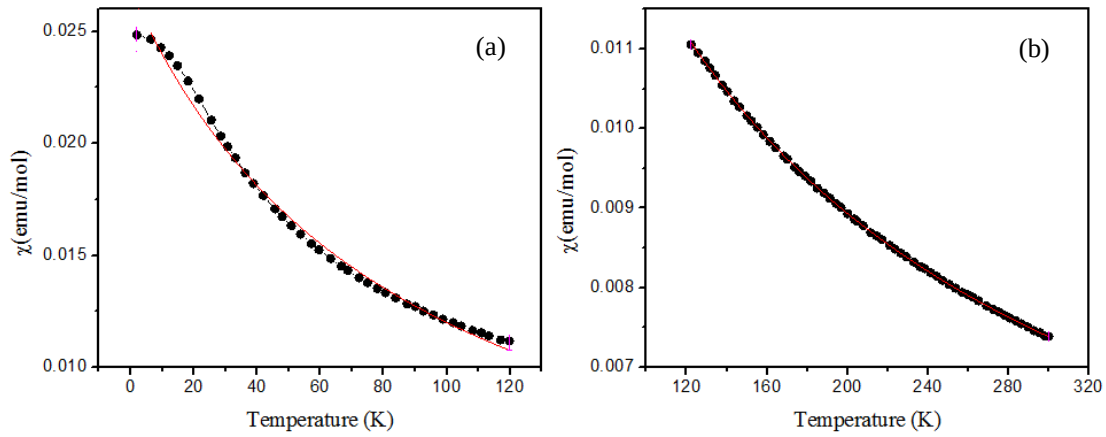

Figure I.22. The magnetic susceptibility for $LiPrNb_2O_7$ at (a) 2-120 K and (b) 120-300 K at 100 Oe. The red line is the Currie-Weiss fitting.

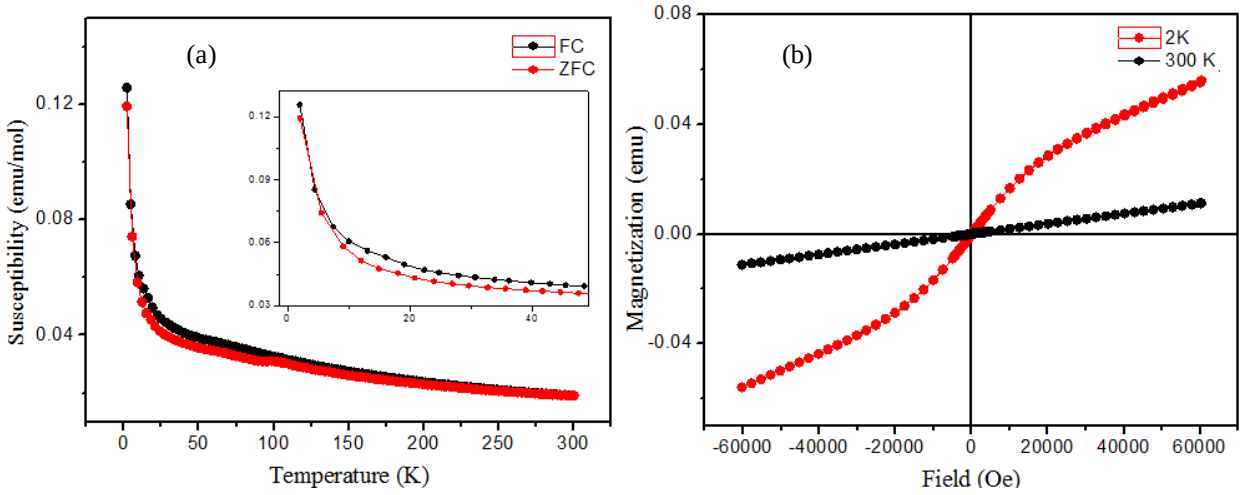

Figure I.23. (a) The magnetic susceptibility for $(MnCl)PrNb_2O_7$ at 100 Oe (b) M(H) at 2 K and 300 K.

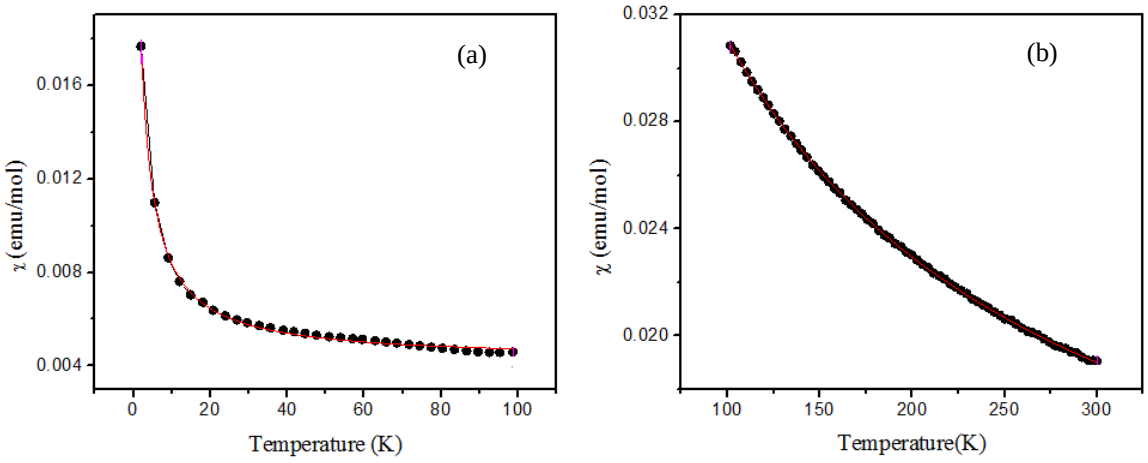

Figure I.24. The magnetic susceptibility for $(MnCl)PrNb_2O_7$ at 100 Oe.

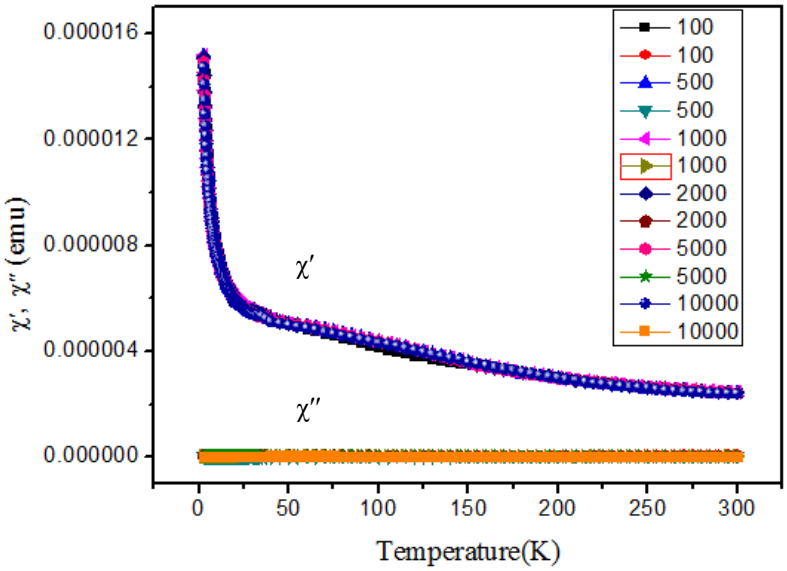

Figure I.25. AC susceptibility of $(MnCl)PrNb_2O_7$ at 10 Oe and 0.1, 0.5, 1, 2, 5, 10 kHz.

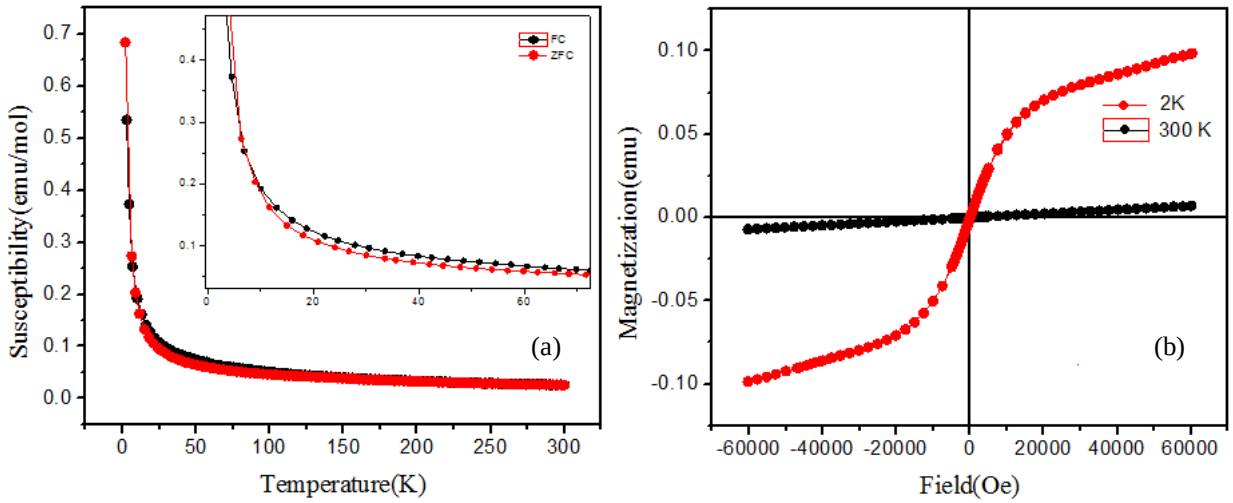

Figure I.26. (a) The magnetic susceptibility for $(MnF)PrNb_2O_7$ at 100 Oe (b) M(H) at 2 K and 300 K.

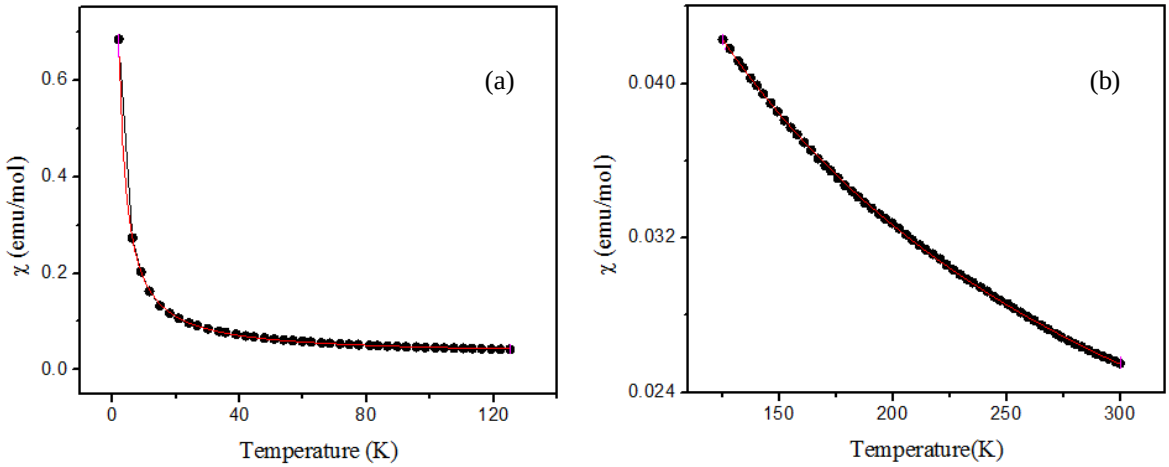

Figure I.27. The magnetic susceptibility for $(MnF)PrNb_2O_7$ at 100 Oe. (a) 2-120 K and (b) 120-300 K.

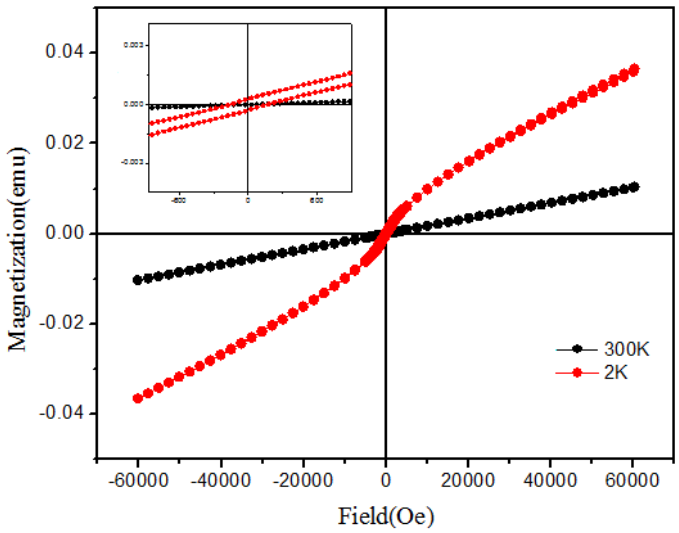

Figure I.28. M(H) for (CoCl)$PrNb_2O_7$ at 2 and 300 K. The inset shows the hysteresis about 400 Oe at 2 K.

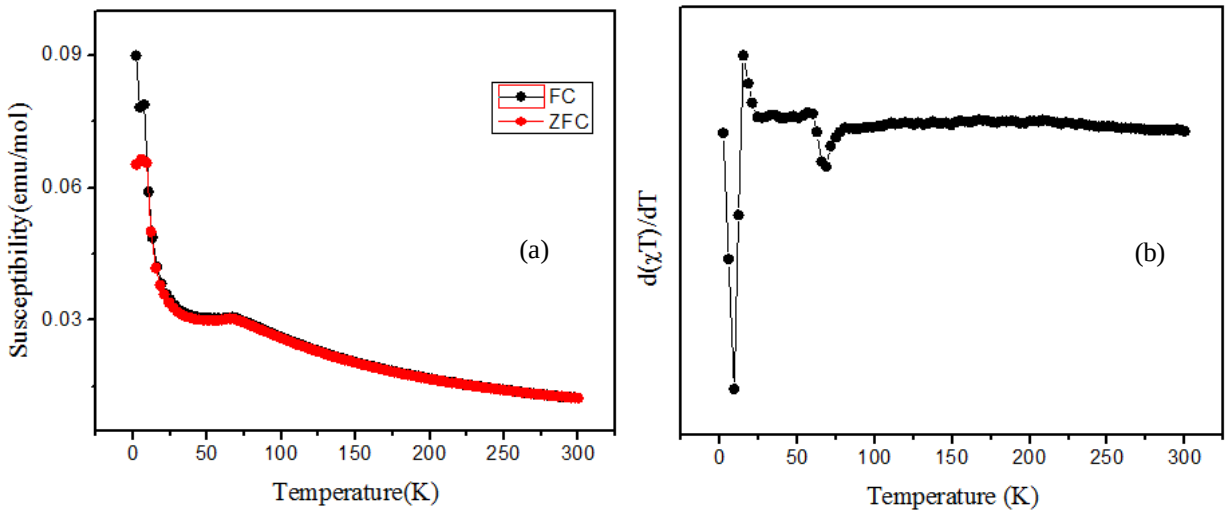

Figure I.29. (a) The magnetic susceptibility for (CoCl)$PrNb_2O_7$ at 100 Oe. (b) Temperature derivative $d(\chi T)/dT$ of the ZFC data.

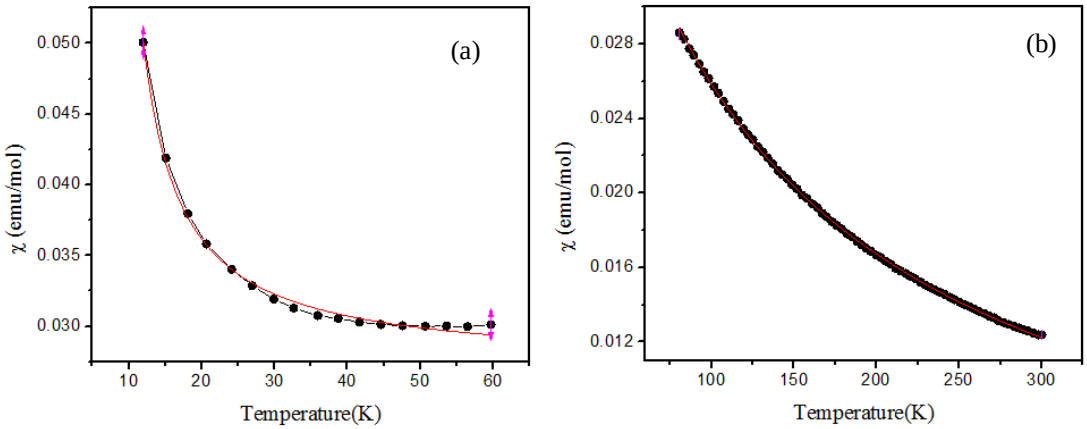

Figure I.30. The magnetic susceptibility for (CoCl)$PrNb_2O_7$ at 100 Oe (a) 10-60 K and (b) 80-300 K.

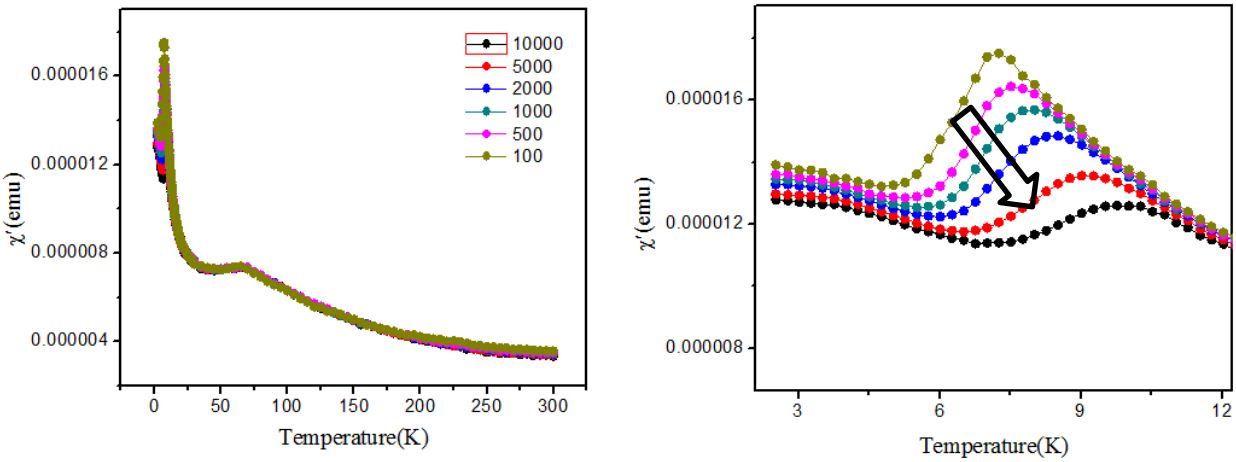

Figure I.31. Real susceptibility of (CoCl)$PrNb_2O_7$ at 10 Oe with 0.1, 0.5, 1.0, 2.0, 5.0 and 10.0 kHz frequencies. (arrow shows movement of cusp at different frequencies)

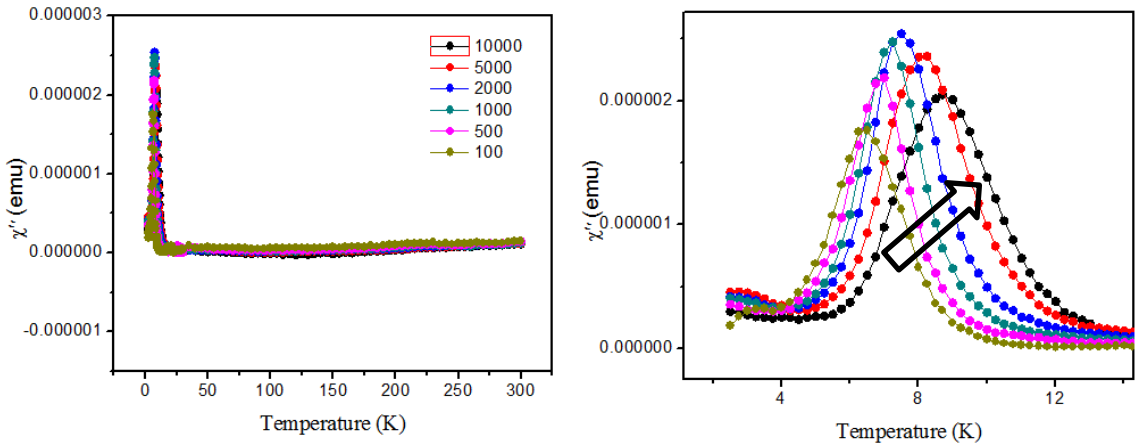

Figure I.32. Imaginary susceptibility of $(CoCl)PrNb_2O_7$ at 10 Oe with 0.1, 0.5, 1.0, 2.0, 5.0 and 10.0 kHz frequencies. (arrow shows movement of cusp at different frequencies)

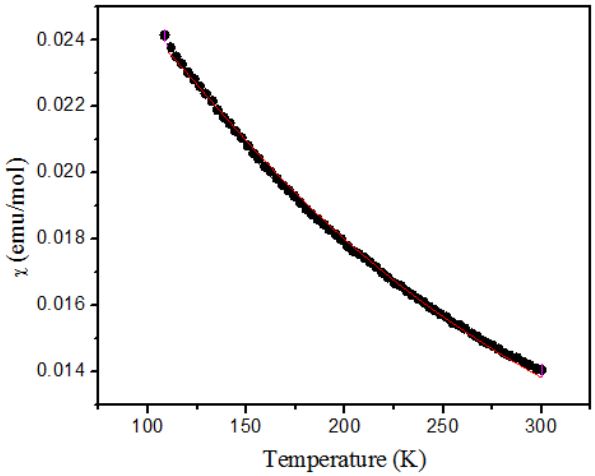

Figure I.33. Rushbrook and Wood model fitting for $(CoCl)PrNb_2O_7$ 2D AFM Heisenberg system with S = 5/2 to DC susceptibility data. The solid red line is the model and the black is DC susceptibility at 100 Oe in 100 - 300 K.

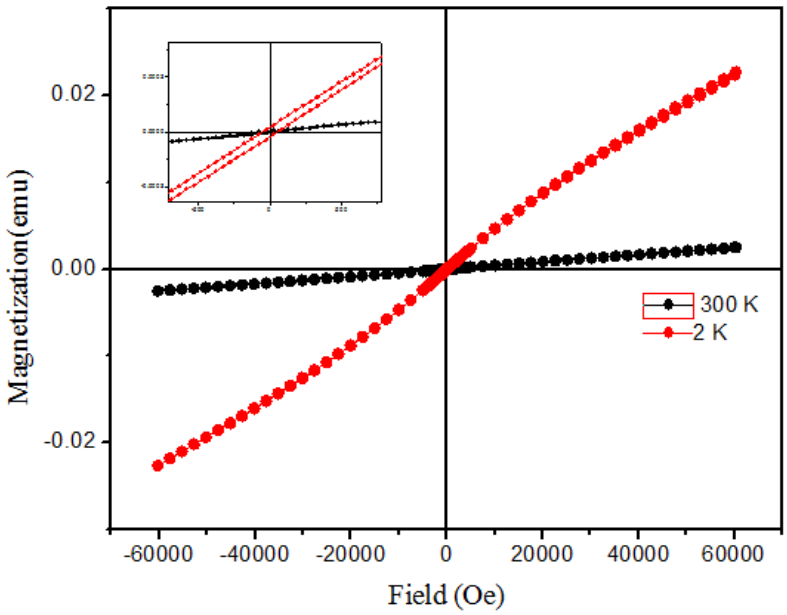

Figure I.34. Magnetization for (CuF)$PrNb_2O_7$ at 2 K and 300 K. The inset shows the hysteresis about 120 Oe at 2 K.

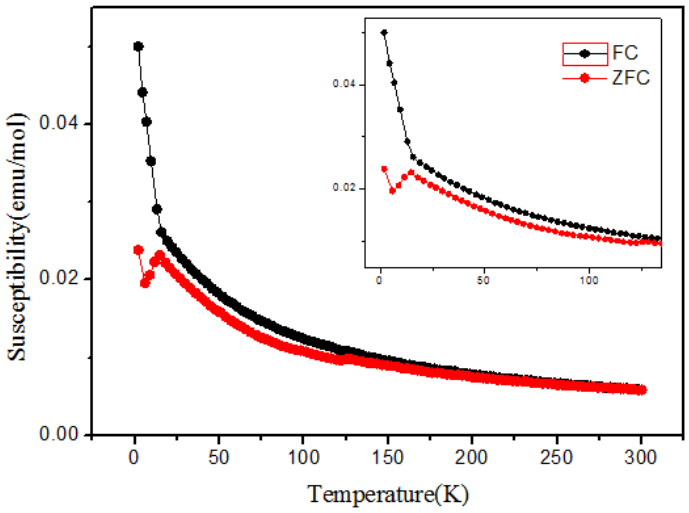

Figure I.35. The magnetic susceptibility for (CuF)$PrNb_2O_7$ at 100 Oe.

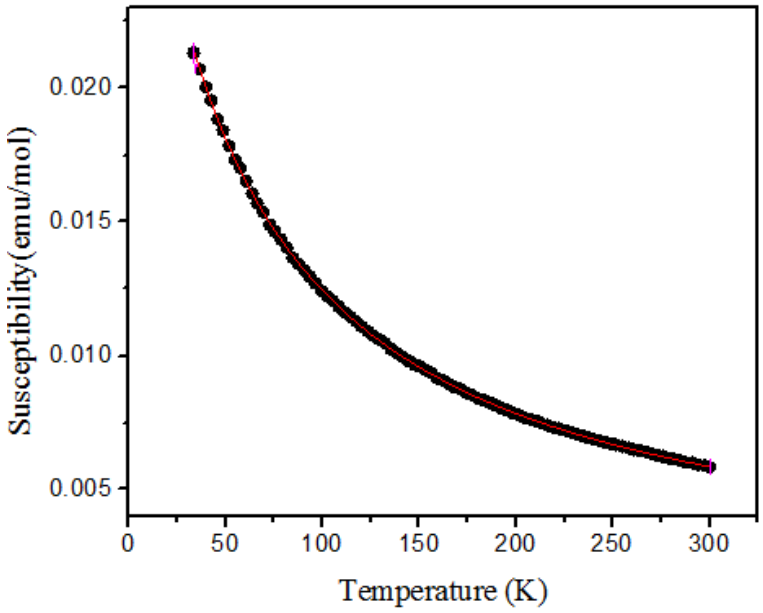

Figure I.36. The magnetic susceptibility for (CuF)$PrNb_2O_7$ at 100 Oe from 30-300 K.

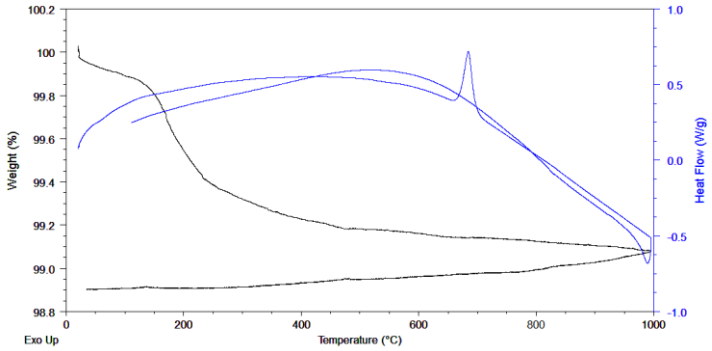

Figure I.37. TGA/DSC of $LiPrNb_2O_7$ under Ar.

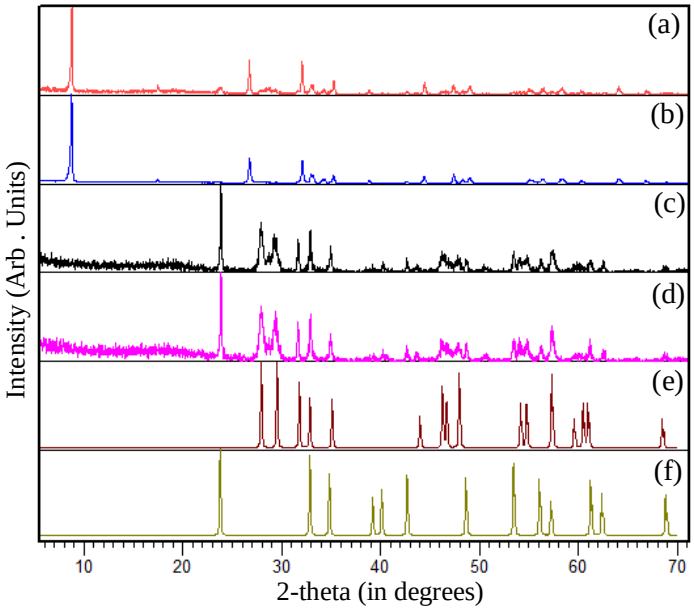

Figure I.38. (a) $LiPrNb_2O_7$ after TGA at 660 under Ar, (b) $LiPrNb_2O_7$, (c) $LiPrNb_2O_7$ after TGA at 1000 (Ar), (d) $LiPrNb_2O_7$ after TGA at 1000 (Ar:O_2 50:50), (e) $PrNbO_4$ and (f) $LiNbO_3$.

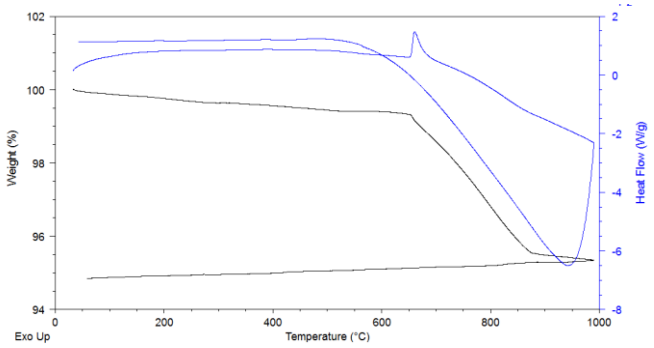

Figure I.39. TGA/DSC result for $(MnCl)PrNb_2O_7$ under Ar.

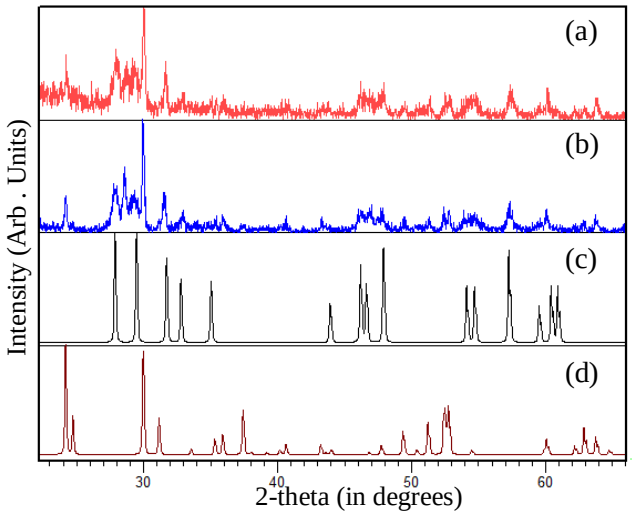

Figure I.40. (a) XRPD for (MnCl)$PrNb_2O_7$ after TGA at 1000 (Ar), (b) (MnCl)$PrNb_2O_7$ after TGA at 1000 (Ar:O_2 50:50), (c) $PrNbO_4$ and (d) $MnNb_2O_6$.

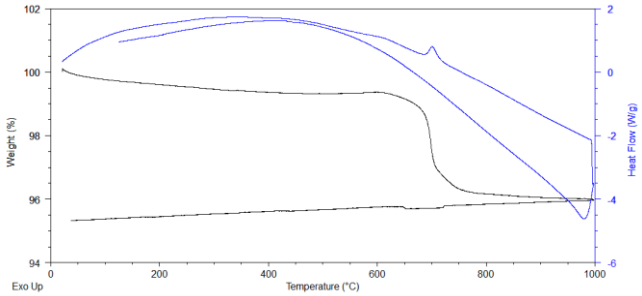

Figure I.41. TGA/DSC of (FeCl)$PrNb_2O_7$ under Ar.

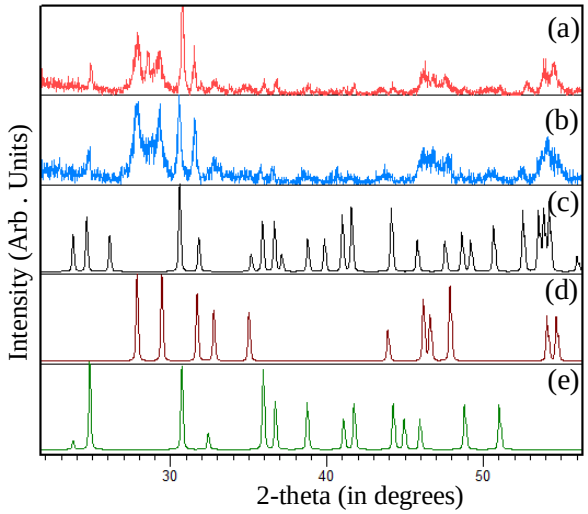

Figure I.42. (a) XRPD of (FeCl)$PrNb_2O_7$ after TGA at 695 (Ar), (b) (FeCl)$PrNb_2O_7$ after TGA at 1000 (Ar:O2 50:50), (c) $FeNb_2O_6$, (d) $PrNbO_4$ and (e) $FeNbO_4$.

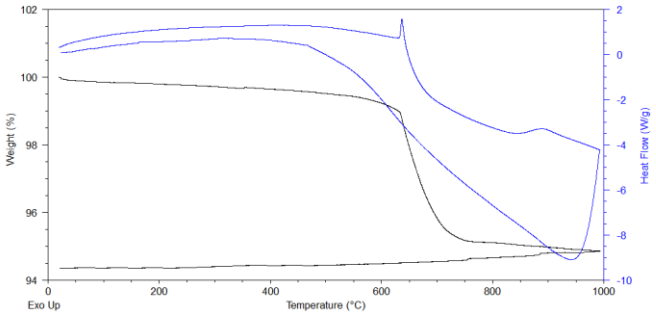

Figure I.43. TGA/DSC of (CoCl)$PrNb_2O_7$ under Ar.

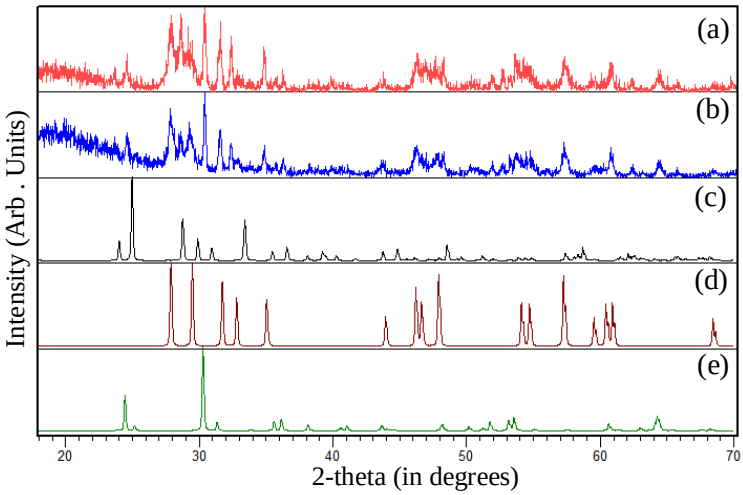

Figure I.44 XRPD of (a) (CoCl)$PrNb_2O_7$ after TGA at 636 (Ar), (b) (CoCl)$PrNb_2O_7$ after TGA at 1000 (Ar:O_2 50:50), (c) $CoNbO_4$, (d) $PrNbO_4$ and (e) $CoNb_2O_6$.

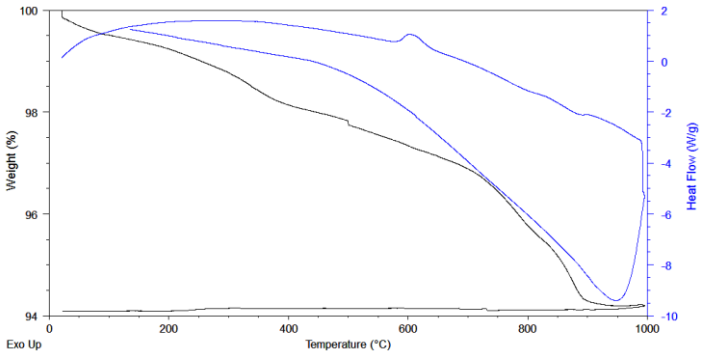

Figure I.45. TGA/DSC of (CuF)$PrNb_2O_7$ under Ar.

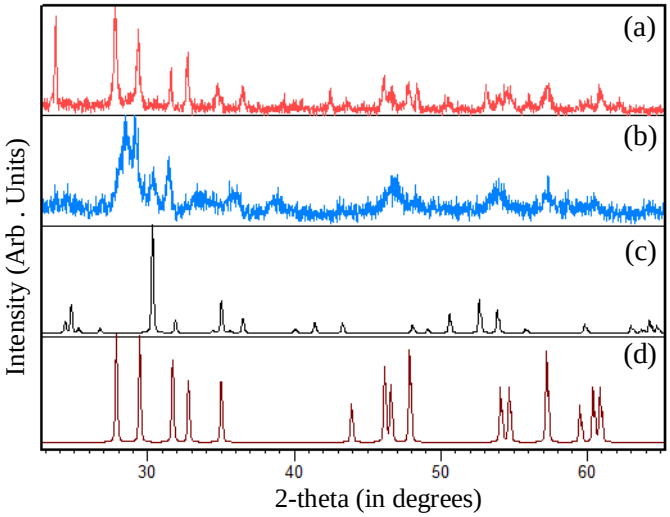

Figure I.46. XRPD of (CuF)$PrNb_2O_7$ after TGA at 1000 (Ar), (b) (CuF)$PrNb_2O_7$ after TGA at 1000 (Ar:O_2 50:50), (c) $CuNb_2O_6$ and (d) $PrNbO_4$.

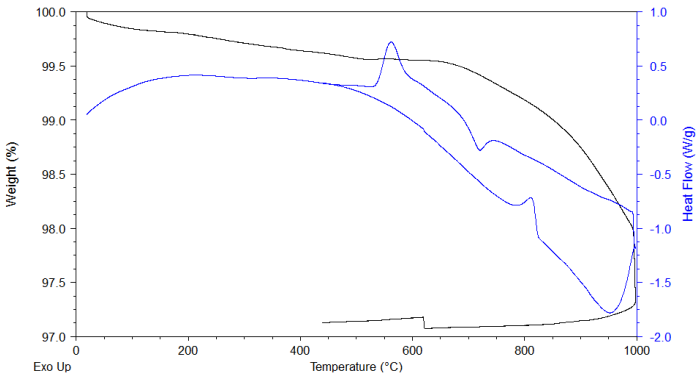

Figure I.47. TGA/DSC (MnF)$PrNb_2O_7$ under Ar.

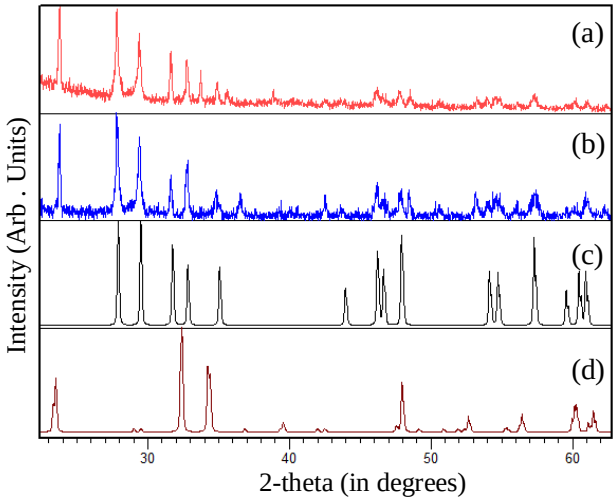

Figure I.48. XRPD of (a)(MnF)$PrNb_2O_7$ after TGA at 1000 (Ar), (b) (MnF)$PrNb_2O_7$ after TGA at 1000 (Ar:O_2 50:50), (c) $PrNbO_4$ and (d) $MnNb_2O_6$.

References

[1] Sato, M.; Jin, T.; Ueda, H. *Chem. Lett*. **1994**, *23 (1),* 161-164.

[2] M. Sato, J. Abo and T. Jin. *Solid State Ionics*. **1992**, *57*, 285-293.

[3] Sato, M.; Abo, J.; Jin, T.; Ohta, M. *J. Alloys Compd*. **1993**, *192(1-2)*, 81-83.

[4] Montasserasadi, D.; Granier, M.; Spinu, L.; Chandra Rai, S.; Zhou, W.; Wiley, J. B., *J. Chem. Soc, Dalton Trans*. (**2015**) Accepted.

[5] Armstrong, A. R.; Anderson, P. A. *Inorg. Chem*. **1994**, *33(19)*, 4366−4369.

[6] Kumada, N.; Kinomura, N.; Sleight, A. W. *Acta Crystallogr*., Sect. C: Cryst. Struct. Commun. **1996**, *52(5)*, 1063−1065.

[7] Tsirlin, A. A.; Abakumov, A. M.; Ritter, C.; Rosner, H. *Phys. Rev. B: Condens. Matter*. **2012**, *86*, 064440.

[8] Viciu, L.; Caruntu, G.; Royant, N.; Koenig, J.; Zhou, W. L.; Kodenkandath, T. A.; Wiley, J. B. *Inorg. Chem*. **2002**, *41(13)*, 3385−3388.

[9] Viciu, L.; Koenig, J.; Spinu, L.; Zhou, W. L.; Wiley, J. B. *Chem. Mater*. **2003**, *15(7)*, 1480-1485.

[10] Viciu, L.; Golub, V. O.; Wiley, J. B. *J. Solid State Chem*. **2003**, *175(1)*, 88-93.

Appendix X

Trials on manipulation of Other Layered Perovskites

Table J.1. Tolerance factor for $ALnM_2O_7$ (A: Rb, Cs and Ln: Lanthanides and M: V, Nb, Ta)

Compound	Final Products	$^*T_f$
$RbCeNb_2O_7$	$CeNbO_4$	0.908
$RbCeTa_2O_7$	$RbCeTa_2O_7 + CeO_2$	0.904
$RbLaV_2O_7$	$LaVO_4$	1.015
$RbLaNb_2O_7$	$RbLaNb_2O_7$	0.960
$RbLaTa_2O_7$	$RbLaTa_2O_7$	0.955
$RbPrNb_2O_7$	$RbPrNb_2O_7$	0.946
$RbPrTa_2O_7$	$RbPrTa_2O_7$	0.942
$RbNdV_2O_7$	NdV_2O_4	0.994
$RbNdNb_2O_7$	$RbNdNb_2O_7$	0.94
$RbNdTa_2O_7$	$RbNdTa_2O_7$	0.936
$RbSmNb_2O_7$	$SmNbO_4$	0.93
$RbSmTa_2O_7$	$RbSmTa_2O_7$	0.925
$RbEuNb_2O_7$	$EuNbO_4$	0.925
$RbEuTa_2O_7$	$EuTa_2O_7$	0.921
$RbGdNb_2O_7$	$GdNbO_4$	0.921
$RbGdTa_2O_7$	$GdTaO_4$	0.917
$RbTbNb_2O_7$	$TbNbO_4$	0.916
$RbTbTa_2O_7$	$TbTa_3O_9 + Tb_4O_7$	0.911
$RbDyNb_2O_7$	$DyNbO_4$	0.911
$RbDyTa_2O_7$	$DyTaO_4$	0.907
$RbHoNb_2O_7$	$HoNbO_4$	0.906
$RbHoTa_2O_7$	$HoTaO_4$	0.902
$RbErNb_2O_7$	$ErNbO_4$	0.902
$RbErTa_2O_7$	$ErTaO_4$	0.898
$RbInNb_2O_7$	$InNbO_4$	0.863
$RbCa_2Nb_3O_{10}$	$RbCa_2Nb_3O_{10}$	0.94

$^*T_f$: Tolerance Factor calculated for $LnMO_3$

The results from Table J.1 reveals the compounds with $0.925 < TF < 0.955$ resulted in layered perovskites otherwise the perovskites is the final phase. $RbSmTa_2O_7$ looks like is the last member of layered perovskite for lanthanum series.

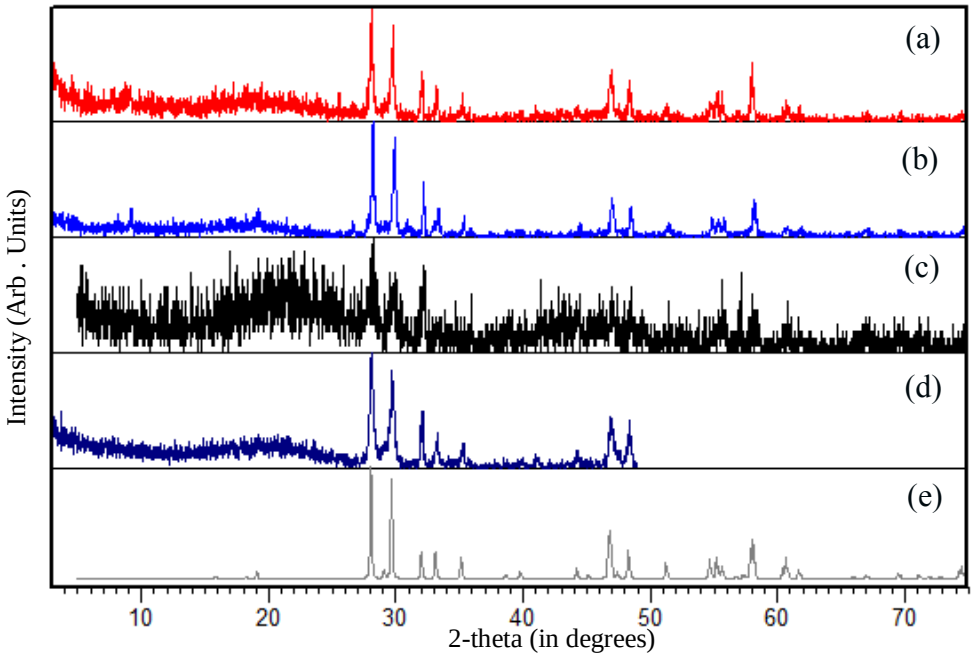

Figure J.1. XRPD of Rb_2CO_3+ Sm_2O_3+ Nb_2O_5 (a) at 1000 for 1 day, (b) 1100 for 1 day, (c) 1100 for 50 hrs, (d) excess 5-fold molar excess of RbCl at 1100 for 26 hrs and (e) $SmNbO_4$.

Table J.2. Ion exchange reactions of $ABiNb_2O_7$/$ALnTa_2O_7$ (A: Rb, Cs and Ln: Pr, Nd, Sm)

	Temp °C	Final Products
$ABiNb_2O_7$+ $ZnCl_2$ $ALnTa_2O_7$	300-375 for 3-14 days	BiOCl + $ZnNb_2O_6$ + RbCl $ALnTa_2O_7$
$ABiNb_2O_7$+ $NiCl_2$ $ALnTa_2O_7$	335-470 for 7-14 days	$ABiNb_2O_7$ $ALnTa_2O_7$
$ABiNb_2O_7$+ $AgNO_3$ $ALnTa_2O_7$	230-430 for 3-14 days	$ABiNb_2O_7$ $ALnTa_2O_7$
$ABiNb_2O_7$+ $CoCl_2$ $ALnTa_2O_7$	300-420 for 5-14 days	$ABiNb_2O_7$ $ALnTa_2O_7$
$ABiNb_2O_7$+ $MnCl_2$ $ALnTa_2O_7$	390-420 for 4-7days	$ABiNb_2O_7$ $ALnTa_2O_7$
$ABiNb_2O_7$+ $CrCl_2$ $ALnTa_2O_7$	400 for 14 days	$ABiNb_2O_7$ $ALnTa_2O_7$
$ABiNb_2O_7$+ VCl_3 $ALnTa_2O_7$	400 for 14 days	$ABiNb_2O_7$ $ALnTa_2O_7$
$ABiNb_2O_7$+ $TiCl_3$ $ALnTa_2O_7$	400 for 14 days	$ABiNb_2O_7$ $ALnTa_2O_7$

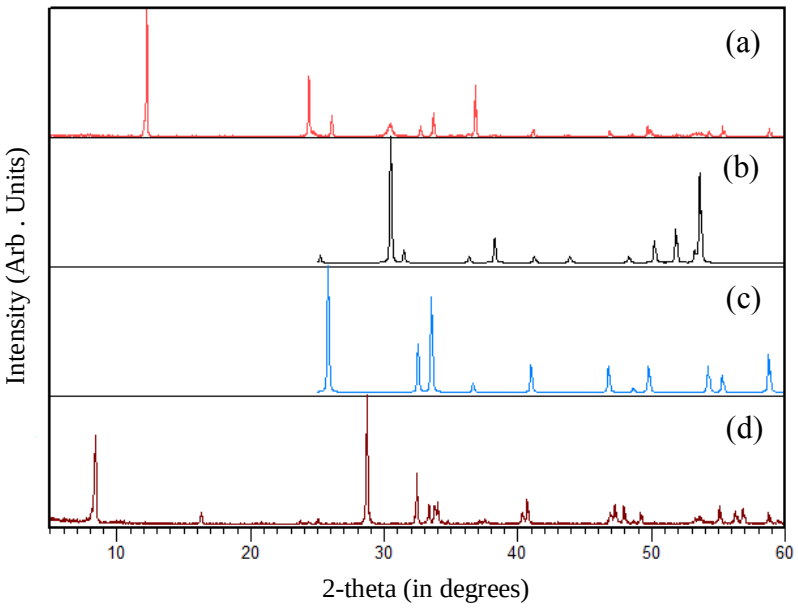

Figure J.2. XRPD of $RbBiNb_2O_7$ and $ZnCl_2$ (a) $RbBiNb_2O_7$ +$ZnCl_2$, (b) BiOCl, (c) $ZnNb_2O_6$ and (d) $RbBiNb_2O_7$.

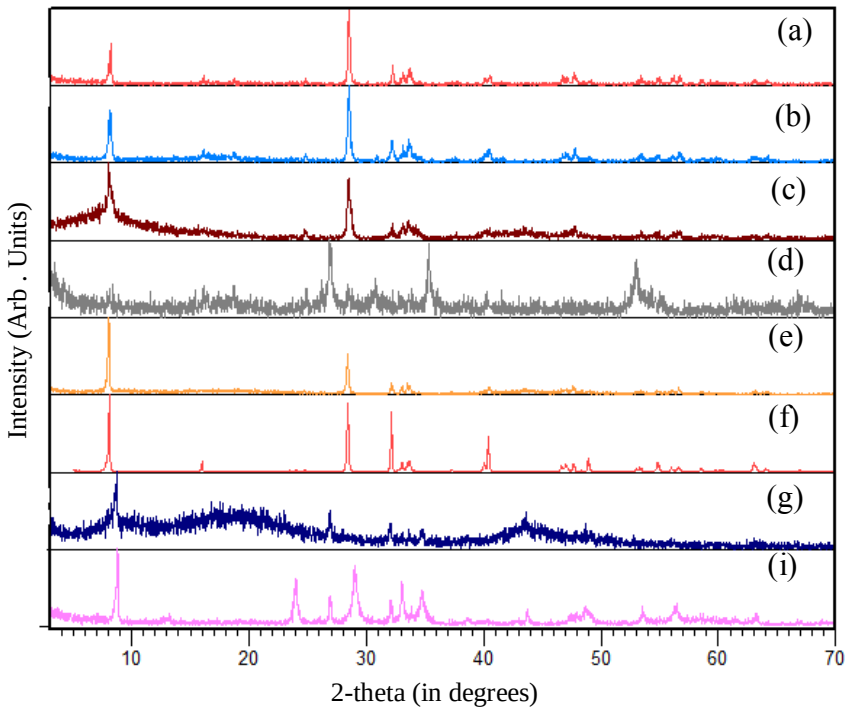

Figure J.3. XRPD of $RbBiNb_2O_7$ and $NiCl_2$ (a) $RbBiNb_2O_7$+ $NiCl_2$ 340 °C 7 days, (b) 400 °C 7 days, (c) 400 °C 10 days, (d) 470 °C 7 days, (e) 80-fold excess of KCl 350 °C 7 days, (f) $RbBiNb_2O_7$, (g) $LiBiNb_2O_7$ + $NiCl_2$ 350 °C 7 days and (i) $LiBiNb_2O_7$.

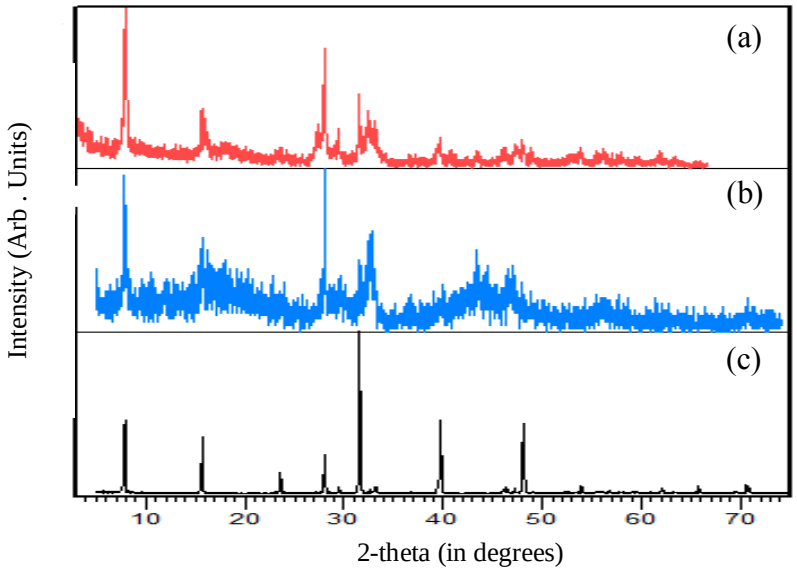

Figure J.4. $RbBiNb_2O_7$ + $AgNO_3$. (a) $RbBiNb_2O_7$+ $AgNO_3$ 260 °C 4 days, (b) 350 °C 3 days17 hrs and (c) $CsBiNb_2O_7$.

Table J.3.$RbBiNb_2O_7$/$RbLnTa_2O_7$ and PPh_4Br

$ALnM_2O_7$+ PPh_4Br	Temp °C	Results
$ABiNb_2O_7$	300,3 days	$ABiNb_2O_7$
$ANdTa_2O_7$	300,3 days	$ANdTa_2O_7$
$APrTa_2O_7$	300,3 days	$APrTa_2O_7$
$RbSmTa_2O_7$	300,3 days	$RbSmTa_2O_7$

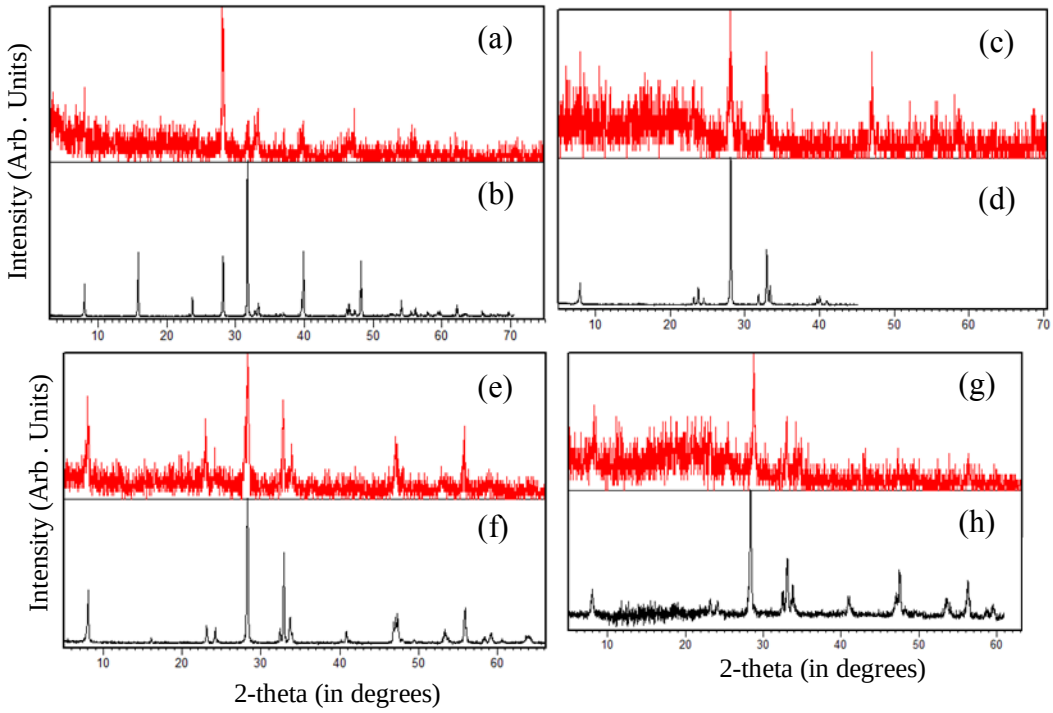

Figure J.5. (a) $CsBiNb_2O_7$ + PPh_4Br 300 °C 3 days, (b) $CsBiNb_2O_7$, (c) $CsNdTa_2O_7$ + PPh_4Br 300 °C 3 days, (d) $CsNdTa_2O_7$, (e) $RbPrTa_2O_7$ + PPh_4Br 300 °C 3 days, (f) $RbPrTa_2O_7$, (g) $RbSmTa_2O_7$ +PPh_4Br 300 °C 3 days and (h) $RbSmTa_2O_7$.

Table J.4.$RbBiNb_2O_7$/$RbLnTa_2O_7$ and $(VO)SO_4$

$ALnM_2O_7$+ $(VO)SO_4.3H_2O$	**Conditions**	**Results**
$ABiNb_2O_7$	65°C,3 days	$ABiNb_2O_7$
$ANdTa_2O_7$	160°C,3 days	$ANdTa_2O_7$
$APrTa_2O_7$	60-200°C,1-3 day(s)	$APrTa_2O_7$
$RbSmTa_2O_7$	145°C,1day	$RbSmTa_2O_7$

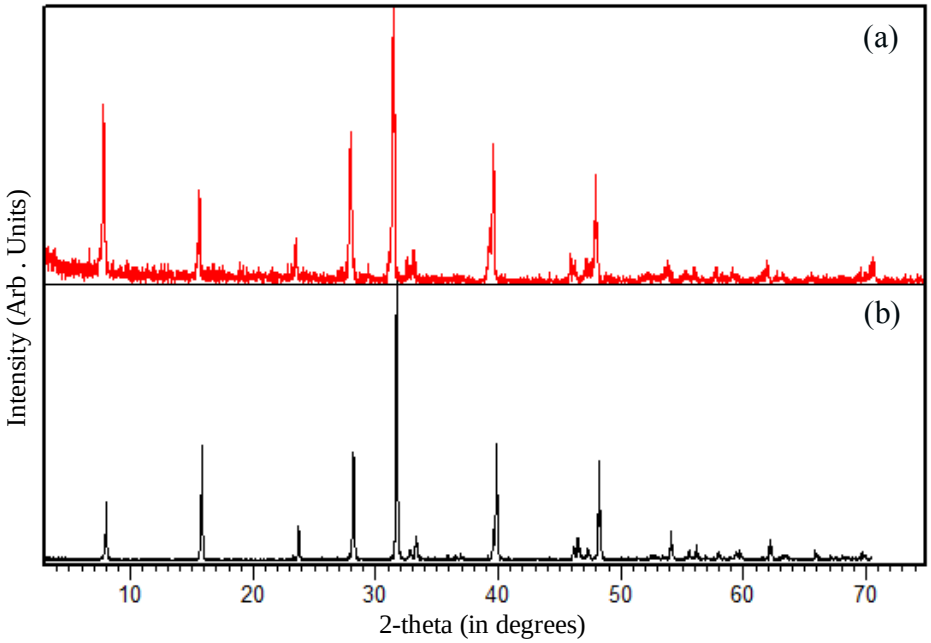

Figure J.6. (a) $CsBiNb_2O_7$ and (b) $CsBiNb_2O_7$ and $(VO)SO_4$ at 65 °C 5 days.

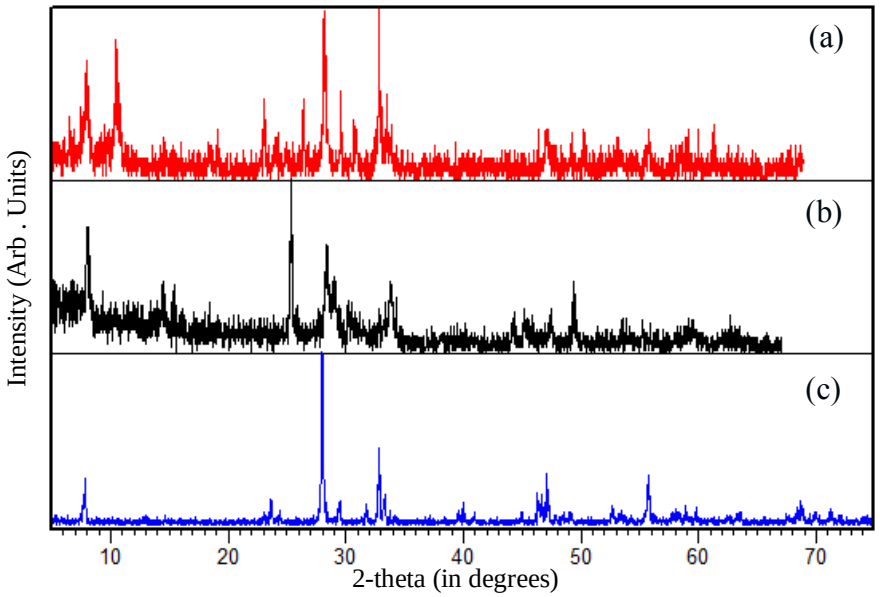

Figure J.7. $CsNdTa_2O_7$ and $(VO)SO_4$ (a) 160 °C in water, (b) 160 °C in toluene and (c) $CsNdTa_2O_7$.

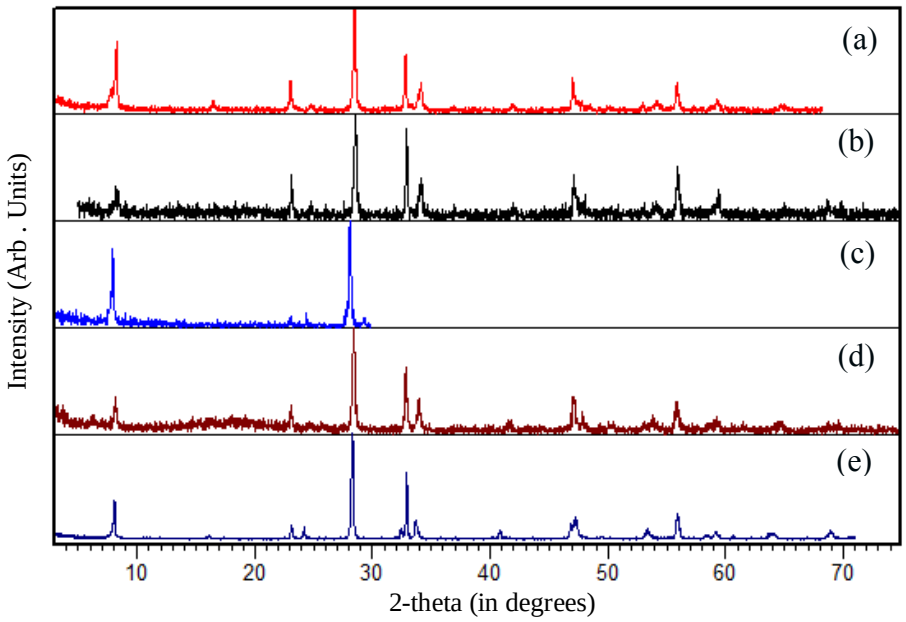

Figure J.8. $RbPrTa_2O_7$ and $(VO)SO_4$ (a) 120 ° C, (b) 145 °C, (c) 200 °C, (d) 60 °C and (e) $RbPrTa_2O_7$.

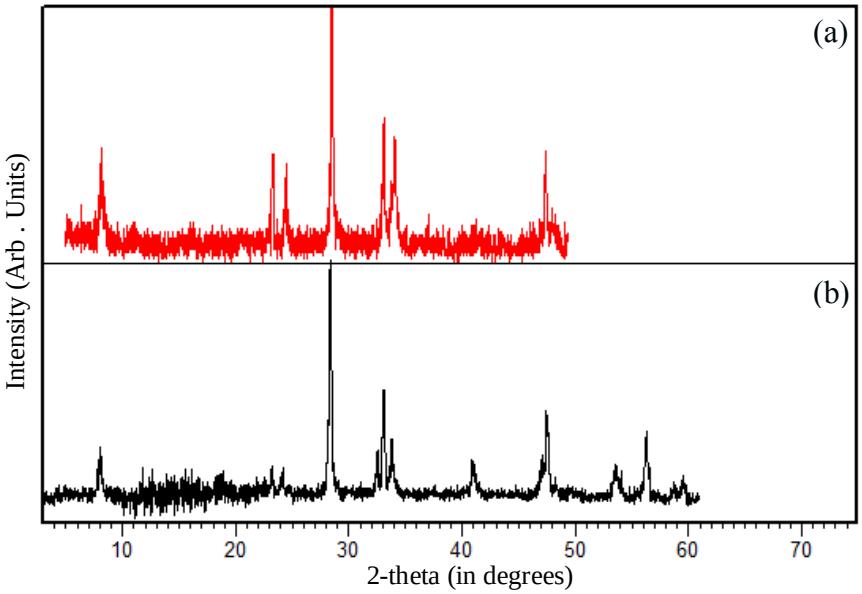

Figure J.9. $RbSmTa_2O_7$ and $(VO)SO_4$ (a) 145 °C and (b) $RbSmTa_2O_7$.

Table J.5.$RbPrTa_2O_7$ and BiOCl

$APrTa_2O_7$+ BiOCl	**Conditions**	**Results**
$APrTa_2O_7$	350-950°C,6 hr-7 day(s)	$APrTa_2O_7$+ BiOCl

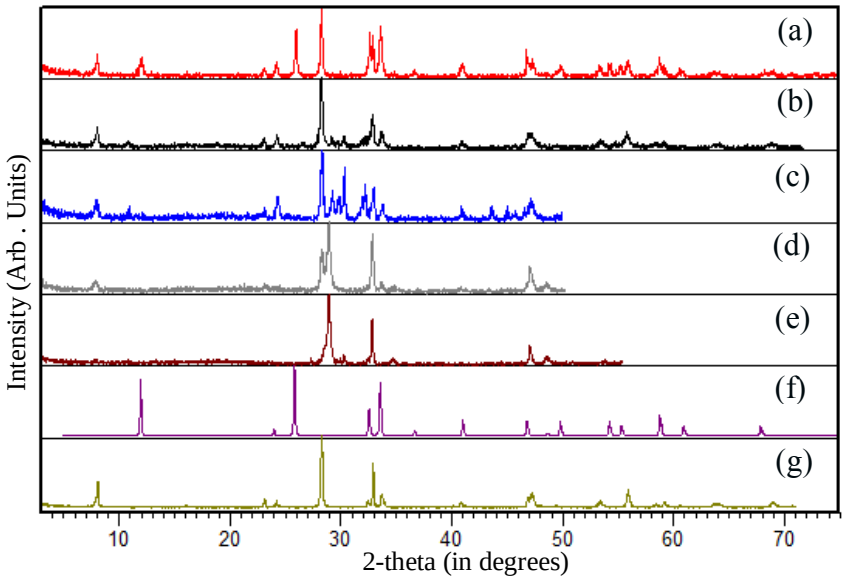

Figure J.10. $RbBiNb_2O_7$/$RbLnTa_2O_7$ and BiOCl (a) 350 °C 7 days, (b) 600 °C 6 hrs, (c) 600 °C 18 hrs, (d) 850 °C1 day, (e) 950 °C 20 hrs, (f) BiOCl and (g) $RbPrTa_2O_7$.

Table J.6. $RbBiNb_2O_7$/$RbLnTa_2O_7$ and HCl

$ALnM_2O_7$+ HCl	**Conditions**	**Results**
$ABiNb_2O_7$	0.1M-1M, 60°C,3 days	$ABiNb_2O_7$
$APrTa_2O_7$	HCl 1M-HNO_3 6M, 100-120°C,1-3 day(s)	$APrTa_2O_7$
$RbSmTa_2O_7$	HCl 0.5-1M-HNO_3 0.1-6M, 60°C,3 days	$RbSmTa_2O_7$

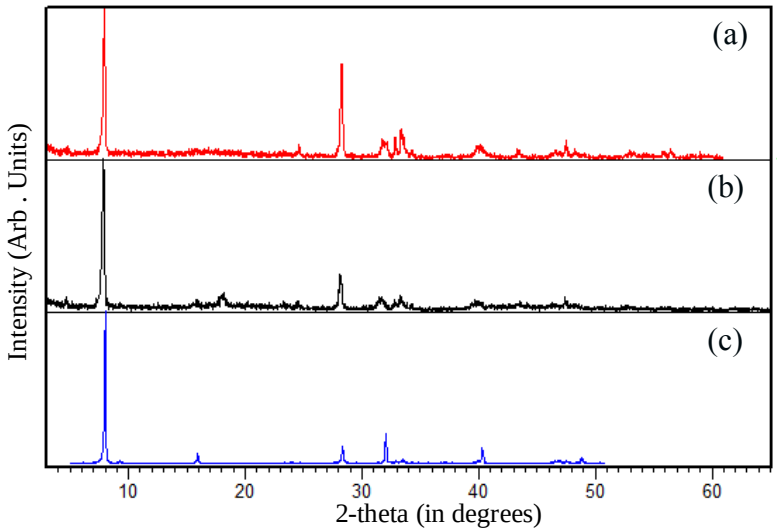

Figure J.11. $RbBiNb_2O_7$ and HCl (a) HCl 0.1 M 60 °C 3 days, (b) HCl 1M 60 °C 3days and (c) $RbBiNb_2O_7$.

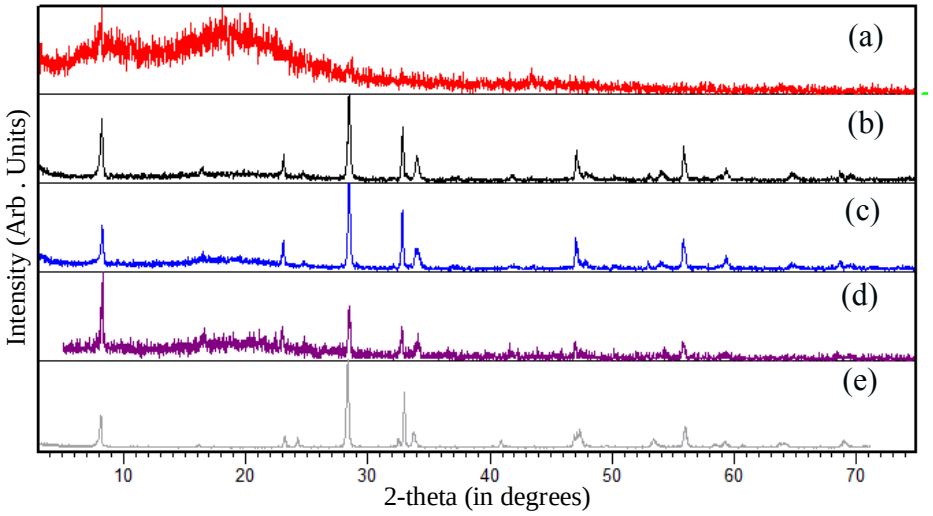

Figure J.12. $RbPrTa_2O_7$and (a) HCl 1 M 60 °C 3 days, (b) HNO_3 6 M 100 °C 2 days, (c) HNO_3 6 M 100 °C 1 day, (d) HNO_3 6 M 120 °C 1 day and (e) $RbPrTa_2O_7$.

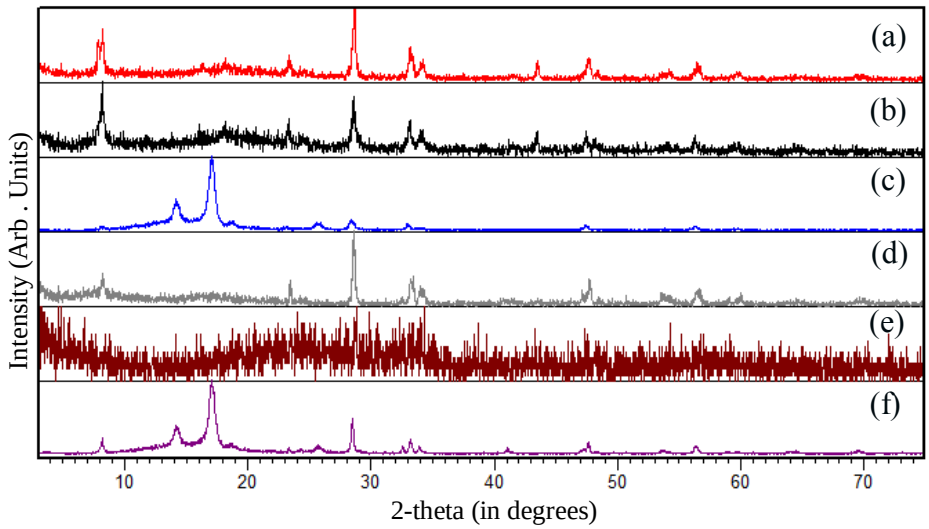

Figure J.13. $RbSmTa_2O_7$ and (a) HCl 0.5 M 60 °C 3 days, (b) HCl 1 M 60 °C 3 days, (c) HNO_3 0.1 M 60 °C 3 days, (d) HNO_3 0.1 M 60 °C 3 days , (e) HNO_3 6 M 60 °C 3 days and (f) $RbSmTa_2O_7$.

Table J.7. $RbBiNb_2O_7$ and NH_4NO_3

$ABiNb_2O_7$+ NH_4NO_3	**Conditions**	**Results**
$ABiNb_2O_7$	210-400°C,1-14day(s)	$ABiNb_2O_7$

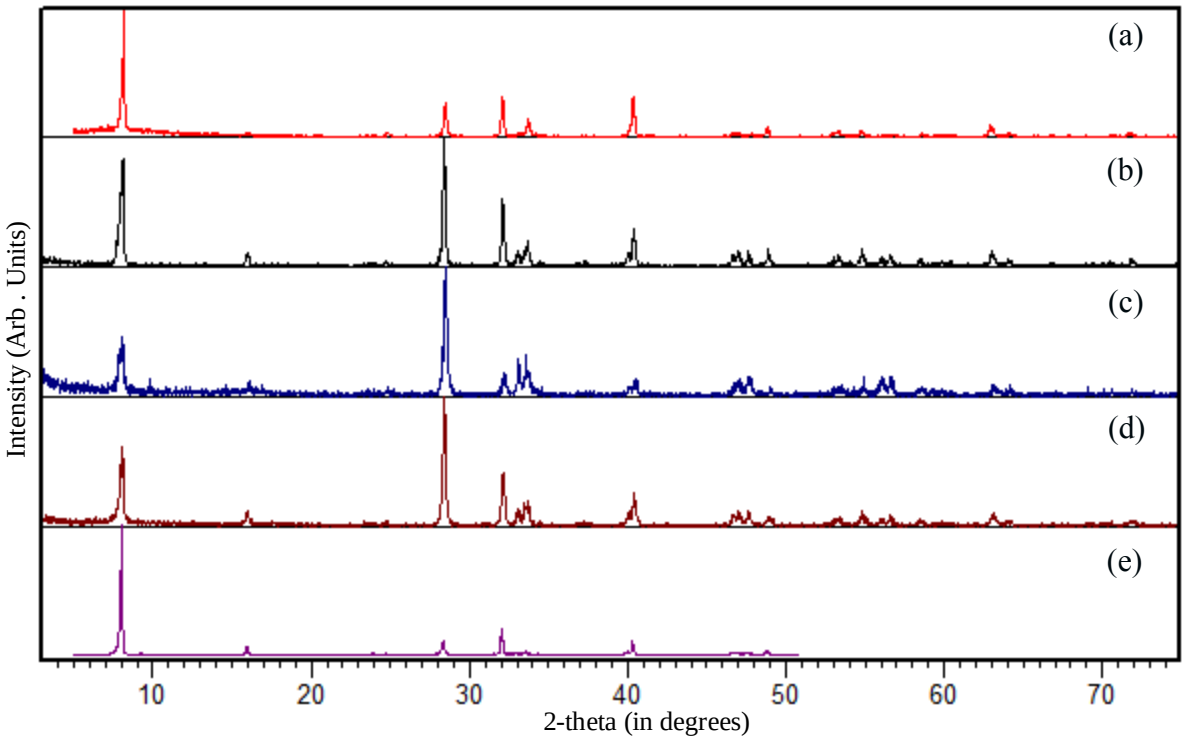

Figure J.14. $RbBiNb_2O_7$ and NH_4NO_3 (a) 210 °C 1 day, (b) 270 °C 7 days, (c) 350 °C 14 days, (d) 400 °C 7 days and (e) $RbBiNb_2O_7$.

Vita

Dariush Montasserasadi was born in Tehran, Iran on April 11, 1979, the middle son of Mercedeh Karimkhani and Reza Montasserasadi. After graduation from Alborz high school, Tehran Iran, in 1997, he entered Khajeh Nasir-al-din Toosi University (K.N.T) Tehran, Iran and graduated 2002 Sep with Bachelor of Science degree in applied chemistry. Dariush continued his study at University of Tehran, Tehran, Iran and received Master of science degree in Inorganic chemistry 2006 Jan. He served as a Navy officer with first lieutenant degree from 2002 for 20 months to fulfill his military duty. In August 2009 he entered University of New Orleans, Louisiana, USA under supervision of Prof John. B Wiley and 2012 he received a Master of Science in solid state chemistry.